



저작자표시-비영리-변경금지 2.0 대한민국

이용자는 아래의 조건을 따르는 경우에 한하여 자유롭게

- 이 저작물을 복제, 배포, 전송, 전시, 공연 및 방송할 수 있습니다.

다음과 같은 조건을 따라야 합니다:



저작자표시. 귀하는 원저작자를 표시하여야 합니다.



비영리. 귀하는 이 저작물을 영리 목적으로 이용할 수 없습니다.



변경금지. 귀하는 이 저작물을 개작, 변형 또는 가공할 수 없습니다.

- 귀하는, 이 저작물의 재이용이나 배포의 경우, 이 저작물에 적용된 이용허락조건을 명확하게 나타내어야 합니다.
- 저작권자로부터 별도의 허가를 받으면 이러한 조건들은 적용되지 않습니다.

저작권법에 따른 이용자의 권리는 위의 내용에 의하여 영향을 받지 않습니다.

이것은 [이용허락규약\(Legal Code\)](#)을 이해하기 쉽게 요약한 것입니다.

[Disclaimer](#)

공학박사 학위논문

**Integrated Simulation Method Based on  
Multibody Dynamics for Production Design  
Verification in Ships and Offshore Structures**

선박 및 해양구조물의 공법 설계 검증을 위한  
다물체 동역학 기반의 통합 시뮬레이션 방법

2018년 8월

서울대학교 대학원  
조선해양공학과  
함 승 호

# **Abstract**

## **Integrated Simulation Method Based on Multibody Dynamics for Production Design Verification in Ships and Offshore Structures**

It is the most important to verify the safety of the production design before the real operation. However, the verification which depends on the experience of the production engineer or the rule and regulation cannot be clearly proven or results in overestimation. Therefore, the verification based on dynamic analysis is widely adopted. However, it is impossible for existing programs to support some mechanical equipment such as the equalizer and SPMT (Self-Propelled Modular Transporter). Therefore, this study analyzes the requirements that are essential to simulate the lifting and erection operation in ships and offshore structures and proposes the integrated simulation framework based on multibody dynamics. The proposed framework is composed of five layers such as simulation core layer for solving the equations of motion, interface layer for data communication, simulation components layer including constraints, forces and collision, equipment layer, and service layer. This study develops a dedicated and differentiated program for dynamic analysis in ships and offshore structures, named SyMAP (SyDLab's Multibody Analysis Program).

The proposed simulation framework integrates several modules based on various theoretical backgrounds. First of all, the equations of motion are based on multibody

dynamics. Among the several formulations, we adopt the DELE (Discrete Euler-Lagrange Equation) to achieve the robustness during numerical integration. Furthermore, we formulate the equations of motion of the 1D frame element and 2D shell element based on ANCF (Absolute Nodal Coordinate Formulation). Kinematic constraints including joints and constraint-based wire rope between the rigid bodies, and between the rigid and flexible bodies are also derived. Especially, an equalizer which distributes the tension of wire ropes between the load and equipment equally is modeled based on the real mechanism by using the constraint-based wire rope.

Meanwhile, we also deal with special issues in collision detection and response. Because the shape exports from the ship CAD system contains unenclosed meshes, we propose the position difference method which checks an intersection using the line segment made by the two vertices or the trigonal prism consisting of the two triangular meshes at time  $t_0$  and  $t_1$ . Furthermore, BVH (Bounding Volume Hierarchy) and exclusion boxes were adopted to increase the performance. For collision response, non-interpenetration constraint method between a vertex and a plane is derived. This method is applicable when two bodies collide at the multiple points, and it does not compulsively violate the kinematic constraint because the collision force was also solved together when the equations of motion were solved numerically. Moreover, the collision force could be determined automatically, reflecting material properties such as restitution and softness.

This study proposes the modeling of the mechanical parts of the SPMT taking into consideration the axle compensation mechanism to maintain the level of the platform when the SPMT drives over an uneven roadway by lifting up and down the wheel. As external forces, hydrodynamic force, wind force, current force, and mooring force are also explained.

For the verification, comparison of the benchmarking tests of multibody systems and



the examples of commercial multibody software DAFUL is conducted. The analytic solutions and the simulation results are compared in case of the flexible multibody dynamics. To verify the characteristics of the motion due to the hydrodynamic forces, the motion of the floating barge is compared with RAO given by WADAM, OrcaFlex, and SIMA. For the validation, the simulation results are compared with the data collected in the real operations.

Finally, we provide four representative applications such as block lifting using equalizers, LPG tank erection considering a collision, thin plate block lifting considering deformation, and block offloading using SPMT, which have not been solved before. We conclude that the problems issued in ships and offshore structures are solved by the proposed or adopted methods. We convince that the developed program based on the proposed integrated simulation framework is able to cover all of the operations in ships and offshore structures.

Keywords: Integrated simulation method; production design verification; Multibody dynamics; Flexible multibody dynamics; Absolute nodal coordinate formulation; Discrete Euler-Lagrange equation; Constraint-based wire rope; Non-interpenetration constraint; Collision; Equalizer; Self-propelled modular transporter (SPMT);

Student number: 2014-30335

# Contents

<b>Abstract</b> .....	<b>i</b>
<b>Nomenclature</b> .....	<b>1</b>
<b>1. Introduction</b> .....	<b>2</b>
<b>1.1. Research necessities</b> .....	<b>2</b>
<b>1.2. Requirements for new design verification software</b> ....	<b>6</b>
1.2.1. Block lifting by the gantry and floating cranes.....	6
1.2.2. Block lifting considering deformation.....	9
1.2.3. Collision detection and response.....	10
1.2.4. Block offloading by SPMTs.....	11
1.2.5. Summary of requirements.....	15
<b>1.3. Related work</b> .....	<b>16</b>
1.3.1. Related work for simulation framework .....	16
1.3.2. Related work for dynamic analysis including flexible bodies .....	17
1.3.1. Related work for collision detection and response .....	18
1.3.2. Related work for the equalizer.....	19
1.3.3. Related work for block offloading .....	22
<b>1.4. Configuration of integrated simulation framework</b> ...	<b>24</b>
1.4.1. Simulation core layer.....	24
1.4.2. Interface layer.....	28
1.4.3. Simulation component layer.....	28
1.4.4. Equipment layer .....	28
1.4.5. Service layer .....	29

1.4.6. Library diagram and relations .....	29
1.4.7. New production design verification program .....	31
<b>1.5. Research objective and work scope .....</b>	<b>32</b>
<b>2. Theoretical backgrounds .....</b>	<b>33</b>
<b>2.1. Multibody dynamics for rigid bodies .....</b>	<b>33</b>
2.1.1. Discretization of the Euler-Lagrange equation .....	33
2.1.2. Discrete Euler-Lagrange equation with constraints .....	38
2.1.3. Discrete Euler-Lagrange equation with constraints and non-conservative forces .....	42
2.1.4. Regularization .....	44
2.1.5. Stabilization.....	47
2.1.6. Final form of the Discrete Euler-Lagrange equation.....	48
2.1.7. Physical meanings of the parameters in DELE .....	50
<b>2.2. Multibody dynamics for deformable bodies (1D frame element) .....</b>	<b>52</b>
2.2.1. Overview of flexible multibody dynamics .....	52
2.2.2. Kinematic description of frame element .....	54
2.2.3. Strain energy.....	61
(1) Axial strain energy .....	61
(2) Bending strain energy .....	65
(3) Torsional strain energy .....	66
(4) Summary of strain energy.....	68
2.2.4. Equations of motion for 1D frame element .....	68
(1) Euler-Lagrange equation revisit .....	68
(2) Kinetic energy of frame element.....	69
(3) Strain energy of frame element.....	71
(4) External forces .....	76
(5) Summary of equations of motion for 1D frame element .....	81
2.2.5. Discrete Euler-Lagrange equation including Flexible body.....	82
<b>2.3. Multibody dynamics for deformable bodies (2D shell</b>	

<b>element) .....</b>	<b>86</b>
2.3.1. Kinematic description of shell element.....	86
2.3.2. Strain energy for shell element.....	90
2.3.3. Strain energy for membrane element .....	94
2.3.4. Equations of motion for 2D shell element.....	95
(1) Kinetic energy of shell element .....	95
(2) Longitudinal and shear strain energy of shell element .....	97
(3) Bending and twisting strain energy of shell element.....	104
(4) External forces .....	105
(5) Summary of equations of motion for 2D shell element.....	110
<b>2.4. Kinematic constraints between rigid bodies.....</b>	<b>111</b>
2.4.1. Ball joint.....	111
2.4.2. Universal joint.....	113
2.4.3. Hinge joint.....	114
2.4.4. Slider joint.....	116
2.4.5. Fixed joint .....	117
2.4.6. Slider-hinge joint .....	119
2.4.7. Wire rope constraint.....	119
<b>2.5. Kinematic constraints between rigid and flexible bodies.....</b>	<b>123</b>
2.5.1. Joints on 1D frame element.....	123
(1) Ball joint between rigid and 1D flexible bodies.....	123
(2) Fixed joint between rigid and 1D flexible bodies .....	125
2.5.2. Joints on 2D shell element .....	127
(1) Ball joint between rigid and 2D flexible bodies.....	127
(2) Fixed joint between rigid and 2D flexible bodies .....	129
<b>2.6. Collision detection and response .....</b>	<b>132</b>
2.6.1. Collision detection.....	132
(1) Position difference method.....	134
(2) Space partitioning.....	141
(3) Exclusion box .....	143
2.6.2. Collision response.....	144

(1) Classification of collision response.....	145
(2) Non-interpenetration constraint method.....	146
(3) Consideration of material properties .....	151
2.6.3. Dynamic analysis including collision detection and response ...	153
2.6.4. Case studies of collision detection and response .....	154
(1) Collision for multibody system .....	154
(2) Performance tests of collision detection .....	158
(3) Collision between complex shapes .....	163
(4) Collision according to material properties.....	165
(5) Comparison with open source program .....	167
2.6.5. Consideration of impulse and impulsive force .....	168
<b>2.7. Modeling of Equalizer .....</b>	<b>173</b>
2.7.1. Real mechanism of the equalizer .....	173
2.7.2. Modeling of pulleys and the equalizer .....	174
2.7.3. Case studies .....	176
(1) Pulleys	176
(2) Equalizer .....	178
<b>2.8. Modeling of Self-propelled modular transporter (SPMT).....</b>	<b>184</b>
2.8.1. Modeling of SPMT and axle compensation mechanism .....	184
2.8.2. Replication of ballasting and de-ballasting for the floaters.....	187
2.8.3. Case studies of SPMT .....	189
(1) Pass through small bump .....	189
(2) Pass through inclined bump .....	192
<b>2.9. External forces.....</b>	<b>196</b>
2.9.1. Hydrodynamic force .....	196
2.9.2. Buoyant force .....	198
2.9.3. Wind force.....	199
2.9.4. Current force.....	201
2.9.5. Catenary mooring.....	202
2.9.6. Wire rope tension .....	203

<b>3. Verification and validation .....</b>	<b>204</b>
<b>3.1. Verification of multibody dynamics for rigid bodies.....</b>	<b>204</b>
3.1.1. Multibody benchmarking tests .....	204
(1) A01. Simple pendulum.....	204
(2) A02. N-four-bar mechanism.....	205
(3) A03. Andrew’s mechanism.....	207
(4) A04. Bricard’s mechanism.....	210
3.1.2. Verification by commercial software.....	213
(1) Three links connected by hinge joints (Open loop system) .....	214
(2) Three links connected by hinge joints (Closed loop) .....	216
<b>3.2. Verification of multibody dynamics for deformable bodies.....</b>	<b>219</b>
3.2.1. Verification of 1D frame element.....	219
3.2.2. Verification of 2D shell element.....	224
<b>3.3. Verification of hydrodynamic force .....</b>	<b>228</b>
3.3.1. Barge motion by a regular wave (I) .....	228
3.3.2. Barge motion by a regular wave (II).....	230
3.3.3. Barge motion connected by 4 springs .....	232
<b>3.4. Verification of catenary mooring .....</b>	<b>238</b>
<b>3.5. Validation by real operation (1) – Module erection</b>	<b>239</b>
3.5.1. Modeling.....	239
3.5.2. Scenario.....	243
3.5.3. Comparison of the posture by images .....	245
3.5.4. Comparison of tensions.....	247
<b>3.6. Validation by real operation (2) – LQ erection .....</b>	<b>250</b>
3.6.1. Modeling.....	250
3.6.2. Operation sequence.....	252
3.6.3. Comparison of tensions.....	253

<b>4. Applications.....</b>	<b>255</b>
<b>4.1. Block lifting using equalizers.....</b>	<b>255</b>
4.1.1. Load lifting simulation using a gantry crane .....	255
4.1.2. Load lifting simulation using a floating crane .....	259
<b>4.2. LPG tank erection considering collision .....</b>	<b>264</b>
<b>4.3. Thin plate block lifting considering deformation ...</b>	<b>270</b>
4.3.1. Thin plate block turn-over by a gantry crane .....	270
4.3.2. Thin plate block lifting by a floating crane .....	273
<b>4.4. Block offloading using SPMTs .....</b>	<b>276</b>
<b>5. Conclusion and future work .....</b>	<b>289</b>
<b>5.1. Summary.....</b>	<b>289</b>
<b>5.2. Contributions (Originality) .....</b>	<b>291</b>
5.2.1. Theoretical contributions .....	291
5.2.2. Contributions for applications .....	291
5.2.3. Other contributions.....	292
<b>5.3. Future works.....</b>	<b>292</b>
<b>Reference .....</b>	<b>293</b>
<b>국문 초록 .....</b>	<b>298</b>

# Figures

Figure 1-1. Design and operating stages of the module erection. ....	2
Figure 1-2. Design verification between design and operating stages. ....	3
Figure 1-3. Existing programs for simulating marine operation. ....	3
Figure 1-4. Front view of hooks, link beams, and hinge joints. ....	4
Figure 1-5. Drawing of the equalizer. ....	4
Figure 1-6. Modular transporter. ....	5
Figure 1-7. Gantry crane. ....	6
Figure 1-8. Mega floating crane. ....	7
Figure 1-9. Components of the equalizer. ....	8
Figure 1-10. Thin plate block. ....	9
Figure 1-11. Examples of dynamic analysis including collision. ....	10
Figure 1-12. Construction, load-out, transportation, lifting, and erection. ....	11
Figure 1-13. Offloading operation using SPMTs. ....	12
Figure 1-14. Overview of block offloading operation. ....	13
Figure 1-15. Collision between wheels and decks. ....	14
Figure 1-16. Ballasting and de-ballasting of the TB and FD. ....	14
Figure 1-17. Approximated mechanism for the equalizer. ....	20
Figure 1-18. Extension pulleys under the equalizer. ....	21
Figure 1-19. Configuration of integrated simulation framework based on multibody dynamics. ....	24
Figure 1-20. Typical formulation of multibody dynamics. ....	25
Figure 1-21. Library diagram and relation of the components in integrated simulation framework. ....	29
Figure 1-22. Main view of SyMAP. ....	31
Figure 2-1. Discretization of the action integral. ....	34
Figure 2-2. Summary of the discretization of the Euler-Lagrange equation. ....	37
Figure 2-3. Procedure to obtain discrete Euler-Lagrange Equation with constraints and non-conservative forces. ....	44
Figure 2-4. Velocity-level constraints and its discretization form. ....	47



Figure 2-5. Procedure of regularization and stabilization to obtain the final form of the discrete Euler-Lagrange equation.....	49
Figure 2-6. Principle how the regularization term works as if it were spring coefficient.	50
Figure 2-7. Physical meaning of the parameters in DELE.....	51
Figure 2-8 Introduction of flexible multibody dynamics.....	53
Figure 2-9. Definition of 1D frame and 2D shell elements.....	54
Figure 2-10. Line segment passing through two points .....	55
Figure 2-11. Cubic spline segment passing through two points and having two slope vectors. ....	57
Figure 2-12. Graphs of cubic Hermite shape function. ....	60
Figure 2-13. Kinematic description of a frame element.....	60
Figure 2-14. Deformation of a frame element.....	61
Figure 2-15. Spring stretched by $\delta$ due to $F$ .....	62
Figure 2-16. Bar element stretched by $\delta$ due to $F$ .....	62
Figure 2-17. Strain energy in bar element.....	64
Figure 2-18. Bending of the frame element. ....	65
Figure 2-19. Torsion of shaft element. ....	66
Figure 2-20. Frame element at time $t_0$ and $t_1$ .....	72
Figure 2-21. External force acting at an arbitrary point. ....	77
Figure 2-22. External force acting on all over the frame element.....	78
Figure 2-23. Damping force acting on the frame element .....	79
Figure 2-24. Summary of equations of motion for 1D frame element.....	81
Figure 2-25. Example of one flexible body and two rigid bodies.....	82
Figure 2-26. Mid-plane of shell element.....	86
Figure 2-27. Arbitrary point $P$ on the deformed mid-plane. ....	87
Figure 2-28. Interpolation of point $P$ using temporary point $A$ , and $B$ .....	87
Figure 2-29. Interpolation of point $A$ and the slope vector.....	88
Figure 2-30. Interpolation of point $B$ and the slope vector.....	89
Figure 2-31. Curvature-strain relation of bending and twisting.....	91
Figure 2-32. External force acting at an arbitrary point. ....	106
Figure 2-33. External force acting on all over the shell element .....	106

Figure 2-34. Damping force acting on the shell element .....	108
Figure 2-35. Summary of equations of motion for 2D shell element.....	110
Figure 2-36. Ball joint. ....	112
Figure 2-37. Universal joint. ....	113
Figure 2-38. Hinge joint. ....	115
Figure 2-39. Slider joint. ....	116
Figure 2-40. Fixed joint. ....	118
Figure 2-41. Slider-hinge joint. ....	119
Figure 2-42. Wire rope with a single element. ....	120
Figure 2-43. Wire rope with pulleys. ....	122
Figure 2-44. Ball joint between a rigid body and a frame element .....	123
Figure 2-45. Position vector of ball joint on the frame element.....	124
Figure 2-46. Slope vector defined on the frame element. ....	126
Figure 2-47. Reference vector initially coincided with a slope vector calculated from the frame element.....	126
Figure 2-48. Ball joint between a rigid body and a shell element.....	128
Figure 2-49. Position vector of ball joint on the shell element. ....	128
Figure 2-50. Slope vector defined on the shell element. ....	130
Figure 2-51. Reference vector initially coincided with a slope vector calculated from the shell element.....	130
Figure 2-52. Broad and narrow phase stages. ....	132
Figure 2-53. Unenclosed mesh in LPG tank. ....	133
Figure 2-54. LPG tank model.....	134
Figure 2-55. Vertex-mesh collision: Vertex on the moving body moves into the fixed body.....	135
Figure 2-56. Collision at the corner.....	136
Figure 2-57. Vertex-mesh collision: Vertex on the fixed body moves into the moving body.....	136
Figure 2-58. Collision between two moving bodies. ....	138
Figure 2-59. Collision detection failure in case of two moving bodies. ....	138
Figure 2-60. Vertex-mesh collision: Both bodies are moving.....	139
Figure 2-61. Edge-edge collision: Edge on the moving body moves into the fixed body.	

.....	140
Figure 2-62. Edge-edge collision: Both bodies are moving. ....	141
Figure 2-63. Procedure of BVH. ....	142
Figure 2-64. Traversal of two BVHs during the collision detection. ....	143
Figure 2-65. Examples of exclusion boxes applied to the LPG tank. ....	144
Figure 2-66. Classification of collision response. ....	146
Figure 2-67. Three statuses between two bodies. ....	146
Figure 2-68. Non-interpenetration constraint between a vertex and a plane. ....	147
Figure 2-69. Calculation of the frictional force. ....	149
Figure 2-70. Collision pair: Mesh and vertex. ....	150
Figure 2-71. Collision pair: two edges. ....	151
Figure 2-72. Spring coefficient proportional to the weight. ....	153
Figure 2-73. A numerical procedure for dynamic analysis including collision detection and response. ....	154
Figure 2-74. Collision test model for the multibody system. ....	155
Figure 2-75. Test results using the impulse-based method. ....	155
Figure 2-76. Test results using the force-based method. ....	156
Figure 2-77. Dropt two links connected by ball joint. ....	156
Figure 2-78. Collision test of multibody system. ....	157
Figure 2-79. Collision force of two links. ....	158
Figure 2-80. Performance test: Collision between two bunny models. ....	159
Figure 2-81. Performance test: Drop two bunny models on the plane. ....	160
Figure 2-82. Performance test: Drop LPG tank model on the plane. ....	161
Figure 2-83. Graphs of computing time of dropping LPG tank model on the plane. ....	162
Figure 2-84. Example of complex shape: LPG tank. ....	163
Figure 2-85. Example of complex shape: Hull structure. ....	163
Figure 2-86. Collision test between complex shapes. ....	164
Figure 2-87. Collision test according to restitution coefficients. ....	165
Figure 2-88. Position and velocity according to restitution coefficient. ....	166
Figure 2-89. Position according to softness of the material. ....	166
Figure 2-90. Unenclosed meshes for testing collision by Bullet. ....	167

Figure 2-91. Comparison of collision with open source program (Bullet). .....	168
Figure 2-92. Compression and expansion in the real collision. ....	169
Figure 2-93. Hard, medium, and soft collisions.....	170
Figure 2-94. Graphs of impulsive forces when the three boxes with different softness drop on the plane. ....	171
Figure 2-95. Estimation of impulsive force. ....	172
Figure 2-96. Internal structure of the equalizer. ....	173
Figure 2-97. Procedure of the adjustment of tensions acting on wire ropes through the equalizer. ....	174
Figure 2-98. Fixed and moving pulleys using the constraint-based wire rope.....	175
Figure 2-99. Arrangement of fixed and moving pulleys of the equalizer.....	176
Figure 2-100. Modeling of moving and fixed pulleys with a wire rope constraint.....	177
Figure 2-101. Simulation result of moving and fixed pulleys with the constraint-based wire rope.....	178
Figure 2-102. Modeling of the equalizer.....	179
Figure 2-103. Modeling of connections between the equalizer and the load.....	180
Figure 2-104. Simulation result: Motion of the equalizer and the load. ....	181
Figure 2-105. Simulation result: Motion of the sheaves in the equalizer.....	182
Figure 2-106. Graphs of wire rope tensions between the load and the equalizer.....	183
Figure 2-107. Modeling of the SPMT.....	185
Figure 2-108. Hydraulic suspension groups.....	186
Figure 2-109. Compensation mechanism of the SPMT. ....	186
Figure 2-110. Deformation of the platform of a SPMT.....	187
Figure 2-111. De-ballasting of the TB. ....	188
Figure 2-112. Trim change without ballasting and de-ballasting.....	188
Figure 2-113. Shift of center of gravity.....	189
Figure 2-114. Modeling of the SPMT. ....	189
Figure 2-115. Modeling of the block, two SPMTs, and the small bump. ....	190
Figure 2-116. SPMT test: Transport the block passing through the small bump. ....	191
Figure 2-117. Wheel height and loads.....	192
Figure 2-118. Modeling of the inclined bump. ....	193

Figure 2-119. SPMT test: Transport the block passing through the inclined bump. ....	194
Figure 2-120. Wheel height and loads. ....	195
Figure 2-121. Calculation of the hydrodynamic force. ....	197
Figure 2-122. Plane intersection under the water plane. ....	199
Figure 2-123. Wind speed, including mean wind speed and wind fluctuation. ....	201
Figure 2-124. Catenary cable with its own weight.....	202
Figure 2-125. Principle of the incompressible spring. ....	203
Figure 3-1. MBS benchmarking test A01. Simple pendulum. ....	204
Figure 3-2. Graphs of the displacement of simple pendulum. ....	205
Figure 3-3. MBS benchmarking test A02. N-four-bar mechanism. ....	206
Figure 3-4. Simulation results of A02 (N four-bar mechanism) ....	206
Figure 3-5. Graphs of the displacement of N four-bar mechanism. ....	207
Figure 3-6. MBS benchmarking test A03. Andrew’s mechanism. ....	208
Figure 3-7. Simulation results of A03 (Andrew’s mechanism).....	209
Figure 3-8. Graphs of the position F. ....	210
Figure 3-9. MBS benchmarking test A04. Bricard’s mechanism.....	211
Figure 3-10. Simulation results of A04 (Bricard’s mechanism). ....	212
Figure 3-11. Graphs of the position of point P3.....	213
Figure 3-12. Three links connected by hinge joints (open loop).....	214
Figure 3-13. Simulation results of three links connected by hinge joints (open loop)....	215
Figure 3-14. Graphs of z displacement of three links. ....	216
Figure 3-15. Three links connected by hinge joints (closed loop). ....	217
Figure 3-16. Simulation results of three links connected by hinge joints (closed loop). ....	217
Figure 3-17. Graphs of z displacement of three links. ....	218
Figure 3-18. Simple support of 1D frame element.....	219
Figure 3-19. Cantilever of 1D frame element. ....	221
Figure 3-20. Free falling pendulum of 1D frame element. ....	222
Figure 3-21. Comparison of the configuration of the free falling pendulum. ....	223
Figure 3-22. Simple support plate.....	224
Figure 3-23. Heavy membrane hanged on four corners: 2x1, 4x2, 8x4, 16x8 elements. ....	226
Figure 3-24. Motion RAO of the floating barge 1. ....	228

Figure 3-25. Motion RAO of the floating barge 2. ....	229
Figure 3-26. Motion RAO of the floating barge 3. ....	229
Figure 3-27. Verification of the barge motion with SIMA (heading angle 0 deg). ....	230
Figure 3-28. Verification of the barge motion with SIMA (heading angle 45 deg). ....	231
Figure 3-29. Verification of the barge motion with SIMA (heading angle 90 deg). ....	232
Figure 3-30. Modeling results in the mega floating crane simulator and OrcaFlex.....	233
Figure 3-31. Profile of catenary mooring.....	238
Figure 3-32. Overall models included in the erection simulation.....	239
Figure 3-33. Main dimensions and weight of the target module.....	240
Figure 3-34. Model of the mega floating crane.....	241
Figure 3-35. The names of the four hooks used in operation.....	242
Figure 3-36. Connection plan and simulation views between hooks and the module. ....	242
Figure 3-37. Mooring/anchoring plan and simulation views. ....	243
Figure 3-38. Graphs of the wind speed and the wind direction. ....	244
Figure 3-39. Simulation results from the different viewpoints. ....	245
Figure 3-40. Comparison of the target module laid on the quay.....	246
Figure 3-41. Comparison of the target module lifted by the mega floating crane. ....	247
Figure 3-42. Graph of the total tension during module erection.....	248
Figure 3-43. Graph of the wire rope tension of hooks 5, 6, 7 and 8.....	249
Figure 3-44. Model of LQ upper part.....	250
Figure 3-45. Overall models and connections.....	251
Figure 3-46. Mooring/anchoring plan and simulation views. ....	251
Figure 3-47 Operation sequence in real world.....	252
Figure 3-48. Tensions of the hooks displayed on the screen.....	253
Figure 3-49. Graphs of the total tension during LQ upper part erection.....	253
Figure 3-50. Graph of the wire rope tension of two pairs of hooks. ....	254
Figure 4-1. Modeling of load lifting using the gantry crane. ....	256
Figure 4-2. Wire ropes connected between the load and three equalizers. ....	256
Figure 4-3. Height change of pulleys of the equalizer during the simulation. ....	257
Figure 4-4. Simulation procedure of load lifting using the Goliath crane. ....	258
Figure 4-5. Graphs of wire rope tensions between the load and each equalizer. ....	259

Figure 4-6. Modeling of load lifting using a floating crane. ....	260
Figure 4-7. Wire ropes connected between the load and four equalizers. ....	261
Figure 4-8. Position change of the equalizers before and after equalizing. ....	262
Figure 4-9. Graphs of wire rope tensions between the load and each equalizer. ....	263
Figure 4-10. Modeling of LPG tank, hull structure, and the floating crane. ....	264
Figure 4-11. Original and collision shape using exclusion boxes. ....	265
Figure 4-12. Simulation results of Case 3: No collision. ....	267
Figure 4-13. Simulation results of Case 4: Occurrence of the collision. ....	268
Figure 4-14. Graphs of maximum collision forces according to time. ....	269
Figure 4-15. Modeling of the gantry crane and the thin plate block. ....	270
Figure 4-16. Scenario of thin plate block turn-over. ....	271
Figure 4-17. Graph of the maximum von-Mises stress. ....	272
Figure 4-18. Modeling of the floating crane and the thin plate block. ....	273
Figure 4-19. Stress inside the thin plate block according to the wave heading angle. ....	274
Figure 4-20. Graphs of the maximum stress according to wave heading angle. ....	275
Figure 4-21. Modeling of the TB, FD, SPMTs, and the block. ....	277
Figure 4-22. Link beams connected between the TB and FD. ....	277
Figure 4-23. Simulation results of the block offloading. ....	280
Figure 4-24. Graphs of block height, pitch angle, wheel height and loads for Case 1. ....	282
Figure 4-25. Graphs of block height, pitch angle, wheel height and loads for Case 2. ....	283
Figure 4-26. Graphs of block height, pitch angle, wheel height and loads for Case 3. ....	284
Figure 4-27. Graphs of block height, pitch angle, wheel height and loads for Case 4. ....	285
Figure 4-28. Graphs of block height, pitch angle, wheel height and loads for Case 5. ....	286
Figure 4-29. Graphs of block height, pitch angle, wheel height and loads for Case 6. ....	287

# Tables

Table 1-1. Requirements for new design verification software.....	15
Table 1-2. Related work for dynamic analysis including flexible bodies. ....	18
Table 1-3. Related work for block offloading. ....	22
Table 1-4. Pros and cons of multibody dynamics formulations. ....	27
Table 2-1. Summary of strain energy .....	68
Table 2-2 Joint type by the restriction on the degrees of freedom. ....	111
Table 2-3. Comparison of computing times: With and without BVH.....	159
Table 2-4. Comparison of computing time: With and without exclusion box.....	161
Table 2-5. Comparison of computing time: Both exclusion box and BVH. ....	162
Table 2-6. Estimation of impulsive forces .....	172
Table 2-7 Dimensions and loads of the SPMT. ....	184
Table 3-1. Analytic solution of simple support beam according to different beam properties.....	220
Table 3-2 Simulation results of simple support beam according to the number of elements.....	220
Table 3-3. Analytic solution of cantilever beam according to different beam properties. ....	221
Table 3-4 Simulation results of cantilever beam according to the number of elements..	222
Table 3-5. Main dimension and properties of free falling pendulum. ....	222
Table 3-6. Analytic solution of simple support plate according to Poisson's ratio. ....	224
Table 3-7 Simulation results of simple support plate according to the number of elements. ....	225
Table 3-8. Analytic solution of simple support plate according to Poisson's ratio. ....	225
Table 3-9 Simulation results of the plate with clamped edges according to the number of elements.....	226
Table 3-10. Main dimension and properties of free falling pendulum. ....	227
Table 3-11 Simulation results of the heavy membrane hanged on four corners according to the number of elements. ....	227
Table 3-12. Simulation cases according to the wave conditions. ....	233
Table 3-13. Comparison of motions according to the wave conditions. ....	234



Table 3-14. Comparison of tensions according to the wave conditions. ....	235
Table 3-15. Simulation cases according to the wind conditions. ....	235
Table 3-16. Comparison of motions according to the wind conditions.....	236
Table 3-17. Comparison of tensions according to the wind conditions. ....	236
Table 3-18. Simulation cases according to the current conditions. ....	236
Table 3-19. Comparison of motions according to the current conditions. ....	237
Table 3-20. Comparison of tensions according to the current conditions. ....	237
Table 3-21. Summary of verification for catenary mooring.....	238
Table 4-1. Wave conditions for LPG tank erection. ....	265
Table 4-2. Maximum stress and dynamic amplification factor .....	275
Table 4-3. Main dimensions and other properties of the models. ....	278
Table 4-4. Wave conditions. ....	279
Table 4-5. Safety criteria for dynamic analysis of block offloading. ....	280
Table 4-6. Comparison of safety criteria with the simulation results according to wave conditions .....	288

## Nomenclature

ANCF	Absolute Nodal Coordinate Formulation
BVH	Boundary Volume Hierarchy
DELE	Discrete Euler-Lagrange Equation
FFRF	Floating Frame of Reference Formulation
FD	Floating Dock
GUI	Graphical User Interface
LQ	Living Quater
PDM	Position Difference Method
RAO	Response Amplitude Operator
SPMT	Self-Propelled Modular Transporter
TB	Transportation Barge

# 1. Introduction

## 1.1. Research necessities

As new lifting methods are tried in the shipbuilding area, it becomes more difficult to predict the risks of the lifting operation. Moreover, as the weight and size of modules of offshore projects increase, it is not easy for production engineers to prove that the lifting plan is perfectly safe and that there is no reason for disqualification. Figure 1-1 shows an example of a lifting operation in the shipyard.

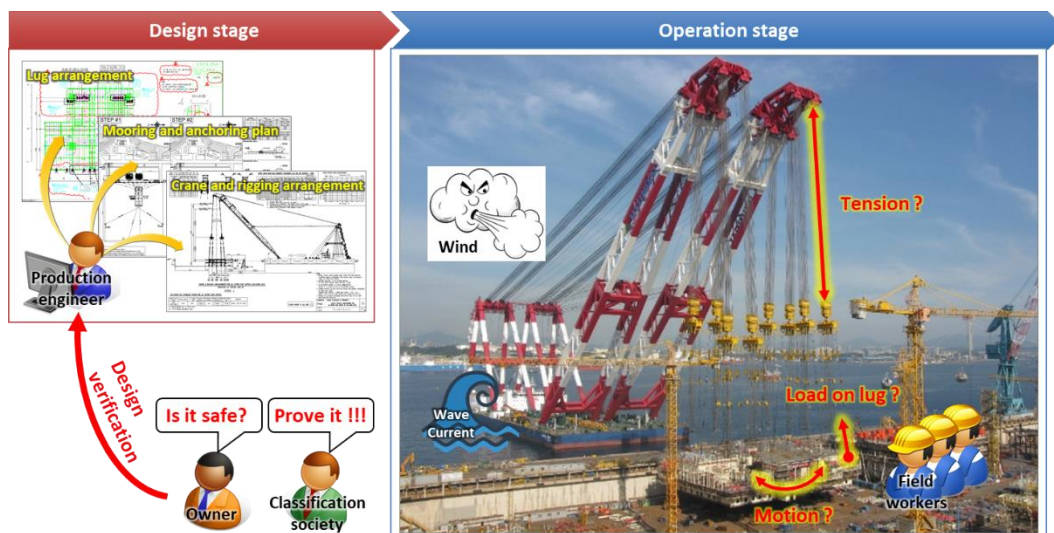


Figure 1-1. Design and operating stages of the module erection.

At the design stage, the production engineer should prepare the several drawings such as lug arrangement, mooring and anchoring plan, and crane and rigging arrangement. At the operation stage, the motion of the module, loads on lugs, and the tensions of wire ropes between the floating crane and the module are induced due to environmental conditions

such as wave, current, and wind. Therefore, a shipowner or a classification society requires design verification between design and operation stages (Figure 1-2).



Figure 1-2. Design verification between design and operating stages.

There are several methods for verifying the design. The first method is to depend on the experience of the production engineer. However, this method is very hard to be proven, and can't be learned. The biggest problem is that design verification depending on the experience is also useless in case of a new lifting concept which has never been tried before. The second method is to follow the rules and regulations. However, the rules and regulations result in overestimation, which increases the construction cost. There is also no appropriate rule to be applied in case of a new lifting concept. The third method is to use the existing programs such as MOSES [1], SIMA [2], and OrcaFlex [3], which can simulate the marine operation (Figure 1-3).

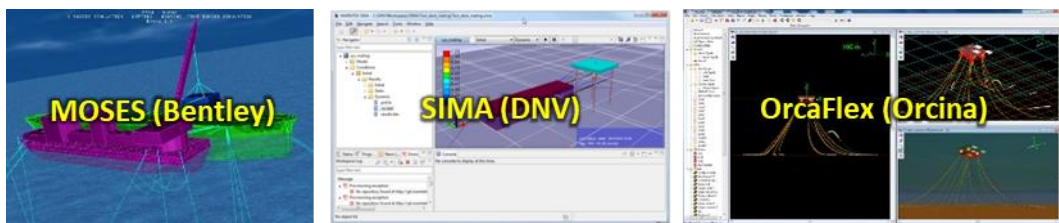


Figure 1-3. Existing programs for simulating marine operation.

It is impossible for existing programs to support some items of mechanical equipment, which are essential to model the floating crane. The first item of equipment is the link beam that is used to connect two hooks by a hinge joint, as shown in Figure 1-4.

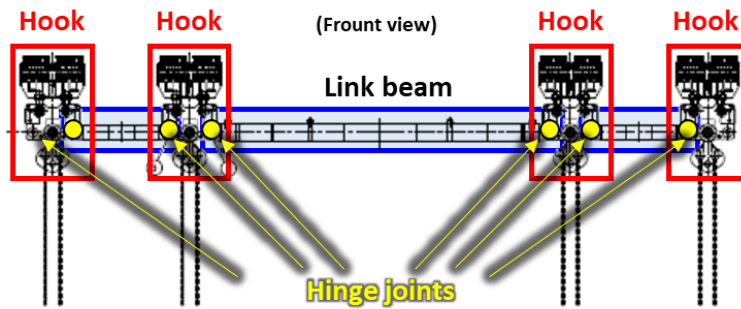


Figure 1-4. Front view of hooks, link beams, and hinge joints.

Another item of equipment is the equalizer. It is installed under the hook to connect multiple wire ropes between the load and the hook. The other purpose of the equalizer is to distribute tensions to all wires equally. This is done by several fixed and moving pulleys, which are components of the equalizer, and are connected by one wire rope, as shown in Figure 1-5.

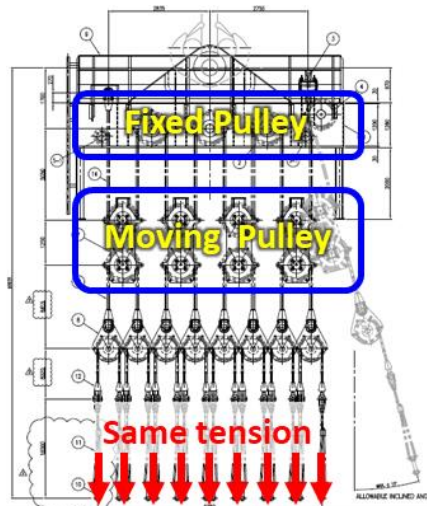


Figure 1-5. Drawing of the equalizer.

The last item of equipment is a transporter which is used to move the heavy block or module from one location to another (Figure 1-6). The transporter should be modeled by connecting many wheels to the platform by hydraulic cylinders, and the axle compensation mechanism should be implemented.



Figure 1-6. Modular transporter.

Furthermore, the existing programs are not suitable to consider collision, flexibility, operation scenarios, etc. Therefore, new design verification software is required. New design verification software can cover various problems to which the commercial software cannot be applied. It can also add new features conveniently, and make special equipment in the shipyard. For this, the requirements for the new design verification software should be defined.



## 1.2. Requirements for new design verification software

In this section, the requirements for the new design verification software will be derived from the examples.

### 1.2.1. Block lifting by the gantry and floating cranes

Figure 1-7 shows the gantry crane, which lifting capacity is 900 ton.

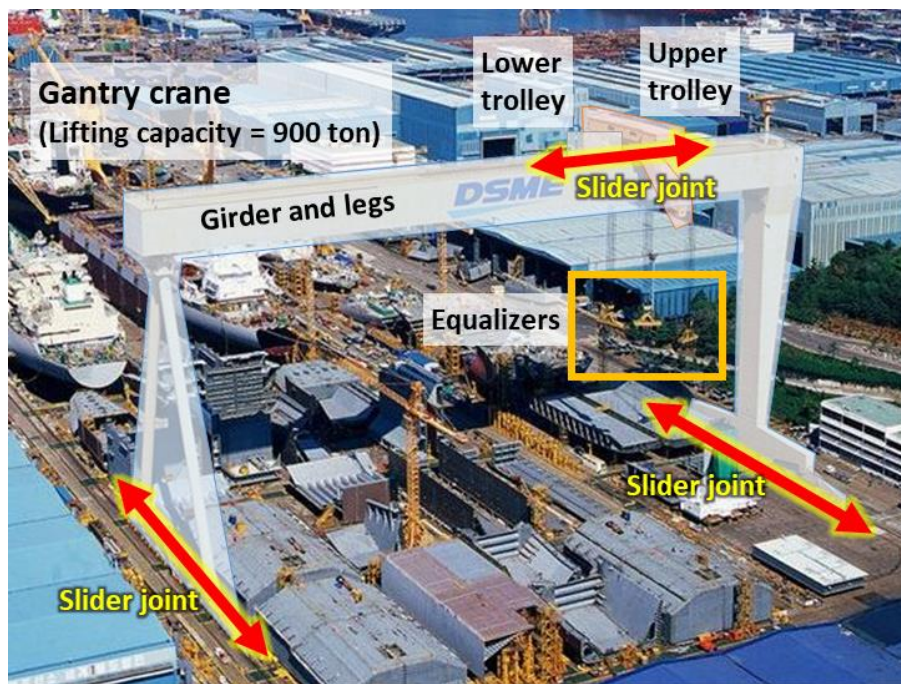


Figure 1-7. Gantry crane.

This crane is representative equipment in the shipyard, and is also called Goliath crane. It is composed of two legs, girder, upper and lower trolleys on the top. The upper and lower trolley can be moved on the girder. The gantry crane is also moved along the rail of the dock. Therefore, it can be modeled by the slider joints. In other words, the gantry crane is

a multibody system which means that multiple bodies are connected with joints or springs. Similarly, the mega floating crane is also a multibody system which is composed of the barge, two jibs, eight hooks, and lifting load as shown in Figure 1-8.

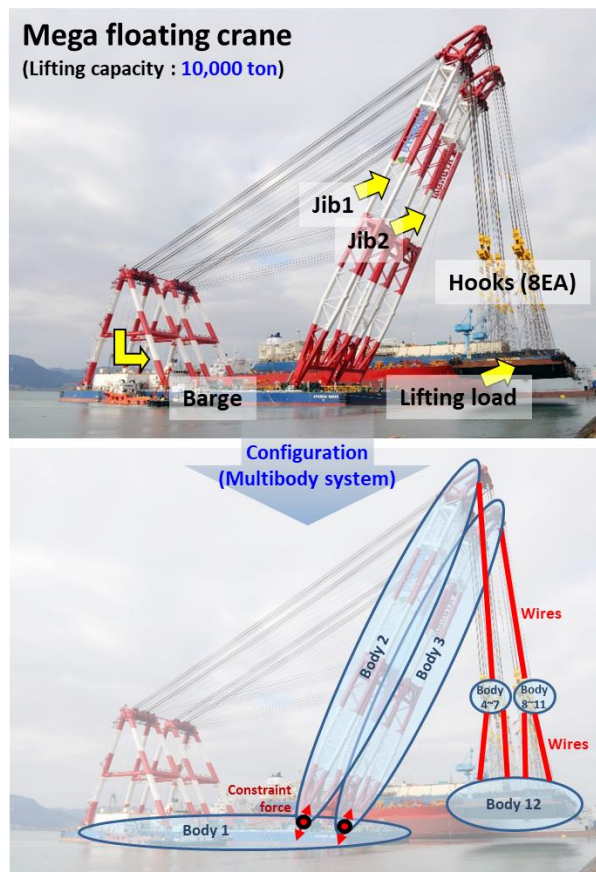


Figure 1-8. Mega floating crane.

The motion of the floating crane is induced by the environmental loads such as wave, wind, and current. To prevent the motion, the floating crane is moored by anchors from the seabed and the wire ropes from the quay. Therefore, the environmental loads and the mooring force should be calculated properly.



Meanwhile, a load has several lifting points that can be lifted, whereas cranes, such as the floating crane and the gantry crane, have only limited hooks. Thus, a special device called by an equalizer is introduced in shipbuilding production. There are equalizers under the trolleys of the gantry crane or the hooks of the floating crane. The first purpose of the equalizer is to connect the lifting points on the target load with the crane. Moreover, because a single load can weigh more than 100 tons, the concentrated load at one lifting point can cause severe accidents, such as being torn out and dropping the load on the ground. Thus, a second purpose of the equalizer is to distribute tensions to all wires equally. This is done by several fixed and moving pulleys, which are components of the equalizer and are connected by one wire rope, as shown in Figure 1-9.

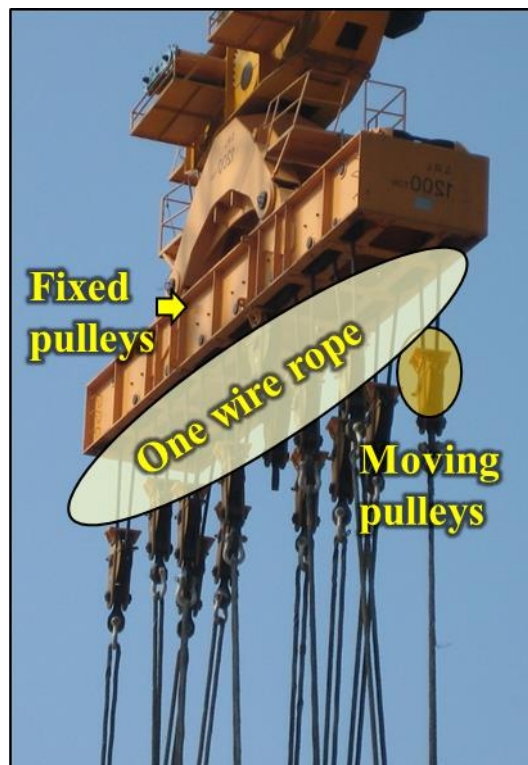


Figure 1-9. Components of the equalizer.

For a load lifting simulation in shipbuilding, the equalizer should be modeled properly. However, despite its seemingly simple combination of pulleys with one wire rope, it is not easy to implement its real mechanism. This is mainly because of the wire rope, which should be bent around the sheaves of the pulleys without disconnection. Thus, it is important to study how to model the wire rope and pulleys for load lifting simulation in shipbuilding.

### 1.2.2. Block lifting considering deformation

The thin plate block is usually used to build a cruise ship or RORO (Roll-On/Roll-Off) ship as shown in Figure 1-10. The thin plate block can be deformed during the lifting or erection.

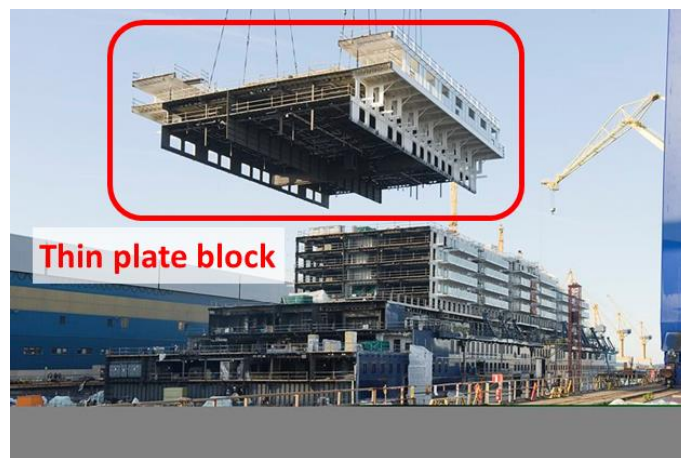


Figure 1-10. Thin plate block.

However, the block motion and wire tensions induced by the environmental condition were our interest until now. It was done by rigid multibody dynamics. Now, our interest is to check the stress or bending moment during the operation. However, the structural analysis cannot apply different tensions according to time. Moreover, it cannot consider

the interaction between the block and the equipment, and cannot make a joint to be connected with the rigid body. Therefore, flexible multibody dynamics is required.

### 1.2.3. Collision detection and response

As shown in Figure 1-11, there are several examples that require dynamic analysis, including a collision in the production and installation of ships and offshore structures. During the erecting or lifting operation, the collision might happen between the lifting body and the sub-structure due to the motion of the body induced by the environmental loads such as winds, currents, and waves. Therefore, the dynamic analysis including the collision detection and response should be performed to decide whether the operation is sufficiently safe or not.

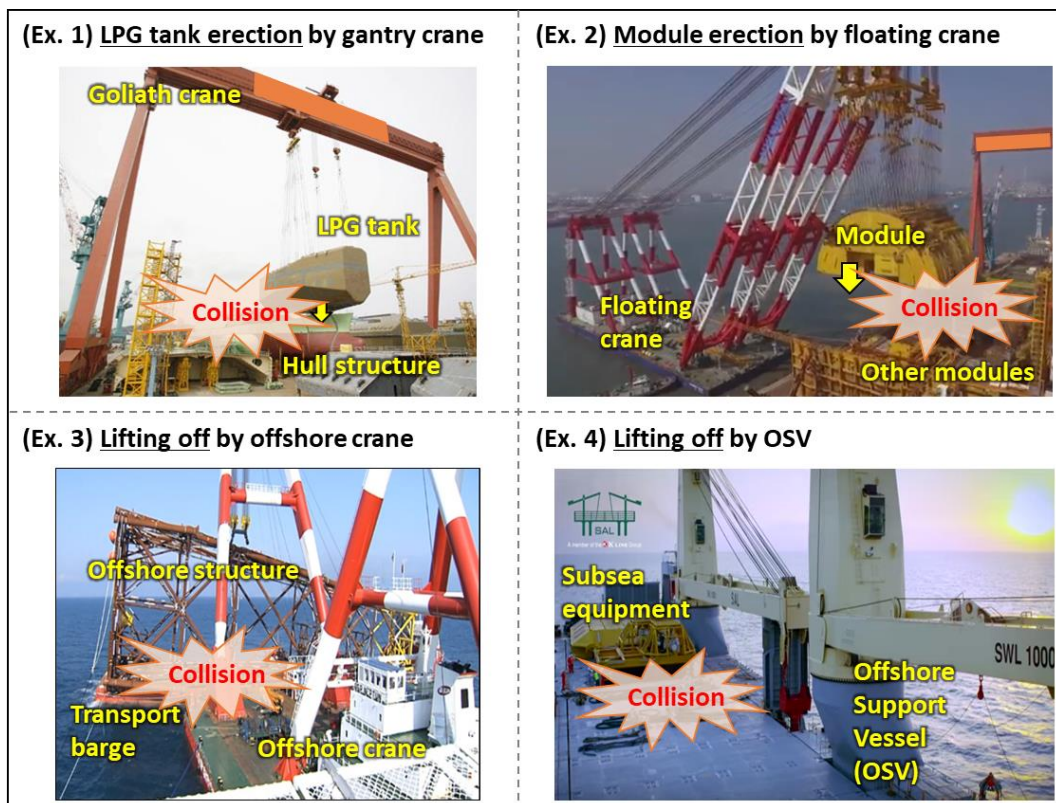


Figure 1-11. Examples of dynamic analysis including collision.

More specifically, the engineer in shipbuilding and offshore installation usually wants to calculate two results from the dynamic analysis. One result is collision positions due to the dynamic motion of the lifting body. The other result is collision forces acting at the collision positions. The collision forces can be used for the input values for structural analysis or structural reinforcement.

### 1.2.4. Block offloading by SPMTs

Many shipyards in Korea established a mega block factory abroad in the mid-2000's. For example, they transported these blocks from Yantai (China) to Geoje (South Korea) through the sea (Figure 1-12). At first, the block is constructed onshore. It is then moved on the TB (transportation barge) using the SPMTs (Self-Propelled Modular Transporters). This operation is called load-out. The transportation barge is towed or self-propelled to the destination. Finally, the floating crane lifts the block and erects it inside the FD (Floating Dock).

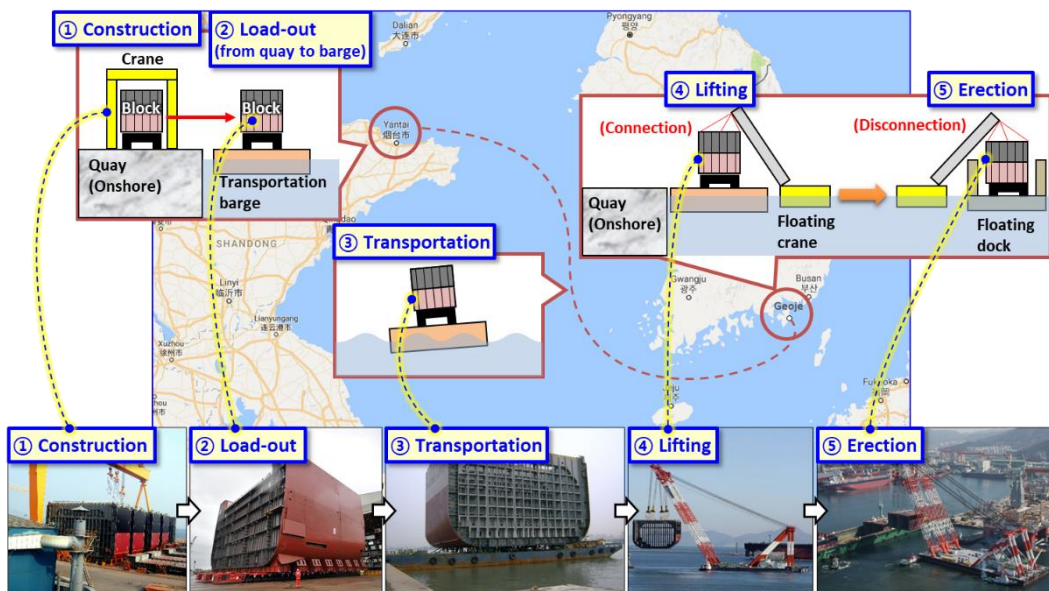


Figure 1-12. Construction, load-out, transportation, lifting, and erection.

Using the floating crane takes much time to prepare the connection and disconnection of wire ropes before and after the erection. Therefore, to increase the productivity and reduce the operation time, the production engineers suggested an offloading, which directly connects the TB and FD, and uses the SPMTs to move the block as same as the load-out (Figure 1-13). This can reduce the operation time dramatically from 3 to 4 hours to only less than 30 minutes. However, the safety of the newly suggested operation should be evaluated in advance. There are two criteria to do this. One is that the wheel load of the SPMT should be less than 20 ton at 0.5 km/h or less. The other is that the stroke length of the hydraulic cylinder connected to the wheel of the SPMT should be within  $\pm 350$  mm.

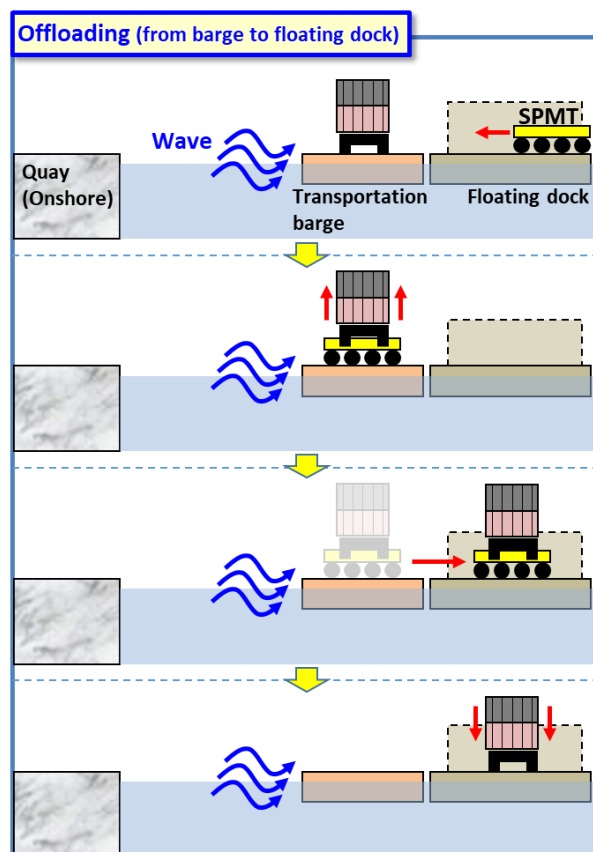


Figure 1-13. Offloading operation using SPMTs.



Several technologies are required for the dynamic analysis of the block offloading operation using SPMTs. At first, two floaters (TB and FD) are connected by the hinge joints by using two link beams (Figure 1-14). Therefore, the equations of motion for the multibody systems should be adopted. Furthermore, the hydrodynamic force should be considered because both the TB and FD are on the sea.

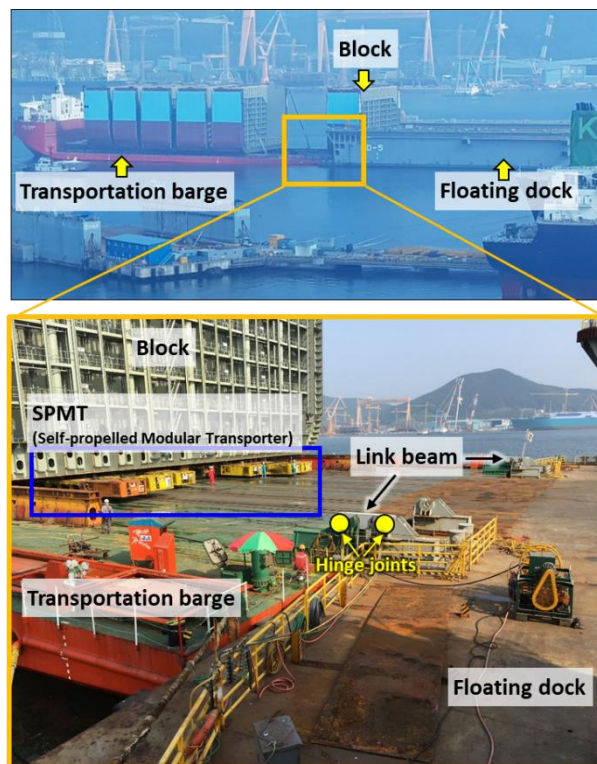


Figure 1-14. Overview of block offloading operation.

Second, the model of the SPMT should be then created. The SPMT is composed of several mechanical parts, such as hydraulic cylinders, wheels and a platform (Figure 1-6). This model should reflect an axle compensation mechanism, which maintains the level of the platform when the SPMT drives over an uneven roadway by lifting up and down the

wheels.

Third, the collision between the wheels of SPMTs and decks should be considered when the SPMTs move from the TB to FD (Figure 1-15).

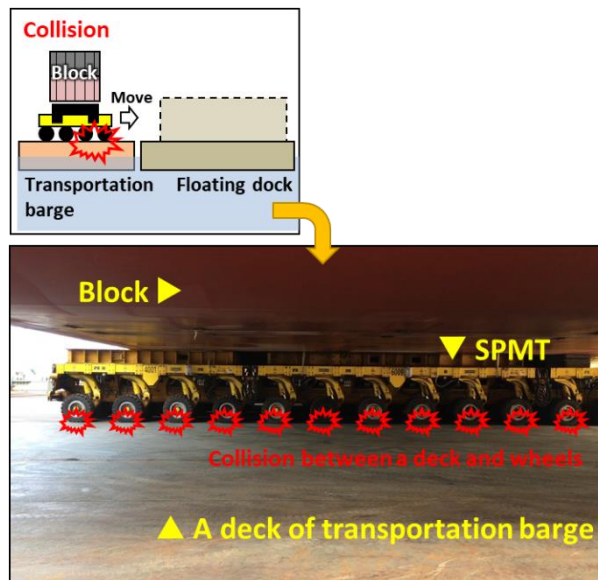


Figure 1-15. Collision between wheels and decks.

Along with the movement, the trim- which means the difference of the draft at the fore and aft- occurs on the TB and FD (Figure 1-16). Fourth, the ballasting and de-ballasting of the TB and FD to maintain the even keel should be considered even though the positions of the block and SPMTs are changed.

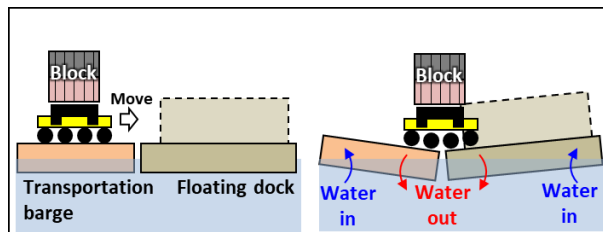


Figure 1-16. Ballasting and de-ballasting of the TB and FD.

### 1.2.5. Summary of requirements

As a result, requirements for new design verification software are summarized in Table 1-1.

Table 1-1. Requirements for new design verification software.

Item	Requirement
Equations of motion	Multibody dynamics for rigid bodies Multibody dynamics for deformable bodies
Collision	Collision detection and response (position difference method, exclusion box, non-interpenetration constraint)
Constraint	Kinematic joints (ball, hinge, slider, slider-hinge, fix, constraint-based wire rope, ...)
External forces	Hydrodynamic (wave) force Hydrostatic (buoyant) force Wind force Current force Mooring force
Special equipment	Equalizer SPMT Gantry crane Floating crane

There are too many components to be integrated at the same time. Therefore, we propose ‘integrated simulation framework based on multibody dynamics’.



## **1.3. Related work**

### **1.3.1. Related work for simulation framework**

Cha et al. [4] already proposed the concept of simulation frameworks for shipbuilding production. They suggested three layers such as simulation kernel, basic simulation components, and application-specific simulation components. Because they were focused on the combined discrete event and time simulate proposed by Zeigler et al. [5] and used an open source [6], dynamics module was only expressed as a simple component.

Cha et al. [7] improved the functionality and usability of the simulation frameworks by introducing simulation middleware, which played a role in transferring simulation data among the dynamics modules. The simulation middleware made it easy to add new modules or to change existing modules with the other.

Meanwhile, to extend the functionalities of the dynamics module, Ku et al. [8] and Cha et al. [9] developed their own dynamics engine based on the recursive formulation and topological modeling approach, respectively. Both of them includes hydrostatic and hydrodynamic forces. They compared simulation results with the benchmark tests and commercial software. Finally, several lifting and turn-over operations were simulated to validate their dynamics module.

There are several limitations of the previous work. None of them can simulate a pulley and an equalizer. They had no choice but to stretch or to shorten the initial length of the wire ropes from the equalizer logically. The other limitation is to simulate hydraulic and pneumatic systems such as hydraulic cylinders attached to the wheels of MTPs. They didn't include hydraulic and pneumatic modules in their simulation frameworks. And because the hydraulic and pneumatic system is usually very stiff, it gives unstable results during

numerical integration.

To overcome these limitations of the previous simulation framework, the integrated simulation framework for the advanced simulation in shipbuilding and offshores structures, which integrates several physical theories in one system simultaneously, is proposed in this study.

### **1.3.2. Related work for dynamic analysis including flexible bodies**

Ham et al. [10] used the multibody dynamics based on discrete Euler-Lagrange equation only for the rigid bodies. Meanwhile, Ku et al. [11] analyzed the crane operation using recursive formulation. The dynamic tension during the analysis was used for structural analysis of the block. However, it was only one time in the simulation period.

TSV-BLS [12] conducted structural analysis during the entire simulation period. However, it did not consider dynamic loads because TSV-BLS used quasi-static analysis method, which found and solved load for static equilibrium at every time. Moreover, TSV-BLS could not consider the effect of hydrodynamic forces.

Park et al. [13] used flexible multibody dynamics and modeled the blade of the wind turbine by 1D frame element. However, it is not suitable to be applied to the structural analysis of the block.

To overcome the limitation listed above, this study adopted flexible multibody system dynamics based on ANCF (Absolute Nodal Coordinate Formulation) for 2D shell element, which is known for la. Therefore, we can model the block approximately as a plate, and analyze the stress during the entire simulation periods.

Table 1-2. Related work for dynamic analysis including flexible bodies.

Authors	Type of equations of motion	Consideration of flexibility	Analysis method	Consideration of wave force	Target
Ham et al.	MBD (Discrete Euler-Lagrange equation)	X	-	O	Floating crane + block
Ku et al.	MBD (Recursive formulation)	$\Delta$	- (Only maximum tension is applied)	O	Gantry crane + block
TSV-BLS	Unknown	O (3D FEM)	Quasi-static analysis	X	Gantry crane + block
Park et al.	FMBD (Floating frame of reference formulation)	O (1D frame element)	Dynamic analysis	O	Floating platform + wind turbine
This study	FMBD (Absolute nodal coordinate formulation)	O (2D shell element)	Dynamic analysis	O	Gantry crane (or floating crane) + block

### 1.3.1. Related work for collision detection and response

The existing studies had the following limitations. Ming et al. [14] analyzed the motion of the offshore wind turbine during the installation. The studies mentioned above did not consider the collision in their dynamic analyses. Meanwhile, Lee et al. [15] only calculated collision between the body and the wire rope during the turn-over operation. Jeong et al. [16] considered collision detection and response of the subsea equipment on the deck of the offshore support vessel. However, they could not calculate collision force because it simply used the impulse-based method which changes velocity after direct collision. In

conclusion, collision detection and response algorithms suitable for shipbuilding and offshore installation are required. Existing dynamic analysis libraries, including collision detection and response such as PhysX [17], Bullet [18], and ODE [6] were tested with complex mesh models. We found that those libraries were not suitable to calculate collision positions and forces.

The objectives of this study are to develop collision detection and response algorithms suitable for shipbuilding and offshore industries. Several strategies such as the position difference method, space partitioning, and exclusion boxes are adapted to increase the performance during collision detection. Collision response algorithm using non-interpenetration constraint method is derived.

### **1.3.2. Related work for the equalizer**

Cha et al. [4] introduced an approximated mechanism to model an equalizer. They had no choice but to stretch or to shorten the initial length of the wire ropes between the equalizer and load logically because wire ropes were implemented as incompressible springs. The equalizer modeled by the approximated mechanism is shown in Figure 1-17.

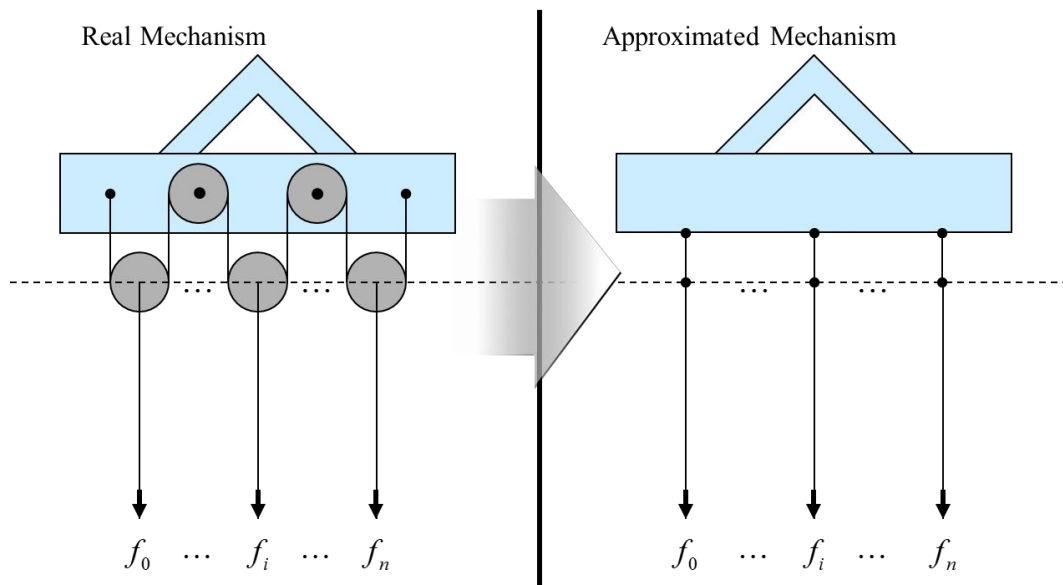


Figure 1-17. Approximated mechanism for the equalizer.

This may cause several problems. First, the simulation may be numerically unstable due to a sudden change in the length. If the wire ropes have their real spring coefficients, which are usually very high, a small variation on one side can cause a large tension. By a length adjustment algorithm, the length of a wire rope that gets a large tension is shortened, and the others should be extended to the next step. Some of the shortening parts now start to get larger tensions. Thus, the tensions of the wire ropes are repeatedly increased or decreased and finally induce unstable motion of the system. Second, although the equalizing is controlled naturally by the pulleys and wire rope, the approximated mechanism should use an artificial factor that controls the length adjustment ratio. The shortening length is the same as the total extended lengths of the other wire ropes. If an artificial factor is equal to 1, the shortening length is calculated to achieve no tension in it. If an artificial factor is less than 1, the shortening length is set to leave some tension in it. Thus, the time required for equalizing is controlled by the artificial coefficient. This can affect the motion of the load before it is lifted or during lifting. Third, although the total

length that can be extended is limited, the approximated mechanism cannot control the total length of the equalizer. Moreover, the approximated mechanism does not calculate the motions of the pulleys of the equalizer. It is also not possible to connect another pulley at the end of the wire rope for an extension, as shown in Figure 1-18.

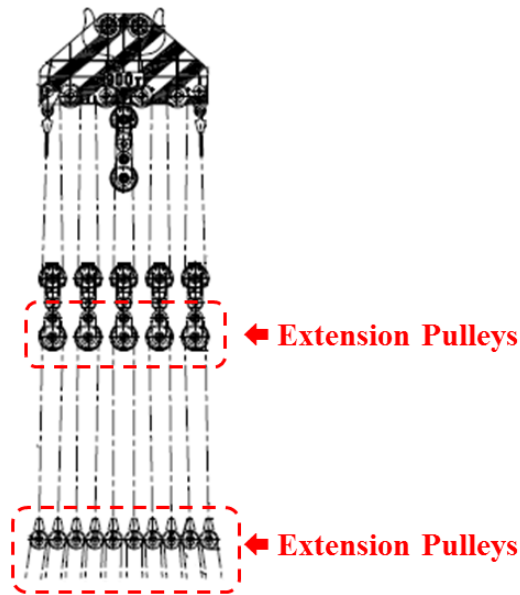


Figure 1-18. Extension pulleys under the equalizer.

Some researchers have tried to model the wire ropes and pulleys mathematically, considering real phenomena. Imanishi et al. [19] presented a wire rope involving contacts with a winch drum using a finite element method. Lugris et al. [20] used a semi-analytical method, which was derived by introducing an analytical model of the rope-sheave interaction in the system. García et al. [21] divided the wire rope into spring segments and calculated the tensions as external forces in the system. They applied their wire rope to represent exact pulleys. However, they did not consider in their study how to represent an equalizer mechanism. Moreover, the constraint-based wire rope is a simpler way to model the equalizer compared with other methods introduced in previous studies.

### 1.3.3. Related work for block offloading

Naqvi et al. [22] only focused on various transportation considerations in the module designs and their impact on the structural configuration of the module. They did not consider the dynamic effects and any model of the SPMTs. Ali [23] studied transportation, lifting, and installation considering the effects of environmental loads for designing an offshore module. He used the dynamic loads for structural analysis. However, he did not analyze the operation dynamically. Meanwhile, Zhao et al. [24] studied the electro-hydraulic control system for the axle compensation of the SPMT. Lu et al. [25] developed functions, such as platform leveling, when encountering uneven road or passing through road obstacles. Vu et al. [26] conducted durability analysis on the parts of the hydraulic suspension system while taking into consideration the multibody dynamics. However, these studies were not focused on the dynamic analysis of the operation. The summary of the related work is listed in Table 1-3. A few of the related studies analyzed the offloading operation using the SPMTs, and did not consider the collision between the wheels and deck, ballasting and de-ballasting, and multibody formulation, including the hydrodynamic force.

Table 1-3. Related work for block offloading.

	Multibody formulation	Hydrodynamic force	Axle compensation mechanism	Collision between wheels and decks	Ballasting and de-ballasting
Naqvi et al.	X	X	X	X	X
Ali	X	X	X	X	X
Zhao et al.	X	X	O	X	X
Lu et al.	X	X	O	X	X
Vu et al.	O	X	X	X	X
This study	O	O	O	O	O

Therefore, the objectives of this study are to develop the dynamic analysis program that makes it possible to simulate the block offloading operation using SPMTs. For this, multibody dynamics was adopted to solve the equations of motion, including the hydrodynamic force. In addition, the modeling method of the SPMT, including axle compensation mechanism, is also proposed. Meanwhile, a collision algorithm using the non-interpenetration constraint method is derived for the collision between the wheels and decks. Finally, the ballasting and de-ballasting method to maintain the even keel of the TB and FD is applied.



## 1.4. Configuration of integrated simulation framework

According to the requirements defined in the previous section, we developed integrated simulation framework based on multibody dynamics as shown in Figure 1-19.

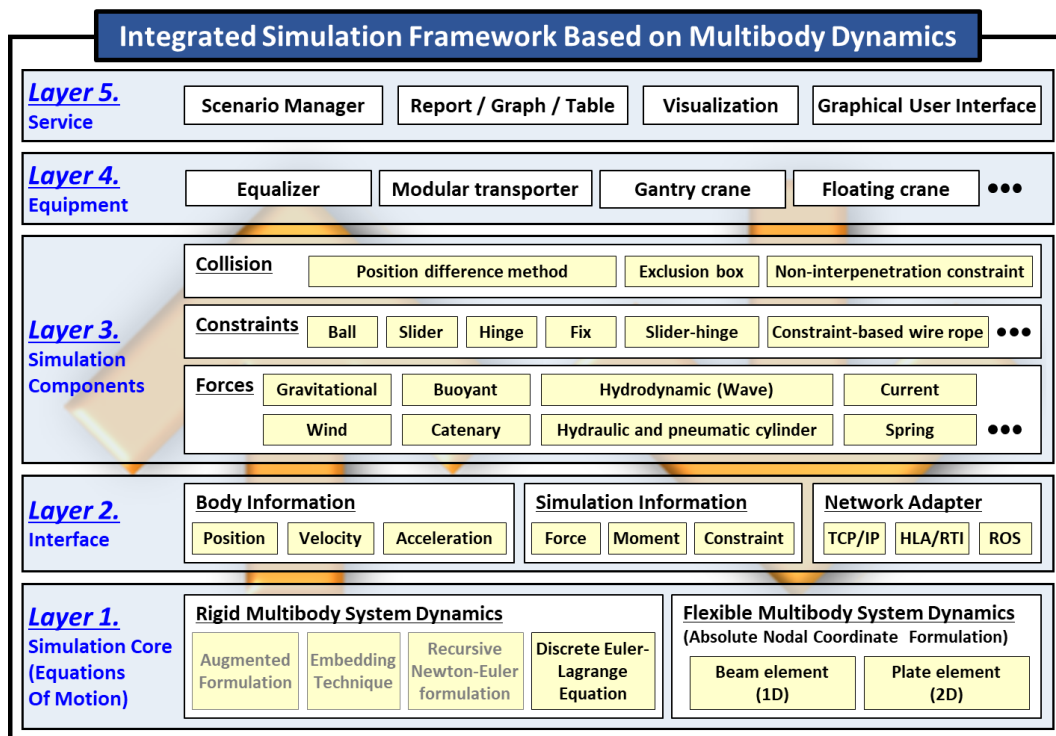


Figure 1-19. Configuration of integrated simulation framework based on multibody dynamics.

The proposed framework is composed of five layers: simulation core layer, interface layer, simulation component layer, equipment layer, and service layer. The following sections will explain the role of each layer briefly.

### 1.4.1. Simulation core layer

Simulation core layer provides equations of motion theoretically based on multibody

dynamics. It is difficult to apply the Newton-Euler equation directly in the case of existing constraints and constraint forces. Therefore, to solve the equations of motion of the multibody system, we have to use one of multibody dynamics formulations. These can be formulated differently according to the expression of the constraint forces. Figure 1-20 shows typical formulations of multibody dynamics.

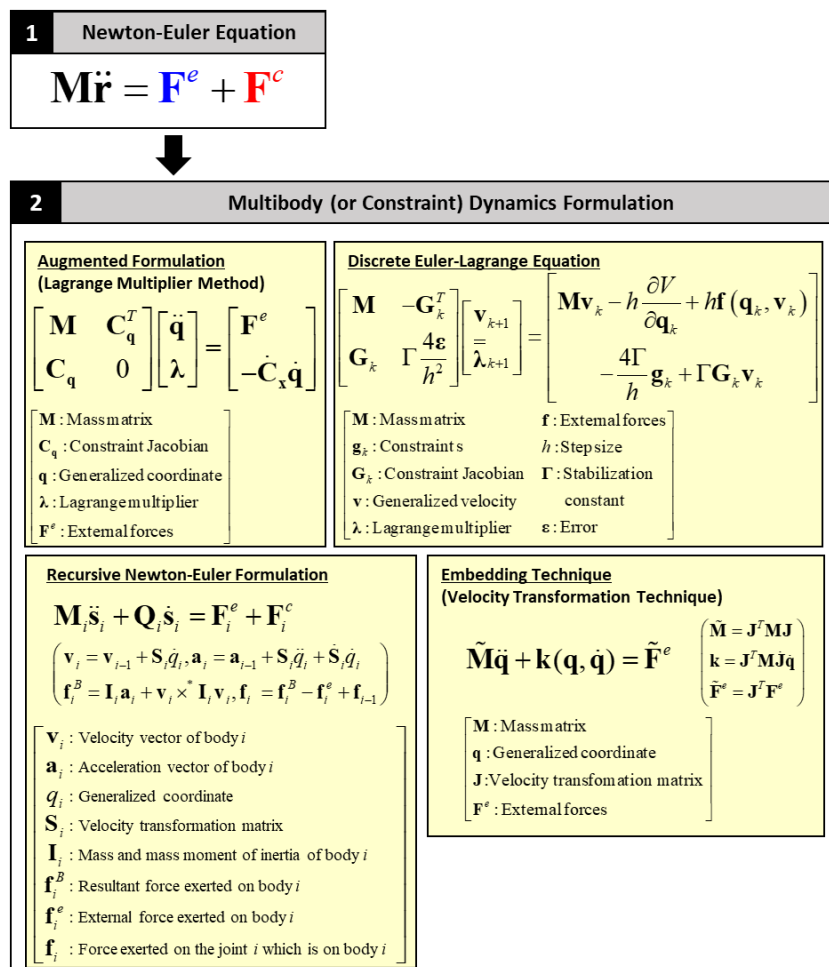


Figure 1-20. Typical formulation of multibody dynamics.

There are the augmented formulation [27], the discrete Euler-Lagrange equation [10], [28], [29], the recursive Newton-Euler formulation [8], [30], [31], and the embedding technique [9], [32]. They are well explained in detail in their references. Each one has its pros and cons.

The augmented formulation is the most common formulation so that the equations of motion can be determined automatically and the constraint force can be obtained from constraint Jacobian and Lagrange multiplier. However, the matrix size of the augmented formulation is getting bigger because it solves all the bodies at once. On the other hand, the discrete Euler-Lagrange equation (DELE) solves the equations of motion very similar to the augmented formulation. However, it is a lot easier to formulate the equations because it doesn't contain time derivative of the constraint Jacobian. The recursive Newton-Euler formulation breaks the connected bodies into the single body to calculate constraint forces between two bodies. Therefore, even though many bodies are included in the simulation, it can solve only 6 by 6 matrix efficiently. In case of the embedding technique, the matrix size of the formulation is small so that the computing time can be minimized. However, the recursive Newton-Euler formulation and the embedding technique are not easy to formulate the equations automatically, and have additionally to treat the closed loop such as cut joint methods. In this study, DELE is chosen because it is suitable to be developed by computer codes, and don't have to calculate time derivative of the constraint Jacobian which is usually not easy to be obtained. DELE also don't have to take account of the closed loop. Details about DELE will be given in section 2.1. The pros and cons of multibody dynamics formulations are summarized in Table 1-4.

Table 1-4. Pros and cons of multibody dynamics formulations.

	Augmented Formulation	Embedding Technique	Recursive Newton-Euler Formulation	Discrete Euler-Lagrange Equation
Formulation	$\begin{bmatrix} \mathbf{M} & \mathbf{C}_x^T \\ \mathbf{C}_x & \mathbf{0} \end{bmatrix} \begin{bmatrix} \ddot{\mathbf{x}} \\ \dot{\lambda}_k \end{bmatrix} = \begin{bmatrix} \mathbf{F}^e \\ -\dot{\mathbf{C}}_x \dot{\mathbf{x}} \end{bmatrix}$	$\tilde{\mathbf{M}}\ddot{\mathbf{q}} + \mathbf{k}(\mathbf{q}, \dot{\mathbf{q}}) = \tilde{\mathbf{F}}^e$ $\begin{pmatrix} \tilde{\mathbf{M}} = \mathbf{J}^T \mathbf{M} \mathbf{J} \\ \mathbf{k} = \mathbf{J}^T \mathbf{M} \mathbf{J} \dot{\mathbf{q}} \\ \tilde{\mathbf{F}}^e = \mathbf{J}^T \mathbf{F}^e \end{pmatrix}$	$\mathbf{M}_i \ddot{\mathbf{s}}_i + \mathbf{Q}_i \dot{\mathbf{s}}_i = \mathbf{F}_i^e + \mathbf{F}_i^c$ $\begin{pmatrix} \mathbf{v}_i = \mathbf{v}_{i-1} + \mathbf{S}_i \dot{q}_i \\ \mathbf{a}_i = \mathbf{a}_{i-1} + \mathbf{S}_i \ddot{q}_i + \dot{\mathbf{S}}_i \dot{q}_i \\ \mathbf{f}_i^e = \mathbf{I}_i \mathbf{a}_i + \mathbf{v}_i \times \mathbf{I}_i \mathbf{v}_i \\ \mathbf{f}_i = \mathbf{f}_i^e - \mathbf{f}_i^c + \mathbf{f}_{i-1} \end{pmatrix}$	$\begin{bmatrix} \mathbf{M} & -\mathbf{G}_k^T \\ \mathbf{G}_k & \varepsilon \end{bmatrix} \begin{bmatrix} \mathbf{v}_{k+1} \\ h\dot{\lambda}_k \end{bmatrix} = \begin{bmatrix} \mathbf{M}\mathbf{v}_k - h\mathbf{F}(\mathbf{q}_k, \mathbf{q}_{k-1}) \\ -\mathbf{g}(\mathbf{q}_k) / h + \Gamma \mathbf{G}_k \mathbf{v}_k \end{bmatrix}$
Automation	Easy	Hard	Hard	Easy
Matrix size	Big	Small	Small	Big
Time complexity for one time step ( $n$ = number of bodies, $m$ = number of constraints)	High $[O((n+m)^3)]$	Middle $[O((n-m)^3)]$	Low $[O(n)]$	High $[O((n+m)^3)]$
Constraint force	Obtainable	Unobtainable	Obtainable	Obtainable
2 <sup>nd</sup> order time derivative of constraint	Necessary	Unnecessary	Unnecessary	Unnecessary
Constraint-based wire rope and collision	Possible (Hard to obtain 2 <sup>nd</sup> order time derivative of constraint)	Impossible	Impossible	Possible (Only 1 <sup>st</sup> order time derivative of constraint)
Consideration of closed loop	Unnecessary	Necessary	Necessary	Unnecessary

Meanwhile, flexible multibody systems, in which both elastic and rigid bodies are connected through mechanical joints and in arbitrary motion with respect to each other, can be divided into linearly elastic multibody systems and nonlinearly elastic multibody systems [33]. For linearly elastic multibody systems, it is assumed that the strain-displacement relationship remains linear, and therefore strain components remain very small at all times for elastic bodies. An efficient analysis technique for this type of problem is the FFRF (Floating Frame of Reference Formulation). However, for elastic bodies, the strain-displacement relationship is nonlinear, or the strain components become large. An efficient analysis technique for this type of problem is the ANCF (Absolute Nodal Coordinate Formulation) which is mainly handled in section 0 and 2.3.

### **1.4.2. Interface layer**

An interface layer is used to exchange information between simulation core layer and simulation component layer. It is similar to the simulation middleware given by Cha et al. [7]. However, the interface layer contains network adapter to allow to communicate with other analysis tools. Furthermore, not only force and moment calculated from the simulation components but also constraint types can be supported.

### **1.4.3. Simulation component layer**

Various physical components are included in the simulation components layer. It is divided into three groups: ‘Forces’, ‘Constraints’, and ‘Collision’. In ‘Forces’ group, a hydrostatics module is used to calculate the buoyancy of the floating body and hydrodynamics module is used to calculate the wave force acting on the floating body. In ‘Constraints’ group, kinematic joints such as a ball joint, hinge joint, slider joint, and fixed joint are included. In addition to kinematic joints, constraint-based wire rope to model the pulleys. In ‘Collision’ group, position difference method for collision detection and non-penetration constraint for collision response are newly defined in this study. The related theories will be explained in section 2.4, 2.5, 2.6 and 2.9.

### **1.4.4. Equipment layer**

There is several equipment such as a gantry crane, a floating crane, a SPMT, and an equalizer, which are specialized in shipbuilding and offshore installation. The equalizer and SPMT are modeled considering the real mechanism. Details will be presented in section 2.7 and 2.8.

### 1.4.5. Service layer

A service layer is composed of scenario manager, report, graph, visualization and GUI (Graphical User Interface). Scenario manager is used to progress the simulation time based on the predefined events such as hoisting up, hoisting down, move, etc. Visualization module shows simulation results on the screen. After simulation, wire rope tension or the position of the block can be provided by report and graph. A user-friendly GUI is also developed to simulate various examples conveniently.

### 1.4.6. Library diagram and relations

Figure 1-21 shows library diagram and relation of the components in the integrated simulation framework. A black label is a library name and the contents in the yellow box is main functions or classes.

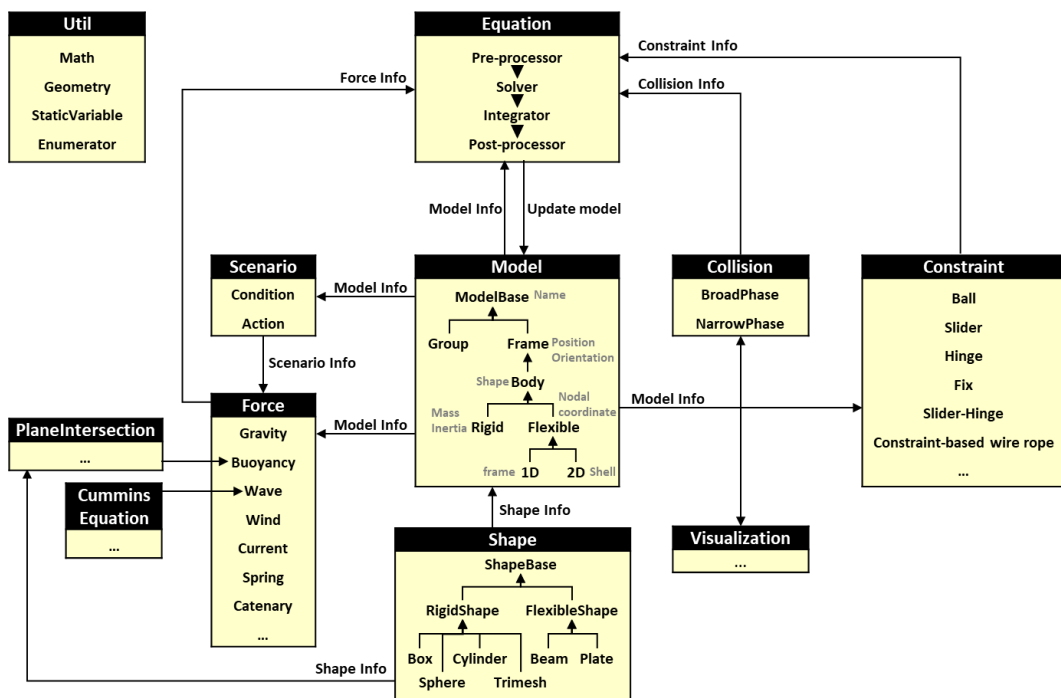


Figure 1-21. Library diagram and relation of the components in integrated simulation framework.

Model library contains model information such as position, orientation, mass, and inertial. In case of the flexible body, the nodal coordinates and material properties such as density, Young's modulus, thickness, etc. are also defined. The shape of the bodies are defined in Shape library. The model info is used to calculate the forces, collisions and constraints. The model info is also used for the visualization. At each time, the equations of motion are solved in Equation library. At first, the pre-processor gathers all data from model, force, collision, constraint libraries, and generate the matrix. And then, the solver calculate the inverse matrix to obtain the acceleration or the velocity. The integrator calculates the position and orientation from the velocity. The results are transferred to Model library to update the model info.

### 1.4.7. New production design verification program

This study develops a new design verification program being able to cover the requirement listed in Table 1-1. It is a dedicated and differentiated program for ships and offshore structures, named SyMAP (SyDLab's Multibody Analysis Program). Figure 1-22 shows the main view of SyMAP. It is developed in C# programming language and Windows Presentation Foundation (WPF) and contains many user-friendly functions.

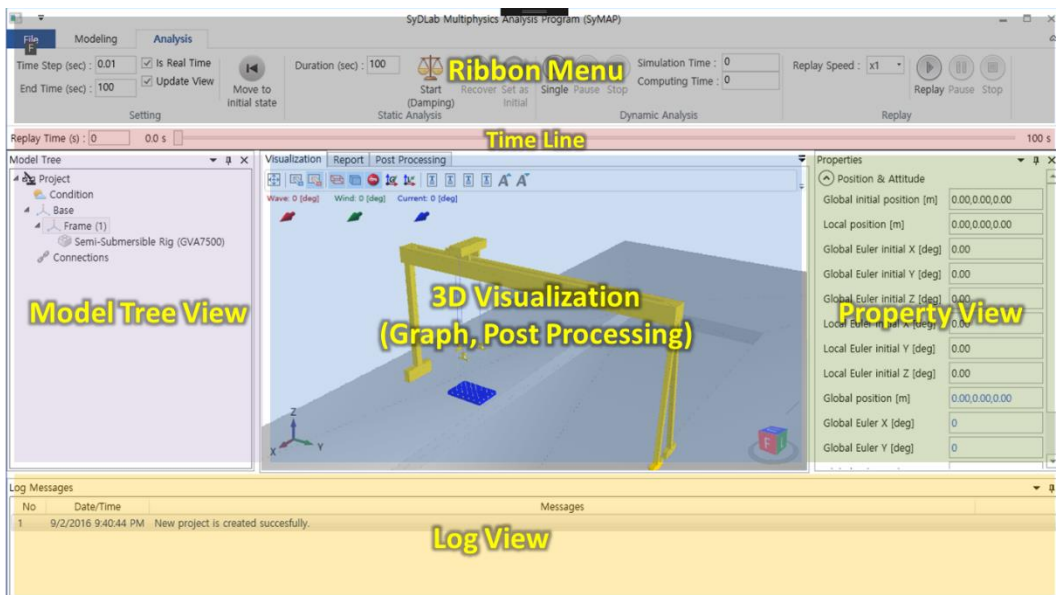


Figure 1-22. Main view of SyMAP.



## **1.5. Research objective and work scope**

The research objective is to develop the integrated simulation method to solve the problems which have not been analyzed by the previous studies or commercial programs in ships and offshore structures. The work scopes of this study are as follows.

- 1) Implementation of the simulation core to solve the equations of motion of the multibody for rigid and flexible bodies
- 2) Collision detection and response between the two objects which shapes are composed of triangular meshes
- 3) Implementation of special equipment such as equalizer and SPMT (Self-Propelled Modular Transporter) in ships and offshore structures
- 4) Proposal of the integrated simulation framework
- 5) Development of the program with commercial level convenience and performance

## 2. Theoretical backgrounds

### 2.1. Multibody dynamics for rigid bodies

Multibody dynamics is a discipline describing the dynamic behavior of mechanical systems that consist of several bodies connected via kinematic constraints called joints that impose restrictions on their relative motion. This study uses a discrete Euler-Lagrange equation which is proven to be numerically stable for the case of linear holonomic constraints. However, Wendlandt et al. [34], Marsden et al. [35], and Lew [36] briefly explain the DELE. Therefore, this chapter deals with the more detailed process to obtain the DELE.

#### 2.1.1. Discretization of the Euler-Lagrange equation

A variational principle is introduced in Fowles and Cassiday [37]. The action integral of the Lagrangian  $L$  means the expenditure of total energy of the system during the motion. This can be expressed as follows:

$$J = \int_{t_0}^{t_N} L dt \quad (1)$$

where  $T$ ,  $V$  are kinetic and potential energy of the particle, and  $L$  is called Lagrangian. During the time interval  $t_0$  and  $t_N$ , the actual motion minimizes the above integral. This can be expressed mathematically as

$$\delta J = \delta \int_{t_1}^{t_2} (T - V) dt = \delta \int_{t_1}^{t_2} L dt \quad (2)$$

From the form (2), we can induce Euler-Lagrange equation known to be

$$\frac{d}{dt} \left( \frac{\partial L}{\partial \dot{\mathbf{q}}} \right) - \frac{\partial L}{\partial \mathbf{q}} = 0 \quad (3)$$

where,  $\mathbf{q}$  is generalized coordinates. The action integral of Lagrangian can be represented with the sum of the infinitesimal area with time divided into small time step  $h$ , as shown in Figure 2-1.

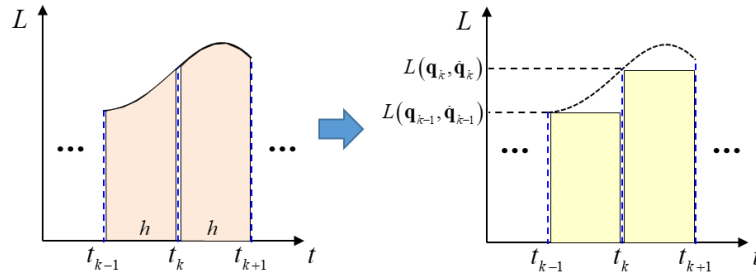


Figure 2-1. Discretization of the action integral.

The discretized  $J$  can be expressed as follows.

$$J = \int_{t_0}^{t_1} L(\mathbf{q}, \dot{\mathbf{q}}) dt + \dots + \int_{t_{k-1}}^{t_k} L(\mathbf{q}, \dot{\mathbf{q}}) dt + \int_{t_k}^{t_{k+1}} L(\mathbf{q}, \dot{\mathbf{q}}) dt + \dots + \int_{t_{N-1}}^{t_N} L(\mathbf{q}, \dot{\mathbf{q}}) dt \quad (4)$$

For simplicity, let  $\mathbf{q}(t_k) = \mathbf{q}_k$ . For an approximation, each integral term can be regarded as a rectangular shape of width  $h$ , and height  $L(\mathbf{q}_k, \dot{\mathbf{q}}_k)$ . This yields:

$$J \approx L(\mathbf{q}_0, \dot{\mathbf{q}}_0)h + \dots + L(\mathbf{q}_{k-1}, \dot{\mathbf{q}}_{k-1})h + L(\mathbf{q}_k, \dot{\mathbf{q}}_k)h + \dots + L(\mathbf{q}_{N-1}, \dot{\mathbf{q}}_{N-1})h \quad (5)$$

Approximate each infinitesimal area as a rectangular shape, and velocity  $\dot{\mathbf{q}}_k$  as  $\frac{\mathbf{q}_{k+1} - \mathbf{q}_k}{h}$ , discrete action integral of Lagrangian  $J_d$  can be expressed as follows.

$$J_d = \sum_{k=1}^N L_d(\mathbf{q}_{k-1}, \mathbf{q}_k, h) \quad (6)$$

$L_d$  is denoted as the discrete Lagrangian. According to Eq. (2), the motion follows the trajectory that minimizes the discretized action integral  $J_d$ , which yields:

$$\begin{aligned} \delta J_d &= \sum_{k=1}^N \delta L_d(\mathbf{q}_{k-1}, \mathbf{q}_k, h) \\ &= \sum_{k=1}^{N-1} [D_2 L_d(\mathbf{q}_{k-1}, \mathbf{q}_k, h) + D_1 L_d(\mathbf{q}_k, \mathbf{q}_{k+1}, h)] \delta \mathbf{q}_k = 0 \end{aligned} \quad (7)$$

where,  $D_i$  is the partial differential operator, which means partial differentiation by the  $i^{\text{th}}$  variable. Eq. (7) gives the DEL equation,

$$D_2L_d(\mathbf{q}_{k-1}, \mathbf{q}_k, h) + D_1L_d(\mathbf{q}_k, \mathbf{q}_{k+1}, h) = 0 \quad (8)$$

Meanwhile, by using the Stömer-Verlet method [38], we set the discrete Lagrangian to be Eq. (9):

$$L_d(\mathbf{q}_{k-1}, \mathbf{q}_k, h) = h \left[ \frac{1}{2} \left( \frac{\mathbf{q}_k - \mathbf{q}_{k-1}}{h} \right)^T \mathbf{M} \left( \frac{\mathbf{q}_k - \mathbf{q}_{k-1}}{h} \right) - V(\mathbf{q}_k) \right] \quad (9)$$

where  $\mathbf{M}$  is the mass matrix, and  $V$  is potential energy defined in Eq. (2). Now, we can calculate  $D_2L_d$  and  $D_1L_d$ , respectively.

$$\begin{aligned} D_2L_d(\mathbf{q}_{k-1}, \mathbf{q}_k, h) &= \frac{1}{h} \mathbf{M} \left( \frac{\mathbf{q}_k - \mathbf{q}_{k-1}}{h} \right) - \frac{\partial V}{\partial \mathbf{q}_k} \\ D_1L_d(\mathbf{q}_k, \mathbf{q}_{k+1}, h) &= -\frac{1}{h} \mathbf{M} \left( \frac{\mathbf{q}_{k+1} - \mathbf{q}_k}{h} \right) \end{aligned} \quad (10)$$

We obtained Eq. (11) by substituting the discrete Lagrangian (10) into Eq. (8).

$$\begin{aligned} D_2L_d(\mathbf{q}_{k-1}, \mathbf{q}_k, h) + D_1L_d(\mathbf{q}_k, \mathbf{q}_{k+1}, h) &= 0 \\ h \left[ \frac{1}{h} \mathbf{M} \left( \frac{\mathbf{q}_k - \mathbf{q}_{k-1}}{h} \right) - \frac{1}{h} \mathbf{M} \left( \frac{\mathbf{q}_{k+1} - \mathbf{q}_k}{h} \right) - \frac{\partial V}{\partial \mathbf{q}_k} \right] &= 0 \\ -\frac{1}{h} \mathbf{M} \left( \frac{\mathbf{q}_{k+1} - 2\mathbf{q}_k + \mathbf{q}_{k-1}}{h} \right) - \frac{\partial V}{\partial \mathbf{q}_k} &= 0 \end{aligned} \quad (11)$$

Leaving  $q_{k+1}$ , and moving the remaining term to the right side, we obtained Eq. (12).

$$\mathbf{M}\mathbf{q}_{k+1} = \mathbf{M}(2\mathbf{q}_k - \mathbf{q}_{k-1}) - h^2 \frac{\partial V}{\partial \mathbf{q}_k} \quad (12)$$

Figure 2-2 summarizes the discretization process.

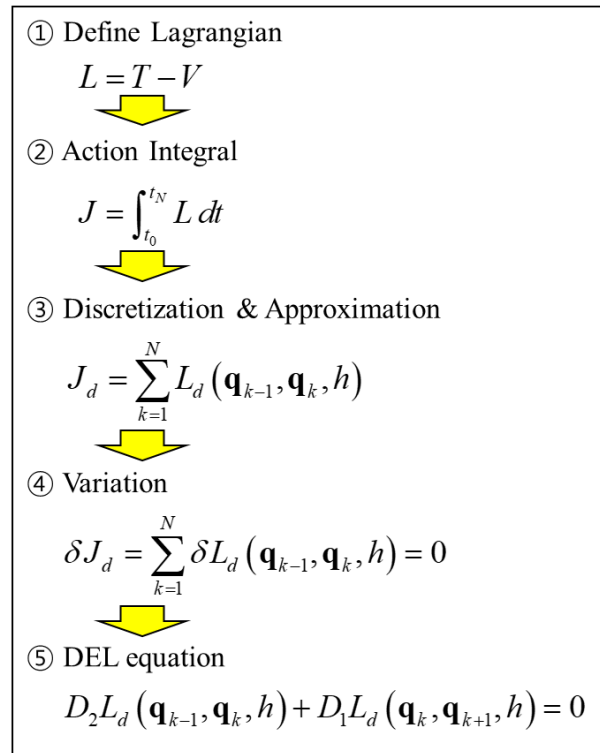


Figure 2-2. Summary of the discretization of the Euler-Lagrange equation.

### 2.1.2. Discrete Euler-Lagrange equation with constraints

Eq. (11) is the basic form of the DEL equation with no constraints. Constraints are kinematic restrictions on the variables in the system, with the form  $g(\mathbf{q})=0$ . In a multibody system, each body is connected by joints or wire ropes, and they limit the motion of bodies into certain areas. Therefore, we should include the constraints in the equations of motion. We can obtain the DEL equation with the number of  $m$  constraints directly from the modified Lagrangian,  $\bar{L}$ .

$$\bar{L} = L + L_C, \left( L_C = \sum_{j=1}^m \lambda_j g_j(\mathbf{q}) \right) \quad (13)$$

where  $L_C$  is constraint Lagrangian and  $\lambda_j$  is a Lagrange multiplier of the  $j^{\text{th}}$  constraint. We can change  $L_C$  as a vector form  $L_C = \mathbf{g}^T(\mathbf{q})\boldsymbol{\lambda}(t)$ , where  $\mathbf{g} = [g_1(\mathbf{q}), \dots, g_m(\mathbf{q})]^T$  and  $\boldsymbol{\lambda} = [\lambda_1, \dots, \lambda_m]^T$ .

With the modified Lagrangian, we can easily derive the DEL equation with constraints from the same procedure in Section 2.1.1. Eq. (9) can be changed as below.

$$\bar{J} = \int_{t_1}^{t_2} \bar{L} dt = \int_{t_0}^{t_N} (L + L_C) dt = \int_{t_0}^{t_N} L dt + \int_{t_0}^{t_N} L_C dt = J + J_C \quad (14)$$

We have already derived the discretization of  $L$  in the previous chapter. Therefore, in this chapter, we only derived  $L_C$ . We can express the discretized  $J_C$  as follows.

$$\begin{aligned}
J_C &= \int_{t_0}^{t_1} L_C(\mathbf{q}, \dot{\mathbf{q}}) dt + \dots + \int_{t_k}^{t_{k+1}} L_C(\mathbf{q}, \dot{\mathbf{q}}) dt + \dots + \int_{t_{N-1}}^{t_N} L_C(\mathbf{q}, \dot{\mathbf{q}}) dt \\
&= \int_{t_0}^{t_1} \mathbf{g}^T(\mathbf{q}) \boldsymbol{\lambda}(t) dt + \dots + \int_{t_k}^{t_{k+1}} \mathbf{g}^T(\mathbf{q}) \boldsymbol{\lambda}(t) dt + \dots + \int_{t_{N-1}}^{t_N} \mathbf{g}^T(\mathbf{q}) \boldsymbol{\lambda}(t) dt
\end{aligned} \tag{15}$$

Now, we applied the midpoint rule to  $J_C$  for approximation.

$$\begin{aligned}
J_{C,d} &= h \left( \frac{\mathbf{g}_0 + \mathbf{g}_1}{2} \right)^T \frac{\boldsymbol{\lambda}_0 + \boldsymbol{\lambda}_1}{2} + \dots + h \left( \frac{\mathbf{g}_k + \mathbf{g}_{k+1}}{2} \right)^T \frac{\boldsymbol{\lambda}_k + \boldsymbol{\lambda}_{k+1}}{2} \\
&\quad + \dots + h \left( \frac{\mathbf{g}_{N-1} + \mathbf{g}_N}{2} \right)^T \frac{\boldsymbol{\lambda}_{N-1} + \boldsymbol{\lambda}_N}{2}
\end{aligned} \tag{16}$$

$$\therefore J_{C,d} = \sum_{k=0}^{N-1} \left[ \frac{h}{4} (\mathbf{g}_k + \mathbf{g}_{k+1})^T (\boldsymbol{\lambda}_k + \boldsymbol{\lambda}_{k+1}) \right] \tag{17}$$

The variation of  $J_{C,d}$  is given by

$$\begin{aligned}
\delta J_{C,d} &= \frac{h}{4} \sum_{k=0}^{N-1} (\delta \mathbf{g}_k + \delta \mathbf{g}_{k+1})^T (\boldsymbol{\lambda}_k + \boldsymbol{\lambda}_{k+1}) \\
&= \frac{h}{4} \sum_{k=0}^{N-1} (\mathbf{G}_k^T \delta \mathbf{q}_k + \mathbf{G}_{k+1}^T \delta \mathbf{q}_{k+1})^T (\boldsymbol{\lambda}_k + \boldsymbol{\lambda}_{k+1}) = 0
\end{aligned} \tag{18}$$

The equation above can be rearranged as follows.

$$\delta J_{C,d} = \sum_{k=1}^{N-1} h \mathbf{G}_k^T \frac{\boldsymbol{\lambda}_{k-1} + 2\boldsymbol{\lambda}_k + \boldsymbol{\lambda}_{k+1}}{4} \delta \mathbf{q}_k \tag{19}$$



Adding Eq. (19) to Eq. (8), we obtained the discretized action integral with constraints.

$$\begin{aligned}\delta\bar{J} &= \delta J + \delta J_{C,d} \\ &= \sum_{k=1}^{N-1} \left[ D_2 L_d(\mathbf{q}_{k-1}, \mathbf{q}_k, h) + D_1 L_d(\mathbf{q}_k, \mathbf{q}_{k+1}, h) + h \mathbf{G}_k^T \frac{\boldsymbol{\lambda}_{k-1} + 2\boldsymbol{\lambda}_k + \boldsymbol{\lambda}_{k+1}}{4} \right] \delta \mathbf{q}_k = 0\end{aligned}\quad (20)$$

In Eq. (20),  $\delta \mathbf{q}_k$  is an independent variable. Therefore, we obtain the following equation:

$$D_2 L_d(\mathbf{q}_{k-1}, \mathbf{q}_k, h) + D_1 L_d(\mathbf{q}_k, \mathbf{q}_{k+1}, h) + h \mathbf{G}_k^T \frac{\boldsymbol{\lambda}_{k-1} + 2\boldsymbol{\lambda}_k + \boldsymbol{\lambda}_{k+1}}{4} = 0 \quad (21)$$

Introducing  $\frac{\bar{\boldsymbol{\lambda}}_{k+1}}{h^2} = \frac{\boldsymbol{\lambda}_{k-1} + 2\boldsymbol{\lambda}_k + \boldsymbol{\lambda}_{k+1}}{4}$  and using Eq. (11), Eq. (21) yields the

following equation.

$$\begin{aligned}h \left[ \frac{1}{h} \mathbf{M} \left( \frac{\mathbf{q}_k - \mathbf{q}_{k-1}}{h} \right) - \frac{1}{h} \mathbf{M} \left( \frac{\mathbf{q}_{k+1} - \mathbf{q}_k}{h} \right) - \frac{\partial V}{\partial \mathbf{q}_k} \right] + h \mathbf{G}_k^T \frac{\bar{\boldsymbol{\lambda}}_{k+1}}{h^2} &= 0 \\ \therefore \mathbf{M} \mathbf{q}_{k+1} - \mathbf{G}_k^T \bar{\boldsymbol{\lambda}}_{k+1} &= \mathbf{M} (2\mathbf{q}_k - \mathbf{q}_{k-1}) - h^2 \frac{\partial V}{\partial \mathbf{q}_k} = 0\end{aligned}\quad (22)$$

Eq. (22) contains  $\boldsymbol{\lambda}_k$  which is an  $m$ -dimensional vector, except for  $\mathbf{q}_k$ . Therefore, we required additional  $m$  equations. We can obtain these by the partial differential of  $\bar{J}$  by  $\boldsymbol{\lambda}_k$ .

$$\frac{\partial \bar{J}_d}{\partial \lambda_k} = \frac{\partial J_d}{\partial \lambda_k} + \frac{\partial J_{C,d}}{\partial \lambda_k} = \frac{\partial J_{C,d}}{\partial \lambda_k} = 0$$

$$\left( \frac{\partial J_{C,d}}{\partial \lambda_k} = \frac{\partial}{\partial \lambda_k} \left[ \dots + h \left( \frac{\mathbf{g}_{k-1} + \mathbf{g}_k}{2} \right)^T \frac{\lambda_{k-1} + \lambda_k}{2} + h \left( \frac{\mathbf{g}_k + \mathbf{g}_{k+1}}{2} \right)^T \frac{\lambda_k + \lambda_{k+1}}{2} + \dots \right] \right) \quad (23)$$

$$= h \frac{\mathbf{g}_{k-1} + \mathbf{g}_k}{4} + h \frac{\mathbf{g}_k + \mathbf{g}_{k+1}}{4}$$

$$= h \frac{\mathbf{g}_{k-1} + 2\mathbf{g}_k + \mathbf{g}_{k+1}}{4}$$

$$\therefore \frac{\partial \bar{J}_d}{\partial \lambda_k} = h \frac{\mathbf{g}_{k-1} + 2\mathbf{g}_k + \mathbf{g}_{k+1}}{4} = 0 \quad (24)$$

By Taylor series approximation, Eq. (24) yields

$$\mathbf{g}_{k+1} = \mathbf{g}_k + \mathbf{G}_k (\mathbf{q}_{k+1} - \mathbf{q}_k) \quad (25)$$

$$\mathbf{g}_{k-1} = \mathbf{g}_k + \mathbf{G}_k (\mathbf{q}_{k-1} - \mathbf{q}_k)$$

$$\therefore \mathbf{G}_k \mathbf{q}_{k+1} = -4\mathbf{g}_k + \mathbf{G}_k (2\mathbf{q}_k - \mathbf{q}_{k-1}) \quad (26)$$

Therefore, the final forms of the DEL equation with constraints are given by Eqs. (22) and (26). Dividing by  $h$ , and organizing for  $\mathbf{q}_{k+1}$  and  $\bar{\lambda}_{k+1}$ , we obtained the following matrix.

$$\begin{bmatrix} \mathbf{M} & -\mathbf{G}_k^T \\ \mathbf{G}_k & \mathbf{0} \end{bmatrix} \begin{bmatrix} \mathbf{q}_{k+1} \\ \bar{\lambda}_{k+1} \end{bmatrix} = \begin{bmatrix} \mathbf{M}(2\mathbf{q}_k - \mathbf{q}_{k-1}) - h^2 \frac{\partial V}{\partial \mathbf{q}_k} \\ -4\mathbf{g}_k + \mathbf{G}_k (2\mathbf{q}_k - \mathbf{q}_{k-1}) \end{bmatrix} \quad (27)$$

### 2.1.3. Discrete Euler-Lagrange equation with constraints and non-conservative forces

The virtual work done by a non-conservative force  $f(\mathbf{q}, \dot{\mathbf{q}})$  during a time interval  $[t_0, t_N]$  is written by Eq. (28).

$$\delta W_{NC} = \int_{t_0}^{t_N} f(\mathbf{q}, \dot{\mathbf{q}}) \delta \mathbf{q} dt \quad (28)$$

The discretized  $\delta W_{NC}$  can be expressed as follows.

$$\delta W_{NC} = \sum_{k=1}^{N-1} [hf^+(\mathbf{q}_{k-1}, \mathbf{q}_k) + hf^-(\mathbf{q}_k, \mathbf{q}_{k+1})] \delta \mathbf{q}_k \quad (29)$$

where,  $f^-$  are  $f^+$  are called the left and right discrete forces, respectively. Adding those forces in Eqs. (20) and (21), we obtained the following DEL equation with constraints and non-conservative forces.

$$\sum_{k=1}^{N-1} \left[ D_2 L_d(\mathbf{q}_{k-1}, \mathbf{q}_k, h) + D_1 L_d(\mathbf{q}_k, \mathbf{q}_{k+1}, h) + h \mathbf{G}_k^T \frac{\lambda_{k-1} + 2\lambda_k + \lambda_{k+1}}{4} + hf^+(\mathbf{q}_{k-1}, \mathbf{q}_k) + hf^-(\mathbf{q}_k, \mathbf{q}_{k+1}) \right] \delta \mathbf{q}_k = 0 \quad (30)$$

$$\begin{aligned} & \therefore D_2 L_d(\mathbf{q}_{k-1}, \mathbf{q}_k, h) + D_1 L_d(\mathbf{q}_k, \mathbf{q}_{k+1}, h) \\ & + h \mathbf{G}_k^T \frac{\lambda_{k-1} + 2\lambda_k + \lambda_{k+1}}{4} + hf^+(\mathbf{q}_{k-1}, \mathbf{q}_k) + hf^-(\mathbf{q}_k, \mathbf{q}_{k+1}) = 0 \end{aligned} \quad (31)$$

The discrete forces of Eq. (31) are given as follows.

$$\begin{aligned} f^+(\mathbf{q}_{k-1}, \mathbf{q}_k) &= \alpha f\left((1-\alpha)\mathbf{q}_{k-1} + \alpha\mathbf{q}_k, \frac{\mathbf{q}_k - \mathbf{q}_{k-1}}{h}\right) \\ f^-(\mathbf{q}_k, \mathbf{q}_{k+1}) &= (1-\alpha)f\left((1-\alpha)\mathbf{q}_k + \alpha\mathbf{q}_{k+1}, \frac{\mathbf{q}_{k+1} - \mathbf{q}_k}{h}\right) \end{aligned} \quad (32)$$

If we chose  $\alpha = 1$ , the discrete force term is reduced as follows.

$$hf^+(\mathbf{q}_{k-1}, \mathbf{q}_k) + hf^-(\mathbf{q}_k, \mathbf{q}_{k+1}) = hf\left(\mathbf{q}_k, \frac{\mathbf{q}_k - \mathbf{q}_{k-1}}{h}\right) \quad (33)$$

Consequently, the final form of the DEL equation with constraints and non-conservative forces is given by Eq. (34).

$$\begin{aligned} &h\left[\frac{1}{h}\mathbf{M}\left(\frac{\mathbf{q}_k - \mathbf{q}_{k-1}}{h}\right) - \frac{1}{h}\mathbf{M}\left(\frac{\mathbf{q}_{k+1} - \mathbf{q}_k}{h}\right) - \frac{\partial V}{\partial \mathbf{q}_k}\right] \\ &+ h\mathbf{G}_k^T \frac{\lambda_{k-1} + 2\lambda_k + \lambda_{k+1}}{4} + hf\left(\mathbf{q}_k, \frac{\mathbf{q}_k - \mathbf{q}_{k-1}}{h}\right) = 0 \end{aligned} \quad (34)$$

We can organize Eqs. (34) and (26) in the matrix form.

$$\begin{bmatrix} \mathbf{M} & -\mathbf{G}_k^T \\ \mathbf{G}_k & \mathbf{0} \end{bmatrix} \begin{bmatrix} \mathbf{q}_{k+1} \\ \tilde{\lambda}_{k+1} \end{bmatrix} = \begin{bmatrix} \mathbf{M}(2\mathbf{q}_k - \mathbf{q}_{k-1}) - h^2 \frac{\partial V}{\partial \mathbf{q}_k} + h^2 \mathbf{f}\left(\mathbf{q}_k, \frac{\mathbf{q}_k - \mathbf{q}_{k-1}}{h}\right) \\ -4\mathbf{g}_k + \mathbf{G}_k(2\mathbf{q}_k - \mathbf{q}_{k-1}) \end{bmatrix} \quad (35)$$

The final form of the DEL equation (35) is an ill-posed problem, which means it can have many solutions, or violate constraints, due to the error of approximation. To solve this problem, we introduced regularization and stabilization methods.

The procedure until we obtain Eq. (35) is summarized in Figure 2-3.

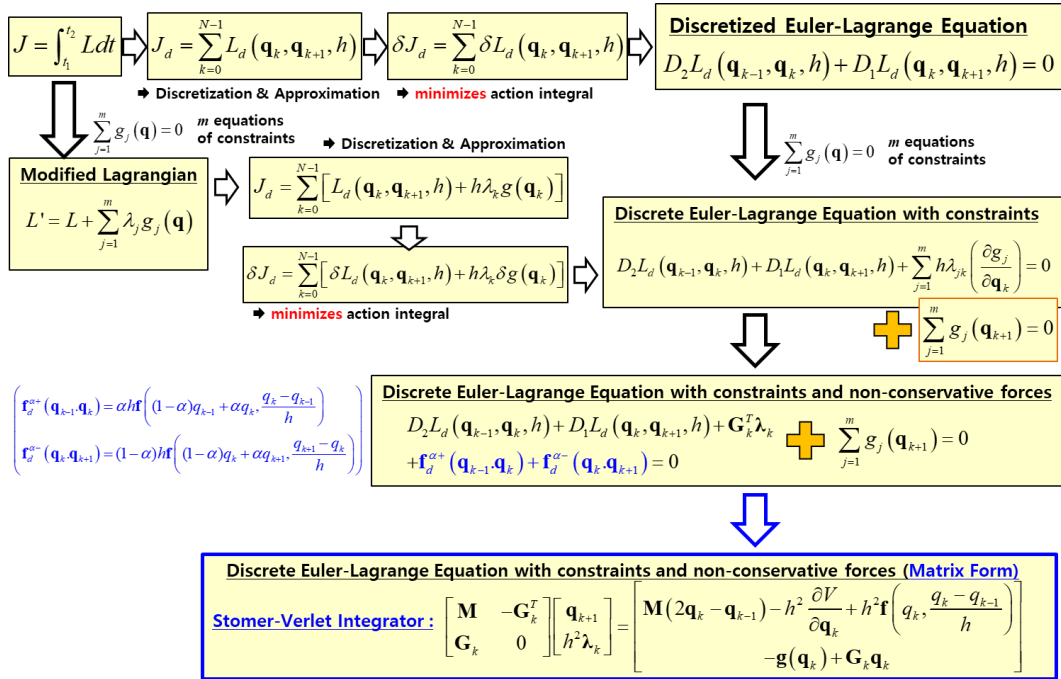


Figure 2-3. Procedure to obtain discrete Euler-Lagrange Equation with constraints and non-conservative forces.

## 2.1.4. Regularization

Baumgarte [39] and Eich et al. [40] explain the basic idea of regularization. In mathematics and statistics, and particularly in the fields of machine learning and inverse problems, regularization refers to the process of introducing additional information, in order to solve an ill-posed problem or to prevent over-fitting. This information is usually in the form of a penalty for complexity, such as restrictions for smoothness, or bounds on

the vector space norm.

The first step to apply regularization is to add augmented terms in the Lagrangian.

$$\bar{L} = L + L_C + L_R, \left( L_R = \sum_{j=1}^m \frac{r_j}{2} g_j^2(\mathbf{q}) \right) \quad (36)$$

$L_R$  means a penalty that is imposed when the motion of a multibody system violates the constraints. By defining auxiliary conditions of the constraints, Lanczos [41] shows that the Lagrangian  $\lambda_j$  and error  $\varepsilon_j$  yields  $g_j = -\varepsilon_j \lambda_j$ . Therefore, the augmented term is given by:

$$L_R = \sum_{j=1}^m \frac{r_j}{2} g_j^2(\mathbf{q}) = \sum_{j=1}^m \frac{\varepsilon_j}{2} \lambda_j^2, \text{ where } r_j = \frac{1}{\varepsilon_j} \quad (37)$$

We now started the discretization process. First, we found the action integral of the regularization term.

$$J_R = \int_{t_1}^{t_2} L_R dt = \frac{1}{2} \int_{t_1}^{t_2} \boldsymbol{\lambda}^T \boldsymbol{\varepsilon} \boldsymbol{\lambda} dt \quad (38)$$

We can express the discretized  $J_R$  as follows.

$$\begin{aligned}
J_R &= \int_{t_0}^{t_1} L_R(\boldsymbol{\lambda}) dt + \cdots + \int_{t_k}^{t_{k+1}} L_R(\boldsymbol{\lambda}) dt + \cdots + \int_{t_{N-1}}^{t_N} L_R(\boldsymbol{\lambda}) dt \\
&= \int_{t_0}^{t_1} \boldsymbol{\lambda}^T \boldsymbol{\varepsilon} \boldsymbol{\lambda} dt + \cdots + \int_{t_k}^{t_{k+1}} \boldsymbol{\lambda}^T \boldsymbol{\varepsilon} \boldsymbol{\lambda} dt + \cdots + \int_{t_{N-1}}^{t_N} \boldsymbol{\lambda}^T \boldsymbol{\varepsilon} \boldsymbol{\lambda} dt
\end{aligned} \tag{39}$$

Now, we applied the midpoint rule to  $J_R$  for approximation.

$$\begin{aligned}
J_{R,d} &= \frac{h}{2} \left( \frac{\boldsymbol{\lambda}_0 + \boldsymbol{\lambda}_1}{2} \right)^T \boldsymbol{\varepsilon} \frac{\boldsymbol{\lambda}_0 + \boldsymbol{\lambda}_1}{2} + \cdots + \frac{h}{2} \left( \frac{\boldsymbol{\lambda}_k + \boldsymbol{\lambda}_{k+1}}{2} \right)^T \boldsymbol{\varepsilon} \frac{\boldsymbol{\lambda}_k + \boldsymbol{\lambda}_{k+1}}{2} \\
&+ \cdots + \frac{h}{2} \left( \frac{\boldsymbol{\lambda}_{N-1} + \boldsymbol{\lambda}_N}{2} \right)^T \boldsymbol{\varepsilon} \frac{\boldsymbol{\lambda}_{N-1} + \boldsymbol{\lambda}_N}{2}
\end{aligned} \tag{40}$$

$$\therefore J_{R,d} = \sum_{i=0}^{N-1} \left[ \frac{h}{8} (\boldsymbol{\lambda}_k + \boldsymbol{\lambda}_{k+1})^T \boldsymbol{\varepsilon} (\boldsymbol{\lambda}_k + \boldsymbol{\lambda}_{k+1}) \right] \tag{41}$$

The variation of  $J_{R,d}$  is zero, because it is only a function of time  $t$ . The following equation is obtained by the partial differential of  $\bar{J}$  by  $\boldsymbol{\lambda}_k$ :

$$\frac{\partial J_{R,d}}{\partial \boldsymbol{\lambda}_k} = h \boldsymbol{\varepsilon} \frac{\boldsymbol{\lambda}_{k-1} + 2\boldsymbol{\lambda}_k + \boldsymbol{\lambda}_{k+1}}{4} = h \boldsymbol{\varepsilon} \frac{\bar{\boldsymbol{\lambda}}_{k+1}}{h^2} \tag{42}$$

From Eqs. (24) and (42), the constraint equation is given by

$$h \frac{\mathbf{g}_{k-1} + 2\mathbf{g}_k + \mathbf{g}_{k+1}}{4} + h \boldsymbol{\varepsilon} \frac{\bar{\boldsymbol{\lambda}}_{k+1}}{h^2} = 0 \tag{43}$$

Following the same sequence of Taylor series approximation, Eq. (43) yields

$$\mathbf{G}_k \mathbf{q}_{k+1} + \frac{4\boldsymbol{\varepsilon}}{h^2} \bar{\boldsymbol{\lambda}}_{k+1} = -4\mathbf{g}_k + \mathbf{G}_k (2\mathbf{q}_k - \mathbf{q}_{k-1}) \quad (44)$$

From Eqs. (34) and (44), we obtained the regularized DEL equation with constraint and non-conservative forces in the matrix form.

$$\begin{bmatrix} \mathbf{M} & -\mathbf{G}_k^T \\ \mathbf{G}_k & \frac{4\boldsymbol{\varepsilon}}{h^2} \end{bmatrix} \begin{bmatrix} \mathbf{q}_{k+1} \\ \bar{\boldsymbol{\lambda}}_{k+1} \end{bmatrix} = \begin{bmatrix} \mathbf{M}(2\mathbf{q}_k - \mathbf{q}_{k-1}) - h^2 \frac{\partial V}{\partial \mathbf{q}_k} + h^2 \mathbf{f} \left( \mathbf{q}_k, \frac{\mathbf{q}_k - \mathbf{q}_{k-1}}{h} \right) \\ -4\mathbf{g}_k + \mathbf{G}_k (2\mathbf{q}_k - \mathbf{q}_{k-1}) \end{bmatrix} \quad (45)$$

### 2.1.5. Stabilization

The numerical solution  $\mathbf{q}_k$  does not satisfy all of the constraint equations at the same time. Moreover, the drift and error grow with time  $t$ . This is not because of the numerical method that is used for integration, but because the system itself is mildly unstable.

To solve this problem, Yoshimura [42] and Lacoursière [29] have proposed many stabilization techniques. The solution can be simply obtained by discretization of the velocity-level constraints, as shown in Figure 2-4.

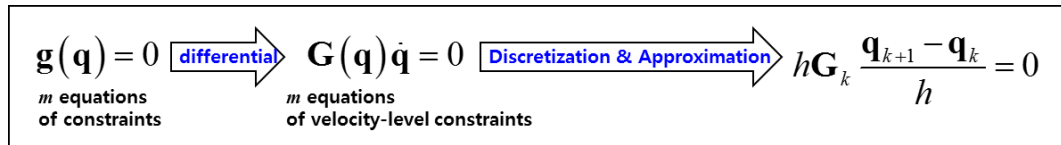


Figure 2-4. Velocity-level constraints and its discretization form.



Adding this to Eq. (43), the solution is given by:

$$h \frac{\mathbf{g}_{k-1} + 2\mathbf{g}_k + \mathbf{g}_{k+1}}{4} + h\boldsymbol{\varepsilon} \frac{\bar{\lambda}_{k+1}}{h^2} + h\tau \mathbf{G}_k \frac{\mathbf{q}_{k+1} - \mathbf{q}_k}{h} = 0 \quad (46)$$

where  $\tau$  is known to be the dissipation rate parameter which plays the same role as violation error. We can re-arrange Eq. (46) as follows.

$$\mathbf{G}_k \mathbf{q}_{k+1} + \Gamma \frac{4\boldsymbol{\varepsilon}}{h^2} \bar{\lambda}_{k+1} = -4\Gamma \mathbf{g}_k + \Gamma \mathbf{G}_k (\mathbf{q}_k - \mathbf{q}_{k-1}) + \mathbf{G}_k \mathbf{q}_k \quad (47)$$

where,  $\Gamma = 1 / \left( 1 + \frac{4\tau}{h} \right)$  is introduced. From Eqs. (34) and (47), we obtained the regularized, stabilized DEL equation with constraint and non-conservative forces in the matrix form.

$$\begin{bmatrix} \mathbf{M} & -\mathbf{G}_k^T \\ \mathbf{G}_k & \Gamma \frac{4\boldsymbol{\varepsilon}}{h^2} \end{bmatrix} \begin{bmatrix} \mathbf{q}_{k+1} \\ \bar{\lambda}_{k+1} \end{bmatrix} = \begin{bmatrix} \mathbf{M}(2\mathbf{q}_k - \mathbf{q}_{k-1}) - h^2 \frac{\partial V}{\partial \mathbf{q}_k} + h^2 \mathbf{f} \left( \mathbf{q}_k, \frac{\mathbf{q}_k - \mathbf{q}_{k-1}}{h} \right) \\ -4\Gamma \mathbf{g}_k + \Gamma \mathbf{G}_k (\mathbf{q}_k - \mathbf{q}_{k-1}) + \mathbf{G}_k \mathbf{q}_k \end{bmatrix} \quad (48)$$

### 2.1.6. Final form of the Discrete Euler-Lagrange equation

Eq. (48) is a two-step method that finds  $\mathbf{q}_{k+1}$  from  $\mathbf{q}_k$  and  $\mathbf{q}_{k-1}$ . The equation is only composed of the displacement. Therefore, we change Eq. (48) to a one-step method with a velocity formulation, which is more convenient to handle. By substituting

$\dot{\mathbf{q}}_k = \mathbf{v}_k = \frac{\mathbf{q}_k - \mathbf{q}_{k-1}}{h}$  and  $\bar{\lambda}_{k+1} = \frac{\lambda_{k+1}}{h}$ , we obtained the final form of the DEL equation

with a one-step method:

$$\begin{bmatrix} \mathbf{M} & -\mathbf{G}_k^T \\ \mathbf{G}_k & \Gamma \frac{4\boldsymbol{\varepsilon}}{h^2} \end{bmatrix} \begin{bmatrix} \mathbf{v}_{k+1} \\ \bar{\lambda}_{k+1} \end{bmatrix} = \begin{bmatrix} \mathbf{M}\mathbf{v}_k - h \frac{\partial V}{\partial \mathbf{q}_k} + h\mathbf{f}(\mathbf{q}_k, \mathbf{v}_k) \\ -\frac{4\Gamma}{h} \mathbf{g}_k + \Gamma \mathbf{G}_k \mathbf{v}_k \end{bmatrix} \quad (49)$$

The procedure of regularization and stabilization until we obtain Eq. (49) is summarized in Figure 2-5.

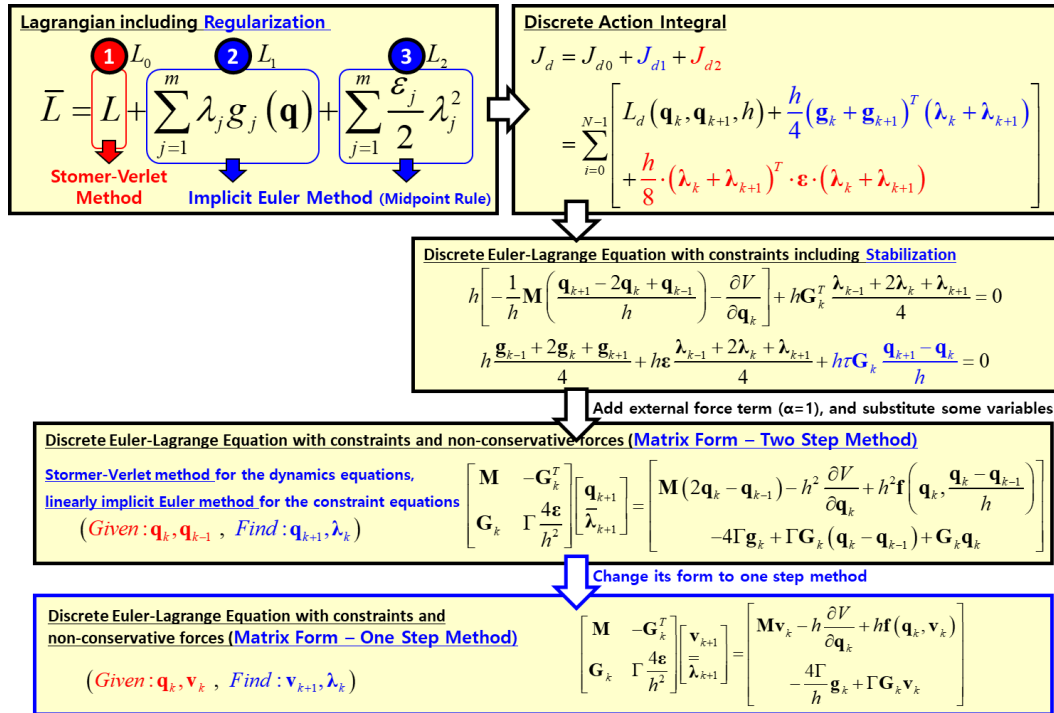


Figure 2-5. Procedure of regularization and stabilization to obtain the final form of the discrete Euler-Lagrange equation.

### 2.1.7. Physical meanings of the parameters in DELE

There are several parameters in DELE, which have the important physical meanings.

The constraint Jacobian ( $\mathbf{G}_k$ ) is the direction of the forces due to the constraint. Lagrange multipliers ( $\lambda$ ) are the magnitude of the constraint forces. Therefore,  $\mathbf{G}_k^T \lambda$  is the constraint forces.

The stabilization term prevents the system from divergence as if it acts like damping. The regularization term  $\epsilon$  determines how strongly the equations of motion are satisfied with constraints.  $\epsilon$  works as if it were inverse of the spring coefficient. For example, the hinge joint is exactly connected at the anchor position at the first time. However, it violates the constraint during the simulation, which means that  $g(\mathbf{q})$  is not zero as shown in Figure 2-6.

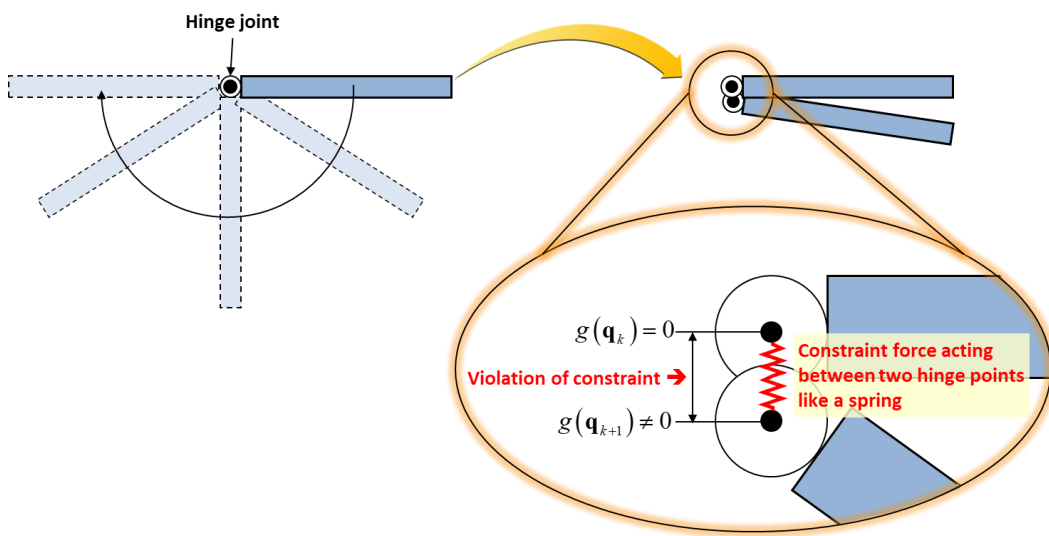


Figure 2-6. Principle how the regularization term works as if it were spring coefficient.

The constraint force is defined as follows.

$$\lambda = kg(\mathbf{q}) = \frac{g(\mathbf{q})}{-\varepsilon} \quad (50)$$

where,  $k$  is spring coefficient. The spring coefficient can be defined by the inverse of  $\varepsilon$  because  $g_j = -\varepsilon_j \lambda_j$  as explained in section 2.1.4.

The physical meaning of the parameters in DELE is summarized in Figure 2-7.

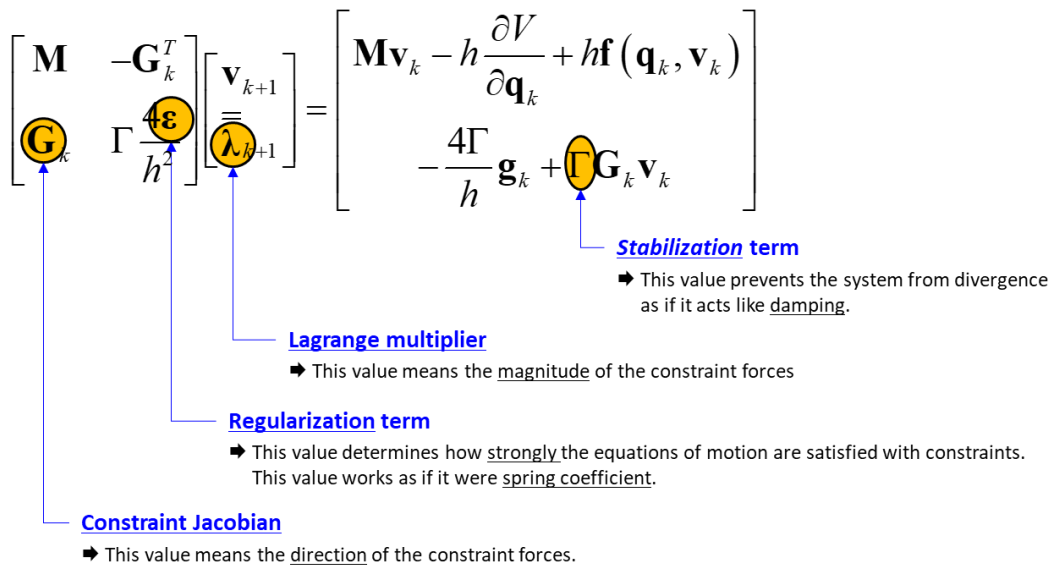


Figure 2-7. Physical meaning of the parameters in DELE.

## **2.2. Multibody dynamics for deformable bodies (1D frame element)**

Flexible multibody systems, in which both elastic and rigid bodies are connected together through mechanical joints and in arbitrary motion with respect to each other, can be divided into linearly elastic multibody systems and nonlinearly elastic multibody systems [33]. For linearly elastic multibody systems, it is assumed that the strain-displacement relationship remains linear, and therefore strain components remain very small at all times for elastic bodies. An efficient analysis technique for this type of problem is the FFRF (Floating Frame of Reference Formulation) [43]. However, for elastic bodies, the strain-displacement relationship is nonlinear or the strain components become large. An efficient analysis technique for this type of problem is the ANCF (Absolute Nodal Coordinate Formulation) which is mainly handled in this study.

### **2.2.1. Overview of flexible multibody dynamics**

Figure 2-8 shows the concept of flexible multibody dynamics, which is combination of multibody dynamics for rigid bodies and structural analysis.

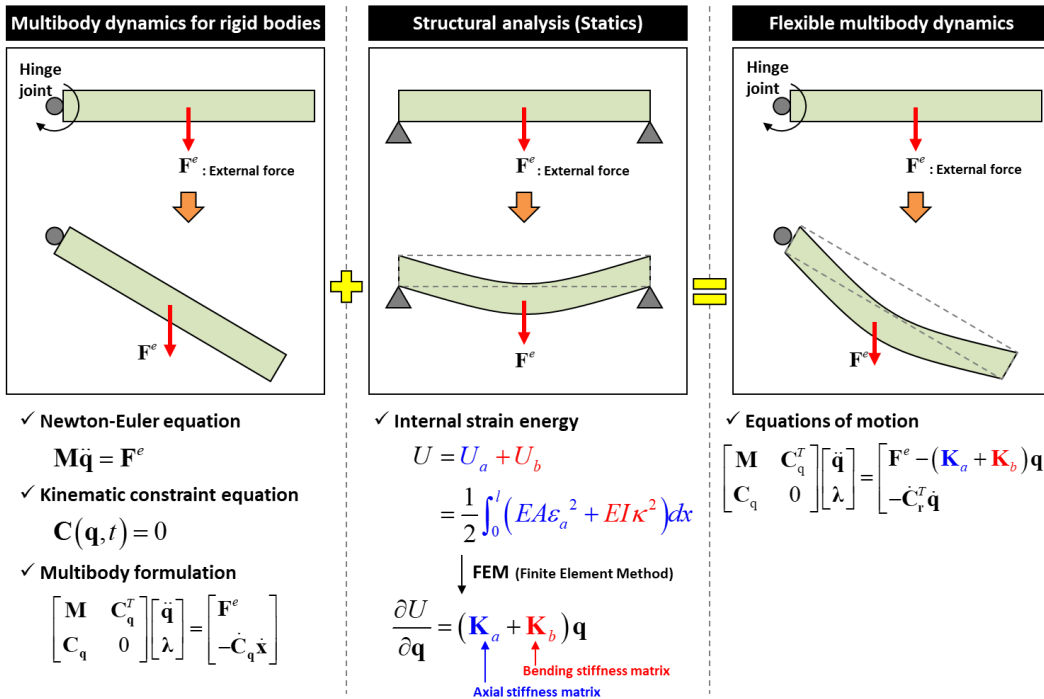


Figure 2-8 Introduction of flexible multibody dynamics.

In this study, we will deal with 1D frame and 2D shell elements. These elements are defined in Figure 2-9. The deformation of 1D frame element is composed of longitudinal stretching and bending. In case of shell element, membrane and plate are combined together. Membrane is deformed along the axial forces, and the plate is deformed due to the moment. Therefore, in case of the shell element, shear and twisting are additionally included.

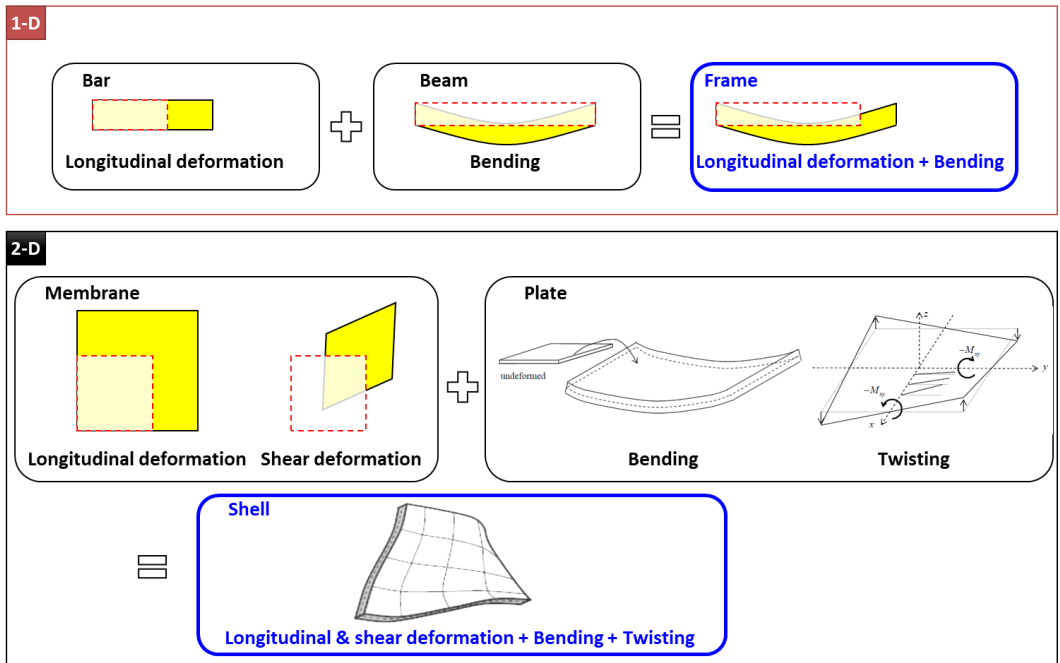


Figure 2-9. Definition of 1D frame and 2D shell elements.

Firstly, we will derive the flexible multibody dynamics for 1D frame element in this section. And then, FMBD for 2D shell element will be derived in the next section.

### 2.2.2. Kinematic description of frame element

A global position on a line segment passing through two given points is shown in Figure 2-10.

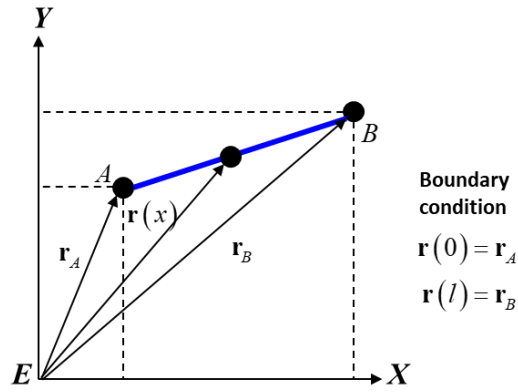


Figure 2-10. Line segment passing through two points

The line segment which is a function of parameter  $x$  ( $0 \leq x \leq l$ ) can be expressed by a linear combination of two points.

$$\begin{aligned}
 \mathbf{r}(x) &= (a_{11} + a_{21}x)\mathbf{r}_A + (a_{12} + a_{22}x)\mathbf{r}_B \\
 &= \begin{bmatrix} a_{11} + a_{21}x & a_{12} + a_{22}x \end{bmatrix} \begin{bmatrix} \mathbf{r}_A \\ \mathbf{r}_B \end{bmatrix} \\
 &= \begin{bmatrix} 1 & x \end{bmatrix} \begin{bmatrix} a_{11} & a_{12} \\ a_{21} & a_{22} \end{bmatrix} \begin{bmatrix} \mathbf{r}_A \\ \mathbf{r}_B \end{bmatrix}
 \end{aligned} \tag{51}$$

where,  $a_{ij}$  is unknowns. From the boundary conditions, we can calculate these unknowns. Applying two boundary conditions, we obtain the following equation.

$$\begin{aligned}
 \mathbf{r}(0) &= \begin{bmatrix} 1 & 0 \end{bmatrix} \begin{bmatrix} a_{11} & a_{12} \\ a_{21} & a_{22} \end{bmatrix} \begin{bmatrix} \mathbf{r}_A \\ \mathbf{r}_B \end{bmatrix} \\
 \mathbf{r}(l) &= \begin{bmatrix} 1 & l \end{bmatrix} \begin{bmatrix} a_{11} & a_{12} \\ a_{21} & a_{22} \end{bmatrix} \begin{bmatrix} \mathbf{r}_A \\ \mathbf{r}_B \end{bmatrix}
 \end{aligned} \tag{52}$$



Eq. (52) can be expressed by the matrix form.

$$\begin{bmatrix} \mathbf{r}(0) \\ \mathbf{r}(l) \end{bmatrix} = \begin{bmatrix} 1 & 0 \\ 1 & l \end{bmatrix} \begin{bmatrix} a_{11} & a_{12} \\ a_{21} & a_{22} \end{bmatrix} \begin{bmatrix} \mathbf{r}_A \\ \mathbf{r}_B \end{bmatrix} \quad (53)$$

By given boundary condition,  $\mathbf{r}(0)$  and  $\mathbf{r}(l)$  is  $\mathbf{r}_A$  and  $\mathbf{r}_B$ , respectively. This means that the matrix multiplied in front of  $\begin{bmatrix} \mathbf{r}_A \\ \mathbf{r}_B \end{bmatrix}$  is an identity matrix. Therefore, we can find unknowns, which is the inverse matrix of  $\begin{bmatrix} 1 & 0 \\ 1 & l \end{bmatrix}$ .

$$\begin{aligned} \mathbf{I} &= \begin{bmatrix} 1 & 0 \\ 1 & l \end{bmatrix} \begin{bmatrix} a_{11} & a_{12} \\ a_{21} & a_{22} \end{bmatrix} \\ \begin{bmatrix} a_{11} & a_{12} \\ a_{21} & a_{22} \end{bmatrix} &= \begin{bmatrix} 1 & 0 \\ 1 & l \end{bmatrix}^{-1} = \frac{1}{l} \begin{bmatrix} l & 0 \\ -1 & 1 \end{bmatrix} \end{aligned} \quad (54)$$

Substituting the unknown values obtained in Eq. (54) into Eq. (51), we can obtain the global position on a line segment passing through two points.

$$\begin{aligned} \therefore \mathbf{r}(x) &= \begin{bmatrix} 1 & x \end{bmatrix} \times \frac{1}{l} \begin{bmatrix} l & 0 \\ -1 & 1 \end{bmatrix} \begin{bmatrix} \mathbf{r}_A \\ \mathbf{r}_B \end{bmatrix} \\ &= \left(1 - \frac{x}{l}\right) \mathbf{r}_A + \frac{x}{l} \mathbf{r}_B \end{aligned} \quad (55)$$

A global position on a cubic spline segment passing through two points and having two slope vectors is shown in Figure 2-11.

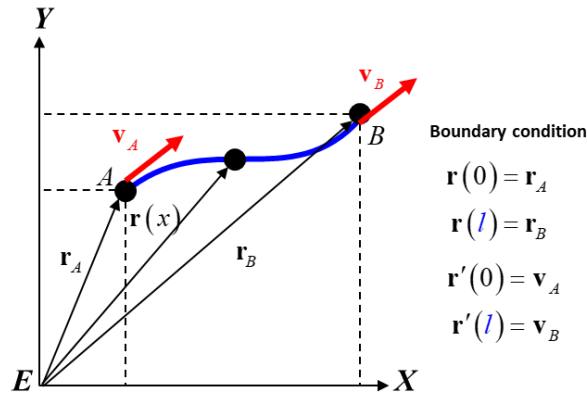


Figure 2-11. Cubic spline segment passing through two points and having two slope vectors.

The cubic spline segment can be expressed by a linear combination of two points and two slope vectors, similar to the line segment derived previously.

$$\begin{aligned}
 \mathbf{r}(x) &= (a_{11} + a_{21}x + a_{31}x^2 + a_{41}x^3)\mathbf{r}_A + (a_{12} + a_{22}x + a_{32}x^2 + a_{42}x^3)\mathbf{v}_A \\
 &\quad + (a_{13} + a_{23}x + a_{33}x^2 + a_{43}x^3)\mathbf{r}_B + (a_{14} + a_{24}x + a_{34}x^2 + a_{44}x^3)\mathbf{v}_B \\
 &= \begin{bmatrix} 1 & x & x^2 & x^3 \end{bmatrix} \begin{bmatrix} a_{11} & a_{12} & a_{13} & a_{14} \\ a_{21} & a_{22} & a_{23} & a_{24} \\ a_{31} & a_{32} & a_{33} & a_{34} \\ a_{41} & a_{42} & a_{43} & a_{44} \end{bmatrix} \begin{bmatrix} \mathbf{r}_A \\ \mathbf{v}_A \\ \mathbf{r}_B \\ \mathbf{v}_B \end{bmatrix} \\
 &= \begin{bmatrix} 1 & x & x^2 & x^3 \end{bmatrix} \mathbf{M} \mathbf{q}
 \end{aligned} \tag{56}$$

By applying boundary condition, we can obtain the following equations.

$$\begin{aligned}
\mathbf{r}(0) &= [1 \ 0 \ 0 \ 0] \mathbf{M} \mathbf{q} \\
\mathbf{r}'(0) &= [0 \ 1 \ 0 \ 0] \mathbf{M} \mathbf{q} \\
\mathbf{r}(l) &= [1 \ l \ l^2 \ l^3] \mathbf{M} \mathbf{q} \\
\mathbf{r}'(l) &= [0 \ 1 \ 2l \ 3l^2] \mathbf{M} \mathbf{q}
\end{aligned} \tag{57}$$

By expressing as a matrix form, we can obtain the following equation.

$$\begin{bmatrix} \mathbf{r}(0) \\ \mathbf{r}'(0) \\ \mathbf{r}(l) \\ \mathbf{r}'(l) \end{bmatrix} = \begin{bmatrix} 1 & 0 & 0 & 0 \\ 0 & 1 & 0 & 0 \\ 1 & l & l^2 & l^3 \\ 0 & 1 & 2l & 3l^2 \end{bmatrix} \mathbf{M} \mathbf{q} \tag{58}$$

The unknown matrix M can be calculated by the inverse matrix.

$$\mathbf{M} = \begin{bmatrix} 1 & 0 & 0 & 0 \\ 0 & 1 & 0 & 0 \\ 1 & l & l^2 & l^3 \\ 0 & 1 & 2l & 3l^2 \end{bmatrix}^{-1} = \begin{bmatrix} 1 & 0 & 0 & 0 \\ 0 & 1 & 0 & 0 \\ -\frac{3}{l^2} & -\frac{2}{l} & \frac{3}{l^2} & -\frac{1}{l} \\ \frac{2}{l^3} & \frac{1}{l^2} & -\frac{2}{l^3} & \frac{1}{l^2} \end{bmatrix} \tag{59}$$

Substituting the unknown values obtained in Eq. (59) into Eq. (56), we can obtain the global position on a cubic segment.

$$\begin{aligned}
\mathbf{r}(t) &= \begin{bmatrix} 1 & x & x^2 & x^3 \end{bmatrix} \begin{bmatrix} 1 & 0 & 0 & 0 \\ 0 & 1 & 0 & 0 \\ -\frac{3}{l^2} & -\frac{2}{l} & \frac{3}{l^2} & -\frac{1}{l} \\ \frac{2}{l^3} & \frac{1}{l^2} & -\frac{2}{l^3} & \frac{1}{l^2} \end{bmatrix} \begin{bmatrix} \mathbf{r}_A \\ \mathbf{v}_A \\ \mathbf{r}_B \\ \mathbf{v}_B \end{bmatrix} \\
&= \left(1 - 3\frac{x^2}{l^2} + 2\frac{x^3}{l^3}\right) \mathbf{r}_A + \left(x - 2\frac{x^2}{l} + \frac{x^3}{l^2}\right) \mathbf{v}_A + \left(3\frac{x^2}{l^2} - 2\frac{x^3}{l^3}\right) \mathbf{r}_B + \left(-\frac{x^2}{l} + \frac{x^3}{l^3}\right) \mathbf{v}_B
\end{aligned} \tag{60}$$

If we introduce  $\xi = \frac{x}{l}$  ( $0 \leq \xi \leq 1$ ), Eq. (60) can be rewritten as follows.

$$\begin{aligned}
\mathbf{r}(\xi) &= \left(1 - 3\xi^2 + 2\xi^3\right) \mathbf{r}_A + l \left(\xi - 2\xi^2 + \xi^3\right) \mathbf{v}_A + \left(3\xi^2 - 2\xi^3\right) \mathbf{r}_B + l \left(-\xi^2 + \xi^3\right) \mathbf{v}_B \\
&= s_1 \mathbf{r}_A + s_2 \mathbf{v}_A + s_3 \mathbf{r}_B + s_4 \mathbf{v}_B \\
&= \begin{bmatrix} s_1 \mathbf{I} & s_2 \mathbf{I} & s_3 \mathbf{I} & s_4 \mathbf{I} \end{bmatrix} \begin{bmatrix} \mathbf{r}_A \\ \mathbf{v}_A \\ \mathbf{r}_B \\ \mathbf{v}_B \end{bmatrix} \\
&= \mathbf{S} \mathbf{q}
\end{aligned} \tag{61}$$

where,  $\mathbf{I}$  is 3 by 3 identity matrix,  $\mathbf{S}$  is the shape function of the frame element, and  $\mathbf{q}$  is the nodal coordinate. The shape function derived from given points and slope vectors are called cubic Hermite shape function (Figure 2-12).

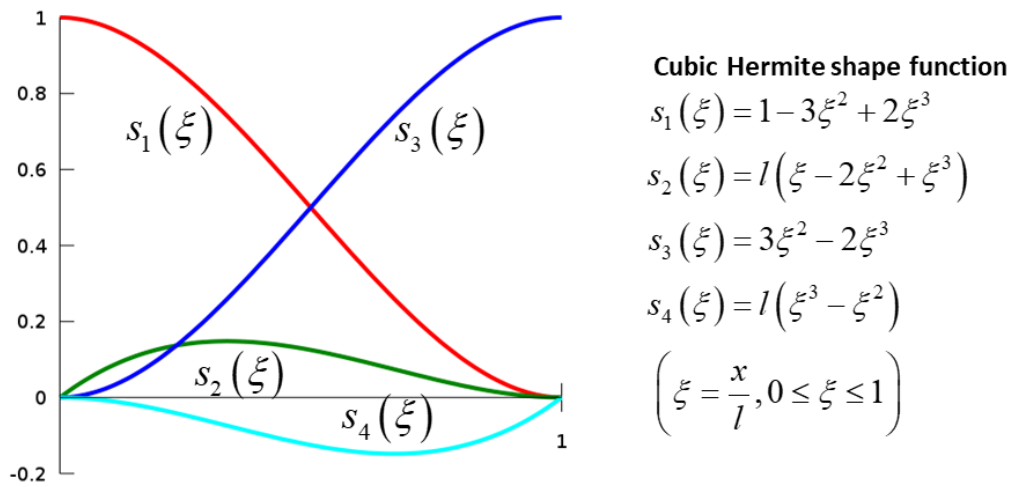


Figure 2-12. Graphs of cubic Hermite shape function.

This cubic segment is used to define the shape of the frame element as shown in Figure 2-13.

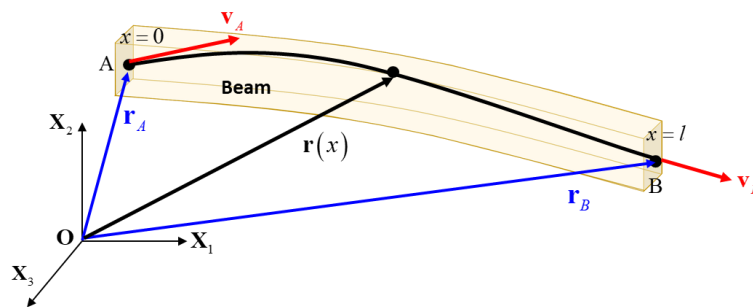


Figure 2-13. Kinematic description of a frame element.

Meanwhile  $\dot{\mathbf{r}}$  is a velocity vector which is obtained by the time derivative of the global position vector.

$$\dot{\mathbf{r}} = \frac{d\mathbf{r}}{dt} = \frac{d\mathbf{S}\mathbf{q}}{dt} = \mathbf{S} \frac{d\mathbf{q}}{dt} = \mathbf{S}\dot{\mathbf{q}} \quad (62)$$

### 2.2.3. Strain energy

Strain energy is the energy stored in the body as a result of applying a force to deform an elastic object. A frame element is deformed due to the forces and moments as shown in Figure 2-14. The deformation of a frame element is decomposed into three components such as longitudinal stretching, bending, and torsion.

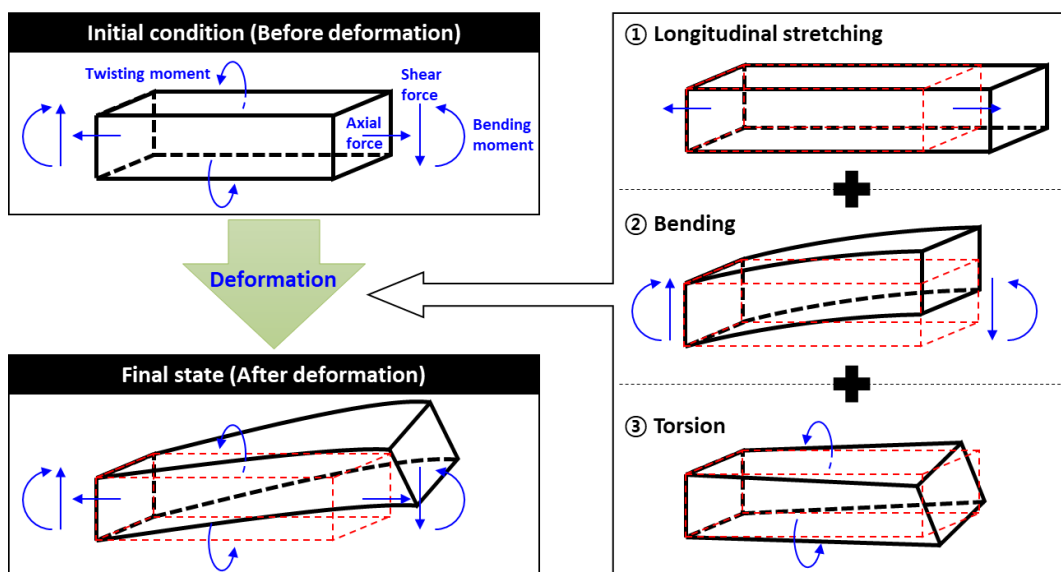


Figure 2-14. Deformation of a frame element.

In the following subsections, axial, bending, and torsional strain energy will be derived.

#### (1) Axial strain energy

Axial strain energy is energy stored due to longitudinal stretching. It is very similar to the elastic potential energy of the spring which is stretched for displacement  $\delta$ . The force to stretch the spring by  $\delta$  is obtained by hook's law as shown in Figure 2-15.

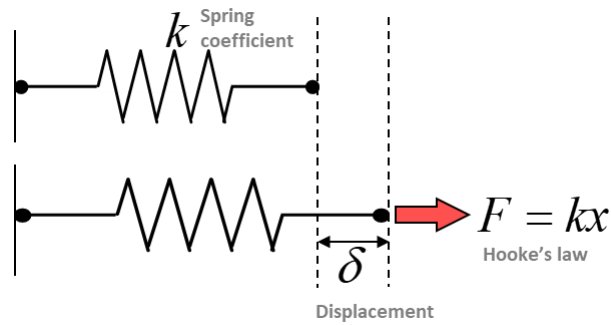


Figure 2-15. Spring stretched by  $\delta$  due to  $F$ .

Work done by force  $F$  is as follows.

$$U = \int_0^\delta kx \, dx = \frac{1}{2} kx^2 \Big|_0^\delta = \frac{1}{2} k\delta^2 \quad (63)$$

The bar element is very similar to the spring as shown in Figure 2-16. Hook's law is exactly derived from the stress-strain relation.

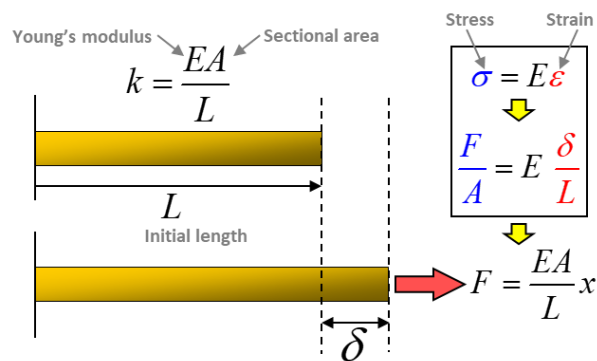


Figure 2-16. Bar element stretched by  $\delta$  due to  $F$ .

Work done by force  $F$  is as follows.

$$\begin{aligned}
U &= \int_0^{\delta} \frac{EA}{L} x dx \\
&= \int_0^{\varepsilon_a} EA \varepsilon (L d\varepsilon) , \\
&= \frac{1}{2} EAL \varepsilon_a^2
\end{aligned}
\left( \begin{array}{l} \varepsilon = \frac{x}{L} \\ \varepsilon_a = \frac{\delta}{L} \\ dx = L d\varepsilon \end{array} \right) \quad (64)$$

Strain energy density is strain energy per unit volume. Therefore, strain energy density  $u$  is as follows.

$$u = \frac{U}{AL} = \frac{1}{2} E \varepsilon_a^2 = \frac{1}{2} \sigma \varepsilon_a \quad (65)$$

s

If the axial force, the cross-sectional area and Young's modulus vary along the bar element, strain energy is only satisfied within a small length  $dx$ . For example, the extended length of  $dx$  at a different position is also different as shown in Figure 2-17. Therefore, they have a different strain and strain energy density.



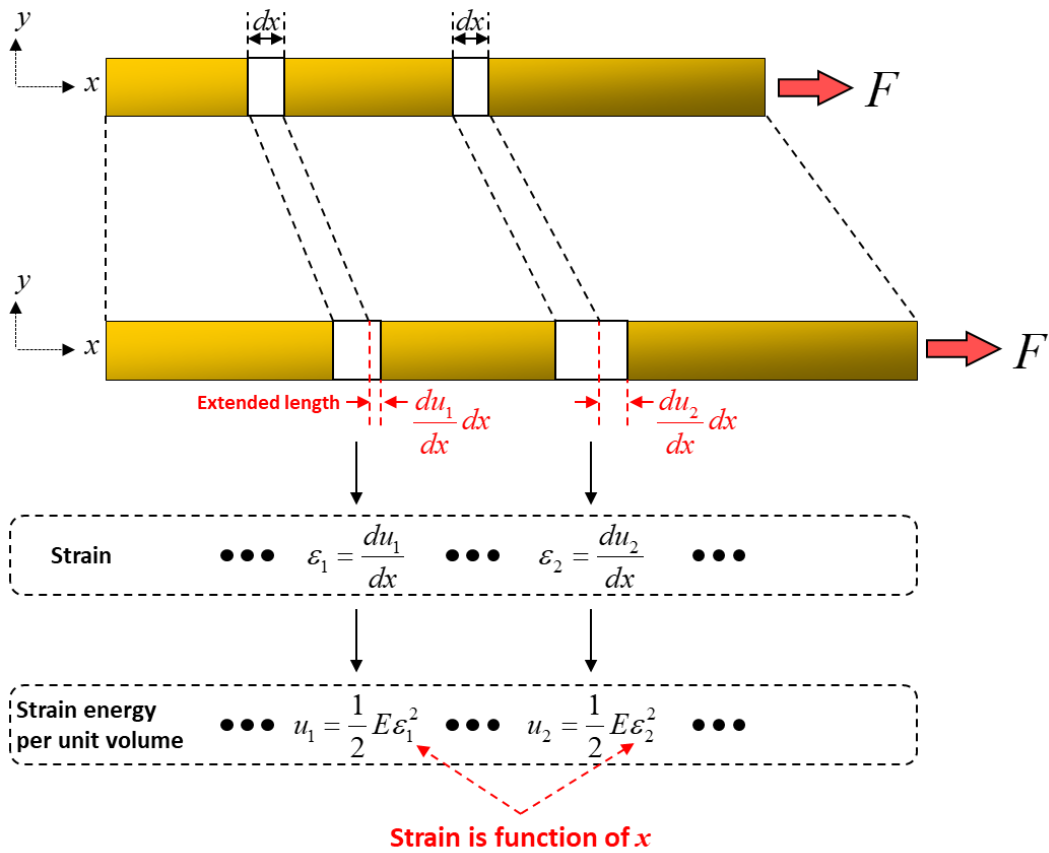


Figure 2-17. Strain energy in bar element.

The total strain energy stored inside bar element is expressed by integral form.

$$\begin{aligned}
 U_a &= \iiint_V u dV \\
 &= \int_0^L \frac{1}{2} E \epsilon_a^2 (A dx) \\
 &= \frac{1}{2} \int_0^L EA \epsilon_a^2 dx
 \end{aligned} \tag{66}$$

## (2) Bending strain energy

Bending strain energy is the energy stored due to bending. Figure 2-18 shows bending of the frame element.

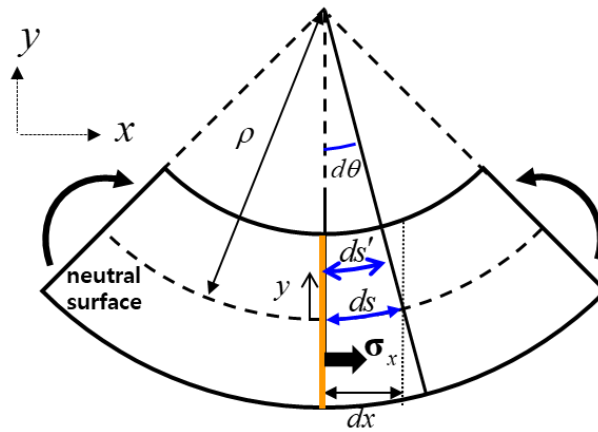


Figure 2-18. Bending of the frame element.

The bending strain  $\varepsilon_b$  at  $y$  from the neutral surface can be derived from the definition.

$$\varepsilon_b = \frac{(\rho - y) \cdot d\theta - \rho d\theta}{ds} = -y \frac{d\theta}{ds} = -\frac{y}{\rho} \quad (67)$$

The bending strain energy density of bending is as same as the axial strain energy density (Eq. (65)).

$$u = \frac{1}{2} E \varepsilon_b^2 = \frac{1}{2} E \left( -\frac{y}{\rho} \right)^2 = \frac{1}{2} E \frac{y^2}{\rho^2} = \frac{1}{2} E \kappa^2 y^2 \quad (68)$$

where,  $\kappa$  is curvature. Finally, total strain energy stored in the frame element due to bending is as follows.

$$\begin{aligned}
 U_b &= \iiint_V u \, dV = \int_0^L \left( \iint u \, dA \right) dx = \int_0^L \left( \iint \frac{1}{2} E \kappa^2 y^2 \, dA \right) dx \\
 &= \frac{1}{2} \int_0^L E \left( \iint y^2 \, dA \right) \kappa^2 dx = \frac{1}{2} \int_0^L EI \kappa^2 dx
 \end{aligned} \tag{69}$$

where,  $I \left( = \iint y^2 \, dA \right)$  is a second moment of inertia.

### (3) Torsional strain energy

Torsional strain energy is the energy stored due to torsion. Figure 2-19 shows torsion of the shaft element.

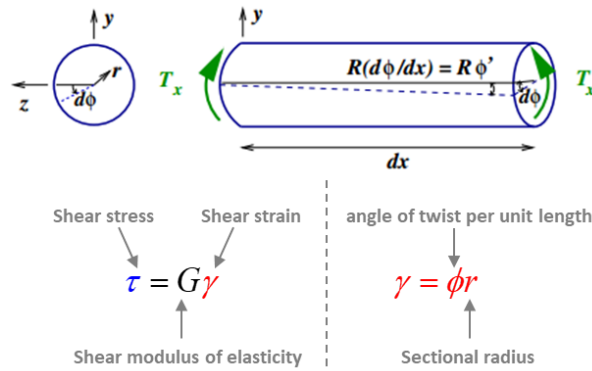


Figure 2-19. Torsion of shaft element.

Similar to axial strain, strain energy density is obtained by the shear stress-strain relation.

$$u = \frac{1}{2} G \gamma^2 = \frac{1}{2} G \phi^2 r^2 \quad (70)$$

Finally, total strain energy stored in the shaft element due to torsion is as follows.

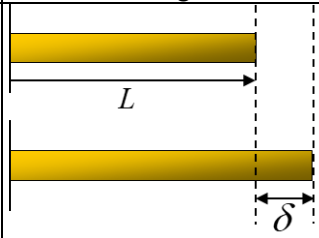
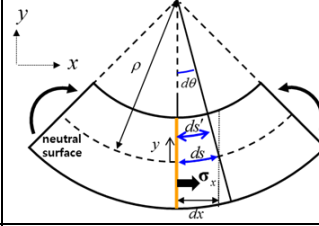
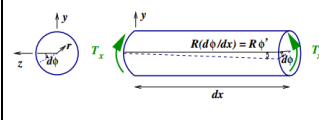
$$\begin{aligned} U_t &= \iiint_V u \, dV = \int_0^L \left( \iint u \, dA \right) dx = \int_0^L \left( \iint \frac{1}{2} G \phi^2 r^2 \, dA \right) dx \\ &= \frac{1}{2} \int_0^L G \left( \iint r^2 \, dA \right) \phi^2 dx = \frac{1}{2} \int_0^L G J \phi^2 dx \end{aligned} \quad (71)$$

where,  $J \left( = \iint r^2 \, dA \right)$  is a polar moment of inertia.

#### (4) Summary of strain energy

Strain energy density and strain energy according to an element type is summarized in Table 2-1.

Table 2-1. Summary of strain energy

Element type	Image	Strain energy density	Strain energy
Bar		$u = \frac{1}{2} E \varepsilon_a^2$	$U_a = \frac{1}{2} \int_0^L EA \varepsilon_a^2 dx$
Beam		$u = \frac{1}{2} E \kappa^2 y^2$	$U_b = \frac{1}{2} \int_0^L EI \kappa^2 dx$ $(I = \iint y^2 dA)$
Shaft		$u = \frac{1}{2} G \phi^2 r^2$	$U_t = \frac{1}{2} \int_0^L GJ \phi^2 dx$ $(J = \iint r^2 dA)$

#### 2.2.4. Equations of motion for 1D frame element

We adopt ANCF well described in Berzeri and Shabana [44] and Shabana [43]. The kinematic description of frame element derived in section 2.2.2, which are composed of the shape function and the nodal coordinate defined in the inertial frame, is used to derive ANCF.

##### (1) Euler-Lagrange equation revisit

The derivation of ANCF is also started from Euler-Lagrange equation defined in Eq.

(3). We rewrite Euler-Lagrange equation below.

$$\frac{d}{dt} \left( \frac{\partial L}{\partial \dot{\mathbf{q}}} \right) - \frac{\partial L}{\partial \mathbf{q}} = \mathbf{0} \quad (72)$$

Eq. (72) does not contain the external force term. It is simply added on the right side of the equation.

$$\frac{d}{dt} \left( \frac{\partial L}{\partial \dot{\mathbf{q}}} \right) - \frac{\partial L}{\partial \mathbf{q}} = \mathbf{Q}_{nc} \quad (73)$$

where,  $\mathbf{Q}_{nc}$  is generalized non-conservative external forces.  $\mathbf{Q}_{nc}$  is defined as follows.

$$\mathbf{Q}_{nc} = \left( \frac{\partial \mathbf{r}}{\partial \mathbf{q}} \right)^T \mathbf{F}_{nc}^e \quad (74)$$

where,  $\mathbf{r}$  is a function of generalized coordinate  $\mathbf{q}$ , and Jacobian  $\frac{\partial \mathbf{r}}{\partial \mathbf{q}}$  is a partial derivative of  $\mathbf{q}$ ,  $\mathbf{F}_{nc}^e$  is non-conservative external forces.

## (2) Kinetic energy of frame element

The kinetic energy of the frame element is defined by the following equation.

$$T = \iiint_M \frac{1}{2} \dot{\mathbf{r}}^T \dot{\mathbf{r}} dm = \iiint_V \frac{1}{2} \dot{\mathbf{r}}^T \dot{\mathbf{r}} \mu dV \quad (75)$$

where,  $\mu$  is density. Substituting The derivative of  $\mathbf{r}$  defined in Eq (62), we can obtain the following equation.

$$\begin{aligned} T &= \iiint_V \frac{1}{2} (\mathbf{S}\dot{\mathbf{q}})^T (\mathbf{S}\dot{\mathbf{q}}) \mu dV \\ &= \iiint_V \frac{1}{2} \dot{\mathbf{q}}^T \mathbf{S}^T \mathbf{S} \dot{\mathbf{q}} \mu dV \\ &= \frac{1}{2} \dot{\mathbf{q}}^T \left( \iiint_V \mu \mathbf{S}^T \mathbf{S} dV \right) \dot{\mathbf{q}} \\ &= \frac{1}{2} \dot{\mathbf{q}}^T \mathbf{M} \dot{\mathbf{q}} \end{aligned} \quad (76)$$

Substituting the kinetic energy into the Euler-Lagrange equation, we can obtain the following equation.

$$\frac{d}{dt} \left( \frac{\partial T}{\partial \dot{\mathbf{q}}} \right) = \frac{d}{dt} (\mathbf{M} \dot{\mathbf{q}}) = \mathbf{M} \ddot{\mathbf{q}} \quad (77)$$

Meanwhile, the mass matrix  $\mathbf{M}$  can be calculated explicitly as follows.

$$\begin{aligned}
\mathbf{M} &= \iiint_V \mu \mathbf{S}^T \mathbf{S} dV \\
&= \int_0^l \mu \mathbf{S}^T \mathbf{S} A dx \\
&= \int_0^1 \mu \mathbf{S}^T \mathbf{S} A l d\xi \\
&= \mu A l \int_0^1 \mathbf{S}^T \mathbf{S} d\xi \\
&= m \int_0^1 \mathbf{S}^T \mathbf{S} d\xi \\
&= m \int_0^1 \begin{bmatrix} s_1 \mathbf{I} \\ s_2 \mathbf{I} \\ s_3 \mathbf{I} \\ s_4 \mathbf{I} \end{bmatrix} [s_1 \mathbf{I} \quad s_2 \mathbf{I} \quad s_3 \mathbf{I} \quad s_4 \mathbf{I}] d\xi \\
&= m \int_0^1 \begin{bmatrix} s_1^2 \mathbf{I} & s_1 s_2 \mathbf{I} & s_1 s_3 \mathbf{I} & s_1 s_4 \mathbf{I} \\ & s_2^2 \mathbf{I} & s_2 s_3 \mathbf{I} & s_2 s_4 \mathbf{I} \\ & & s_3^2 \mathbf{I} & s_3 s_4 \mathbf{I} \\ sym. & & & s_4^2 \mathbf{I} \end{bmatrix} d\xi \\
&= m \begin{bmatrix} \frac{13}{35} \mathbf{I} & \frac{11l}{210} \mathbf{I} & \frac{9}{70} \mathbf{I} & -\frac{13l}{420} \mathbf{I} \\ & \frac{l^2}{105} \mathbf{I} & \frac{13l}{420} \mathbf{I} & -\frac{l^2}{140} \mathbf{I} \\ & & \frac{13}{35} \mathbf{I} & -\frac{11l}{210} \mathbf{I} \\ sym. & & & \frac{l^2}{105} \mathbf{I} \end{bmatrix}
\end{aligned} \tag{78}$$

### (3) Strain energy of frame element

This study ignored the torsional strain energy. Therefore, we use axial and bending strain energies.



$$\begin{aligned}
U &= U_a + U_b \\
&= \frac{1}{2} \int_0^l EA \varepsilon_a^2 dx + \frac{1}{2} \int_0^l EI \kappa^2 dx
\end{aligned} \tag{79}$$

where,  $U_a$  is axial strain energy,  $U_b$  is bending strain energy,  $\varepsilon_a$  and  $\kappa$  are a longitudinal strain and a curvature which are a function of  $\mathbf{r}(x)$ . To calculate strain energy, we have to calculate  $\varepsilon_a$  and  $\kappa$  first. Figure 2-20 shows the frame element at time  $t_0$  and  $t_1$ .

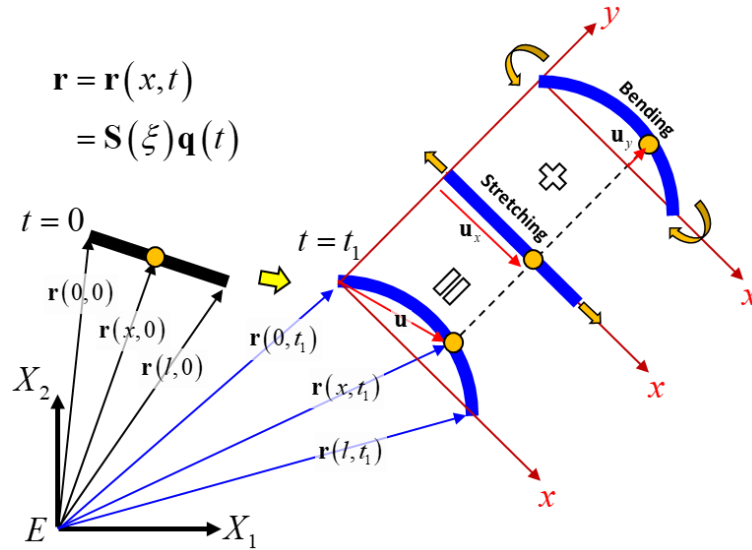


Figure 2-20. Frame element at time  $t_0$  and  $t_1$ .

The displacement vector  $\mathbf{u}$  is defined as follows.

$$\begin{aligned}
\mathbf{u} &= \mathbf{r}(x, t_1) - \mathbf{r}(0, t_1) \\
&= \mathbf{S}(\xi) \mathbf{q}(t_1) - \mathbf{S}(0) \mathbf{q}(t_1) \\
&= \{\mathbf{S}(\xi) - \mathbf{S}(0)\} \mathbf{q}(t_1)
\end{aligned} \tag{80}$$

By definition, the axial strain and curvature can be calculated as follows.

$$\begin{aligned}
 \varepsilon_a &= \frac{d\mathbf{u}}{dx} = \frac{d}{dx}(\mathbf{r}(x) - \mathbf{r}(0)) \\
 &= \frac{d\mathbf{r}}{dx} = \frac{d\mathbf{S}}{dx} \mathbf{q} \\
 &= \frac{d\mathbf{S}}{d\xi} \frac{d\xi}{dx} \mathbf{q} = \frac{d\mathbf{S}}{d\xi} \frac{\mathbf{q}}{l} = \mathbf{S}_{,\xi} \frac{\mathbf{q}}{l}
 \end{aligned} \tag{81}$$

$$\kappa = \frac{d^2\mathbf{r}}{dx^2} = \frac{d^2\mathbf{S}}{dx^2} \mathbf{q} = \frac{d^2\mathbf{S}}{d\xi^2} \frac{\mathbf{q}}{l^2} = \mathbf{S}_{,\xi\xi} \frac{\mathbf{q}}{l^2} \tag{82}$$

Now, the axial and bending strain energy is calculated as follows.

$$\begin{aligned}
 U_a &= \frac{1}{2} \int_0^l \left( \frac{EA}{l^2} \mathbf{q}^T \mathbf{S}_{,\xi}^T \mathbf{S}_{,\xi} \mathbf{q} \right) dx \\
 &= \frac{1}{2} \int_0^1 \left( \frac{EA}{l^2} \mathbf{q}^T \mathbf{S}_{,\xi}^T \mathbf{S}_{,\xi} \mathbf{q} \right) l d\xi \\
 &= \frac{1}{2} \int_0^1 \left( \frac{EA}{l} \mathbf{q}^T \mathbf{S}_{,\xi}^T \mathbf{S}_{,\xi} \mathbf{q} \right) d\xi \\
 &= \frac{1}{2} \frac{EA}{l} \mathbf{q}^T \left( \int_0^1 \mathbf{S}_{,\xi}^T \mathbf{S}_{,\xi} d\xi \right) \mathbf{q} \\
 &= \frac{1}{2} \frac{EA}{l} \mathbf{q}^T \bar{\bar{\mathbf{S}}}_{,\xi} \mathbf{q}
 \end{aligned} \tag{83}$$

$$\begin{aligned}
U_b &= \frac{1}{2} \int_0^l \left( \frac{EI}{l^4} \mathbf{q}^T \mathbf{S}_{\xi\xi\xi}^T \mathbf{S}_{\xi\xi\xi} \mathbf{q} \right) dx \\
&= \frac{1}{2} \int_0^1 \left( \frac{EI}{l^4} \mathbf{q}^T \mathbf{S}_{\xi\xi\xi}^T \mathbf{S}_{\xi\xi\xi} \mathbf{q} \right) l d\xi \\
&= \frac{1}{2} \int_0^1 \left( \frac{EI}{l^3} \mathbf{q}^T \mathbf{S}_{\xi\xi\xi}^T \mathbf{S}_{\xi\xi\xi} \mathbf{q} \right) d\xi \\
&= \frac{1}{2} \frac{EI}{l^3} \mathbf{q}^T \left( \int_0^1 \mathbf{S}_{\xi\xi\xi}^T \mathbf{S}_{\xi\xi\xi} d\xi \right) \mathbf{q} \\
&= \frac{1}{2} \frac{EI}{l^3} \mathbf{q}^T \bar{\mathbf{S}}_{\xi\xi\xi} \mathbf{q}
\end{aligned} \tag{84}$$

Substituting  $U_a$  and  $U_b$  into Euler-Lagrange equation, we obtain the following results.

$$\begin{aligned}
\frac{\partial U_a}{\partial \mathbf{q}} &= \frac{EA}{l} \bar{\mathbf{S}}_{\xi} \mathbf{q} = \mathbf{K}_a \mathbf{q} \\
\frac{\partial U_b}{\partial \mathbf{q}} &= \frac{EI}{l^3} \bar{\mathbf{S}}_{\xi\xi\xi} \mathbf{q} = \mathbf{K}_b \mathbf{q}
\end{aligned} \tag{85}$$

where,  $\mathbf{K}_a$  is axial stiffness matrix, and  $\mathbf{K}_b$  is bending stiffness matrix. The axial and bending stiffness matrices can be calculated explicitly as follows.

$$\mathbf{K}_a = \frac{EA}{l} \begin{bmatrix} \frac{6}{5} \mathbf{I} & \frac{l}{10} \mathbf{I} & -\frac{6}{5} \mathbf{I} & \frac{l}{10} \mathbf{I} \\ & \frac{2l^2}{15} \mathbf{I} & -\frac{l}{10} \mathbf{I} & -\frac{l^2}{30} \mathbf{I} \\ & & \frac{6}{5} \mathbf{I} & -\frac{l}{10} \mathbf{I} \\ \text{sym.} & & & \frac{2l^2}{15} \mathbf{I} \end{bmatrix} \tag{86}$$

$$\mathbf{K}_b = \frac{EI}{l^3} \begin{bmatrix} 12\mathbf{I} & 6\mathbf{I} & -12\mathbf{I} & 6\mathbf{I} \\ & 4l^2\mathbf{I} & -6\mathbf{I} & 2l^2\mathbf{I} \\ & & 12\mathbf{I} & -6\mathbf{I} \\ \text{sym.} & & & 4l^2\mathbf{I} \end{bmatrix} \quad (87)$$

Meanwhile, the results obtained in Eq. (86) is based on the engineering strain, which is suitable to small deformation. For large deformation, we have to use Green-Lagrange strain defined as follows.

$$\begin{aligned} \varepsilon_a &= \frac{1}{2} \left( \left( \frac{d\mathbf{u}}{dx} \right)^T \left( \frac{d\mathbf{u}}{dx} \right) - 1 \right) \\ &= \frac{1}{2} \left( \left( \frac{d\mathbf{r}}{dx} \right)^T \left( \frac{d\mathbf{r}}{dx} \right) - 1 \right) \\ &= \frac{1}{2} \left( \left( \frac{d\mathbf{S}}{dx} \mathbf{q} \right)^T \left( \frac{d\mathbf{S}}{dx} \mathbf{q} \right) - 1 \right) \\ &= \frac{1}{2} \left( \left( \frac{d\mathbf{S}}{d\xi} \frac{\mathbf{q}}{l} \right)^T \left( \frac{d\mathbf{S}}{d\xi} \frac{\mathbf{q}}{l} \right) - 1 \right) \\ &= \frac{1}{2} \left( \frac{\mathbf{q}^T \mathbf{S}_\xi^T \mathbf{S}_\xi \mathbf{q}}{l^2} - 1 \right) \end{aligned} \quad (88)$$

Based on Green-Lagrange strain, we can derive the stiffness matrix as follows.

$$\mathbf{K}_a = \frac{EA}{l} \begin{bmatrix} \text{AI} & \text{BI} & -\text{AI} & \text{CI} \\ & \text{DI} & -\text{BI} & \text{EI} \\ & & \text{AI} & \text{CI} \\ \text{sym.} & & & \text{FI} \end{bmatrix} \quad (89)$$

$$A = \frac{3}{70l^2} (a^2 + b^2 - 14l^2 - 6a_x d_x - 6b_x d_x - 6a_y d_y - 6b_y d_y - 6a_z d_z - 6b_z d_z + 24d^2)$$

$$B = \frac{1}{280l} (b^2 - a^2 + 2a_x b_x + 2a_y b_y + 2a_z b_z - 14l^2 - 24a_x d_x - 24a_y d_y - 24a_z d_z + 36d^2)$$

$$C = \frac{1}{280l} (a^2 - b^2 + 2a_x b_x + 2a_y b_y + 2a_z b_z - 14l^2 - 24b_x d_x - 24b_y d_y - 24b_z d_z + 36d^2)$$

$$D = \frac{1}{420} (12a^2 + b^2 - 3a_x b_x - 3a_y b_y - 3a_z b_z - 28l^2 + 3a_x d_x + 3a_y d_y + 3a_z d_z - 3b_x d_x - 3b_y d_y - 3b_z d_z + 18d^2)$$

$$E = \frac{-1}{840} (3a^2 + 3b^2 - 4a_x b_x - 4a_y b_y - 4a_z b_z - 14l^2 + 6a_x d_x + 6a_y d_y + 6a_z d_z + 6b_x d_x + 6b_y d_y + 6b_z d_z)$$

$$F = \frac{1}{420} (a^2 + 12b^2 - 3a_x b_x - 3a_y b_y - 3a_z b_z - 28l^2 - 3a_x d_x - 3a_y d_y - 3a_z d_z + 3b_x d_x + 3b_y d_y + 3b_z d_z + 18d^2)$$

$$\left( \begin{array}{l} d_x = e_7 - e_1, \quad a_x = le_4, \quad a_y = le_5, \quad a_z = le_6, \quad a = \sqrt{a_x^2 + a_y^2 + a_z^2} \\ d_y = e_8 - e_2, \quad b_x = le_{10}, \quad b_y = le_{11}, \quad b_z = le_{12}, \quad b = \sqrt{b_x^2 + b_y^2 + b_z^2} \\ d_z = e_9 - e_3, \quad d = \sqrt{d_x^2 + d_y^2 + d_z^2} \end{array} \right)$$

#### (4) External forces

If the force is a point load at an arbitrary point on the frame element as shown in Figure 2-21, the generalized non-conservative external force is obtained as follows.

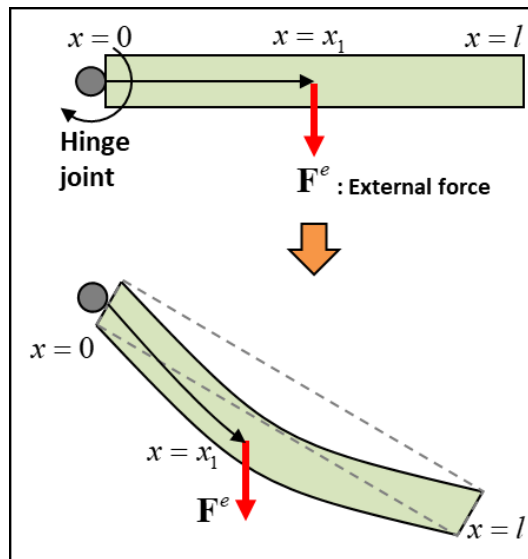


Figure 2-21. External force acting at an arbitrary point.

$$\begin{aligned}
 \mathbf{Q}_{nc} &= \left( \frac{\partial \mathbf{r}}{\partial \mathbf{q}} \right)^T \mathbf{F}_{nc}^e \\
 &= \left( \frac{\partial (\mathbf{S}\mathbf{q})}{\partial \mathbf{q}} \right)^T \mathbf{F}_{nc}^e \\
 &= \mathbf{S}^T \mathbf{F}_{nc}^e
 \end{aligned} \tag{90}$$

If a distributed force acts on the frame element as shown in Figure 2-22, the force is expressed by the integral form.

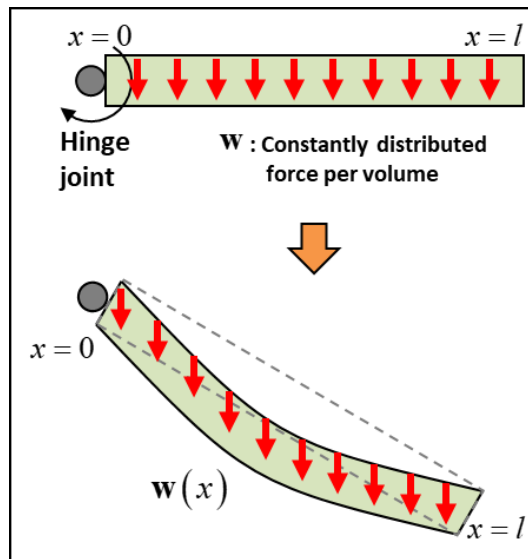


Figure 2-22. External force acting on all over the frame element

$$\begin{aligned}
 \mathbf{Q}_{nc} &= \iiint_V \mathbf{S}^T \mathbf{w}^e dV \\
 &= \int_0^l \mathbf{S}^T \mathbf{w}^e A dx \\
 &= \int_0^l \mathbf{S}^T \mathbf{w}^e A l d\xi \\
 &= Al \left( \int_0^1 \mathbf{S}^T d\xi \right) \mathbf{w}^e \\
 &= Al \bar{\mathbf{S}}^T \mathbf{w}^e
 \end{aligned} \tag{91}$$

where,  $\mathbf{w}^e$  is distributed external force per unit volume, and  $\bar{\mathbf{S}}$  can be calculated as follows.

$$\bar{\mathbf{S}} = \int_0^1 \mathbf{S} d\xi = \begin{bmatrix} \frac{1}{2} \mathbf{I} & \frac{l}{12} \mathbf{I} & \frac{1}{2} \mathbf{I} & -\frac{l}{12} \mathbf{I} \end{bmatrix} \tag{92}$$

A damping force acting on the frame element is proportional to the velocity at  $x$  ( $0 \leq x \leq l$ ) as shown in Figure 2-23.

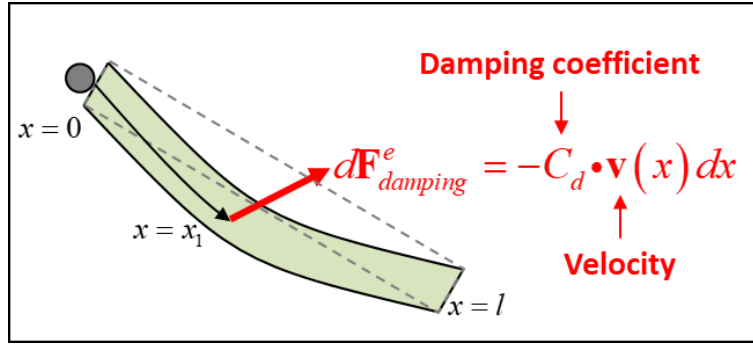


Figure 2-23. Damping force acting on the frame element

The velocity is the same as the derivative of the position vector  $\mathbf{r}$ .

$$\mathbf{v}(x, t) = \dot{\mathbf{r}}(x, t) = \mathbf{S}(\xi) \dot{\mathbf{q}}(t) \quad (93)$$

The damping force acting on a small length  $dx$  is multiplying damping coefficient and the velocity.

$$\begin{aligned} d\mathbf{F}_{damping}^e &= -C_d \cdot \mathbf{v}(x) dx \\ &= -C_d \cdot \{\mathbf{S}(\xi) dx\} \dot{\mathbf{q}}(t) \\ &= -C_d l \cdot \{\mathbf{S}(\xi) d\xi\} \dot{\mathbf{q}}(t) \end{aligned} \quad (94)$$

For the coordinate transformation, Jacobian is multiplied in front of the damping force obtained in Eq. (94).



$$\begin{aligned}
d\mathbf{Q}_{damping} &= \left( \frac{\partial \mathbf{r}}{\partial \mathbf{q}} \right)^T d\mathbf{F}_{damping}^e \\
&= \mathbf{S}^T d\mathbf{F}_{damping}^e \\
&= \mathbf{S}^T \cdot \left[ -C_d l \cdot \{ \mathbf{S}(\xi) d\xi \} \dot{\mathbf{q}}(t) \right] \\
&= -C_d l \cdot \{ \mathbf{S}^T \mathbf{S} d\xi \} \dot{\mathbf{q}}(t)
\end{aligned} \tag{95}$$

Finally, we can obtain generalized damping force all over the frame element as follows.

$$\begin{aligned}
\mathbf{Q}_{damping} &= \int_0^l d\mathbf{Q}_{damping} \\
&= -C_d l \left( \int_0^l \mathbf{S}^T \mathbf{S} d\xi \right) \dot{\mathbf{q}}(t) \\
&= -C_d l \bar{\mathbf{S}} \dot{\mathbf{q}}(t)
\end{aligned} \tag{96}$$

### (5) Summary of equations of motion for 1D frame element

Now, we substitute kinetic energy, strain energy, and the generalized non-conservative external forces into the Euler-Lagrange equation. And then, finally, we can obtain the equations of motion for 1D frame element.

$$\mathbf{M}\ddot{\mathbf{q}} + (\mathbf{K}_a + \mathbf{K}_b)\mathbf{q} = \mathbf{S}^T \mathbf{F}^e + A l \bar{\mathbf{S}}^T \mathbf{w} - C_d l \bar{\bar{\mathbf{S}}}\dot{\mathbf{q}}(t) \quad (97)$$

Figure 2-24 shows a summary of equations of motion for 1D frame element.

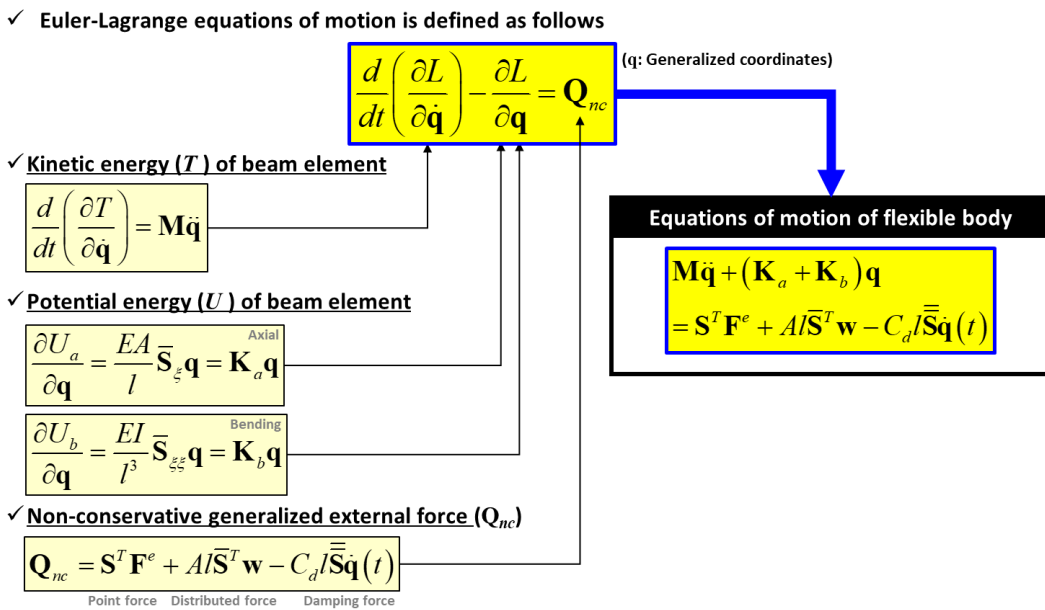


Figure 2-24. Summary of equations of motion for 1D frame element.

### 2.2.5. Discrete Euler-Lagrange equation including Flexible body

The final form of DELE (Eq. (49)) derived in section 2.1 and equations of motion for 1D frame element (Eq. (97)) should be solved together in one equation. We will explain this with a simple example as shown in Figure 2-25. There is one flexible body with three frame elements and two rigid bodies connected by ball and fixed joints. The two rigid bodies, and one flexible body are denoted by  $A$ ,  $B$ , and  $f$ , respectively. The joint constraint is denoted by index 1 and 2.

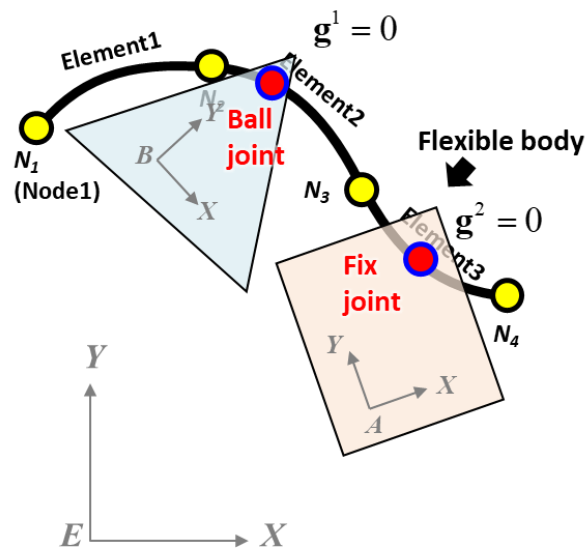


Figure 2-25. Example of one flexible body and two rigid bodies

We rewrite DELE below. Potential energy is erased because it can be included in the force  $\mathbf{f}$ .

$$\begin{bmatrix} \mathbf{M} & -\mathbf{G}_k^T \\ \mathbf{G}_k & \Gamma \frac{4\boldsymbol{\varepsilon}}{h^2} \end{bmatrix} \begin{bmatrix} \mathbf{v}_{k+1} \\ \boldsymbol{\lambda}_{k+1} \end{bmatrix} = \begin{bmatrix} \mathbf{M}\mathbf{v}_k + h\mathbf{f}(\mathbf{q}_k, \mathbf{v}_k) \\ -\frac{4\Gamma}{h} \mathbf{g}_k + \Gamma \mathbf{G}_k \mathbf{v}_k \end{bmatrix} \quad (98)$$

Decomposing the component in Eq. (98) according to the bodies and constraints, we obtain the following equation.

$$\begin{bmatrix} \mathbf{M}^A & \mathbf{0} & \mathbf{0} & -(\mathbf{G}_A^1)^T & \mathbf{0} \\ \mathbf{0} & \mathbf{M}^B & \mathbf{0} & \mathbf{0} & -(\mathbf{G}_B^2)^T \\ \mathbf{0} & \mathbf{0} & \mathbf{M}^f & -(\mathbf{G}_f^1)^T & -(\mathbf{G}_f^2)^T \\ (\mathbf{G}_A^1)_k & \mathbf{0} & (\mathbf{G}_f^1)_k & \Gamma_1 \frac{4\boldsymbol{\varepsilon}_1}{h^2} & \mathbf{0} \\ \mathbf{0} & (\mathbf{G}_B^2)_k & (\mathbf{G}_f^2)_k & \mathbf{0} & \Gamma_2 \frac{4\boldsymbol{\varepsilon}_2}{h^2} \end{bmatrix} \begin{bmatrix} \mathbf{v}_{k+1}^A \\ \mathbf{v}_{k+1}^B \\ \mathbf{v}_{k+1}^f \\ \boldsymbol{\lambda}_{k+1}^1 \\ \boldsymbol{\lambda}_{k+1}^2 \end{bmatrix} = \begin{bmatrix} \mathbf{M}^A \mathbf{v}_k^A + h\mathbf{f}^A \\ \mathbf{M}^B \mathbf{v}_k^B + h\mathbf{f}^B \\ \mathbf{M}^f \mathbf{v}_k^f + h\mathbf{f}^f \\ \frac{4\Gamma_1}{h^2} \mathbf{g}_k^1 + \Gamma_1 \mathbf{G}_k^1 \mathbf{v}_k \\ \frac{4\Gamma_2}{h^2} \mathbf{g}_k^2 + \Gamma_2 \mathbf{G}_k^2 \mathbf{v}_k \end{bmatrix} \quad (99)$$

$\frac{\partial \mathbf{g}^1}{\partial \mathbf{q}} = \mathbf{G}^1 \quad \frac{\partial \mathbf{g}^2}{\partial \mathbf{q}} = \mathbf{G}^2$

$\mathbf{G}_A^1 = \frac{\partial \mathbf{g}^1}{\partial \mathbf{q}_A} \quad \mathbf{G}_f^2 = \frac{\partial \mathbf{g}^2}{\partial \mathbf{q}_f}$

Because the flexible body is composed of three elements, the mass matrix  $\mathbf{M}^f$  is also divided into three parts.

$$\mathbf{M}^f = \begin{pmatrix} \mathbf{M}_{element1}^f & & \mathbf{0} \\ & \mathbf{M}_{element2}^f & \\ \mathbf{0} & & \mathbf{M}_{element3}^f \end{pmatrix}, \quad \mathbf{M}_{element}^f = m \begin{bmatrix} \frac{13}{35} \mathbf{I} & \frac{11l}{210} \mathbf{I} & \frac{9}{70} \mathbf{I} & -\frac{13l}{420} \mathbf{I} \\ & \frac{l^2}{105} \mathbf{I} & \frac{13l}{420} \mathbf{I} & -\frac{l^2}{140} \mathbf{I} \\ & & \frac{13}{35} \mathbf{I} & -\frac{11l}{210} \mathbf{I} \\ sym. & & & \frac{l^2}{105} \mathbf{I} \end{bmatrix} \quad (100)$$

Similarly, the force  $\mathbf{f}^f$  is also composed of three elements as follows.

$$\mathbf{f}^f = \begin{pmatrix} \mathbf{K}_{element1} & & \mathbf{0} \\ & \mathbf{K}_{element2} & \\ \mathbf{0} & & \mathbf{K}_{element3} \end{pmatrix} \mathbf{q}^f + \begin{pmatrix} \mathbf{S}^T(\xi_1) & \mathbf{0} & \mathbf{0} \\ & \mathbf{S}^T(\xi_2) & \mathbf{0} \\ \mathbf{0} & & \mathbf{S}^T(\xi_3) \end{pmatrix} \begin{bmatrix} \mathbf{F}_{element1}^e \\ \mathbf{F}_{element2}^e \\ \mathbf{F}_{element3}^e \end{bmatrix} \quad (101)$$

$$+ \begin{pmatrix} A_1 l_1 \bar{\mathbf{S}}^T & \mathbf{0} & \mathbf{0} \\ & A_2 l_2 \bar{\mathbf{S}}^T & \mathbf{0} \\ \mathbf{0} & & A_3 l_3 \bar{\mathbf{S}}^T \end{pmatrix} \begin{bmatrix} \mathbf{w}_{element1} \\ \mathbf{w}_{element2} \\ \mathbf{w}_{element3} \end{bmatrix}$$

The constraint Jacobian between the rigid body and the frame element is expressed as follows. The derivation of the joint constraint and constraint Jacobian will be explained in section 2.5.1.

$$\begin{aligned}
 \text{Ball joint : } \mathbf{G}_f^1 &= \begin{bmatrix} \mathbf{0} & \mathbf{S}(\xi_1) & \mathbf{0} \\ \mathbf{0} & \mathbf{0} & \mathbf{S}(\xi_2) \\ \mathbf{0} & \mathbf{0} & -\tilde{\mathbf{v}}_r \mathbf{S}_\xi(\xi_2) \end{bmatrix} \\
 \text{Fixed joint : } \mathbf{G}_f^2 &= \begin{bmatrix} \mathbf{0} & \mathbf{0} & \mathbf{S}(\xi_2) \\ \mathbf{0} & \mathbf{0} & -\tilde{\mathbf{v}}_r \mathbf{S}_\xi(\xi_2) \end{bmatrix}
 \end{aligned} \tag{102}$$

Global reference vector which parallel to the position derivative vector on the flexible body

## 2.3. Multibody dynamics for deformable bodies (2D shell element)

In this section, flexible multibody dynamics for 2D shell element will be explained. As 1D frame element is derived based on ANCF, we will extend it to 2D shell element.

### 2.3.1. Kinematic description of shell element

The kinematic description of the shell element is well defined in Dmitrochenko and Pogorelov [45]. Here, we will explain the procedure of derivation more specifically. Figure 2-26 shows the shell element which length, width, and thickness are  $a$ ,  $b$ , and  $h$ , respectively. The mid-plane (neutral plane) has four corner points indexed by 1, 2, 3, and 4.

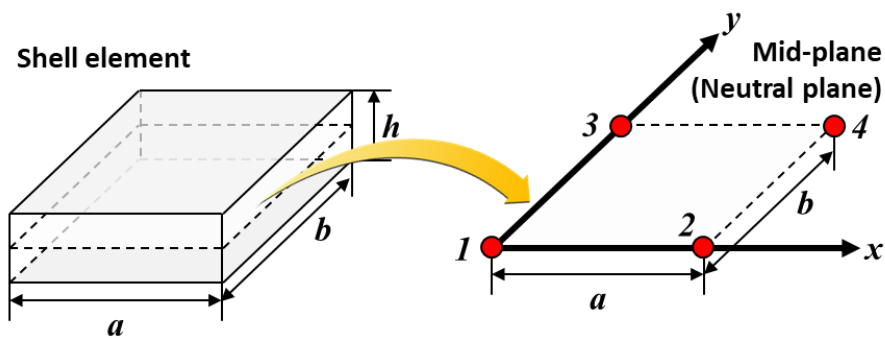


Figure 2-26. Mid-plane of shell element.

After deformation, we want to describe the arbitrary point  $P$  on the mid-plane using the four corner points and slope vectors at the corners (Figure 2-27).

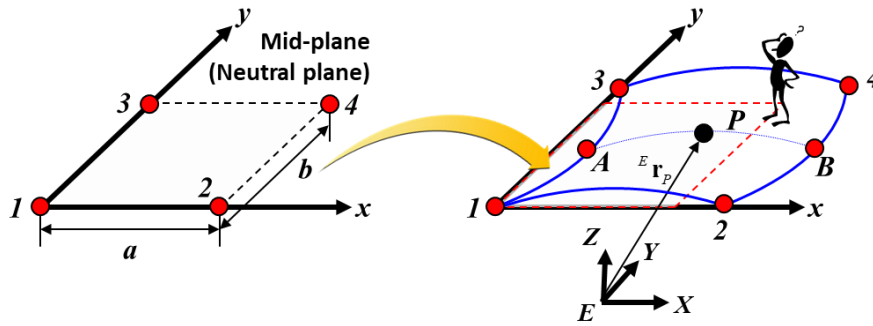


Figure 2-27. Arbitrary point  $P$  on the deformed mid-plane.

Temporary point  $A$  and  $B$  are introduced to use the kinematic description defined for the cubic spline segment (Figure 2-28).

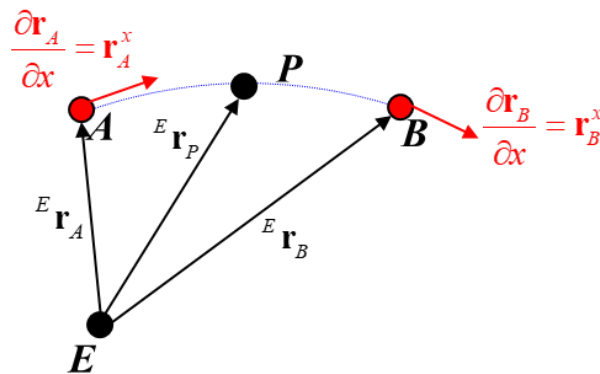


Figure 2-28. Interpolation of point  $P$  using temporary point  $A$ , and  $B$ .

It is expressed as follows. A hat of  $s_i$  means that the shape function is a function of  $\xi$ .

$${}^E \mathbf{r}_P = \mathbf{S}(\xi) \mathbf{q}_{AB} = [\hat{s}_1 \mathbf{I} \quad \hat{s}_2 \mathbf{I} \quad \hat{s}_3 \mathbf{I} \quad \hat{s}_4 \mathbf{I}] \begin{bmatrix} \mathbf{r}_A \\ \mathbf{r}_A^x \\ \mathbf{r}_B \\ \mathbf{r}_B^x \end{bmatrix}, \begin{pmatrix} 0 \leq x \leq a \\ 0 \leq \xi = \frac{x}{a} \leq 1 \end{pmatrix} \quad (103)$$



Meanwhile, the points  $A$ ,  $B$ , and the slope vectors are also calculated using the kinematic description of a cubic spline segment defined by the position vectors and slope vectors at the four corners. The point  $A$ ,  $B$  and the slope vector at point  $A$ ,  $B$  are defined as follows. A double hat of  $s_i$  means that the shape function is a function of  $\eta$ . To interpolate the slope vector, the derivative of the slope vector at the corner points is used.

$${}^E \mathbf{r}_A = \mathbf{S}(\eta) \mathbf{q}_{13} = \begin{bmatrix} \hat{\hat{s}}_1 \mathbf{I} & \hat{\hat{s}}_2 \mathbf{I} & \hat{\hat{s}}_3 \mathbf{I} & \hat{\hat{s}}_4 \mathbf{I} \end{bmatrix} \begin{bmatrix} \mathbf{r}_1 \\ \mathbf{r}_1^y \\ \mathbf{r}_3 \\ \mathbf{r}_3^y \end{bmatrix}, \begin{pmatrix} 0 \leq y \leq b \\ 0 \leq \eta = \frac{y}{b} \leq 1 \end{pmatrix} \quad (104)$$

$${}^E \mathbf{r}_A^x = \mathbf{S}(\eta) \mathbf{q}_{13}^x = \begin{bmatrix} \hat{\hat{s}}_1 \mathbf{I} & \hat{\hat{s}}_2 \mathbf{I} & \hat{\hat{s}}_3 \mathbf{I} & \hat{\hat{s}}_4 \mathbf{I} \end{bmatrix} \begin{bmatrix} \mathbf{r}_1^x \\ \mathbf{r}_1^{xy} \\ \mathbf{r}_3^x \\ \mathbf{r}_3^{xy} \end{bmatrix}, \begin{pmatrix} 0 \leq y \leq b \\ 0 \leq \eta = \frac{y}{b} \leq 1 \end{pmatrix} \quad (105)$$

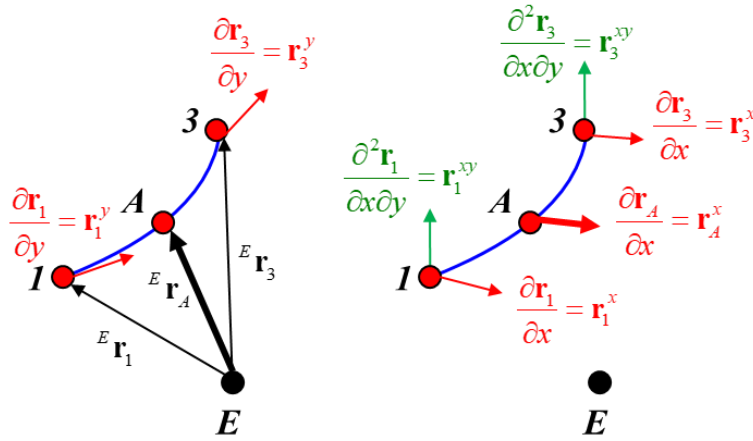


Figure 2-29. Interpolation of point  $A$  and the slope vector.

$${}^E \mathbf{r}_B = \mathbf{S}(\eta) \mathbf{q}_{24} = \begin{bmatrix} \hat{s}_1 \mathbf{I} & \hat{s}_2 \mathbf{I} & \hat{s}_3 \mathbf{I} & \hat{s}_4 \mathbf{I} \end{bmatrix} \begin{bmatrix} \mathbf{r}_2 \\ \mathbf{r}_2^y \\ \mathbf{r}_4 \\ \mathbf{r}_4^y \end{bmatrix}, \begin{cases} 0 \leq y \leq b \\ 0 \leq \eta = \frac{y}{b} \leq 1 \end{cases} \quad (106)$$

$${}^E \mathbf{r}_B^x = \mathbf{S}(\eta) \mathbf{q}_{24}^x = \begin{bmatrix} \hat{s}_1 \mathbf{I} & \hat{s}_2 \mathbf{I} & \hat{s}_3 \mathbf{I} & \hat{s}_4 \mathbf{I} \end{bmatrix} \begin{bmatrix} \mathbf{r}_2^x \\ \mathbf{r}_2^{xy} \\ \mathbf{r}_4^x \\ \mathbf{r}_4^{xy} \end{bmatrix}, \begin{cases} 0 \leq y \leq b \\ 0 \leq \eta = \frac{y}{b} \leq 1 \end{cases} \quad (107)$$

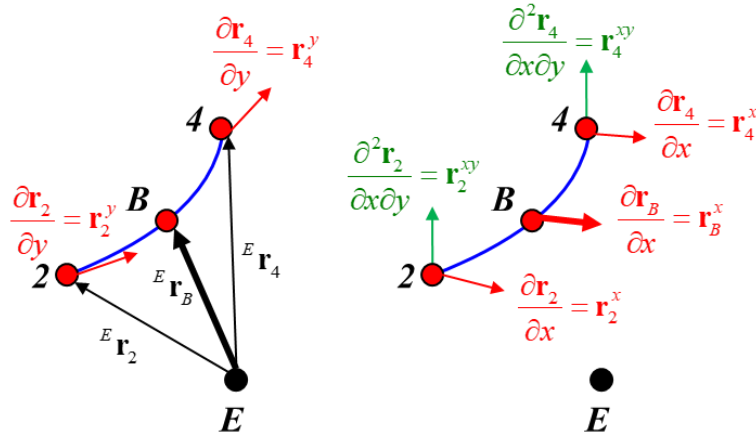


Figure 2-30. Interpolation of point  $B$  and the slope vector.

Finally, the position vector  $P({}^E \mathbf{r}_P)$  can be expressed by the vectors at the four corners by substituting Eq. (104) ~ (107) into Eq. (103).

$$\begin{aligned}
{}^E \mathbf{r}_p &= \mathbf{S}(\xi) \mathbf{q}_{AB} = \mathbf{S}(\xi) \begin{bmatrix} \mathbf{r}_A \\ \mathbf{r}_A^x \\ \mathbf{r}_B \\ \mathbf{r}_B^x \end{bmatrix} = \mathbf{S}(\xi) \begin{bmatrix} \mathbf{S}(\eta) \mathbf{q}_{13} \\ \mathbf{S}(\eta) \mathbf{q}_{13}^x \\ \mathbf{S}(\eta) \mathbf{q}_{24} \\ \mathbf{S}(\eta) \mathbf{q}_{24}^x \end{bmatrix} \\
&= [\hat{\delta}_1 \mathbf{I} \quad \hat{\delta}_2 \mathbf{I} \quad \hat{\delta}_3 \mathbf{I} \quad \hat{\delta}_4 \mathbf{I}] \begin{bmatrix} \hat{\delta}_1 \mathbf{I} \hat{\delta}_2 \mathbf{I} \hat{\delta}_3 \mathbf{I} \hat{\delta}_4 \mathbf{I} & \mathbf{0} & \mathbf{0} & \mathbf{0} & \mathbf{0} & \mathbf{0} & \mathbf{0} & \mathbf{0} & \mathbf{0} & \mathbf{0} & \mathbf{0} & \mathbf{0} & \mathbf{0} & \mathbf{0} & \mathbf{0} & \mathbf{0} & \mathbf{0} \\ \mathbf{0} & \mathbf{0} & \mathbf{0} & \mathbf{0} & \hat{\delta}_1 \mathbf{I} \hat{\delta}_2 \mathbf{I} \hat{\delta}_3 \mathbf{I} \hat{\delta}_4 \mathbf{I} & \mathbf{0} & \mathbf{0} & \mathbf{0} & \mathbf{0} & \mathbf{0} & \mathbf{0} & \mathbf{0} & \mathbf{0} & \mathbf{0} & \mathbf{0} & \mathbf{0} & \mathbf{0} \\ \mathbf{0} & \mathbf{0} & \mathbf{0} & \mathbf{0} & \mathbf{0} & \mathbf{0} & \mathbf{0} & \mathbf{0} & \hat{\delta}_1 \mathbf{I} \hat{\delta}_2 \mathbf{I} \hat{\delta}_3 \mathbf{I} \hat{\delta}_4 \mathbf{I} & \mathbf{0} & \mathbf{0} & \mathbf{0} & \mathbf{0} & \mathbf{0} & \mathbf{0} & \mathbf{0} & \mathbf{0} \\ \mathbf{0} & \mathbf{0} & \mathbf{0} & \mathbf{0} & \mathbf{0} & \mathbf{0} & \mathbf{0} & \mathbf{0} & \mathbf{0} & \mathbf{0} & \mathbf{0} & \mathbf{0} & \hat{\delta}_1 \mathbf{I} \hat{\delta}_2 \mathbf{I} \hat{\delta}_3 \mathbf{I} \hat{\delta}_4 \mathbf{I} & \mathbf{0} & \mathbf{0} & \mathbf{0} & \mathbf{0} \end{bmatrix} \begin{bmatrix} \mathbf{q}_{13} \\ \mathbf{q}_{13}^x \\ \mathbf{q}_{24} \\ \mathbf{q}_{24}^x \end{bmatrix} \\
&= [\hat{\delta}_1 \hat{\delta}_1 \mathbf{I} \quad \hat{\delta}_1 \hat{\delta}_2 \mathbf{I} \quad \hat{\delta}_1 \hat{\delta}_3 \mathbf{I} \quad \hat{\delta}_1 \hat{\delta}_4 \mathbf{I} \quad \hat{\delta}_2 \hat{\delta}_1 \mathbf{I} \quad \hat{\delta}_2 \hat{\delta}_2 \mathbf{I} \quad \cdots \quad \hat{\delta}_4 \hat{\delta}_3 \mathbf{I} \quad \hat{\delta}_4 \hat{\delta}_4 \mathbf{I}] \mathbf{q} \\
&= [\mathbf{S}_{11} \quad \mathbf{S}_{12} \quad \mathbf{S}_{13} \quad \mathbf{S}_{14} \quad \mathbf{S}_{21} \quad \cdots \quad \mathbf{S}_{43} \quad \mathbf{S}_{44}] \mathbf{q}
\end{aligned} \tag{108}$$

The generalized coordinate  $\mathbf{q}$  is composed of the position vectors, the slope vectors, and the derivatives of the slope vectors.

$$\begin{aligned}
\mathbf{q} &= [\mathbf{r}_1 \quad \mathbf{r}_1^y \quad \mathbf{r}_3 \quad \mathbf{r}_3^y \quad \mathbf{r}_1^x \quad \mathbf{r}_1^{xy} \quad \mathbf{r}_3^x \quad \mathbf{r}_3^{xy} \quad \mathbf{r}_2 \quad \mathbf{r}_2^y \quad \mathbf{r}_4 \quad \mathbf{r}_4^y \quad \mathbf{r}_2^x \quad \mathbf{r}_2^{xy} \quad \mathbf{r}_4^x \quad \mathbf{r}_4^{xy}]^T \\
&= [\mathbf{e}_1 \quad \mathbf{e}_2 \quad \mathbf{e}_3 \quad \mathbf{e}_4 \quad \mathbf{e}_5 \quad \mathbf{e}_6 \quad \mathbf{e}_7 \quad \mathbf{e}_8 \quad \mathbf{e}_9 \quad \mathbf{e}_{10} \quad \mathbf{e}_{11} \quad \mathbf{e}_{12} \quad \mathbf{e}_{13} \quad \mathbf{e}_{14} \quad \mathbf{e}_{15} \quad \mathbf{e}_{16}]^T
\end{aligned} \tag{109}$$

### 2.3.2. Strain energy for shell element

A plate is a flat structural element for which the thickness is small compared with the surface dimensions. The thickness is usually constant but may be variable and is measured normal to the middle surface of the plate. Plate theory is concerned mainly with lateral loading. It is very like the beam theory. It turns out to be an accurate theory provided the plate is relatively thin (as in the beam theory) but also that the deflections are small relative to the thickness. Things are more complicated for plates than for the beams. For one, the plate not only bends, but torsion may occur (it can twist).

To derive the equations of motion for 2D shell element, strain energy due to bending and twisting should be derived. The curvature-strain relation of bending and twisting is

shown in Figure 2-31.  $\kappa_x$  and  $\kappa_y$  are the curvatures in the  $x$  and  $y$  directions, which is the rate of change of the slope with respect to arc length.  $\kappa_{xy}$  is the twist, which is a slope  $\partial^2 z / \partial x \partial y$ .

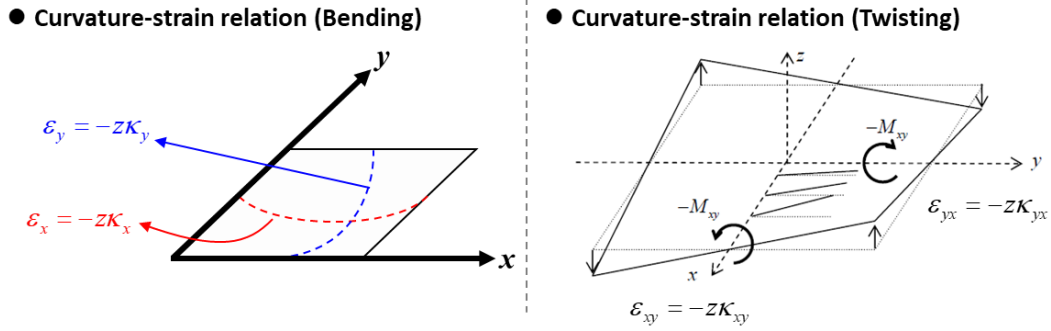


Figure 2-31. Curvature-strain relation of bending and twisting.

The stress-strain relation is defined as follows.

$$\begin{aligned}
 \sigma_x &= \frac{E}{1-\nu^2} (\varepsilon_x + \nu\varepsilon_y) = -\frac{Ez}{1-\nu^2} (\kappa_x + \nu\kappa_y) \\
 \sigma_y &= \frac{E}{1-\nu^2} (\varepsilon_y + \nu\varepsilon_x) = -\frac{Ez}{1-\nu^2} (\kappa_y + \nu\kappa_x) \\
 \sigma_{xy} &= \sigma_{yx} = G\varepsilon_{xy} = -\frac{Ez}{1+\nu} \kappa_{xy}, \left( G = \frac{E}{1+\nu} \right)
 \end{aligned} \tag{110}$$

where,  $\nu$  is Poisson's ratio,  $E$  is Young's modulus,  $G$  is shear modulus. The infinitesimal force per unit length is defined as follows.

$$dF_x = \sigma_x dA = -\frac{Ez}{1-\nu^2} (\kappa_x + \nu\kappa_y) dz \tag{111}$$

The infinitesimal moment per unit length is obtained by multiplying the moment arm  $z$  and the infinitesimal force defined in Eq. (111).

$$dM_x = -z \times dF = -z \times \sigma dz = \frac{Ez^2}{1-\nu^2} (\kappa_x + \nu\kappa_y) dz \quad (112)$$

The moment per unit length is obtained by the integral over the thickness.

$$\begin{aligned} M_x &= \int dM = \int_{-h/2}^{h/2} \frac{Ez^2}{1-\nu^2} (\kappa_x + \nu\kappa_y) dz \\ &= \frac{E}{1-\nu^2} \left( \int_{-h/2}^{h/2} z^2 dz \right) (\kappa_x + \nu\kappa_y) \\ &= \frac{Eh^3}{12(1-\nu^2)} (\kappa_x + \nu\kappa_y) = D (\kappa_x + \nu\kappa_y) \end{aligned} \quad (113)$$

where,  $D$  is flexural rigidity. Similarly, the moment along the  $y$  axis and twisting moment are as follows.

$$\begin{aligned} M_y &= D (\kappa_y + \nu\kappa_x) \\ M_{xy} &= M_{yx} = -D(1-\nu)\kappa_{xy} \end{aligned} \quad (114)$$

Therefore, the strain energy due to bending and twisting is calculated as follows. Firstly, the infinitesimal strain energy along the  $x$  direction is defined as follows.

$$\begin{aligned}
dU_x &= \frac{1}{2}(M_x dy) d\theta \\
&= \frac{1}{2}\left(D(\kappa_x + \nu\kappa_y) dy\right) \kappa_x dx \\
&= \frac{D}{2}\left(\kappa_x^2 + \nu\kappa_x\kappa_y\right) dx dy
\end{aligned} \tag{115}$$

Similarly, the infinitesimal strain energy along the y direction and twisting strain energy are as follows.

$$\begin{aligned}
dU_y &= \frac{D}{2}\left(\nu\kappa_x\kappa_y + \kappa_y^2\right) dx dy \\
dU_{xy} &= dU_{yx} = \frac{D}{2}(1-\nu)\kappa_{xy}^2 dx dy
\end{aligned} \tag{116}$$

Total infinitesimal strain energy is a summation of the above results.

$$\begin{aligned}
dU_{bt} &= dU_x + dU_y + 2dU_{xy} \\
&= \frac{D}{2}\left(\kappa_x^2 + 2\nu\kappa_x\kappa_y + \kappa_y^2 + 2(1-\nu)\kappa_{xy}^2\right) dx dy
\end{aligned} \tag{117}$$

Finally, the strain energy due to bending and twisting is obtained as follows.

$$\begin{aligned}
U_{bt} &= \iint dU_{bt} \\
&= \frac{D}{2} \int_0^b \int_0^a \left\{ \kappa_x^2 + 2\nu\kappa_x\kappa_y + \kappa_y^2 + 2(1-\nu)\kappa_{xy}^2 \right\} dx dy
\end{aligned} \tag{118}$$

### 2.3.3. Strain energy for membrane element

Stress-strain relation of membrane element is defined as follows.

$$\begin{aligned}
 \sigma_x &= \frac{E}{1-\nu^2} (\varepsilon_x + \nu\varepsilon_y) \\
 \sigma_y &= \frac{E}{1-\nu^2} (\varepsilon_y + \nu\varepsilon_x) \\
 \sigma_{xy} &= \sigma_{yx} = G\varepsilon_{xy}, \left( G = \frac{E}{1+\nu} \right)
 \end{aligned} \tag{119}$$

The strain energy due to longitudinal and shear deformation is calculated as follows.

$$\begin{aligned}
 dU_x &= \frac{1}{2} \sigma_x \varepsilon_x h = \frac{1}{2} \frac{Eh}{1-\nu^2} (\varepsilon_x + \nu\varepsilon_y) \varepsilon_x = \frac{Eh}{2(1-\nu^2)} (\varepsilon_x^2 + \nu\varepsilon_x \varepsilon_y) \\
 dU_y &= \frac{1}{2} \sigma_y \varepsilon_y h = \frac{Eh}{2(1-\nu^2)} (\varepsilon_y^2 + \nu\varepsilon_x \varepsilon_y) \\
 dU_{xy} &= \frac{1}{2} \sigma_{xy} \varepsilon_{xy} h = \frac{Eh}{2(1+\nu)} \varepsilon_{xy}^2
 \end{aligned} \tag{120}$$

$$\begin{aligned}
 dU_{ls} &= dU_x + 2dU_{xy} + dU_y \\
 &= \frac{Eh}{2(1-\nu^2)} (\varepsilon_x^2 + \nu\varepsilon_x \varepsilon_y) + \frac{Eh}{1+\nu} \varepsilon_{xy}^2 + \frac{Eh}{2(1-\nu^2)} (\varepsilon_y^2 + \nu\varepsilon_x \varepsilon_y) \\
 &= \frac{Eh}{2(1-\nu^2)} (\varepsilon_x^2 + 2\nu\varepsilon_x \varepsilon_y + \varepsilon_y^2) + \frac{Eh}{2(1-\nu^2)} \times 2(1-\nu) \varepsilon_{xy}^2
 \end{aligned} \tag{121}$$

$$U_{ls} = \frac{Eh}{2(1-\nu^2)} \int_0^b \int_0^a \left\{ (\varepsilon_x^2 + 2\nu\varepsilon_x\varepsilon_y + \varepsilon_y^2) + 2(1-\nu)\varepsilon_{xy}^2 \right\} dx dy \quad (122)$$

### 2.3.4. Equations of motion for 2D shell element

We adopt ANCF well described in Dmitrochenko and Pogorelov [45]. Similar to the 1D frame element, Euler-Lagrange equation is also used to derive the equations of motion for 2D shell element.

#### (1) Kinetic energy of shell element

The mass matrix can be obtained as a result of kinetic energy. It was already derived in section 2.2.4(2). Therefore, the mass matrix of the shell element is calculated with reference to Eq. (78).



$$\begin{aligned}
\mathbf{M} &= \iiint_V \mu \mathbf{S}^T \mathbf{S} dV \\
&= \int_0^b \int_0^a \mu \mathbf{S}^T \mathbf{S} h dx dy \\
&= \int_0^1 \int_0^1 \mu \mathbf{S}^T \mathbf{S} h ab d\xi d\eta \\
&= m \int_0^1 \int_0^1 \mathbf{S}^T \mathbf{S} d\xi d\eta \\
&= m \int_0^1 \int_0^1 \begin{bmatrix} \mathbf{S}_{11} \\ \mathbf{S}_{12} \\ \vdots \\ \mathbf{S}_{44} \end{bmatrix} [\mathbf{S}_{11} \quad \mathbf{S}_{12} \quad \cdots \quad \mathbf{S}_{44}] d\xi d\eta \\
&= m \int_0^1 \int_0^1 \begin{bmatrix} \mathbf{S}_{11}\mathbf{S}_{11} & \mathbf{S}_{11}\mathbf{S}_{12} & \cdots & \mathbf{S}_{11}\mathbf{S}_{44} \\ & \mathbf{S}_{12}\mathbf{S}_{11} & \cdots & \mathbf{S}_{12}\mathbf{S}_{44} \\ & & \ddots & \vdots \\ sym. & & & \mathbf{S}_{44}\mathbf{S}_{44} \end{bmatrix} d\xi d\eta
\end{aligned} \tag{123}$$

Each component of the mass matrix can be calculated explicitly.  $\mathbf{S}_{ij}$  is composed of the multiplication of two shape functions with different parameters ( $\xi, \eta$ ). Therefore, the shape functions are divided into two integrals as follows.

$$\int_0^1 \int_0^1 \mathbf{S}_{ij} \mathbf{S}_{kl} d\xi d\eta = \int_0^1 \int_0^1 \hat{s}_i \hat{s}_j \hat{s}_k \hat{s}_l \mathbf{I} d\xi d\eta = \mathbf{I} \left( \int_0^1 \hat{s}_i \hat{s}_k d\xi \right) \left( \int_0^1 \hat{s}_j \hat{s}_l d\eta \right) \tag{124}$$

Each integral can be calculated as follows.

$$\int_0^1 \hat{s}_i \hat{s}_k d\xi = \begin{bmatrix} \frac{13}{35} & \frac{11a}{210} & \frac{9}{70} & -\frac{13a}{420} \\ & \frac{a^2}{105} & \frac{13a}{420} & -\frac{a^2}{140} \\ & & \frac{13}{35} & -\frac{11a}{210} \\ \text{sym.} & & & \frac{a^2}{105} \end{bmatrix}_{ik} \quad (125)$$

$$\int_0^1 \hat{s}_j \hat{s}_l d\eta = \begin{bmatrix} \frac{13}{35} & \frac{11b}{210} & \frac{9}{70} & -\frac{13b}{420} \\ & \frac{b^2}{105} & \frac{13b}{420} & -\frac{b^2}{140} \\ & & \frac{13}{35} & -\frac{11b}{210} \\ \text{sym.} & & & \frac{b^2}{105} \end{bmatrix}_{jl} \quad (126)$$

The result is obtained by multiplying the value from  $i^{\text{th}}$  row and  $k^{\text{th}}$  column of Eq. (125) and the value from  $j^{\text{th}}$  row and  $l^{\text{th}}$  column of Eq. (126). For example,  $\mathbf{S}_{12}\mathbf{S}_{34}$  is the multiplication of  $9/70$  (first row and third column) and  $-b^2/140$  (second row and fourth column).

## (2) Longitudinal and shear strain energy of shell element

Green-Lagrange strain is defined for 2D shell element as follows.

$$\begin{aligned}
\varepsilon_x &= \frac{1}{2} \left( \left( \frac{d\mathbf{u}}{dx} \right)^T \left( \frac{d\mathbf{u}}{dx} \right) - 1 \right) \\
&= \frac{1}{2} \left( \left( \frac{d\mathbf{r}}{dx} \right)^T \left( \frac{d\mathbf{r}}{dx} \right) - 1 \right) \\
&= \frac{1}{2} \left( \left( \frac{d\mathbf{S}}{dx} \mathbf{q} \right)^T \left( \frac{d\mathbf{S}}{dx} \mathbf{q} \right) - 1 \right) \\
&= \frac{1}{2} \left( \left( \frac{d\mathbf{S}}{d\xi} \frac{\mathbf{q}}{a} \right)^T \left( \frac{d\mathbf{S}}{d\xi} \frac{\mathbf{q}}{a} \right) - 1 \right) \\
&= \frac{1}{2} \left( \frac{\mathbf{q}^T \mathbf{S}_\xi^T \mathbf{S}_\xi \mathbf{q}}{a^2} - 1 \right) \\
\varepsilon_y &= \frac{1}{2} \left( \frac{\mathbf{q}^T \mathbf{S}_\eta^T \mathbf{S}_\eta \mathbf{q}}{b^2} - 1 \right) \\
\varepsilon_{xy} &= \frac{1}{2} \left( \frac{\mathbf{q}^T \mathbf{S}_\xi^T \mathbf{S}_\eta \mathbf{q}}{ab} \right)
\end{aligned} \tag{127}$$

The derivatives of the strains by  $\mathbf{q}$  are also defined as follows.

$$\begin{aligned}
\frac{\partial \varepsilon_x}{\partial \mathbf{q}} &= \frac{\mathbf{S}_\xi^T \mathbf{S}_\xi}{a^2} \mathbf{q} \\
\frac{\partial \varepsilon_y}{\partial \mathbf{q}} &= \frac{\mathbf{S}_\eta^T \mathbf{S}_\eta}{b^2} \mathbf{q} \\
\frac{\partial \varepsilon_{xy}}{\partial \mathbf{q}} &= \frac{\partial \varepsilon_{yx}}{\partial \mathbf{q}} = \frac{\mathbf{S}_\xi^T \mathbf{S}_\eta + \mathbf{S}_\eta^T \mathbf{S}_\xi}{2ab} \mathbf{q}
\end{aligned} \tag{128}$$

Now, the mid-plane elastic force of the shell element due to longitudinal and shear deformation is obtained by the derivative of the strain energy (Eq. (122)) by  $\mathbf{q}$ .

$$\begin{aligned}
\mathbf{Q}_{ls} &= \frac{\partial U_{ls}}{\partial \mathbf{q}} \\
&= \frac{Eh}{2(1-\nu^2)} \int_0^b \int_0^a \left\{ 2\varepsilon_x \frac{\partial \varepsilon_x}{\partial \mathbf{q}} + 2\nu \left( \frac{\partial \varepsilon_x}{\partial \mathbf{q}} \varepsilon_y + \varepsilon_x \frac{\partial \varepsilon_y}{\partial \mathbf{q}} \right) + 2\varepsilon_y \frac{\partial \varepsilon_y}{\partial \mathbf{q}} + 4(1-\nu) \varepsilon_{xy} \frac{\partial \varepsilon_{xy}}{\partial \mathbf{q}} \right\} dx dy \\
&= \frac{Eh}{1-\nu^2} \int_0^b \int_0^a \left\{ \varepsilon_x \frac{\partial \varepsilon_x}{\partial \mathbf{q}} + \nu \left( \frac{\partial \varepsilon_x}{\partial \mathbf{q}} \varepsilon_y + \varepsilon_x \frac{\partial \varepsilon_y}{\partial \mathbf{q}} \right) + \varepsilon_y \frac{\partial \varepsilon_y}{\partial \mathbf{q}} + 2(1-\nu) \varepsilon_{xy} \frac{\partial \varepsilon_{xy}}{\partial \mathbf{q}} \right\} dx dy \\
&= \frac{Eh}{1-\nu^2} \int_0^b \int_0^a \left\{ (\varepsilon_x + \nu \varepsilon_y) \frac{\partial \varepsilon_x}{\partial \mathbf{q}} + (\varepsilon_y + \nu \varepsilon_x) \frac{\partial \varepsilon_y}{\partial \mathbf{q}} + 2(1-\nu) \varepsilon_{xy} \frac{\partial \varepsilon_{xy}}{\partial \mathbf{q}} \right\} dx dy
\end{aligned} \tag{129}$$

Substituting the derivatives of the strain, we can obtain the following equation.

$$\begin{aligned}
\mathbf{Q}_{ls} &= \frac{Eh}{1-\nu^2} \int_0^b \int_0^a \left\{ (\varepsilon_x + \nu \varepsilon_y) \frac{\mathbf{S}_\xi^T \mathbf{S}_\xi}{a^2} \mathbf{q} + (\varepsilon_y + \nu \varepsilon_x) \frac{\mathbf{S}_\eta^T \mathbf{S}_\eta}{b^2} \mathbf{q} + 2(1-\nu) \varepsilon_{xy} \frac{\mathbf{S}_\xi^T \mathbf{S}_\eta + \mathbf{S}_\eta^T \mathbf{S}_\xi}{2ab} \mathbf{q} \right\} dx dy \\
&= \left[ \frac{Eh}{1-\nu^2} \int_0^b \int_0^a \left\{ (\varepsilon_x + \nu \varepsilon_y) \frac{\mathbf{S}_\xi^T \mathbf{S}_\xi}{a^2} + (\varepsilon_y + \nu \varepsilon_x) \frac{\mathbf{S}_\eta^T \mathbf{S}_\eta}{b^2} + (1-\nu) \varepsilon_{xy} \frac{\mathbf{S}_\xi^T \mathbf{S}_\eta + \mathbf{S}_\eta^T \mathbf{S}_\xi}{ab} \right\} dx dy \right] \mathbf{q} \\
&= \frac{Eh}{1-\nu^2} \int_0^1 \int_0^1 \left\{ (\varepsilon_x + \nu \varepsilon_y) \frac{\mathbf{S}_\xi^T \mathbf{S}_\xi}{a^2} + (\varepsilon_y + \nu \varepsilon_x) \frac{\mathbf{S}_\eta^T \mathbf{S}_\eta}{b^2} + (1-\nu) \varepsilon_{xy} \frac{\mathbf{S}_\xi^T \mathbf{S}_\eta + \mathbf{S}_\eta^T \mathbf{S}_\xi}{ab} \right\} ab d\xi d\eta \\
&= \mathbf{K}_{ls} \mathbf{q}
\end{aligned} \tag{130}$$

where,  $\mathbf{K}_{ls}$  is stiffness matrix due to longitudinal and shear deformation. If we assume that deformations are constant over the element, the strains are possible to be treated as constant values. Therefore, they can be moved out from the integral.

$$\mathbf{K}_{ls} = \frac{Ehab}{1-\nu^2} \left[ \begin{aligned} & \frac{(\bar{\varepsilon}_x + \nu \bar{\varepsilon}_y)}{a^2} \int_0^1 \int_0^1 \mathbf{S}_\xi^T \mathbf{S}_\xi d\xi d\eta + \frac{(\bar{\varepsilon}_y + \nu \bar{\varepsilon}_x)}{b^2} \int_0^1 \int_0^1 \mathbf{S}_\eta^T \mathbf{S}_\eta d\xi d\eta \\ & + \frac{(1-\nu) \bar{\varepsilon}_{xy}}{ab} \left\{ \int_0^1 \int_0^1 \mathbf{S}_\xi^T \mathbf{S}_\eta d\xi d\eta + \int_0^1 \int_0^1 \mathbf{S}_\eta^T \mathbf{S}_\xi d\xi d\eta \right\} \end{aligned} \right] \tag{131}$$

where,  $\bar{\varepsilon}_x = \frac{1}{2} \left( \frac{\|\mathbf{r}_2 - \mathbf{r}_1\|}{a} + \frac{\|\mathbf{r}_4 - \mathbf{r}_3\|}{a} \right) - 1$ ,  $\bar{\varepsilon}_y = \frac{1}{2} \left( \frac{\|\mathbf{r}_3 - \mathbf{r}_1\|}{b} + \frac{\|\mathbf{r}_4 - \mathbf{r}_2\|}{b} \right) - 1$ , and

$\bar{\varepsilon}_{xy} = \frac{1}{8} (\mathbf{r}_1^x \cdot \mathbf{r}_1^y + \mathbf{r}_2^x \cdot \mathbf{r}_2^y + \mathbf{r}_3^x \cdot \mathbf{r}_3^y + \mathbf{r}_4^x \cdot \mathbf{r}_4^y)$ . There are four integrals in Eq. (131). Each

integral can be calculated as follows.

$$\int_0^1 \int_0^1 \mathbf{S}_\xi^T \mathbf{S}_\xi d\xi d\eta = \int_0^1 \int_0^1 \frac{d\hat{s}_i}{d\xi} \hat{s}_j \frac{d\hat{s}_k}{d\xi} \hat{s}_l \mathbf{I} d\xi d\eta = \mathbf{I} \left( \int_0^1 \frac{d\hat{s}_i}{d\xi} \frac{d\hat{s}_k}{d\xi} d\xi \right) \left( \int_0^1 \hat{s}_j \hat{s}_l d\eta \right) \quad (132)$$

$$\int_0^1 \int_0^1 \mathbf{S}_\eta^T \mathbf{S}_\eta d\xi d\eta = \int_0^1 \int_0^1 \hat{s}_i \frac{d\hat{s}_j}{d\eta} \hat{s}_k \frac{d\hat{s}_l}{d\eta} \mathbf{I} d\xi d\eta = \mathbf{I} \left( \int_0^1 \hat{s}_i \hat{s}_k d\xi \right) \left( \int_0^1 \frac{d\hat{s}_j}{d\eta} \frac{d\hat{s}_l}{d\eta} d\eta \right) \quad (133)$$

$$\int_0^1 \int_0^1 \mathbf{S}_\xi^T \mathbf{S}_\eta d\xi d\eta = \int_0^1 \int_0^1 \frac{d\hat{s}_i}{d\xi} \hat{s}_j \hat{s}_k \frac{d\hat{s}_l}{d\eta} \mathbf{I} d\xi d\eta = \mathbf{I} \left( \int_0^1 \frac{d\hat{s}_i}{d\xi} \hat{s}_k d\xi \right) \left( \int_0^1 \hat{s}_j \frac{d\hat{s}_l}{d\eta} d\eta \right) \quad (134)$$

$$\int_0^1 \int_0^1 \mathbf{S}_\eta^T \mathbf{S}_\xi d\xi d\eta = \int_0^1 \int_0^1 \hat{s}_i \frac{d\hat{s}_j}{d\eta} \frac{d\hat{s}_k}{d\xi} \hat{s}_l \mathbf{I} d\xi d\eta = \mathbf{I} \left( \int_0^1 \hat{s}_i \frac{d\hat{s}_k}{d\xi} d\xi \right) \left( \int_0^1 \frac{d\hat{s}_j}{d\eta} \hat{s}_l d\eta \right) \quad (135)$$

This model is quite simple. However, this assumption is not suitable for the large deformation. Therefore, we should derive the stiffness matrix without any assumption.

$$\begin{aligned} \mathbf{Q}_{ls} &= \frac{Eh}{1-\nu^2} \int_0^b \int_0^a \left\{ \left( \varepsilon_x \frac{\partial \varepsilon_x}{\partial \mathbf{q}} + \nu \left( \frac{\partial \varepsilon_x}{\partial \mathbf{q}} \varepsilon_y + \varepsilon_x \frac{\partial \varepsilon_y}{\partial \mathbf{q}} \right) + \varepsilon_y \frac{\partial \varepsilon_y}{\partial \mathbf{q}} \right) + 2(1-\nu) \varepsilon_{xy} \frac{\partial \varepsilon_{xy}}{\partial \mathbf{q}} \right\} dx dy \\ &= \frac{Ehab}{1-\nu^2} \int_0^1 \int_0^1 \left\{ \left( \varepsilon_x \frac{\partial \varepsilon_x}{\partial \mathbf{q}} + \nu \left( \frac{\partial \varepsilon_x}{\partial \mathbf{q}} \varepsilon_y + \varepsilon_x \frac{\partial \varepsilon_y}{\partial \mathbf{q}} \right) + \varepsilon_y \frac{\partial \varepsilon_y}{\partial \mathbf{q}} \right) + 2(1-\nu) \varepsilon_{xy} \frac{\partial \varepsilon_{xy}}{\partial \mathbf{q}} \right\} d\xi d\eta \end{aligned} \quad (136)$$

There are five terms inside the integral. Each term is calculated as follows.

$$\begin{aligned}
\int_0^1 \int_0^1 \left( \frac{\partial \varepsilon_x}{\partial \mathbf{q}} \varepsilon_x \right) d\xi d\eta &= \int_0^1 \int_0^1 \left\{ \frac{\mathbf{S}_\xi^T \mathbf{S}_\xi}{a^2} \mathbf{q} \times \frac{1}{2} \left( \frac{\mathbf{q}^T \mathbf{S}_\xi^T \mathbf{S}_\xi \mathbf{q}}{a^2} - 1 \right) \right\} d\xi d\eta \\
&= \frac{1}{2} \int_0^1 \int_0^1 \left( \frac{\mathbf{S}_\xi^T \mathbf{S}_\xi \mathbf{q} \mathbf{q}^T \mathbf{S}_\xi^T \mathbf{S}_\xi \mathbf{q}}{a^4} - \frac{\mathbf{S}_\xi^T \mathbf{S}_\xi \mathbf{q}}{a^2} \right) d\xi d\eta \\
&= \frac{1}{2} \left\{ \int_0^1 \int_0^1 \left( \frac{\mathbf{S}_\xi^T \mathbf{S}_\xi \mathbf{q} \mathbf{q}^T \mathbf{S}_\xi^T \mathbf{S}_\xi}{a^4} - \frac{\mathbf{S}_\xi^T \mathbf{S}_\xi}{a^2} \right) d\xi d\eta \right\} \mathbf{q}
\end{aligned} \tag{137}$$

$$\begin{aligned}
\int_0^1 \int_0^1 \left( \frac{\partial \varepsilon_x}{\partial \mathbf{q}} \varepsilon_y \right) d\xi d\eta &= \int_0^1 \int_0^1 \left\{ \frac{\mathbf{S}_\xi^T \mathbf{S}_\xi}{a^2} \mathbf{q} \times \frac{1}{2} \left( \frac{\mathbf{q}^T \mathbf{S}_\eta^T \mathbf{S}_\eta \mathbf{q}}{b^2} - 1 \right) \right\} d\xi d\eta \\
&= \frac{1}{2} \int_0^1 \int_0^1 \left( \frac{\mathbf{S}_\xi^T \mathbf{S}_\xi \mathbf{q} \mathbf{q}^T \mathbf{S}_\eta^T \mathbf{S}_\eta}{a^2 b^2} - \frac{\mathbf{S}_\xi^T \mathbf{S}_\xi \mathbf{q}}{a^2} \right) d\xi d\eta \\
&= \frac{1}{2} \left\{ \int_0^1 \int_0^1 \left( \frac{\mathbf{S}_\xi^T \mathbf{S}_\xi \mathbf{q} \mathbf{q}^T \mathbf{S}_\eta^T \mathbf{S}_\eta}{a^2 b^2} - \frac{\mathbf{S}_\xi^T \mathbf{S}_\xi}{a^2} \right) d\xi d\eta \right\} \mathbf{q}
\end{aligned} \tag{138}$$

$$\begin{aligned}
\int_0^1 \int_0^1 \left( \frac{\partial \varepsilon_y}{\partial \mathbf{q}} \varepsilon_x \right) d\xi d\eta &= \int_0^1 \int_0^1 \left\{ \frac{\mathbf{S}_\eta^T \mathbf{S}_\eta}{b^2} \mathbf{q} \times \frac{1}{2} \left( \frac{\mathbf{q}^T \mathbf{S}_\xi^T \mathbf{S}_\xi \mathbf{q}}{a^2} - 1 \right) \right\} d\xi d\eta \\
&= \frac{1}{2} \int_0^1 \int_0^1 \left( \frac{\mathbf{S}_\eta^T \mathbf{S}_\eta \mathbf{q} \mathbf{q}^T \mathbf{S}_\xi^T \mathbf{S}_\xi}{a^2 b^2} - \frac{\mathbf{S}_\eta^T \mathbf{S}_\eta \mathbf{q}}{b^2} \right) d\xi d\eta \\
&= \frac{1}{2} \left\{ \int_0^1 \int_0^1 \left( \frac{\mathbf{S}_\eta^T \mathbf{S}_\eta \mathbf{q} \mathbf{q}^T \mathbf{S}_\xi^T \mathbf{S}_\xi}{a^2 b^2} - \frac{\mathbf{S}_\eta^T \mathbf{S}_\eta}{b^2} \right) d\xi d\eta \right\} \mathbf{q}
\end{aligned} \tag{139}$$

$$\begin{aligned}
\int_0^1 \int_0^1 \left( \frac{\partial \varepsilon_y}{\partial \mathbf{q}} \varepsilon_y \right) d\xi d\eta &= \int_0^1 \int_0^1 \left\{ \frac{\mathbf{S}_\eta^T \mathbf{S}_\eta}{b^2} \mathbf{q} \times \frac{1}{2} \left( \frac{\mathbf{q}^T \mathbf{S}_\eta^T \mathbf{S}_\eta \mathbf{q}}{b^2} - 1 \right) \right\} d\xi d\eta \\
&= \frac{1}{2} \int_0^1 \int_0^1 \left( \frac{\mathbf{S}_\eta^T \mathbf{S}_\eta \mathbf{q} \mathbf{q}^T \mathbf{S}_\eta^T \mathbf{S}_\eta}{b^4} - \frac{\mathbf{S}_\eta^T \mathbf{S}_\eta \mathbf{q}}{b^2} \right) d\xi d\eta \\
&= \frac{1}{2} \left\{ \int_0^1 \int_0^1 \left( \frac{\mathbf{S}_\eta^T \mathbf{S}_\eta \mathbf{q} \mathbf{q}^T \mathbf{S}_\eta^T \mathbf{S}_\eta}{b^4} - \frac{\mathbf{S}_\eta^T \mathbf{S}_\eta}{b^2} \right) d\xi d\eta \right\} \mathbf{q}
\end{aligned} \tag{140}$$

$$\begin{aligned}
\int_0^1 \int_0^1 \left( \frac{\partial \varepsilon_{xy}}{\partial \mathbf{q}} \varepsilon_{xy} \right) d\xi d\eta &= \int_0^1 \int_0^1 \left\{ \frac{\mathbf{S}_\xi^T \mathbf{S}_\eta + \mathbf{S}_\eta^T \mathbf{S}_\xi}{2ab} \mathbf{q} \times \frac{1}{2} \left( \frac{\mathbf{q}^T \mathbf{S}_\xi^T \mathbf{S}_\eta \mathbf{q}}{ab} \right) \right\} d\xi d\eta \\
&= \frac{1}{4} \int_0^1 \int_0^1 \left( \frac{\mathbf{S}_\xi^T \mathbf{S}_\eta \mathbf{q} \mathbf{q}^T \mathbf{S}_\xi^T \mathbf{S}_\eta \mathbf{q}}{a^2 b^2} + \frac{\mathbf{S}_\eta^T \mathbf{S}_\xi \mathbf{q} \mathbf{q}^T \mathbf{S}_\eta^T \mathbf{S}_\xi \mathbf{q}}{a^2 b^2} \right) d\xi d\eta \quad (141) \\
&= \frac{1}{4} \left\{ \int_0^1 \int_0^1 \left( \frac{\mathbf{S}_\xi^T \mathbf{S}_\eta \mathbf{q} \mathbf{q}^T \mathbf{S}_\xi^T \mathbf{S}_\eta}{a^2 b^2} + \frac{\mathbf{S}_\eta^T \mathbf{S}_\xi \mathbf{q} \mathbf{q}^T \mathbf{S}_\eta^T \mathbf{S}_\xi}{a^2 b^2} \right) d\xi d\eta \right\} \mathbf{q}
\end{aligned}$$

After adding all of the above equations, we summarize as follows.

$$\begin{aligned}
\mathbf{Q}_{is} &= \frac{Ehab}{1-\nu^2} \left\{ \begin{aligned} &\frac{1}{2} \int_0^1 \int_0^1 \left( \frac{\mathbf{S}_\xi^T \mathbf{S}_\xi \mathbf{q} \mathbf{q}^T \mathbf{S}_\xi^T \mathbf{S}_\xi}{a^4} - \frac{\mathbf{S}_\xi^T \mathbf{S}_\xi}{a^2} \right) d\xi d\eta + \frac{\nu}{2} \int_0^1 \int_0^1 \left( \frac{\mathbf{S}_\xi^T \mathbf{S}_\xi \mathbf{q} \mathbf{q}^T \mathbf{S}_\eta^T \mathbf{S}_\eta}{a^2 b^2} - \frac{\mathbf{S}_\xi^T \mathbf{S}_\xi}{a^2} \right) d\xi d\eta \\ &+ \frac{\nu}{2} \int_0^1 \int_0^1 \left( \frac{\mathbf{S}_\eta^T \mathbf{S}_\eta \mathbf{q} \mathbf{q}^T \mathbf{S}_\xi^T \mathbf{S}_\xi}{a^2 b^2} - \frac{\mathbf{S}_\eta^T \mathbf{S}_\eta}{b^2} \right) d\xi d\eta + \frac{1}{2} \int_0^1 \int_0^1 \left( \frac{\mathbf{S}_\eta^T \mathbf{S}_\eta \mathbf{q} \mathbf{q}^T \mathbf{S}_\eta^T \mathbf{S}_\eta}{b^4} - \frac{\mathbf{S}_\eta^T \mathbf{S}_\eta}{b^2} \right) d\xi d\eta \\ &+ \frac{1-\nu}{2} \int_0^1 \int_0^1 \left( \frac{\mathbf{S}_\xi^T \mathbf{S}_\eta \mathbf{q} \mathbf{q}^T \mathbf{S}_\xi^T \mathbf{S}_\eta}{a^2 b^2} + \frac{\mathbf{S}_\eta^T \mathbf{S}_\xi \mathbf{q} \mathbf{q}^T \mathbf{S}_\eta^T \mathbf{S}_\xi}{a^2 b^2} \right) d\xi d\eta \end{aligned} \right\} \mathbf{q} \quad (142) \\
&= \frac{Ehab}{2(1-\nu^2)} \left[ \begin{aligned} &\int_0^1 \int_0^1 \left\{ \frac{\mathbf{S}_\xi^T \mathbf{S}_\xi \mathbf{q} \mathbf{q}^T \mathbf{S}_\xi^T \mathbf{S}_\xi}{a^4} + \nu \left( \frac{\mathbf{S}_\xi^T \mathbf{S}_\xi \mathbf{q} \mathbf{q}^T \mathbf{S}_\eta^T \mathbf{S}_\eta}{a^2 b^2} + \frac{\mathbf{S}_\eta^T \mathbf{S}_\eta \mathbf{q} \mathbf{q}^T \mathbf{S}_\xi^T \mathbf{S}_\xi}{a^2 b^2} \right) + \frac{\mathbf{S}_\eta^T \mathbf{S}_\eta \mathbf{q} \mathbf{q}^T \mathbf{S}_\eta^T \mathbf{S}_\eta}{b^4} \right\} d\xi d\eta \\ &+ (1-\nu) \left( \frac{\mathbf{S}_\xi^T \mathbf{S}_\eta \mathbf{q} \mathbf{q}^T \mathbf{S}_\xi^T \mathbf{S}_\eta}{a^2 b^2} + \frac{\mathbf{S}_\eta^T \mathbf{S}_\xi \mathbf{q} \mathbf{q}^T \mathbf{S}_\eta^T \mathbf{S}_\xi}{a^2 b^2} \right) \\ &- (1+\nu) \int_0^1 \int_0^1 \left( \frac{\mathbf{S}_\xi^T \mathbf{S}_\xi}{a^2} + \frac{\mathbf{S}_\eta^T \mathbf{S}_\eta}{b^2} \right) d\xi d\eta \end{aligned} \right] \mathbf{q}
\end{aligned}$$

It is hard to calculate integral because  $\mathbf{q} \mathbf{q}^T$  is located in the middle. Abbas et al. and García-Vallejo et al. [46], [47] suggested the method how to calculate the matrix form  $\mathbf{A} \mathbf{e} \mathbf{e}^T \mathbf{B}$ . For example,  $\mathbf{A}$ ,  $\mathbf{B}$  is 3 by 3 matrix and  $\mathbf{e}$  is 3 by 1 column vector.

$$\begin{aligned}
\mathbf{A}\mathbf{e}\mathbf{e}^T\mathbf{B} &= \begin{bmatrix} \mathbf{a}_{row1} \\ \mathbf{a}_{row2} \\ \mathbf{a}_{row3} \end{bmatrix} \mathbf{e}\mathbf{e}^T \begin{bmatrix} \mathbf{b}_{col1} & \mathbf{b}_{col2} & \mathbf{b}_{col3} \end{bmatrix} \\
&= \begin{bmatrix} \mathbf{a}_{row1}\mathbf{e}\mathbf{e}^T \\ \mathbf{a}_{row2}\mathbf{e}\mathbf{e}^T \\ \mathbf{a}_{row3}\mathbf{e}\mathbf{e}^T \end{bmatrix} \begin{bmatrix} \mathbf{b}_{col1} & \mathbf{b}_{col2} & \mathbf{b}_{col3} \end{bmatrix} \\
&= \begin{bmatrix} \mathbf{a}_{row1}\mathbf{e}\mathbf{e}^T\mathbf{b}_{col1} & \mathbf{a}_{row1}\mathbf{e}\mathbf{e}^T\mathbf{b}_{col2} & \mathbf{a}_{row1}\mathbf{e}\mathbf{e}^T\mathbf{b}_{col3} \\ \mathbf{a}_{row2}\mathbf{e}\mathbf{e}^T\mathbf{b}_{col1} & \mathbf{a}_{row2}\mathbf{e}\mathbf{e}^T\mathbf{b}_{col2} & \mathbf{a}_{row2}\mathbf{e}\mathbf{e}^T\mathbf{b}_{col3} \\ \mathbf{a}_{row3}\mathbf{e}\mathbf{e}^T\mathbf{b}_{col1} & \mathbf{a}_{row3}\mathbf{e}\mathbf{e}^T\mathbf{b}_{col2} & \mathbf{a}_{row3}\mathbf{e}\mathbf{e}^T\mathbf{b}_{col3} \end{bmatrix}
\end{aligned} \tag{143}$$

Now it is possible to exchange  $\mathbf{a}_{row}$  and  $\mathbf{e}$  or to exchange  $\mathbf{e}^T$  and  $\mathbf{b}_{col}$ . Therefore, the equation is summarized as follows.

$$\mathbf{A}\mathbf{e}\mathbf{e}^T\mathbf{B} = \begin{bmatrix} \mathbf{e}^T\mathbf{a}_{row1}^T\mathbf{b}_{col1}^T\mathbf{e} & \mathbf{e}^T\mathbf{a}_{row1}^T\mathbf{b}_{col2}^T\mathbf{e} & \mathbf{e}^T\mathbf{a}_{row1}^T\mathbf{b}_{col3}^T\mathbf{e} \\ \mathbf{e}^T\mathbf{a}_{row2}^T\mathbf{b}_{col1}^T\mathbf{e} & \mathbf{e}^T\mathbf{a}_{row2}^T\mathbf{b}_{col2}^T\mathbf{e} & \mathbf{e}^T\mathbf{a}_{row2}^T\mathbf{b}_{col3}^T\mathbf{e} \\ \mathbf{e}^T\mathbf{a}_{row3}^T\mathbf{b}_{col1}^T\mathbf{e} & \mathbf{e}^T\mathbf{a}_{row3}^T\mathbf{b}_{col2}^T\mathbf{e} & \mathbf{e}^T\mathbf{a}_{row3}^T\mathbf{b}_{col3}^T\mathbf{e} \end{bmatrix} \tag{144}$$

Generalized the above results, it is as follows.

$$\therefore (\mathbf{A}\mathbf{e}\mathbf{e}^T\mathbf{B})_{ij} = \mathbf{e}^T \left( \mathbf{A}_{i^{th} row}^T \mathbf{B}_{j^{th} colum}^T \right) \mathbf{e} \tag{145}$$

For example, the integral changes to another form as follows.



$$\begin{aligned}\bar{\mathbf{S}}_{\xi\xi\xi\xi} &= \int_0^1 \int_0^1 (\mathbf{S}_{\xi}^T \mathbf{S}_{\xi} \mathbf{q} \mathbf{q}^T \mathbf{S}_{\xi}^T \mathbf{S}_{\xi}) d\xi d\eta \\ (\bar{\mathbf{S}}_{\xi\xi\xi\xi})_{ij} &= \mathbf{q}^T \left( \int_0^1 \int_0^1 (\mathbf{S}_{\xi}^T \mathbf{S}_{\xi})_{i^{th} \text{ row}}^T (\mathbf{S}_{\xi}^T \mathbf{S}_{\xi})_{j^{th} \text{ column}} d\xi d\eta \right) \mathbf{q}\end{aligned}\quad (146)$$

### (3) Bending and twisting strain energy of shell element

From now on, the strain energy of the shell element due to bending and twisting will be provided. For this, the curvature should be defined as follows.

$$\begin{aligned}\kappa_x &= \frac{\partial^2 \mathbf{r}}{\partial x^2} = \frac{\partial^2 \mathbf{S}}{\partial \xi^2} \mathbf{q} = \frac{\partial^2 \mathbf{S}}{\partial \xi^2} \frac{\mathbf{q}}{a^2} = \mathbf{S}_{\xi\xi} \frac{\mathbf{q}}{a^2} \\ \kappa_y &= \mathbf{S}_{\eta\eta} \frac{\mathbf{q}}{b^2} \\ \kappa_{xy} &= \frac{\partial^2 \mathbf{r}}{\partial x \partial y} = \mathbf{S}_{\xi\eta} \frac{\mathbf{q}}{ab}\end{aligned}\quad (147)$$

Substituting the curvature expressed by the shape function and the generalized coordinate into Eq. (118), we obtain the following equations.

$$\begin{aligned}U_{br} &= \frac{D}{2} \int_0^b \int_0^a \left\{ \kappa_x^2 + 2\nu \kappa_x \kappa_y + \kappa_y^2 + 2(1-\nu) \kappa_{xy}^2 \right\} dx dy \\ &= \frac{D}{2} \int_0^b \int_0^a \left\{ \frac{\mathbf{q}^T \mathbf{S}_{\xi\xi}^T \mathbf{S}_{\xi\xi} \mathbf{q}}{a^4} + 2\nu \frac{\mathbf{q}^T \mathbf{S}_{\xi\xi}^T \mathbf{S}_{\eta\eta} \mathbf{q}}{a^2 b^2} + \frac{\mathbf{q}^T \mathbf{S}_{\eta\eta}^T \mathbf{S}_{\eta\eta} \mathbf{q}}{b^4} + 2(1-\nu) \frac{\mathbf{q}^T \mathbf{S}_{\xi\eta}^T \mathbf{S}_{\xi\eta} \mathbf{q}}{a^2 b^2} \right\} dx dy\end{aligned}\quad (148)$$

Midplane elastic force ( $\mathbf{Q}_{br}$ ) of the shell element due to bending and twisting is obtained by the derivative of the strain energy by  $\mathbf{q}$ .

$$\begin{aligned}
\mathbf{Q}_{bt} &= \frac{\partial U_{bt}}{\partial \mathbf{q}} \\
&= D \int_0^b \int_0^a \left\{ \frac{\mathbf{S}_{\xi\xi}^T \mathbf{S}_{\xi\xi}}{a^4} \mathbf{q} + 2\nu \frac{\mathbf{S}_{\xi\xi}^T \mathbf{S}_{\eta\eta}}{a^2 b^2} \mathbf{q} + \frac{\mathbf{S}_{\eta\eta}^T \mathbf{S}_{\eta\eta}}{b^4} \mathbf{q} + 2(1-\nu) \frac{\mathbf{S}_{\xi\eta}^T \mathbf{S}_{\xi\eta}}{a^2 b^2} \mathbf{q} \right\} dx dy \quad (149) \\
&= Dab \int_0^1 \int_0^1 \left\{ \frac{\mathbf{S}_{\xi\xi}^T \mathbf{S}_{\xi\xi}}{a^4} + 2\nu \frac{\mathbf{S}_{\xi\xi}^T \mathbf{S}_{\eta\eta}}{a^2 b^2} + \frac{\mathbf{S}_{\eta\eta}^T \mathbf{S}_{\eta\eta}}{b^4} + 2(1-\nu) \frac{\mathbf{S}_{\xi\eta}^T \mathbf{S}_{\xi\eta}}{a^2 b^2} \right\} d\xi d\eta \\
&= \mathbf{K}_{bt} \mathbf{q}
\end{aligned}$$

where,  $\mathbf{K}_{bt}$  is the stiffness matrix due to bending and twisting. There are four integrals in  $\mathbf{K}_{bt}$ . Each integral can be calculated as follows.

$$\int_0^1 \int_0^1 \mathbf{S}_{\xi\xi}^T \mathbf{S}_{\xi\xi} d\xi d\eta = \int_0^1 \int_0^1 \frac{d^2 \hat{s}_i}{d\xi^2} \hat{s}_j \frac{d^2 \hat{s}_k}{d\xi^2} \hat{s}_l \mathbf{I} d\xi d\eta = \mathbf{I} \left( \int_0^1 \frac{d^2 \hat{s}_i}{d\xi^2} \frac{d^2 \hat{s}_k}{d\xi^2} d\xi \right) \left( \int_0^1 \hat{s}_j \hat{s}_l d\eta \right) \quad (150)$$

$$\int_0^1 \int_0^1 \mathbf{S}_{\xi\xi}^T \mathbf{S}_{\eta\eta} d\xi d\eta = \int_0^1 \int_0^1 \frac{d^2 \hat{s}_i}{d\xi^2} \hat{s}_j \hat{s}_k \frac{d^2 \hat{s}_l}{d\eta^2} \mathbf{I} d\xi d\eta = \mathbf{I} \left( \int_0^1 \frac{d^2 \hat{s}_i}{d\xi^2} \hat{s}_k d\xi \right) \left( \int_0^1 \hat{s}_j \frac{d^2 \hat{s}_l}{d\eta^2} d\eta \right) \quad (151)$$

$$\int_0^1 \int_0^1 \mathbf{S}_{\eta\eta}^T \mathbf{S}_{\eta\eta} d\xi d\eta = \int_0^1 \int_0^1 \hat{s}_i \frac{d^2 \hat{s}_j}{d\eta^2} \hat{s}_k \frac{d^2 \hat{s}_l}{d\eta^2} \mathbf{I} d\xi d\eta = \mathbf{I} \left( \int_0^1 \hat{s}_i \hat{s}_k d\xi \right) \left( \int_0^1 \frac{d^2 \hat{s}_j}{d\eta^2} \frac{d^2 \hat{s}_l}{d\eta^2} d\eta \right) \quad (152)$$

$$\int_0^1 \int_0^1 \mathbf{S}_{\xi\eta}^T \mathbf{S}_{\xi\eta} d\xi d\eta = \int_0^1 \int_0^1 \frac{d\hat{s}_i}{d\xi} \frac{d\hat{s}_j}{d\eta} \frac{d\hat{s}_k}{d\xi} \frac{d\hat{s}_l}{d\eta} \mathbf{I} d\xi d\eta = \mathbf{I} \left( \int_0^1 \frac{d\hat{s}_i}{d\xi} \frac{d\hat{s}_k}{d\xi} d\xi \right) \left( \int_0^1 \frac{d\hat{s}_j}{d\eta} \frac{d\hat{s}_l}{d\eta} d\eta \right) \quad (153)$$

#### (4) External forces

If the force is a point load at an arbitrary point on the shell element as shown in Figure 2-32, the generalized non-conservative external force is obtained as follows.

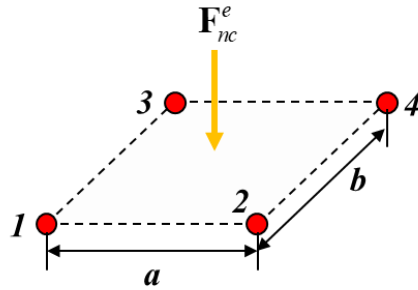


Figure 2-32. External force acting at an arbitrary point.

$$\begin{aligned}
 \mathbf{Q}_{nc} &= \left( \frac{\partial \mathbf{r}}{\partial \mathbf{q}} \right)^T \mathbf{F}_{nc}^e \\
 &= \left( \frac{\partial (\mathbf{S}\mathbf{q})}{\partial \mathbf{q}} \right)^T \mathbf{F}_{nc}^e \\
 &= \mathbf{S}^T \mathbf{F}_{nc}^e
 \end{aligned} \tag{154}$$

If a distributed force acts on the shell element as shown in Figure 2-33, the force is expressed by the integral form.

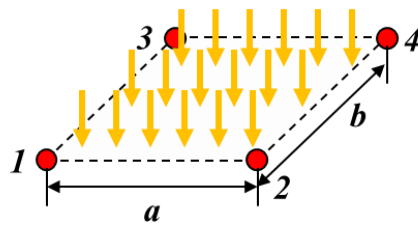


Figure 2-33. External force acting on all over the shell element

$$\begin{aligned}
\mathbf{Q}_{nc} &= \iiint_V \mathbf{S}^T \mathbf{w}^e dV \\
&= \int_0^b \int_0^a \mathbf{S}^T \mathbf{w}^e h dx dy \\
&= \int_0^1 \int_0^1 \mathbf{S}^T \mathbf{w}^e hab d\xi d\eta \\
&= hab \left( \int_0^1 \int_0^1 \mathbf{S}^T d\xi d\eta \right) \mathbf{w}^e \\
&= hab \bar{\mathbf{S}}^T \mathbf{w}^e
\end{aligned} \tag{155}$$

where,  $\mathbf{w}^e$  is distributed external force per unit volume, and  $\bar{\mathbf{S}}$  can be calculated as follows.

$$\begin{aligned}
\bar{\mathbf{S}}^T &= \int_0^1 \int_0^1 \mathbf{S}^T d\xi d\eta \\
&= \left[ \frac{1}{4} \mathbf{I} \quad \frac{b}{24} \mathbf{I} \quad \frac{1}{4} \mathbf{I} \quad -\frac{b}{24} \mathbf{I} \quad \frac{a}{24} \mathbf{I} \quad \frac{ab}{144} \mathbf{I} \quad \frac{a}{24} \mathbf{I} \quad -\frac{ab}{144} \mathbf{I} \right. \\
&\quad \left. \frac{1}{4} \mathbf{I} \quad \frac{b}{24} \mathbf{I} \quad \frac{1}{4} \mathbf{I} \quad -\frac{b}{24} \mathbf{I} \quad -\frac{a}{24} \mathbf{I} \quad -\frac{ab}{144} \mathbf{I} \quad -\frac{a}{24} \mathbf{I} \quad \frac{ab}{144} \mathbf{I} \right]^T
\end{aligned} \tag{156}$$

A damping force acting on the shell element is proportional to the velocity at  $x, y$  ( $0 \leq x \leq a, 0 \leq y \leq b$ ) as shown in Figure 2-34.

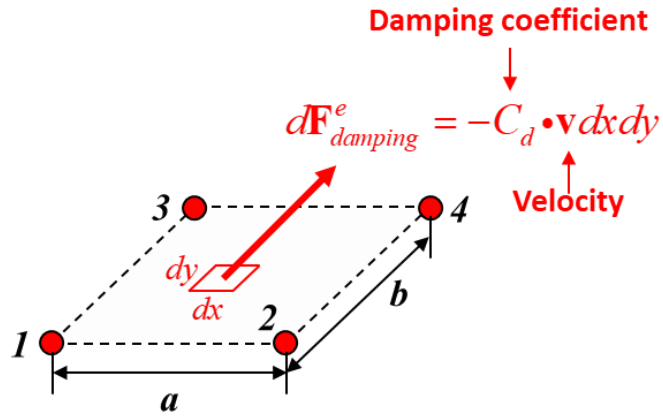


Figure 2-34. Damping force acting on the shell element

The velocity is the same as the derivative of the position vector  $\mathbf{r}$ .

$$\mathbf{v}(x, y, t) = \dot{\mathbf{r}}(x, y, t) = \mathbf{S}(\xi, \eta) \dot{\mathbf{q}}(t) \quad (157)$$

The damping force acting on a small length  $dx$  is multiplying damping coefficient and the velocity.

$$\begin{aligned} d\mathbf{F}_{damping}^e &= -C_d \cdot \mathbf{v}(x, y) dx dy \\ &= -C_d \cdot \{\mathbf{S}(\xi, \eta) dx dy\} \dot{\mathbf{q}}(t) \\ &= -C_d ab \cdot \{\mathbf{S}(\xi, \eta) d\xi d\eta\} \dot{\mathbf{q}}(t) \end{aligned} \quad (158)$$

For the coordinate transformation, Jacobian is multiplied in front of the damping force obtained in Eq. (158).

$$\begin{aligned}
d\mathbf{Q}_{damping} &= \left( \frac{\partial \mathbf{r}}{\partial \mathbf{q}} \right)^T d\mathbf{F}_{damping}^e \\
&= \mathbf{S}^T d\mathbf{F}_{damping}^e \\
&= -\mathbf{S}^T \cdot \left[ -C_d ab \cdot \{ \mathbf{S}(\xi, \eta) d\xi d\eta \} \dot{\mathbf{q}}(t) \right] \\
&= -C_d ab \cdot \{ \mathbf{S}^T \mathbf{S} d\xi d\eta \} \dot{\mathbf{q}}(t)
\end{aligned} \tag{159}$$

Finally, we can obtain generalized damping force all over the shell element as follows.

$$\begin{aligned}
\mathbf{Q}_{damping} &= \iint d\mathbf{Q}_{damping} \\
&= -C_d ab \left( \int_0^1 \int_0^1 \mathbf{S}^T \mathbf{S} d\xi d\eta \right) \dot{\mathbf{q}}(t) \\
&= -C_d ab \overline{\mathbf{S}} \dot{\mathbf{q}}(t)
\end{aligned} \tag{160}$$

### (5) Summary of equations of motion for 2D shell element

Now, we substitute kinetic energy, strain energy, and the generalized non-conservative external forces into the Euler-Lagrange equation. And then, finally, we can obtain the equations of motion for 2D shell element.

$$\mathbf{M}\ddot{\mathbf{q}} + (\mathbf{K}_{ls} + \mathbf{K}_{bt})\mathbf{q} = \mathbf{S}^T \mathbf{F}^e + hab\bar{\mathbf{S}}^T - C_d ab\bar{\mathbf{S}}\dot{\mathbf{q}} \quad (161)$$

Figure 2-35 shows a summary of equations of motion for 2D shell element.

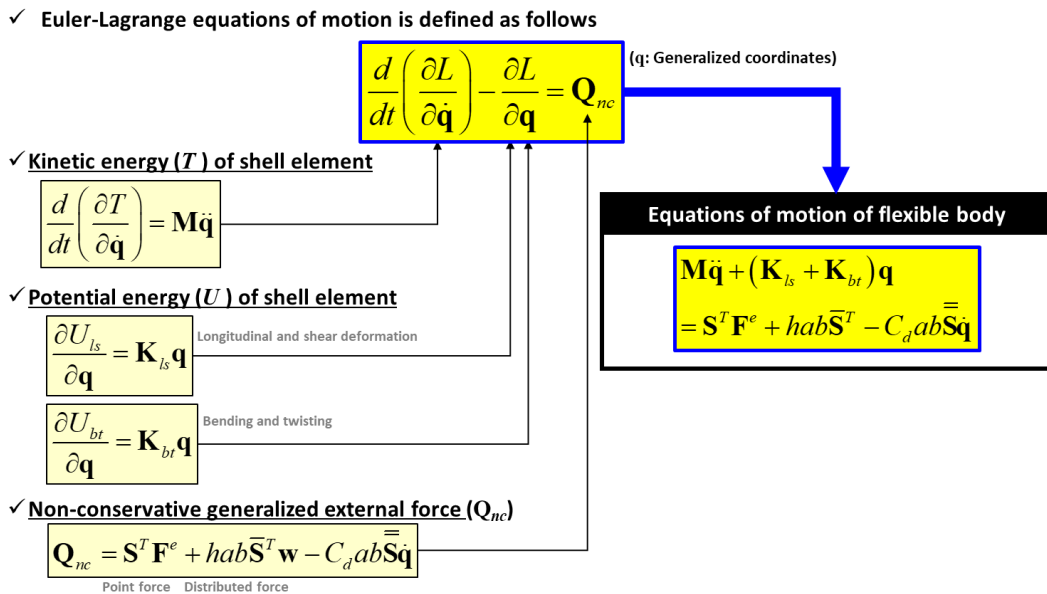


Figure 2-35. Summary of equations of motion for 2D shell element.

## 2.4. Kinematic constraints between rigid bodies

In 3-dimensional space, an unconstrained rigid body has 6 degrees of freedom, which are the translational and rotational motions about 3 independent axes. Joints restrain bodies by lower degrees of freedom. Table 2-2 lists the many kinds of joint by their restriction of degrees of freedom.

Table 2-2 Joint type by the restriction on the degrees of freedom.

Joint Type (3D)	Restriction on the degrees of freedom					
	Translation			Rotation		
	X	Y	Z	X	Y	Z
Ball	×	×	×	○	○	○
Universal	×	×	×	○	×	○
Hinge (Revolute)	×	×	×	×	×	○
Cylindrical	○	×	×	○	×	×
Slider (Prismatic)	○	×	×	×	×	×
Fixed	×	×	×	×	×	×
Slider-hinge	(Translational axis)			(Rotational axis)		

In this chapter, we derived the terms  $\mathbf{g}_k$  and  $\mathbf{G}_k$  for each joint listed in Table 1 with reference to Shabana [27], and Nikravesh [48]. We expressed the vector that connects point  $P$  and the origin of the global coordinate  $E$  as  ${}^E\mathbf{r}_P$ , or simply  $\mathbf{r}_P$ . We expressed the local vector that connects point  $A$  and the origin of the local coordinate  $G$  as  ${}^E\mathbf{r}_{P,G}$ . The rotation matrix that transforms the local coordinates  $G$  into global coordinates  $E$  is  ${}^E\mathbf{R}_G$ .

### 2.4.1. Ball joint

A ball joint constrains translational motion about every axis between bodies. As Figure 2-36 shows, the ball joint allows only rotational motion between body 1 (Green) and body 2 (Blue).  $P$  represents the center of the ball joint, and the  $E$ -XYZ is the global coordinate that is fixed in the space. The constraint equations are then:



$$\mathbf{g}_{ball} = {}^E \mathbf{r}_{G_1} + \mathbf{r}_{P/G_1} - {}^E \mathbf{r}_{G_2} - \mathbf{r}_{P/G_2} = 0 \quad (162)$$

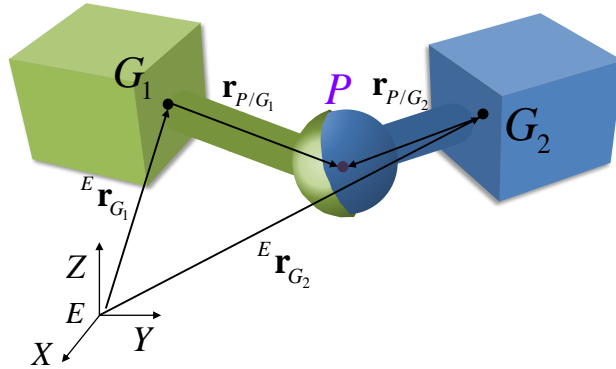


Figure 2-36. Ball joint.

As the location of the ball joint  $P$  is calculated about the local coordinates of body 1 and body 2, it needs to be transformed to the global coordinates E-XYZ. This yields:

$$\mathbf{g}_{ball,3} = \mathbf{g}_{trans,3} = {}^E \mathbf{r}_{G_1} + {}^E R_{G_1} \mathbf{r}_{P/G_1} - {}^E \mathbf{r}_{G_2} - {}^E R_{G_2} \mathbf{r}_{P/G_2} = 0 \quad (163)$$

As the equations above are obtained in 3-dimensional space, Eq. (163) consists of 3 constraint equations, about the X, Y, and Z axes, respectively. As Table 1 shows, the ball joint restrains 3 degrees of freedom. The subscript (ball, 3) means the equations above are for a ball joint and include 3 equations. Also,  $\mathbf{g}_{trans,3}$  is the constraint equations that restrain the 3 translational motions. Then,  $\mathbf{G}_k$  is expressed as follows.

$$\mathbf{G}_{(ball,3)} = \left[ \mathbf{I} \quad -\left( {}^E \mathbf{R}_{G_1} \mathbf{r}_{P/G_1} \right) \quad -\mathbf{I} \quad \left( {}^E \mathbf{R}_{G_2} \mathbf{r}_{P/G_2} \right) \right] \quad (164)$$

The tilde above the second and fourth terms in Eq. (48) means the transformation the vector to a skew-symmetric matrix. For example, the skew-symmetric matrix of the vector

$$\mathbf{v} = [a, b, c]^T \text{ is } \tilde{\mathbf{v}} = \begin{bmatrix} 0 & -c & b \\ c & 0 & -a \\ -b & a & 0 \end{bmatrix}.$$

### 2.4.2. Universal joint

A universal joint constrains translational motion about every direction and rotational motion about one axis. Figure 2-37 shows an example of a universal joint between body 1 and body 2. The two lines perpendicular to each other in the purple joint represent the two axes that allow rotation.  $P$  is the point of intersection of the two axes.

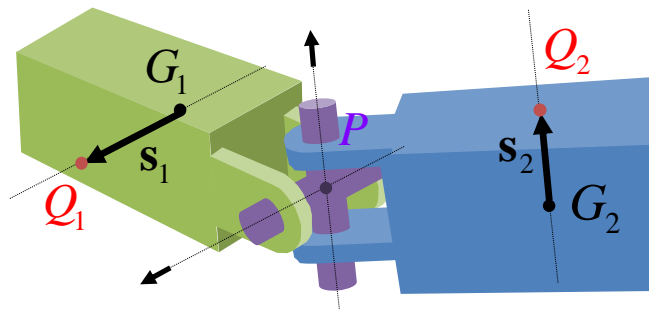


Figure 2-37. Universal joint.

Meanwhile, the constraint equations of a ball joint (163) are also included in those of a

universal joint, as they also restrain translational motion about every axis. The constraint equations of a universal joint consist of 4 equations, which restrain 3 translational motions and 1 rotational motion. Therefore, one more equation constraining rotational motion is needed for a universal joint. As Figure 2-37 shows, we can assume a straight line passing through  $G_1$ , the center of mass of body 1, and parallel to one of the two perpendicular axes of the joint. Assume a random point  $Q_1$  in body 1 that lies on the straight line; we can define a vector  $\mathbf{s}_1$  between the two points  $G_1$  and  $Q_1$ . With the same procedure in body 2, we can obtain vector  $\mathbf{s}_2$ , parallel to another axis of the joint. Then, the two vectors  $\mathbf{s}_1$  and  $\mathbf{s}_2$  are perpendicular to each other, and always keep the same direction relative to the joint. Thus, the constraints equation that restrains rotational motion can be derived as follows.

$$g_{rot,1} = \mathbf{s}_1 \cdot \mathbf{s}_2 = \mathbf{s}_1^T \mathbf{s}_2 = 0 \quad (165)$$

As a result, we derived the constraint equations and the  $\mathbf{G}_k$  for a universal joint.

$$\mathbf{g}_{universal,4} = \begin{bmatrix} \mathbf{g}_{trans,3} \\ g_{rot,1} \end{bmatrix} = \mathbf{0} \quad (166)$$

$$\mathbf{G}_{(universal,4)} = \begin{bmatrix} \mathbf{G}_{(trans,3)} \\ \mathbf{G}_{(rot,1)} \end{bmatrix} = \begin{bmatrix} \mathbf{I} & -({}^E \mathbf{R}_{G_1} \mathbf{r}_{P/G_1}) & -\mathbf{I} & ({}^E \mathbf{R}_{G_2} \mathbf{r}_{P/G_2}) \\ \mathbf{O} & -({}^E \mathbf{R}_{G_2} \mathbf{r}_{Q_2/G_2})^T ({}^E \mathbf{R}_{G_1} \mathbf{r}_{Q_1/G_1}) & \mathbf{O} & -({}^E \mathbf{R}_{G_1} \mathbf{r}_{Q_1/G_1})^T ({}^E \mathbf{R}_{G_2} \mathbf{r}_{Q_2/G_2}) \end{bmatrix} \quad (167)$$

### 2.4.3. Hinge joint

A hinge joint constraints every translational motion and 2 rotational motions, which means that rotational motion about 1 axis is allowed. As the constraint equations for a ball joint restrain every translational motion, Eq. (163) is included in the constraint equations

of a hinge joint. The following figure shows an example of a hinge joint that allows rotational motion about the Z axis.

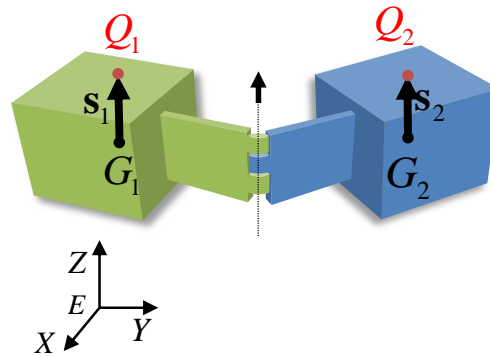


Figure 2-38. Hinge joint.

Figure 2-38 shows the Z axis that allows rotation. Set a random point  $Q_i$  in body 1, so that the vector from  $G_i$  to  $Q_i$  is parallel to the axis of rotation. With the same step in body 2, we obtained the vectors  $\mathbf{s}_1$  and  $\mathbf{s}_2$ , as Figure 5 shows. As the vectors are parallel to the axis of rotation, the directions of the vectors are constant. This can be mathematically formulated as:

$$\mathbf{g}_{rot,2} = \mathbf{s}_1 \times \mathbf{s}_2 = \tilde{\mathbf{s}}_1 \mathbf{s}_2 = \mathbf{0} \quad (168)$$

Eq. (168) consists of 3 equations; however, one of them is dependent on the others. Therefore, Eq. (168) includes 2 independent equations. The constraint equations of a hinge joint and its derivative are then,

$$\mathbf{g}_{hinge,5} = \begin{bmatrix} \mathbf{g}_{trans,3} \\ \mathbf{g}_{rot,2} \end{bmatrix} = \mathbf{0} \quad (169)$$

$$\mathbf{G}_{(hinge,5)} = \begin{bmatrix} \mathbf{G}_{(trans,3)} \\ \mathbf{G}_{(rot,2)} \end{bmatrix} = \begin{bmatrix} \mathbf{I} & -({}^E\mathbf{R}_{G_1}\mathbf{r}_{P/G_1}) & -\mathbf{I} & ({}^E\mathbf{R}_{G_2}\mathbf{r}_{P/G_2}) \\ \mathbf{O} & ({}^E\mathbf{R}_{G_2}\mathbf{r}_{Q_2/G_2})({}^E\mathbf{R}_{G_1}\mathbf{r}_{Q_1/G_1}) & \mathbf{O} & -({}^E\mathbf{R}_{G_1}\mathbf{r}_{Q_1/G_1})({}^E\mathbf{R}_{G_2}\mathbf{r}_{Q_2/G_2}) \end{bmatrix} \quad (170)$$

#### 2.4.4. Slider joint

A slider joint allows translational and rotational motion about 1 axis. Accordingly, we required 4 equations. Figure 2-39 shows an example of a prismatic joint. The dotted line is the axis that translation and rotation are allowed about.

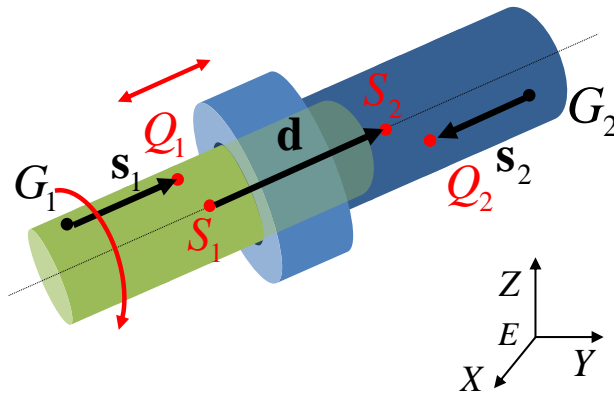


Figure 2-39. Slider joint.

Meanwhile, the random points in bodies 1 and 2,  $Q_1$  and  $Q_2$  can be chosen so that the vectors  $G_1Q_1$  ( $\mathbf{s}_1$ ) and  $G_2Q_2$  ( $\mathbf{s}_2$ ) are parallel to the dotted line. As body 1 and body 2 only move along the dotted line, the two vectors are parallel, no matter how the two bodies move. As this constraint only allows rotation about the dotted line, this yields the following constraint equations.

$$\mathbf{g}_{rot,2} = \mathbf{s}_1 \times \mathbf{s}_2 = \tilde{\mathbf{s}}_1 \mathbf{s}_2 = \mathbf{0} \quad (171)$$

Likewise, two random points in bodies 1 and 2 lying on the dotted line can be chosen as  $S_1$  and  $S_2$ . To exclude translational motion about any axis except for the dotted line, the vector  $\mathbf{s}_1$  in body 1 should be parallel to the vector  $S_1 S_2$  ( $\mathbf{d}$ ). Therefore,

$$\mathbf{g}_{trans,2} = \mathbf{s}_1 \times \mathbf{d} = \tilde{\mathbf{s}}_1 \mathbf{d} = \mathbf{0} \quad (172)$$

Finally, the constraint equations of a slider joint and its derivative are given by:

$$\mathbf{g}_{slider,4} = \begin{bmatrix} \mathbf{g}_{rot,2} \\ \mathbf{g}_{trans,2} \end{bmatrix} = \mathbf{0} \quad (173)$$

$$\mathbf{G}_{(slider,4)} = \begin{bmatrix} \mathbf{G}_{(rot,2)} \\ \mathbf{G}_{(trans,2)} \end{bmatrix} = \begin{bmatrix} \mathbf{0} & ({}^E \mathbf{R}_{G_2} \mathbf{r}_{Q_2/G_2}) ({}^E \mathbf{R}_{G_1} \mathbf{r}_{Q_1/G_1}) & \mathbf{0} & -({}^E \mathbf{R}_{G_1} \mathbf{r}_{Q_1/G_1}) ({}^E \mathbf{R}_{G_2} \mathbf{r}_{Q_2/G_2}) \\ ({}^E \mathbf{R}_{G_1} \mathbf{r}_{Q_1/G_1}) & ({}^E \mathbf{r}_{G_1} + {}^E \mathbf{R}_{G_1} \mathbf{r}_{S_1/G_1} - {}^E \mathbf{r}_{G_2} - {}^E \mathbf{R}_{G_2} \mathbf{r}_{S_2/G_2}) ({}^E \mathbf{R}_{G_1} \mathbf{r}_{Q_1/G_1}) - ({}^E \mathbf{R}_{G_1} \mathbf{r}_{Q_1/G_1}) ({}^E \mathbf{R}_{G_2} \mathbf{r}_{S_2/G_2}) & -({}^E \mathbf{R}_{G_1} \mathbf{r}_{Q_1/G_1}) & ({}^E \mathbf{R}_{G_1} \mathbf{r}_{Q_1/G_1}) ({}^E \mathbf{R}_{G_2} \mathbf{r}_{S_2/G_2}) \end{bmatrix} \quad (174)$$

### 2.4.5. Fixed joint

A fixed joint restrains every translational or rotational motion. As Figure 2-40 shows that a fixed joint restrains any motion between the two bodies.

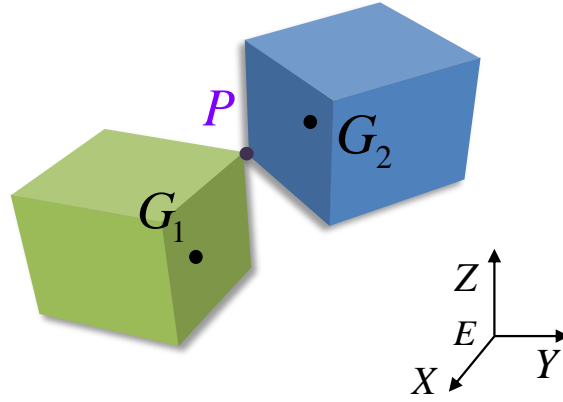


Figure 2-40. Fixed joint.

Therefore, we needed the constraint equations that restrain 3 translational motions, Eq. (163). In addition, the equations to constrain 3 rotational motions are easily given by:

$$\mathbf{g}_{rot,3} = \boldsymbol{\theta}_1 - \boldsymbol{\theta}_2 - (\boldsymbol{\theta}_1^0 - \boldsymbol{\theta}_2^0) = 0 \quad (175)$$

The final form of the constraint equations for a fixed joint and its derivative are then,

$$\mathbf{g}_{fix,6} = \begin{bmatrix} \mathbf{g}_{trans,3} \\ \mathbf{g}_{rot,3} \end{bmatrix} \quad (176)$$

$$\mathbf{G}_{(fix,6)} = \begin{bmatrix} \mathbf{G}_{(trans,3)} \\ \mathbf{G}_{(rot,3)} \end{bmatrix} = \begin{bmatrix} \mathbf{I} & -({}^E\mathbf{R}_{G_1}\mathbf{r}_{P/G_1}) & -\mathbf{I} & ({}^E\mathbf{R}_{G_2}\mathbf{r}_{P/G_2}) \\ \mathbf{O} & \mathbf{I} & \mathbf{O} & -\mathbf{I} \end{bmatrix} \quad (177)$$

### 2.4.6. Slider-hinge joint

A slider-hinge joint is the combination of slider and hinge joints as shown in Figure 2-41

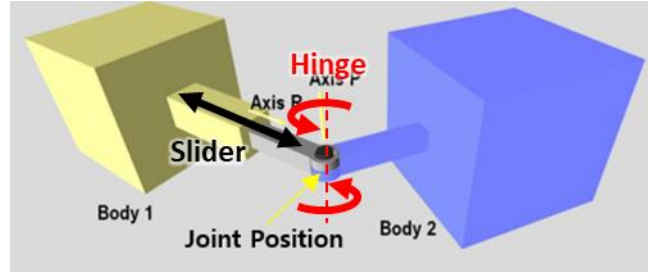


Figure 2-41. Slider-hinge joint.

For the slider-hinge joint, the constraint equations of slider joint and hinge joint are simply combined as follows.

$$\mathbf{g}_{trans,2} = \mathbf{s}_1 \times \mathbf{d} = \tilde{\mathbf{s}}_1 \mathbf{d} = 0 \quad (178)$$

$$\mathbf{g}_{rot,2} = \mathbf{s}_3 \times \mathbf{s}_4 = \tilde{\mathbf{s}}_3 \mathbf{s}_4 = 0 \quad (179)$$

where,  $\mathbf{s}_1$  and  $\mathbf{d}$  are the same vectors in Eq. (172),  $\mathbf{s}_3$  and  $\mathbf{s}_4$  are the same vectors of  $\mathbf{s}_1$  and  $\mathbf{s}_2$  in Eq. (168), respectively. Therefore, the constraint Jacobian is also given as follows.

$$\mathbf{G}_{(hinge,5)} = \begin{bmatrix} \mathbf{G}_{(trans,2)} \\ \mathbf{G}_{(rot,2)} \end{bmatrix} = \begin{bmatrix} \left( {}^E \mathbf{R}_{G_1} \mathbf{r}_{Q_1/G_1} \right) & \left( {}^E \mathbf{r}_{G_1} + {}^E \mathbf{R}_{G_1} \mathbf{r}_{S_1/G_1} - {}^E \mathbf{r}_{G_2} - {}^E \mathbf{R}_{G_2} \mathbf{r}_{S_2/G_2} \right) \left( {}^E \mathbf{R}_{G_1} \mathbf{r}_{Q_1/G_1} \right) - \left( {}^E \mathbf{R}_{G_1} \mathbf{r}_{Q_1/G_1} \right) \left( {}^E \mathbf{R}_{G_1} \mathbf{r}_{S_1/G_1} \right) & - \left( {}^E \mathbf{R}_{G_1} \mathbf{r}_{Q_1/G_1} \right) & \left( {}^E \mathbf{R}_{G_1} \mathbf{r}_{Q_1/G_1} \right) \left( {}^E \mathbf{R}_{G_2} \mathbf{r}_{S_2/G_2} \right) \\ \mathbf{0} & \left( {}^E \mathbf{R}_{G_2} \mathbf{r}_{Q_2/G_2} \right) \left( {}^E \mathbf{R}_{G_1} \mathbf{r}_{Q_1/G_1} \right) & \mathbf{0} & - \left( {}^E \mathbf{R}_{G_1} \mathbf{r}_{Q_1/G_1} \right) \left( {}^E \mathbf{R}_{G_2} \mathbf{r}_{Q_2/G_2} \right) \end{bmatrix} \quad (180)$$

### 2.4.7. Wire rope constraint



As shown in Figure 2-42, *Body1* and *Body2* are connected to each other with a wire rope. To simulate stretching with a constraint-based wire rope, the length of the wire rope should be equal to the constant value  $l_{total}$ . If the distance between the wire connection points is larger than  $l_{total}$ , this means that the constraint is violated. If *Body2* violates the constraint, the constraint force is acting on the *Body2*, which is equal to the spring force.

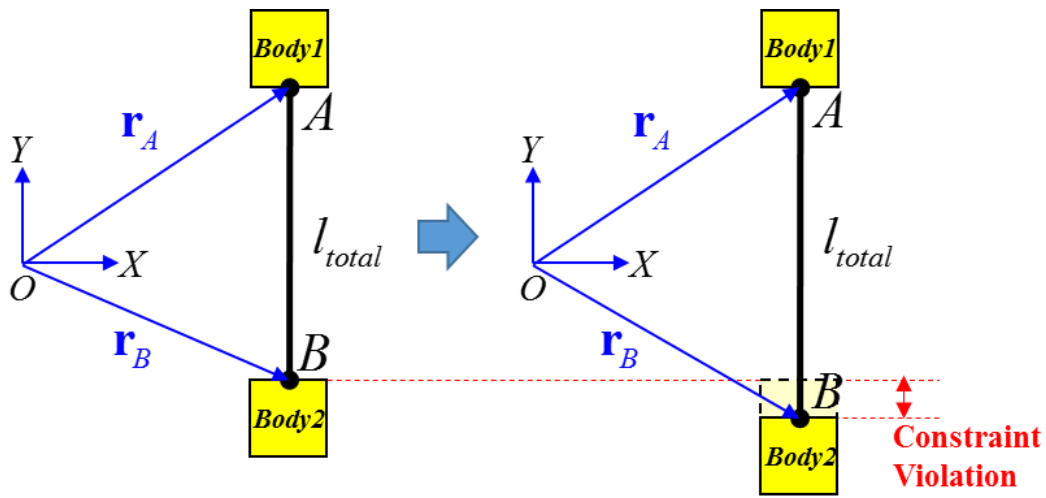


Figure 2-42. Wire rope with a single element.

Then, the constraint equation of stretching is given by:

$$g(\mathbf{q}) = |\mathbf{r}_A - \mathbf{r}_B| - l_{total} = 0 \quad (181)$$

where,  $\mathbf{r}_A$  and  $\mathbf{r}_B$  are position vectors from the origin  $O$  to point  $A$  and  $B$ , respectively. The position vector can be expressed using the rotation matrix and the position vector of the center of gravity. Thus, the constraint equation of the wire rope can be rewritten as:

$$g(\mathbf{q}) = |\mathbf{r}_{G1} + \mathbf{R}_1 \mathbf{r}_{A/G1} - \mathbf{r}_{G2} - \mathbf{R}_2 \mathbf{r}_{B/G2}| - l_{total} = 0 \quad (182)$$

where,  $\mathbf{r}_{G1}$  and  $\mathbf{r}_{G2}$  are the position vectors, and  $\mathbf{R}_1$  and  $\mathbf{R}_2$  are the rotation matrixes of *Body1* and *Body2*, respectively.  $\mathbf{r}_{A/G1}$  means the vector from  $G_1$  to  $A$  and  $\mathbf{r}_{B/G2}$  means the vector from  $G_2$  to  $B$ . If we let  $\mathbf{l} = \mathbf{r}_{G_1} + \mathbf{R}_{G_1} \mathbf{r}_{A/G_1} - \mathbf{r}_{G_2} - \mathbf{R}_{G_2} \mathbf{r}_{B/G_2}$ , and  $\mathbf{n} = \frac{\mathbf{l}}{\|\mathbf{l}\|}$ , we obtain the derivation of the constraint equation as follows:

$$\mathbf{G} = \begin{bmatrix} \mathbf{n} & -(\mathbf{n} \times \mathbf{r}_{A/G_1}) & -\mathbf{n} & (\mathbf{n} \times \mathbf{r}_{B/G_2}) \end{bmatrix} \quad (183)$$

In Eq. (37),  $\frac{r}{2} g^2$  is the same form of spring energy  $\frac{k}{2} g^2$ , where  $k$  is the spring coefficient. Therefore,  $r = k = \frac{1}{\varepsilon}$ . This implies that the epsilon is in inverse proportion to the spring coefficient.

The stretching constraint can be used to connect several bodies with one wire rope. In this case, we express the constraint equation with a summation of the length between the points.

$$g(\mathbf{q}) = \sum_{i,j} |\mathbf{r}_i - \mathbf{r}_j| - l_{total} = 0 \quad (184)$$

We can apply this to make fixed and moving pulleys. Figure 2-43 shows an example of pulleys.

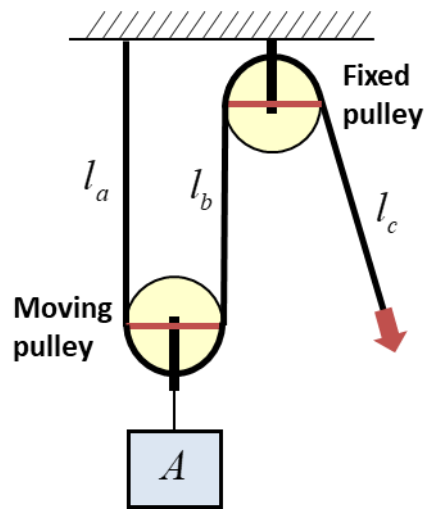


Figure 2-43. Wire rope with pulleys.

As the main wire winding around the pulleys has constant length, the constraint equation of the wire is simply formulated as follows.

$$g = (l_a + l_b + l_c) - l_{total} = 0 \quad (185)$$

## 2.5. Kinematic constraints between rigid and flexible bodies

### bodies

In the multibody system, the bodies may be interconnected by one or more kinematic constraints which can be described as algebraic constraint equations that constrain some degrees of freedom of the body. This section explains the constraint equation between a flexible body and a rigid body.

### 2.5.1. Joints on 1D frame element

#### (1) Ball joint between rigid and 1D flexible bodies

Figure 2-44 shows a ball joint attached between a rigid body and one of frame elements.

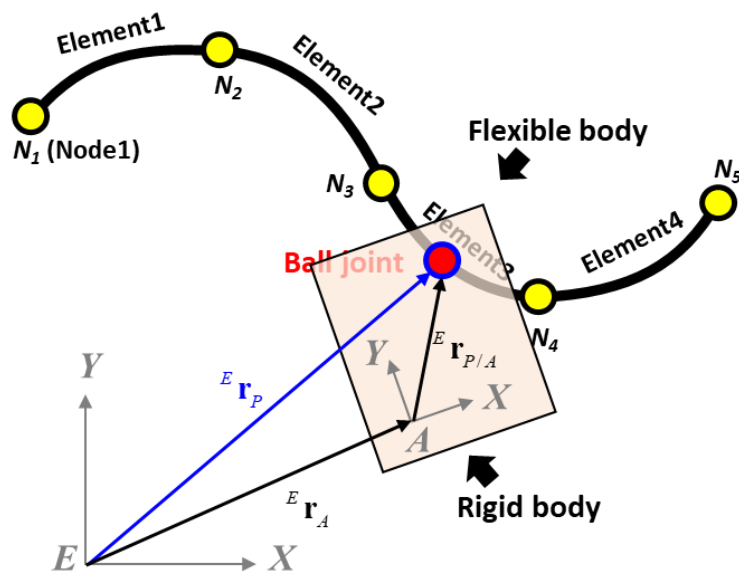


Figure 2-44. Ball joint between a rigid body and a frame element

The position vector using the coordinate of the rigid body is expressed as follows.

$${}^E \mathbf{r}_{P,rigid} = {}^E \mathbf{r}_A + {}^E \mathbf{R}_A {}^A \mathbf{r}_P \quad (186)$$

Meanwhile, the position vector on the third element (Element3) is defined by the nodal coordinate of  $N_3$  and  $N_4$  as shown in Figure 2-45.

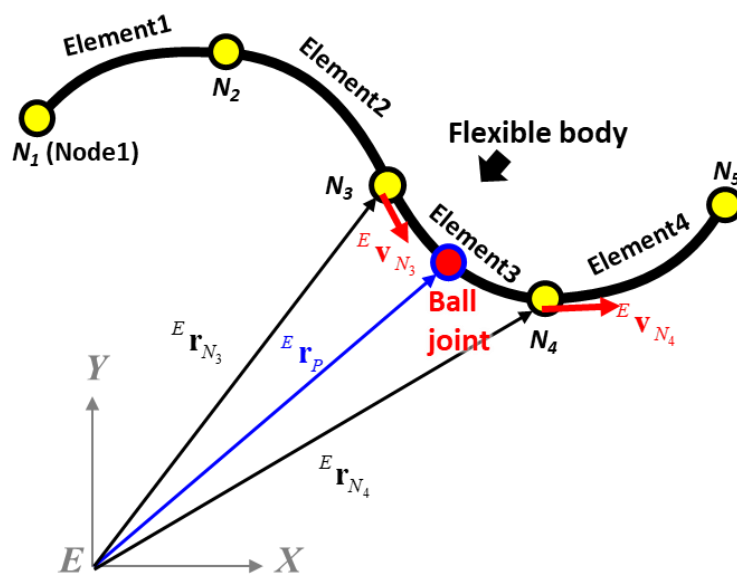


Figure 2-45. Position vector of ball joint on the frame element.

It is expressed by the position vectors and slope vectors on  $N_3$ , and  $N_4$ .

$${}^E \mathbf{r}_{P,flexible} = \mathbf{S}(\xi) \mathbf{q}_f = \mathbf{S}(\xi) \begin{bmatrix} {}^E \mathbf{r}_{N_3} \\ {}^E \mathbf{v}_{N_3} \\ {}^E \mathbf{r}_{N_4} \\ {}^E \mathbf{v}_{N_4} \end{bmatrix} \quad (187)$$

The constraint equation of the ball joint is to restrict the translational motion. This is done by the following equation.

$$\mathbf{g} = {}^E \mathbf{r}_{P,flexible} - {}^E \mathbf{r}_{P,rigid} = \mathbf{S}(\xi) \mathbf{q}_f - ({}^E \mathbf{r}_A + {}^E \mathbf{R}_A {}^A \mathbf{r}_P) = \mathbf{0} \quad (188)$$

The constraint Jacobian is also derived as follows.

$$\frac{\partial \mathbf{g}}{\partial \mathbf{q}} = \begin{bmatrix} \mathbf{S}(\xi) & -\mathbf{I}_{3 \times 3} & {}^E \mathbf{r}_{P/A} \end{bmatrix} \quad (189)$$

## (2) Fixed joint between rigid and 1D flexible bodies

A fixed joint is to restrict the rotation in addition to the translation. The slope vector at the fixed joint is defined as follows.

$${}^E \mathbf{v}_{P,flexible} = \mathbf{v}_f = \frac{d\mathbf{S}}{d\xi} \mathbf{q}_f = \mathbf{S}_\xi \begin{bmatrix} {}^E \mathbf{r}_{N_3} \\ {}^E \mathbf{v}_{N_3} \\ {}^E \mathbf{r}_{N_4} \\ {}^E \mathbf{v}_{N_4} \end{bmatrix} \quad (190)$$

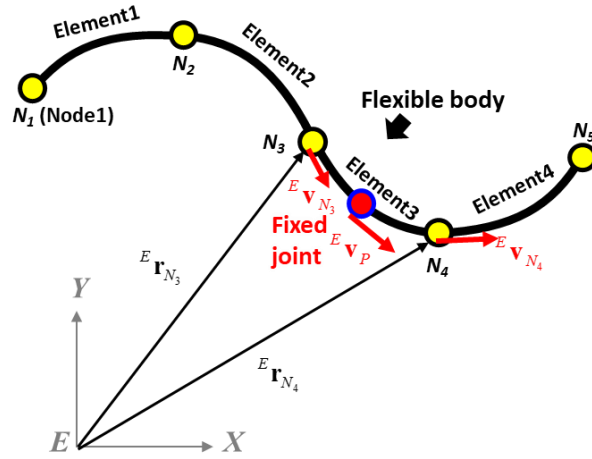


Figure 2-46. Slope vector defined on the frame element.

Meanwhile, the reference vector initially coincided with a slope vector calculated from frame element is defined as follows.

$${}^E \mathbf{v}_{P,rigid} = \mathbf{v}_r = {}^E \mathbf{R}_A {}^A \dot{\mathbf{r}}_P \quad (191)$$

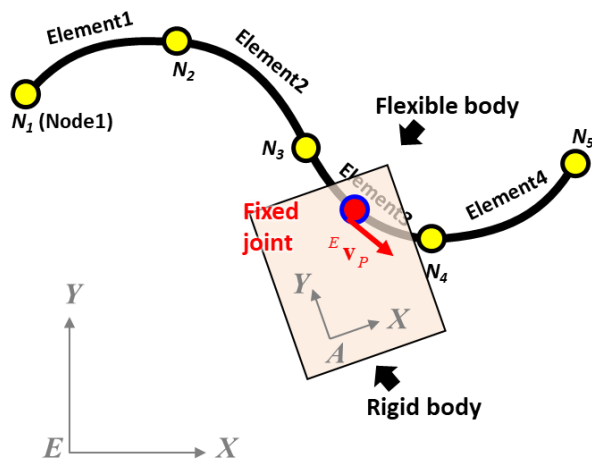


Figure 2-47. Reference vector initially coincided with a slope vector calculated from the frame element.

Two vectors ( $\mathbf{v}_f$  and  $\mathbf{v}_r$ ) should parallel to restrict the rotation. Therefore, the constraint equation and constraint Jacobian are given as follows.

$$\mathbf{g} = \mathbf{v}_f \times \mathbf{v}_r = \mathbf{0} \quad (192)$$

$$\frac{\partial \mathbf{g}}{\partial \mathbf{q}} = \begin{bmatrix} -\mathbf{v}_r \mathbf{S}_{\xi} & \mathbf{0} & -\mathbf{v}_f \mathbf{v}_r \end{bmatrix} \quad (193)$$

The calculation procedure of the constraint Jacobian is explained in detail in the following equation.

$$\begin{aligned} \frac{d\mathbf{g}}{dt} &= \dot{\mathbf{v}}_f \times \mathbf{v}_r + \mathbf{v}_f \times \dot{\mathbf{v}}_r \\ &= -\mathbf{v}_r \times \dot{\mathbf{v}}_f + \mathbf{v}_f \times (\boldsymbol{\omega} \times \mathbf{v}_r) \\ &= -\mathbf{v}_r \times \mathbf{S}_{\xi\eta} \mathbf{q} - \mathbf{v}_f \times (\mathbf{v}_r \times \boldsymbol{\omega}) \\ &= -\mathbf{v}_r \mathbf{S}_{\xi\eta} \dot{\mathbf{q}} - \mathbf{v}_f \mathbf{v}_r \boldsymbol{\omega} \\ &= \begin{bmatrix} -\mathbf{v}_r \mathbf{S}_{\xi\eta} & \mathbf{0} & -\mathbf{v}_f \mathbf{v}_r \end{bmatrix} \begin{bmatrix} \dot{\mathbf{q}} \\ {}^E \mathbf{r}_A \\ {}^E \boldsymbol{\omega}_A \end{bmatrix} \end{aligned} \quad (194)$$

## 2.5.2. Joints on 2D shell element

### (1) Ball joint between rigid and 2D flexible bodies

Figure 2-48 shows a ball joint attached between a rigid body and one of shell elements.



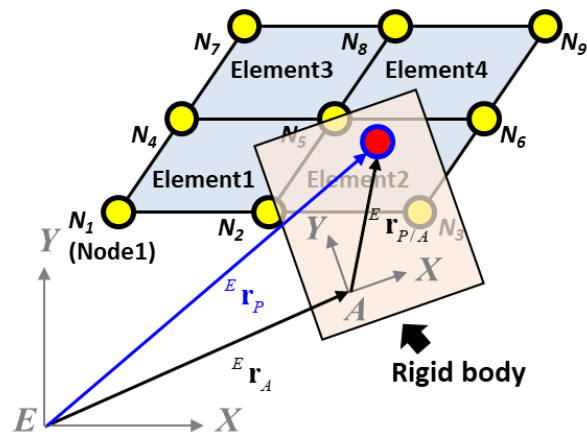


Figure 2-48. Ball joint between a rigid body and a shell element

The position vector using the coordinate of the rigid body is expressed as follows.

$${}^E \mathbf{r}_{P,rigid} = {}^E \mathbf{r}_A + {}^E \mathbf{R}_A {}^A \mathbf{r}_P \quad (195)$$

Meanwhile, the position vector on 'Element2' is defined by the nodal coordinate of  $N_2$ ,  $N_3$ ,  $N_5$ , and  $N_6$  as shown in Figure 2-49.

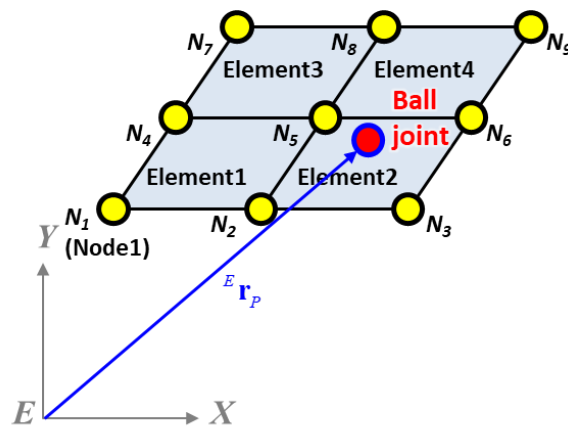


Figure 2-49. Position vector of ball joint on the shell element.

It is expressed by the position vectors and slope vectors on  $N_2$ ,  $N_3$ ,  $N_5$ , and  $N_6$ .

$${}^E \mathbf{r}_{P,flexible} = \mathbf{S}(\xi, \eta) \mathbf{q}_{N_2 N_3 N_5 N_6} \quad (196)$$

The constraint equation of the ball joint is to restrict the translational motion. This is done by the following equation.

$$\mathbf{g} = {}^E \mathbf{r}_{P,flexible} - {}^E \mathbf{r}_{P,rigid} = \mathbf{S}(\xi, \eta) \mathbf{q} - ({}^E \mathbf{r}_A + {}^E \mathbf{R}_A {}^A \mathbf{r}_P) = \mathbf{0} \quad (197)$$

The constraint Jacobian is also derived as follows.

$$\frac{\partial \mathbf{g}}{\partial \mathbf{q}} = \left[ \mathbf{S}(\xi, \eta) \quad -\mathbf{I}_{3 \times 3} \quad {}^E \mathbf{r}_{P/A} \right] \quad (198)$$

## (2) Fixed joint between rigid and 2D flexible bodies

A fixed joint is to restrict the rotation in addition to the translation. The slope vector at the fixed joint is defined as follows.

$${}^E \mathbf{v}_{P,flexible} = \mathbf{v}_f = \frac{\partial^2 \mathbf{S}}{\partial \xi \partial \eta} \mathbf{q}_{N_2 N_3 N_5 N_6} = \mathbf{S}_{\xi \eta} \mathbf{q}_{N_2 N_3 N_5 N_6} \quad (199)$$

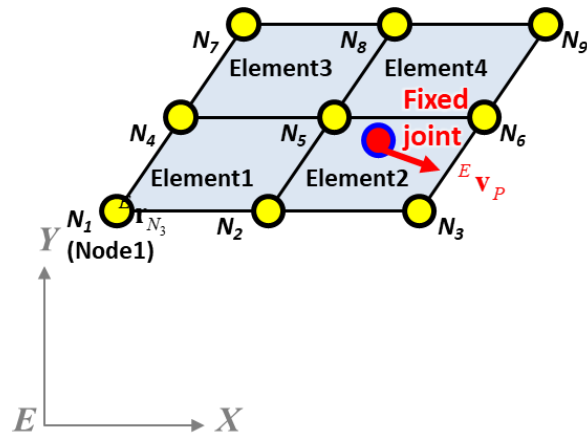


Figure 2-50. Slope vector defined on the shell element.

Meanwhile, the reference vector initially coincided with a slope vector calculated from shell element is defined as follows.

$${}^E \mathbf{v}_{P,rigid} = \mathbf{v}_r = {}^E \mathbf{R}_A {}^A \dot{\mathbf{r}}_P \quad (200)$$

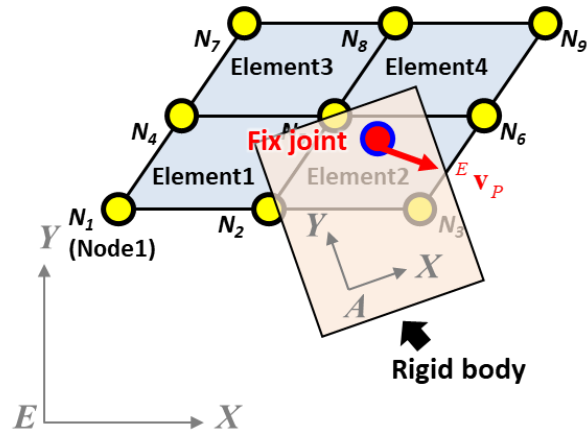


Figure 2-51. Reference vector initially coincided with a slope vector calculated from the shell element.

Two vectors ( $\mathbf{v}_f$  and  $\mathbf{v}_r$ ) should parallel to restrict the rotation. Therefore, the constraint equation and constraint Jacobian are given as follows.

$$\mathbf{g} = \mathbf{v}_f \times \mathbf{v}_r = \mathbf{0} \quad (201)$$

$$\frac{\partial \mathbf{g}}{\partial \mathbf{q}} = \begin{bmatrix} -\mathbf{v}_r \mathbf{S}_{\xi\eta} & \mathbf{0} & -\mathbf{v}_f \mathbf{v}_r \end{bmatrix} \quad (202)$$

## 2.6. Collision detection and response

Theoretical backgrounds of the collision detection and response proposed in this study will be explained in the following sections.

### 2.6.1. Collision detection

Collision detection is to find the mesh pair and the penetration depth when two bodies collide. Collision detection is generally composed of two stages, as shown in Figure 2-52. One is a broad phase stage which checks collisions between two bounding boxes. The other is a narrow phase stage which checks collisions between the meshes.

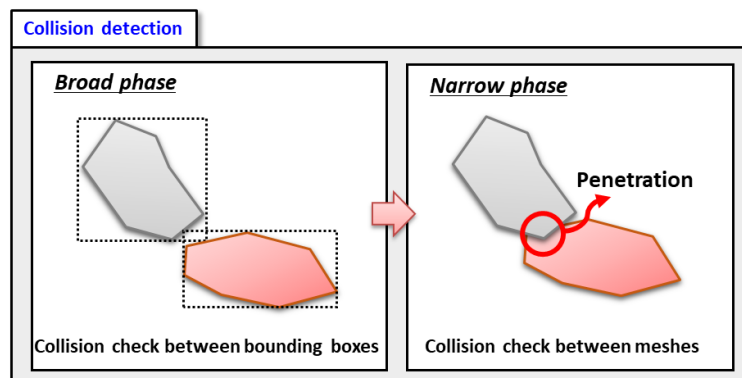


Figure 2-52. Broad and narrow phase stages.

There are mainly two specialized problems in the shipbuilding and offshore industries during the collision detection. The first problem is that the shape is not a polyhedron, but contains unenclosed meshes. Figure 2-53 shows the example of meshes which are not enclosed. In this case, the well-known collision detection algorithms [49]–[51] which are suitable to convex and concave shapes cannot be applied.

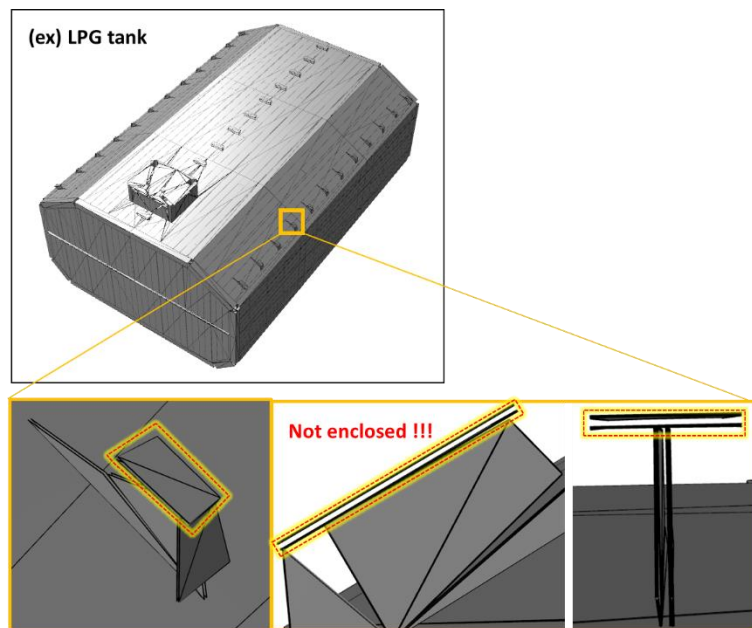


Figure 2-53. Unenclosed mesh in LPG tank.

Secondly, there are too many meshes in one body shape which is exported from the ship CAD (Computer-Aided Design) system. Figure 2-54 shows an LPG tank model in which the number of vertices is 57,696, and the number of triangular meshes is 19,232. Therefore, it takes a lot of time to detect the collision.

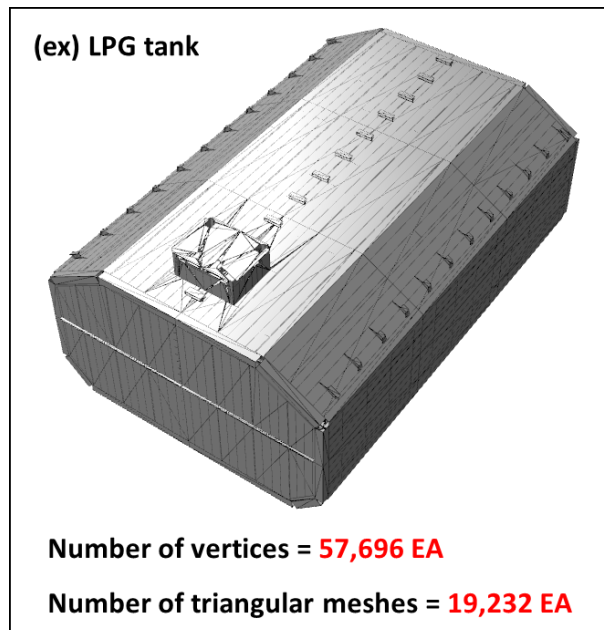


Figure 2-54. LPG tank model.

To solve the first problem, we propose the position difference method which checks an intersection using the line segment made by the two vertices or the trigonal prism consisting of the two triangular meshes at time  $t$  and  $t+1$ . To solve the second problem, we must reduce the number of meshes. Therefore, space partitioning and exclusion boxes are adopted. In the following sub-sections, the methods to solve those problems will be explained.

### (1) Position difference method

PDM (Position Difference Method) uses the positions of the meshes at time  $t$  and  $t+1$ . Therefore, it is only available in dynamic analysis. This method is very similar to continuous collision detection which is derived from polyhedra [52], [53]. This method is divided into two states such as vertex-mesh collision and edge-edge collision.

PDM for vertex-mesh collision is further divided into three cases according to the colliding position and the existence of movement. The first case is that a colliding vertex

on the moving body (Body2) moves into the fixed body (Body1) as shown in Figure 2-55.

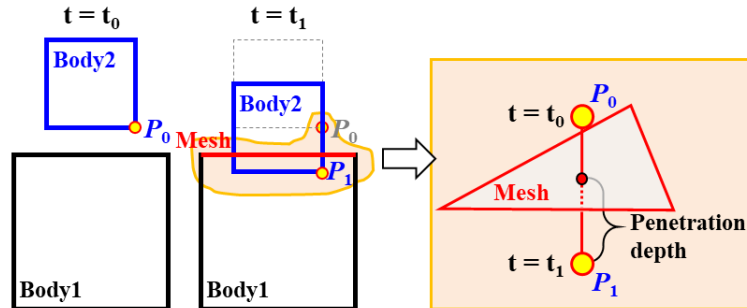


Figure 2-55. Vertex-mesh collision: Vertex on the moving body moves into the fixed body.

At time  $t_0$ , Body1 and Body2 do not collide. However, the vertex ( $P$ ) passes through the mesh on the top of Body1 at time  $t_1$ . The first step is to find  $P_0$  and  $P_1$  which are the positions of the vertex ( $P$ ) at times  $t_0$  and  $t_1$ , respectively. The next step is to draw a line segment  $\overline{P_0P_1}$ . The last step is to check whether or not  $\overline{P_0P_1}$  intersects with one of the meshes. The penetration depth is the minimum distance from  $P_1$  to the mesh. The sequence is summarized in the pseudocode below.

<b>Vertex-mesh collision algorithm 1</b>
<b>FOR</b> each vertex of Body2 $P_0$ = Previous vertex position $P_1$ = Current vertex position Set segment using $P_0$ and $P_1$ <b>FOR</b> each mesh of Body1 <b>IF</b> Intersect mesh with segment <b>THEN</b> Set mesh and $P_1$ to Collision Pair <b>END IF</b> <b>END FOR</b> <b>END FOR</b>



However, this algorithm has a problem. Even though we apply the first algorithm, collision at the corner cannot be detected, as shown in Figure 2-56.

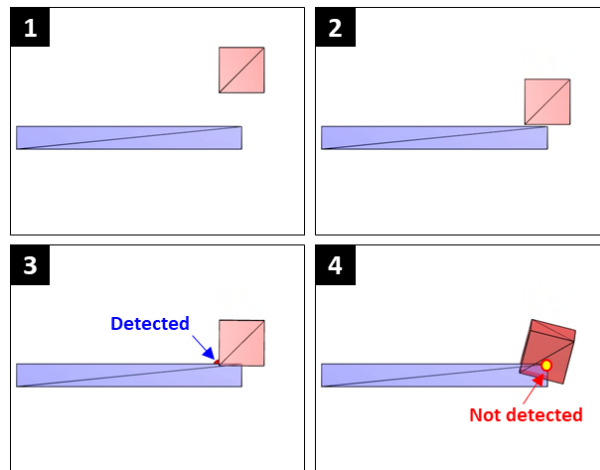


Figure 2-56. Collision at the corner.

Therefore, the second case of PDM for the vertex-mesh collision is that a colliding vertex on the fixed body (Body1) moves into the moving body (Body2), as shown in Figure 2-57.

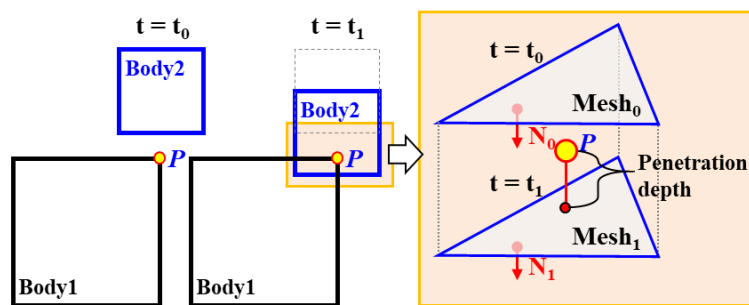


Figure 2-57. Vertex-mesh collision: Vertex on the fixed body moves into the moving body.

At time  $t_0$ , the vertex ( $P$ ) of Body1 is located outside Body2. However, the vertex ( $P$ ) is

located inside Body2 at time  $t_1$ . The first step is to find Mesh<sub>0</sub> and Mesh<sub>1</sub> at times  $t_0$  and  $t_1$ . The next step is to make a trigonal prism connecting vertices at time  $t_0$  and  $t_1$ . The last step is to check that  $P$  is located inside the trigonal prism. It is done by five plane equations. The penetration depth is the minimum distance from  $P$  to Mesh<sub>1</sub>. The sequence is summarized in the pseudo code below.

<b>Vertex-mesh collision algorithm 2</b>
<b>FOR</b> each mesh of Body2 Mesh <sub>0</sub> = Previous mesh position Mesh <sub>1</sub> = Current mesh position Calculate five planes using Mesh <sub>0</sub> and Mesh <sub>1</sub> <b>FOR</b> each vertex of Body1 <b>IF</b> vertex inside trigonal prism <b>THEN</b> Set Mesh <sub>1</sub> and vertex to Collision Pair <b>END IF</b> <b>END FOR</b> <b>END FOR</b>

Even though both the first and second algorithms are applied, there is still a problem when both bodies are moving, as shown in Figure 2-58.

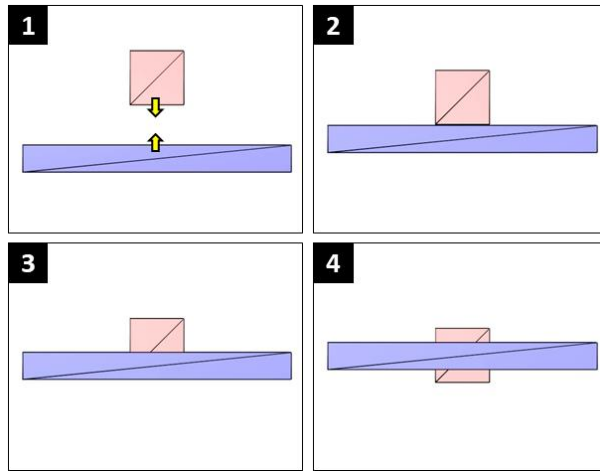


Figure 2-58. Collision between two moving bodies.

It is because both the vertex and the mesh are moved, and the line segment  $\overline{P_0P_1}$  unfortunately gets out of the mesh<sub>1</sub> at time  $t_1$ , as shown in Figure 2-59.

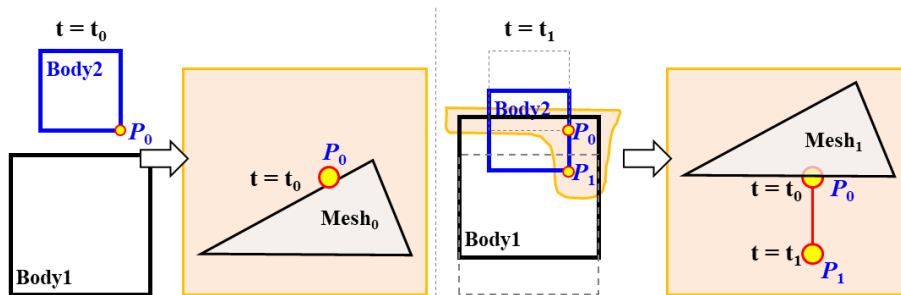


Figure 2-59. Collision detection failure in case of two moving bodies.

Therefore, we modify the first and second algorithm a little bit to solve this problem. We call this the third case of PDM for vertex-mesh collision. Basically, the first algorithm uses  $P_0$  at time  $t_0$ , and  $P_1$ , Mesh<sub>1</sub> at time  $t_1$ . In the third algorithm, Mesh<sub>0</sub> is used for collision detection instead of Mesh<sub>1</sub> (See Figure 2-60-(1)). Besides, the second algorithm uses Mesh<sub>0</sub> at time  $t_0$ , and  $P_1$ , Mesh<sub>1</sub> at time  $t_1$ . In the third algorithm,  $P_0$  is used instead of  $P_1$  (See

Figure 2-60-(2)).

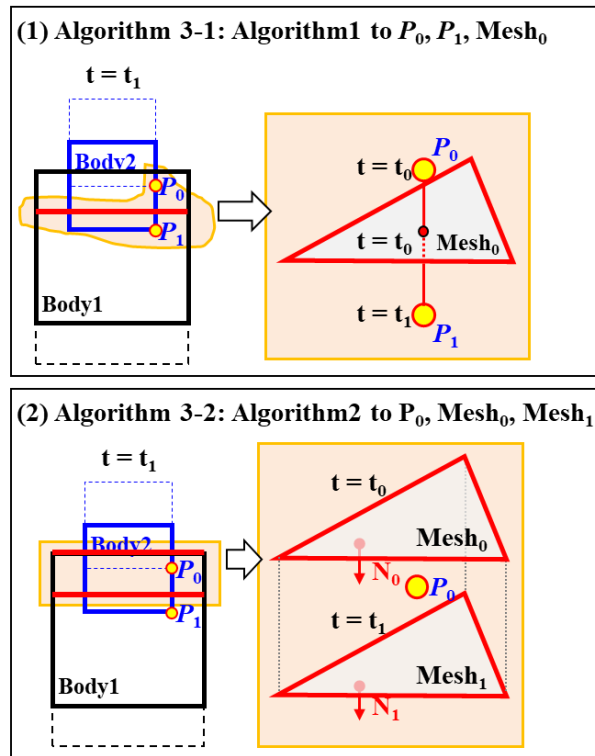


Figure 2-60. Vertex-mesh collision: Both bodies are moving.

PDM for edge-edge collision is further divided into two cases like PDM for vertex-mesh collision. The first case is that a colliding edge on the moving body (Body2) moves into the fixed body (Body1), as shown in Figure 2-61.

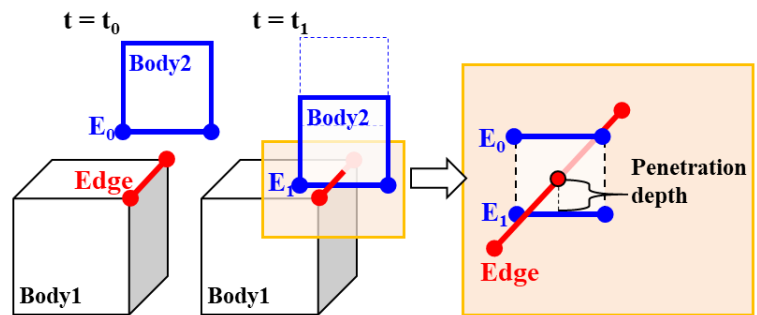


Figure 2-61. Edge-edge collision: Edge on the moving body moves into the fixed body.

At time  $t_0$ , Body1 and Body2 do not collide. However, the edge ( $E_0$ ) passes through the edge of Body1 at time  $t_1$ . The first step is to find  $E_0$  and  $E_1$  which are the edges at times  $t_0$  and  $t_1$ . The next step is to draw a rectangle using  $E_0$  and  $E_1$ . The last step is to check whether or not the rectangle intersects with one of the edges of Body1. The penetration depth is the minimum distance from  $E_1$  to the intersected edge. The sequence is summarized in the pseudocode below.

Edge-Edge collision algorithm
<b>FOR</b> each edge of Body2 $E_0$ = Previous edge position $E_1$ = Current edge position Set Rectangle using $E_0$ and $E_1$ <b>FOR</b> each edge of Body1 <b>IF</b> Intersect edge with Rectangle <b>THEN</b> Set edge and $E_1$ to Collision Pair <b>END IF</b> <b>END FOR</b> <b>END FOR</b>

If both bodies are moving, the edge-edge collision algorithm has the same problem

compared to the vertex-mesh collision algorithm, as shown in Figure 2-58. Instead of the edge of Body1 at time  $t_1$  ( $E_{1, \text{Body1}}$ ), the edge of Body1 at time  $t_0$  ( $E_{0, \text{Body1}}$ ) is used to solve this problem (See Figure 2-62-(1)). As an alternative, the edge of Body2 at time  $t_0$  ( $E_{0, \text{Body2}}$ ) is used instead of the edge of Body2 at time  $t_1$  ( $E_{1, \text{Body2}}$ ) (See Figure 2-62-(2)).

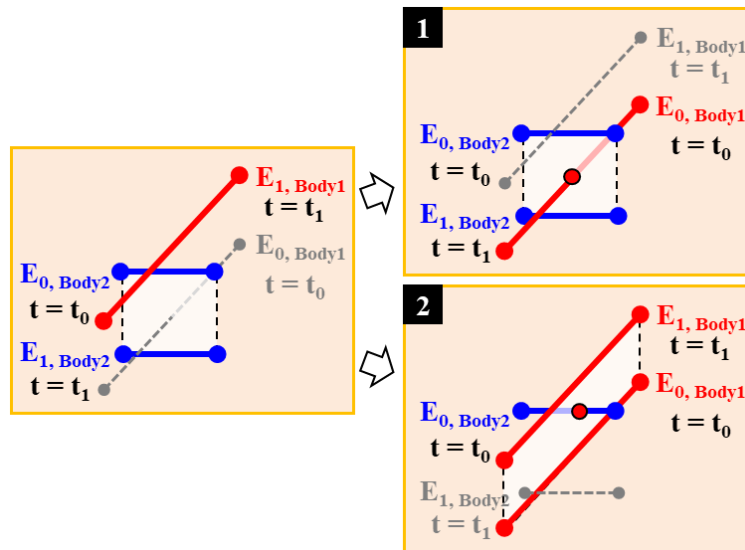


Figure 2-62. Edge-edge collision: Both bodies are moving.

## (2) Space partitioning

PDM requires a lot of computational costs if the shape contains many meshes. Space partitioning is the process of dividing a space into two or more non-overlapping regions. There are many kinds of space-partitioning techniques. In this study, BVH (Boundary Volume Hierarchy) is adopted [54], [55]. BVH is a tree structure on a set of geometric shapes. All geometric shapes are wrapped in bounding volumes that form the leaf nodes of a tree. The procedure to build BVH is depicted in Figure 2-63.

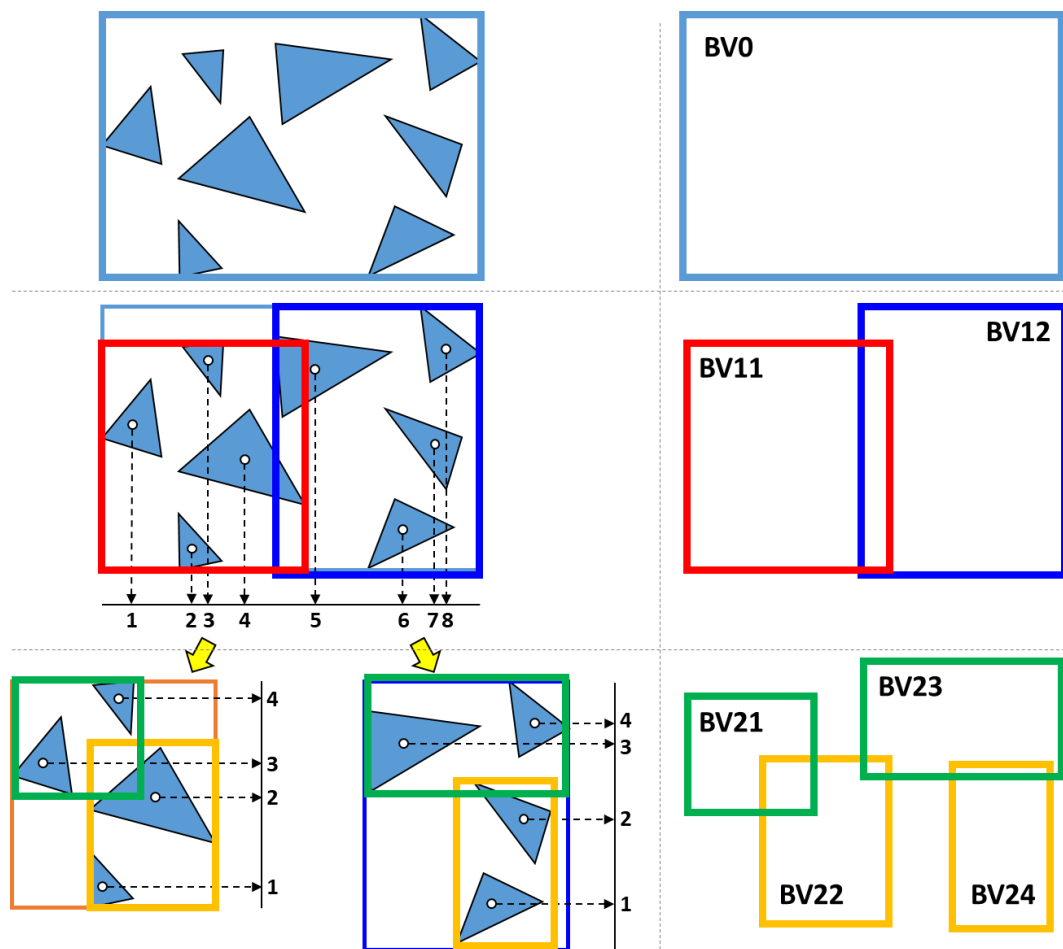


Figure 2-63. Procedure of BVH.

The first step is to organize the centroids of meshes in the ascending order. The next step is to split the centroids into left and right sides. These two steps are repeated for the different axis until the bound volume is a leaf.

BVH can dramatically reduce the computational costs of the collision detection. Bounding boxes of BVH are used instead of calculating collision detection between the meshes of the two bodies. Figure 2-64 shows a method demonstrating how to use BVH during the collision detection.

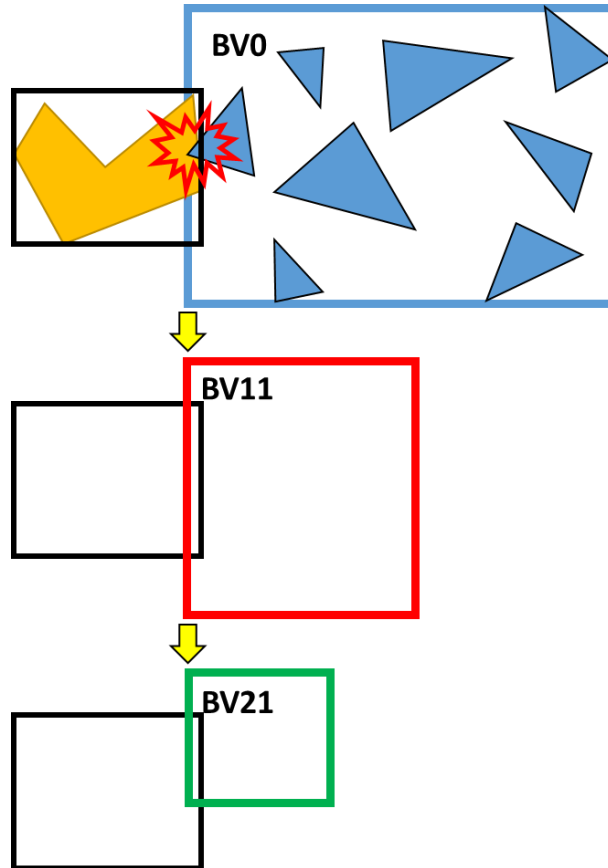


Figure 2-64. Traversal of two BVHs during the collision detection.

At first, top-level bounding volume (BV0) is used to detect the collision. If the detection is noticed, the next level of bound volume (BV11, BV12) is used to check the detection. This procedure is repeated until the leaf bounding volume is found. Finally, the meshes inside the leaf nodes are used to calculate collision detection.

### (3) Exclusion box

Even though space partitioning reduces a lot of computational costs, it still takes a long time to detect the collision if there are too many meshes. If we take a close look, there are



also many meshes which are not involved in the collision from the beginning. However, it is not easy to erase unnecessary meshes before the simulation using third-party programs. Sometimes, meshes which belong to a different part of the body want to be excluded according to the simulation conditions. Therefore, we developed exclusion boxes to exclude meshes inside boxes dynamically in the program. Figure 2-65 shows several examples of exclusion boxes applied to the LPG tank.

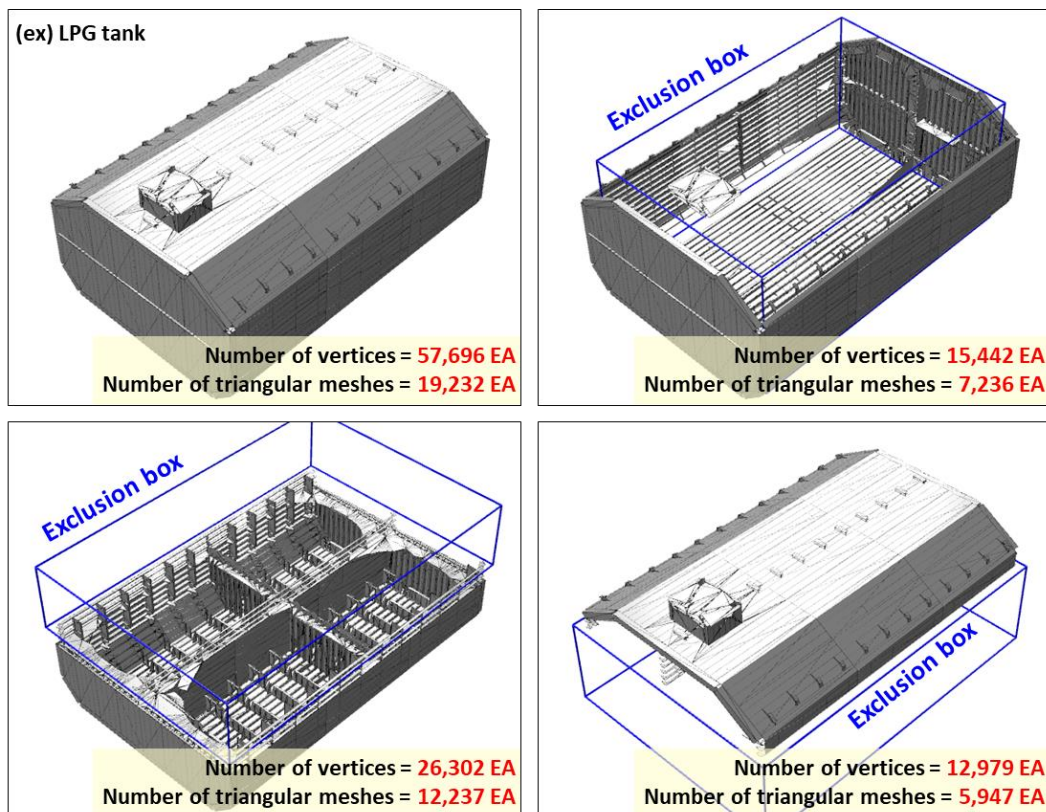


Figure 2-65. Examples of exclusion boxes applied to the LPG tank.

## 2.6.2. Collision response

Collision response is to find the forces acting at the collision position or velocities of

bodies directly after the collision. The classification of the collision response and the method we choose in this study will be explained in the following sub-sections.

### **(1) Classification of collision response**

There are basically two methods to describe the collision response [56]. One is an impulse-based method, which directly modifies the velocity as a result of impulse. This method is very simple. However, it is not applicable when two bodies collide at multiple points. It also makes the system unstable, because the direct change of the velocity after solving the equations of motion violates kinematic constraints. In other words, it is not applicable to a multibody system.

The other is a force-based method, which is further divided into two methods such as a spring-damper method, and a non-interpenetration constraint method. The spring-damper method exerts the collision force modeled by a spring-damper at the collision position. Unlike the impulse-based method, the spring-damper method is applicable when two bodies collide at the multiple points, and it does not compulsively violate the kinematic constraint because the collision force is also solved together when the equations of motion are solved numerically. However, it is not easy to select the proper parameters such as the exponent of the penetration depth ( $n$ ), spring and damping coefficient ( $k, d$ ), which vary according to material properties, the weight, the number of contact points, and so on.

The non-interpenetration constraint method exerts a collision force modeled by the constraint. This method has the same advantages as the spring-damper method. Moreover, the collision force can be determined automatically, reflecting material properties such as restitution and softness. Therefore, we choose the non-interpenetration constraint method for the collision response. Classification of the collision response is summarized in Figure 2-66.

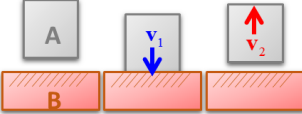
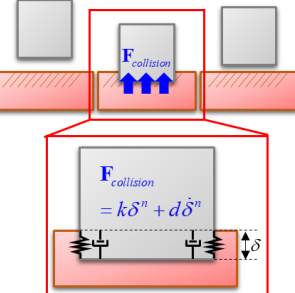
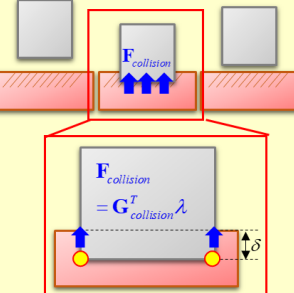
	Impulse-based method	Force-based method	
		Spring-damper method	Non-Interpenetration constraint method
Concept	<p>Modify velocity directly as a result of impulse</p>  $V^2 = V^1 + \frac{\text{Impulse}}{\text{Mass}}$	<p>Exert collision force modelled by spring-damper</p>  $F_{\text{collision}} = k\delta^n + d\dot{\delta}^n$	<p>Exert collision force modelled by constraint</p>  $F_{\text{collision}} = G^T_{\text{collision}} \lambda$
Feature	<ul style="list-style-type: none"> <li>• Simple</li> <li>• Not applicable for collision at multiple point</li> <li>• Not applicable for multibody system</li> </ul>	<ul style="list-style-type: none"> <li>• Applicable for collision at multiple point</li> <li>• Applicable for multibody system</li> <li>• No general approach to select parameters (<math>k, d, n</math>)</li> </ul>	<ul style="list-style-type: none"> <li>• Applicable for collision at multiple point</li> <li>• Applicable for multibody system</li> <li>• Collision force can be determined automatically.</li> </ul>

Figure 2-66. Classification of collision response.

## (2) Non-interpenetration constraint method

There are three statuses such as ‘no collision,’ ‘exact contact,’ and ‘interpenetration’ between two bodies as shown in Figure 2-67.  $\Phi_1$  and  $\Phi_2$  are the shape functions of the body surfaces which are continuously differentiable.

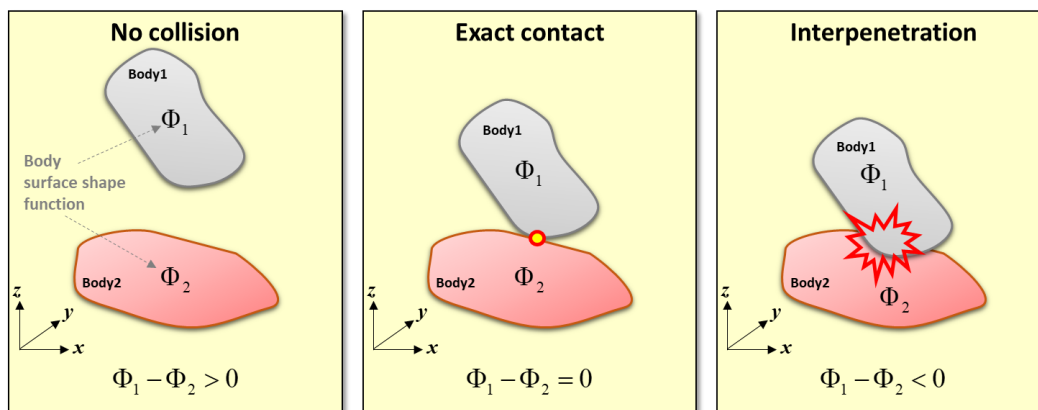


Figure 2-67. Three statuses between two bodies.

Non-interpenetration constraint equation can be expressed mathematically as follows [57], [58].

$$g_{collision} = \Phi_1 - \Phi_2 \geq 0 \quad (203)$$

If two bodies violate the non-interpenetration constraint, the collision (normal) force is acting on the bodies. The collision force can be expressed by the constraint Jacobian ( $\mathbf{G}_{collision}$ ) which is the direction, and the Lagrange multiplier ( $\lambda$ ), which is the magnitude.

$$\mathbf{F}_{collision} = \mathbf{G}_{collision}^T \lambda, \left( \mathbf{G}_{collision}^T = \left[ \frac{\partial g_{collision}}{\partial \mathbf{q}} \right]^T \right) \quad (204)$$

However, it is not easy to represent the body surface as continuously differentiable functions. Therefore, we derive a simple non-interpenetration constraint equation between a vertex and a plane, as shown in Figure 2-68.

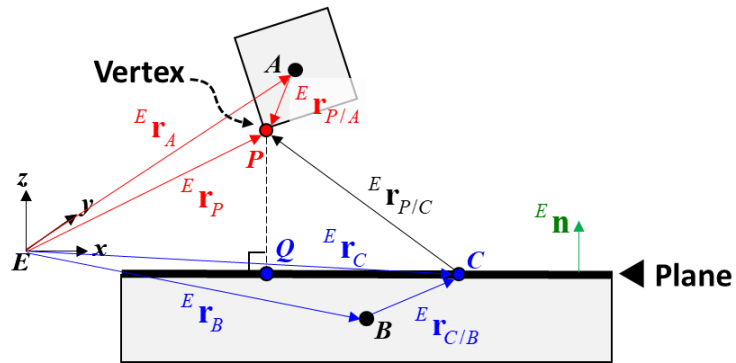


Figure 2-68. Non-interpenetration constraint between a vertex and a plane.

${}^E\mathbf{r}_{P/C}$  means that the vector direction is from point  $C$  to  $P$ , and the reference frame is the inertial frame ( $E$ - $xyz$ ). The starting point can be omitted if the origin of the reference frame and the starting point are the same ( ${}^E\mathbf{r}_A, {}^E\mathbf{r}_B$ ). Since two bodies are separated, the line segment  $\overline{PQ}$  should be larger than or equal to zero. This constraint and constraint Jacobian can be expressed as follows.

$$g_{collision} = \overline{PQ} \geq 0$$

$$\left( \begin{array}{l} \overline{PQ} = {}^E\mathbf{n} \cdot {}^E\mathbf{r}_{P/C} \\ = {}^E\mathbf{n} \cdot ({}^E\mathbf{r}_P - {}^E\mathbf{r}_C) \\ = {}^E\mathbf{n} \cdot \left\{ ({}^E\mathbf{r}_A + {}^E\mathbf{r}_{P/A}) - ({}^E\mathbf{r}_B + {}^E\mathbf{r}_{C/B}) \right\} \end{array} \right) \quad (205)$$

$$\mathbf{G}_{collision}^T = \begin{bmatrix} {}^E\mathbf{n} \\ {}^E\mathbf{r}_{P/A} \times {}^E\mathbf{n} \\ -{}^E\mathbf{n} \\ -({}^E\mathbf{r}_P - {}^E\mathbf{r}_B) \times {}^E\mathbf{n} \end{bmatrix} \quad (206)$$

Using Eq. (206), the collision force is calculated as follows.

$$\mathbf{F}_{collision} = \mathbf{G}_{collision}^T \lambda = \begin{bmatrix} {}^E\mathbf{n} \\ {}^E\mathbf{r}_{P/A} \times {}^E\mathbf{n} \\ -{}^E\mathbf{n} \\ -({}^E\mathbf{r}_P - {}^E\mathbf{r}_B) \times {}^E\mathbf{n} \end{bmatrix} \lambda = \begin{bmatrix} {}^E\mathbf{n}\lambda \\ {}^E\mathbf{r}_{P/A} \times {}^E\mathbf{n}\lambda \\ -{}^E\mathbf{n}\lambda \\ -({}^E\mathbf{r}_P - {}^E\mathbf{r}_B) \times {}^E\mathbf{n}\lambda \end{bmatrix} \quad (207)$$

Meanwhile, there are not only the normal force but also the frictional force at the collision position. The magnitude of the frictional force ( $\mathbf{F}_{friction}$ ) is simply proportional to

the normal force ( $\mathbf{F}_{normal}$ ), and the direction is the opposite of the projected relative velocity ( ${}^E\mathbf{v}_{rel}$ ) on the plane, as shown in Figure 2-69.

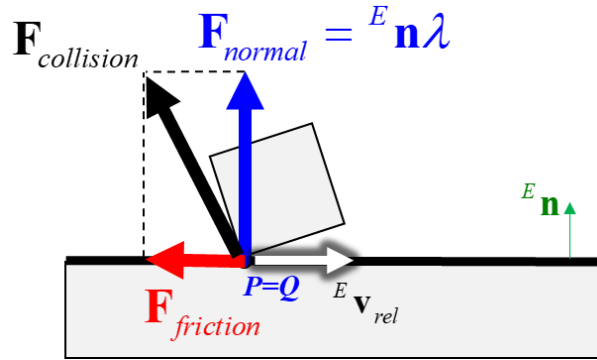


Figure 2-69. Calculation of the frictional force.

Therefore, the frictional force is calculated as follows.

$$\mathbf{F}_{friction} = \mu \left( -\frac{{}^E\mathbf{v}_{rel}}{|{}^E\mathbf{v}_{rel}|} \right) \lambda = \mu {}^E\mathbf{t} \lambda \quad (208)$$

where,  ${}^E\mathbf{t}$  is the unit vector, which is obtained by projection of the relative velocity at the collision position on the plane, and  $\mu$  is a frictional coefficient. Finally, we obtain the collision force including both the normal and frictional forces by replacing the normal vector  ${}^E\mathbf{n}$  with  ${}^E\mathbf{n} + \mu {}^E\mathbf{t}$  in Eq. (206).

$$\mathbf{F}_{collision} = \mathbf{G}_{collision}^T \lambda = \begin{bmatrix} {}^E \mathbf{n} + \mu {}^E \mathbf{t} \\ {}^E \mathbf{r}_{P/A} \times ({}^E \mathbf{n} + \mu {}^E \mathbf{t}) \\ -({}^E \mathbf{n} + \mu {}^E \mathbf{t}) \\ -({}^E \mathbf{r}_P - {}^E \mathbf{r}_B) \times ({}^E \mathbf{n} + \mu {}^E \mathbf{t}) \end{bmatrix} \lambda \quad (209)$$

So far, we explained the non-interpenetration constraint equation between a vertex and a plane. This equation can also be extended to the collision response between two bodies by using the collision pair which is obtained from the collision detection. There are two types of collision pairs. One is the mesh and the vertex which are obtained from vertex-mesh collision detection algorithm, as shown in Figure 2-70. The mesh becomes the plane and  $P$  becomes the vertex.

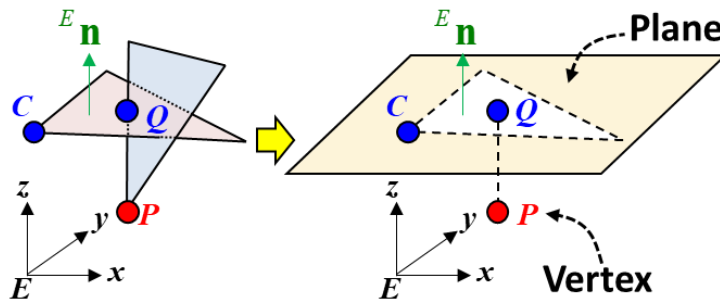


Figure 2-70. Collision pair: Mesh and vertex.

The other type of collision pair is two edges from edge-edge collision detection algorithm, as shown in Figure 2-71. The closest point ( $P$ ) from  $E_{l, Body1}$  becomes the vertex. The other closest point ( $Q$ ) becomes the point on the plane, and the normalized vector from  $P$  to  $Q$  becomes the normal vector of the plane.

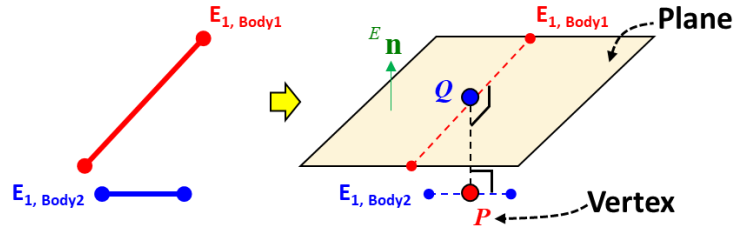


Figure 2-71. Collision pair: two edges.

### (3) Consideration of material properties

In section 2.6.2 (1), we insist that one of the advantages using a non-interpenetration constraint method is to consider material properties such as restitution and softness. This advantage is closely related to DELE (Eq. (49)) which is adopted for our equations of motion. The second row of DELE is rewritten as follows.

$$\mathbf{G}_k \mathbf{v}_{k+1} + \Gamma \frac{4\varepsilon}{h^3} \bar{\lambda}_{k+1} = -\frac{4\Gamma}{h} \mathbf{g}_k + \Gamma \mathbf{G}_k \mathbf{v}_k \quad (210)$$

If the right side of Eq. (210) is transposed to the left side, we obtain the following equation.

$$\mathbf{G}_k \mathbf{v}_{k+1} - \Gamma \mathbf{G}_k \mathbf{v}_k + \Gamma \frac{4\varepsilon}{h^3} \bar{\lambda}_{k+1} + \frac{4\Gamma}{h} \mathbf{g}_k = 0 \quad (211)$$

$$\mathbf{G}_k (\mathbf{v}_{k+1} - \Gamma \mathbf{v}_k) + \frac{4\Gamma}{h} \left( \varepsilon \frac{\bar{\lambda}_{k+1}}{h^2} + \mathbf{g}_k \right) = 0 \quad (212)$$

Eq. (212) is an identical equation. Therefore, the first and the second terms inside the bracket should be zero.



$$\mathbf{v}_{k+1} - \Gamma \mathbf{v}_k = 0 \quad (213)$$

$$\boldsymbol{\varepsilon} \frac{\bar{\lambda}_{k+1}}{h^2} + \mathbf{g}_k = 0 \quad (214)$$

The stabilization term ( $\Gamma$ ) in Eq. (213) is the ratio between the velocity before and after the collision, which is known as the restitution coefficient. If the regularization term ( $\boldsymbol{\varepsilon}$ ) in Eq. (214) is zero, the constraint is strictly satisfied. In other words,  $\boldsymbol{\varepsilon}$  allows the violation of the constraint, and decide the softness of the material when two bodies collide. The collision force is automatically obtained from DELE with respect to  $\Gamma$  and  $\boldsymbol{\varepsilon}$ .

The collision between the rigid bodies is affected by the several factors. However, we want to make the non-interpenetration constraint independent of weight and time step. This can be done by the regularization term  $\boldsymbol{\varepsilon}$ . For this, we can change Eq. (214) in the form of  $\bar{\lambda}_{k+1}$ .

$$\bar{\lambda}_{k+1} = -h^2 \boldsymbol{\varepsilon}^{-1} \mathbf{g}_k \quad (215)$$

$\bar{\lambda}_{k+1}$  is constraint force magnitude,  $\mathbf{g}_k$  is violation of the constraint which means the penetration depth. Therefore,  $-h^2 \boldsymbol{\varepsilon}^{-1}$  can be regarded as a spring coefficient ( $\mathbf{k}$ ). To determine the result independent of the time step ( $h$ ),  $\boldsymbol{\varepsilon}$  should be proportional to  $h^2$ . The collision force should be proportional to the weight to determine the value of  $\boldsymbol{\varepsilon}$  independent of the weight as shown in Figure 2-72. Therefore, the value of  $\boldsymbol{\varepsilon}$  should be inversely proportional to the weight.

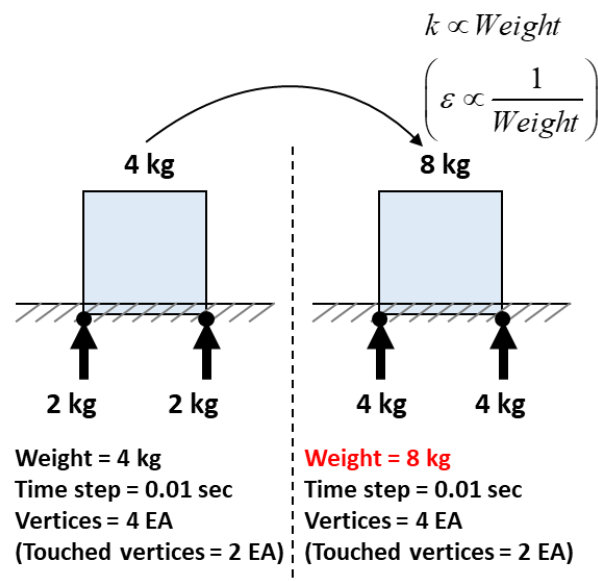


Figure 2-72. Spring coefficient proportional to the weight.

### 2.6.3. Dynamic analysis including collision detection and response

This section explains how to conduct the dynamic analysis, including collision detection and response algorithms, proposed in the previous sections. Figure 2-73 shows the numerical procedure for dynamic analysis, including collision detection and response. At first, we solve the equations of motion expressed by DELE. Then, we obtain a position, attitude, velocity, and acceleration of the bodies by the time integration. These results are used to calculate external forces for the next time. At the same time, the collision detection which is composed of two stages (broad-phase and narrow-phase) is conducted. Then, the collision response is executed using the collision pair data. The results from the collision response are used to formulate the constraint equation ( $\mathbf{g}_k$ ) and Jacobian ( $\mathbf{G}_k$ ) in the equations of motion. This procedure is repeated until the dynamic analysis is finished.

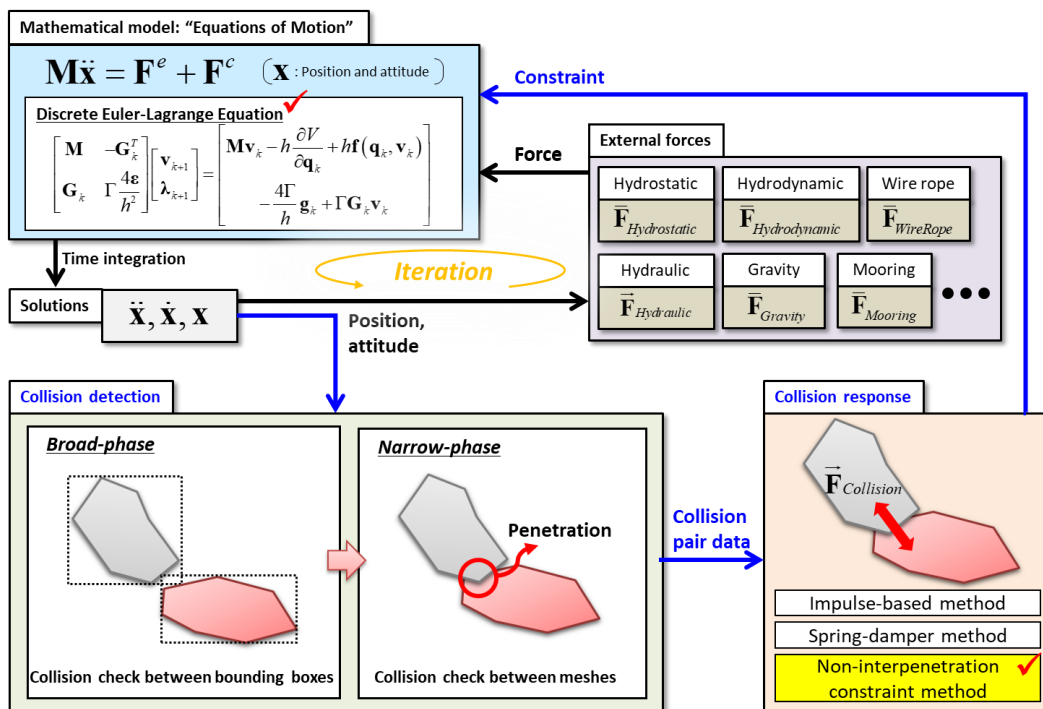


Figure 2-73. A numerical procedure for dynamic analysis including collision detection and response.

## 2.6.4. Case studies of collision detection and response

This section presents several case studies of the dynamic analysis including collision detection and response.

### (1) Collision for multibody system

It was explained in the previous section that the impulse-based method which directly changes the velocity was not applicable to the multibody system which has a kinematic constraint. In contrast to the impulse-based method, the force-based method is applicable to the multibody system. For the test, two bodies (Link A, Link B) are connected by ball joints, and the small box hits 'Link B,' as shown in Figure 2-74.

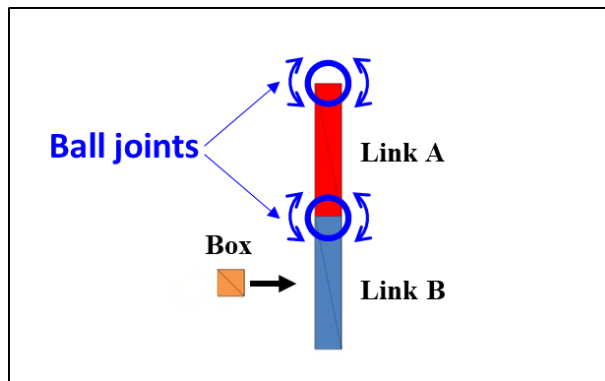


Figure 2-74. Collision test model for the multibody system.

When the box hits 'Link B,' the kinematic constraint between 'Link A' and 'Link B' is violated because the velocity of 'Link B' is compulsively changed (See Figure 2-75-(1)). Therefore, the enormous constraint force is exerted to fix the kinematic constraint, and the system diverges (See Figure 2-75-(2)).

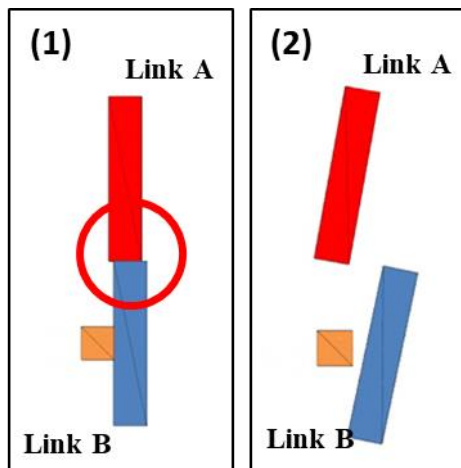


Figure 2-75. Test results using the impulse-based method.

Meanwhile, in case of using the force-based method, it is successfully simulated without divergence of the system, as shown in Figure 2-76.

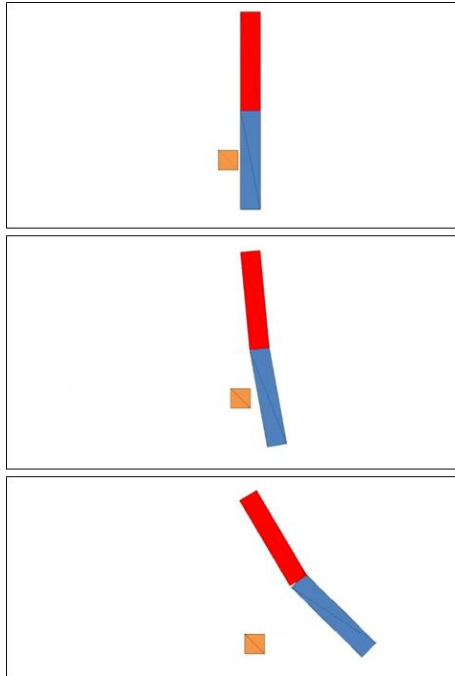


Figure 2-76. Test results using the force-based method.

The next examples are to drop two links connected by ball joint on the plate. The link is 10 m length, and 1 ton. Their initial tilt angles are different as shown in Figure 2-77.

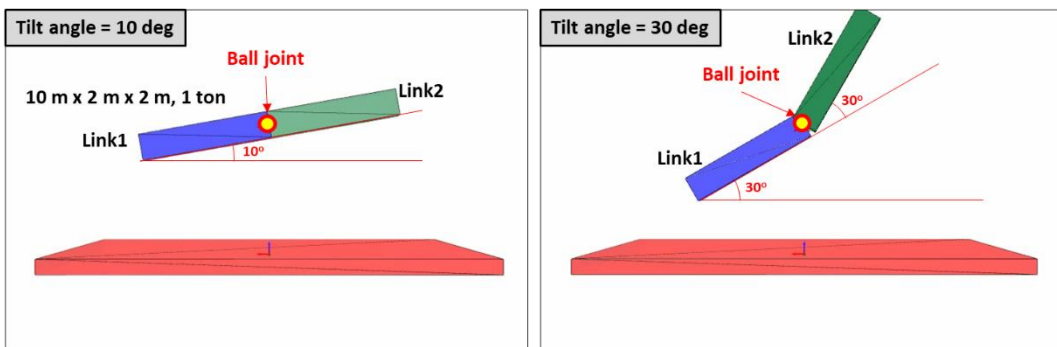


Figure 2-77. Dropt two links connected by ball joint.

The simulation results are depicted in Figure 2-78. The collision is successfully conducted even though there are the constraint between two bodies.

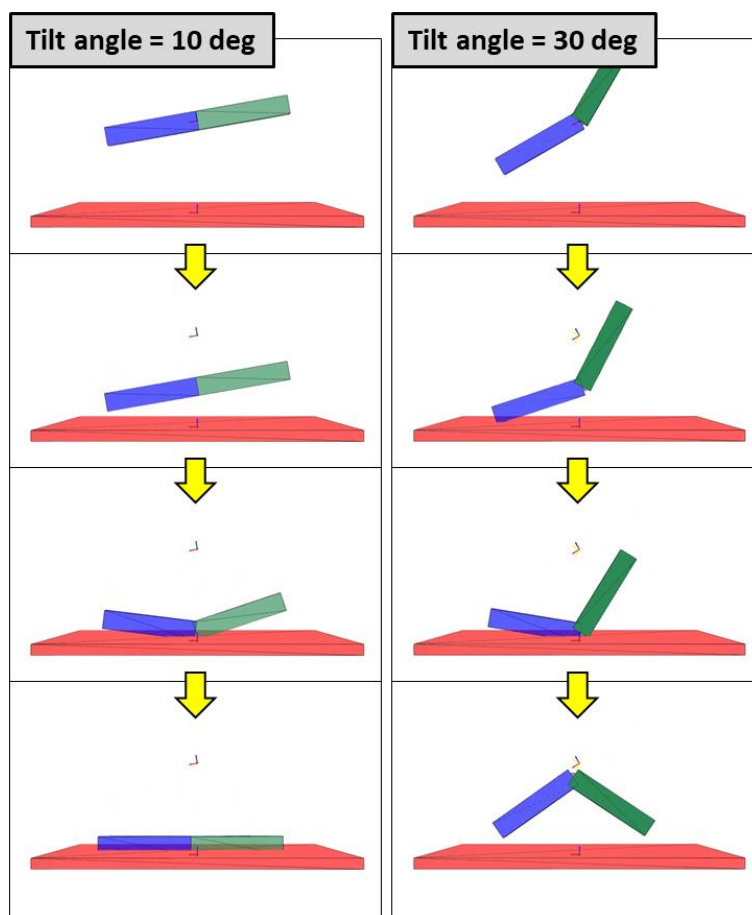


Figure 2-78. Collision test of multibody system.

Furthermore, the collision forces of the two links are calculated as shown in Figure 2-79.

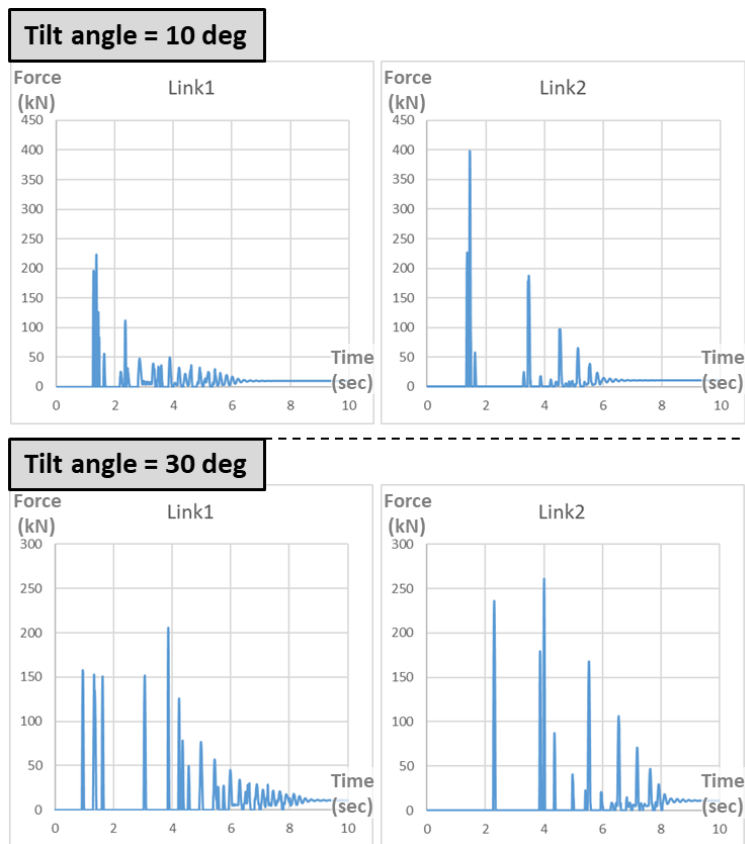


Figure 2-79. Collision force of two links.

## (2) Performance tests of collision detection

The first test is to check the collision between two bunny models, as shown in Figure 2-80. The bunny model contains 292 meshes and 148 vertices.

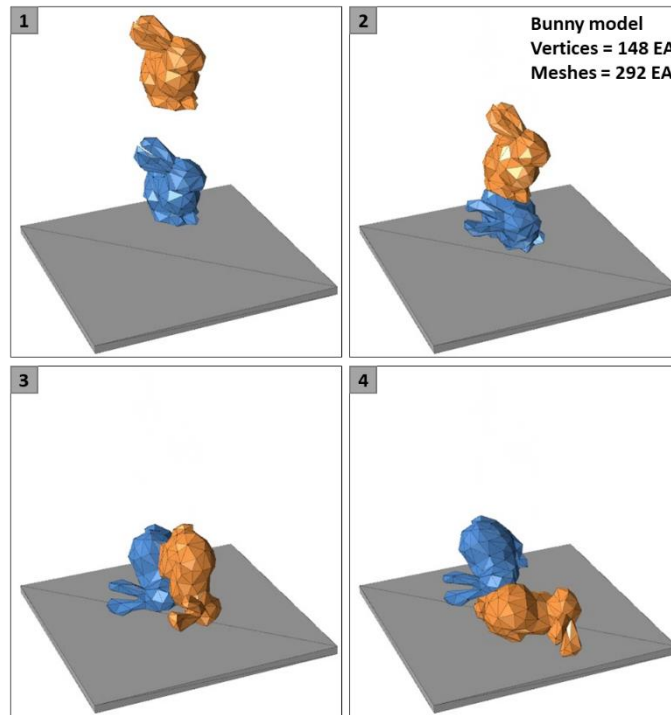


Figure 2-80. Performance test: Collision between two bunny models.

The computing time is compared with and without applying BVH. The results are summarized in Table 2-3. We set the leaf node of BVH which has less than eight meshes. As a result, the computing time for the one-time step decreased about 95 %. Total computing time is also decreased about 77 %. Total computing time and one-time step are not the same because total computing time includes the time when the collision between two bunnies does not occur.

Table 2-3. Comparison of computing times: With and without BVH.

		Without BVH	With BVH	Ratio
Simulation time		10 sec		-
Computing time	One-time step	94 msec	5 msec	95 % ↓
	Total time	30 sec	7 sec	77 % ↓



The second test is to drop two bunny models on the plane (Figure 2-81). In this case, the meshes of right bunny model staying out of the collision is excluded using the exclusion box. The right bunny model contains 172 meshes and 87 vertices.

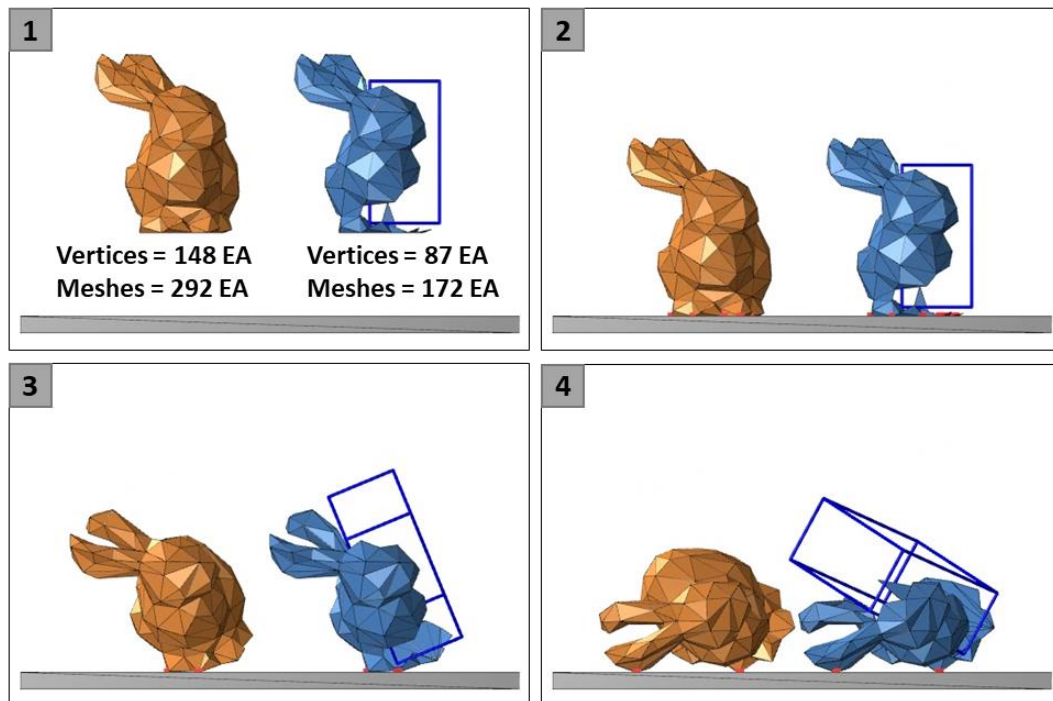


Figure 2-81. Performance test: Drop two bunny models on the plane.

We compared the computing time with and without applying the exclusion box. The results are summarized in Table 2-4. The result shows that the computing time for a one-time step is also reduced about 57% as the number of meshes is reduced to about 60%. Total computing time is also decreased by 33 %.

Table 2-4. Comparison of computing time: With and without exclusion box.

		Without exclusion box (292 meshes)	With exclusion box (172 meshes)	Ratio
Simulation time		10 sec		-
Computing time	One-time step	7 msec	3 msec	57 % ↓
	Total time	3.3 sec	2.2 sec	33 % ↓

The third test is to drop the LPG tank model on the plane to check the performance using both the exclusion box and the BVH at the same time, as shown in Figure 2-82. The original LPG tank model contains 19,232 meshes and 57,696 vertices.

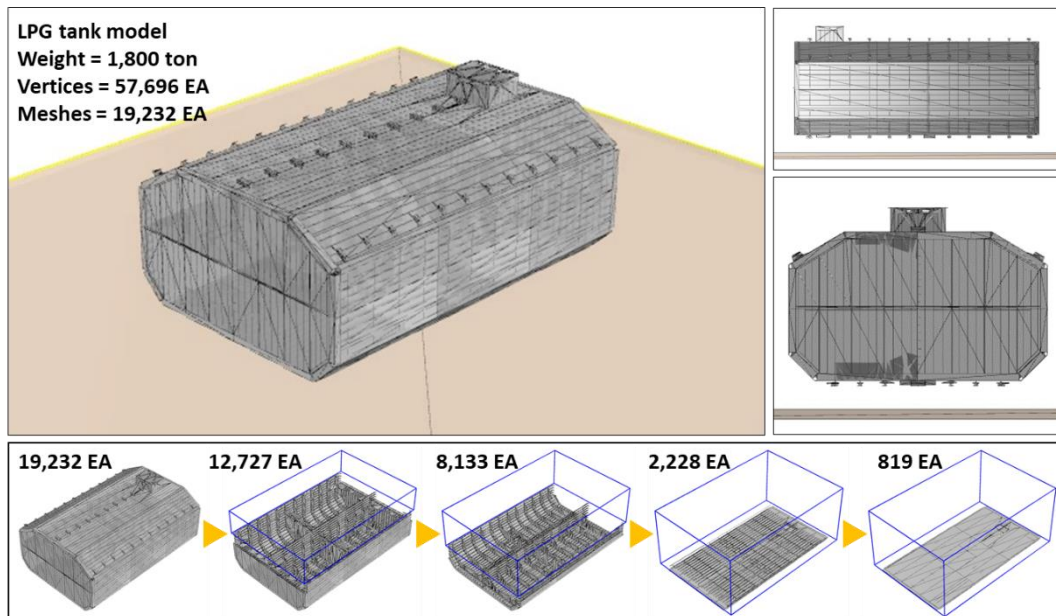


Figure 2-82. Performance test: Drop LPG tank model on the plane.

The results are summarized in Table 2-5, and computation time is depicted by graphs in Figure 2-83. When applying only BVH, the computing time is reduced by 62 %. As the

number of meshes is reduced, the computing time is also reduced from 75% to 98 %. In conclusion, both BVH and the exclusion box are effective to increase the performance of the collision detection.

Table 2-5. Comparison of computing time: Both exclusion box and BVH.

		Without BVH	With BVH				
		Full meshes (19,232)	Full meshes (19,232)	Exclusion box			
			(12,727)	(8,133)	(2,228)	(819)	
Simulation time		5 sec					
Computing time	One-time step	800 msec	300 msec	200 msec	100 msec	30 msec	15 msec
		100 %	62.5 % ↓	75.0 % ↓	87.5 % ↓	96.3 % ↓	98.1 % ↓
	Total time	356.6 sec	139.0 sec	92.3 sec	45.0 sec	10.1 sec	4.7 sec
		100 %	61.0 % ↓	74.1 % ↓	87.4 % ↓	97.2 % ↓	98.7 % ↓

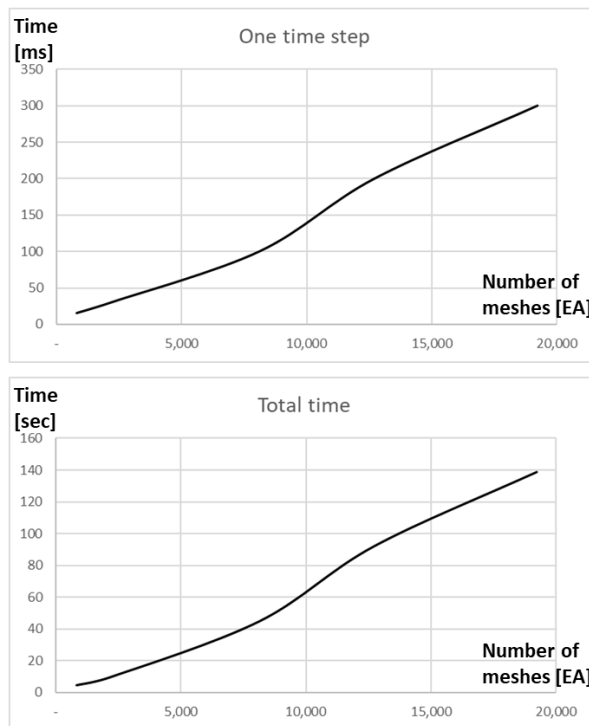


Figure 2-83. Graphs of computing time of dropping LPG tank model on the plane.

### (3) Collision between complex shapes

The model exported from the ship CAD system has very complex shapes, as shown in Figure 2-84, and Figure 2-85. Both LPG tank and hull structure models have many unenclosed meshes. Furthermore, stiffeners attached to the side shell is very sharp.

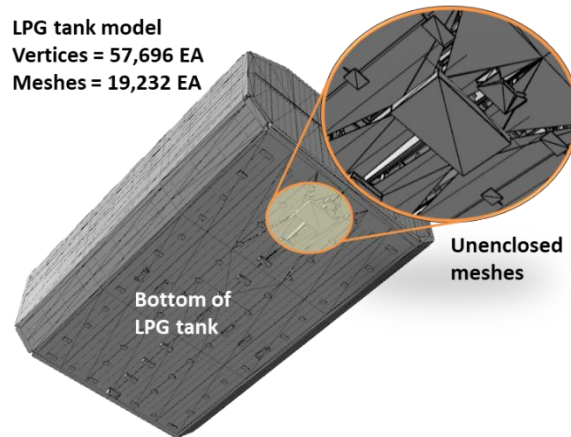


Figure 2-84. Example of complex shape: LPG tank.

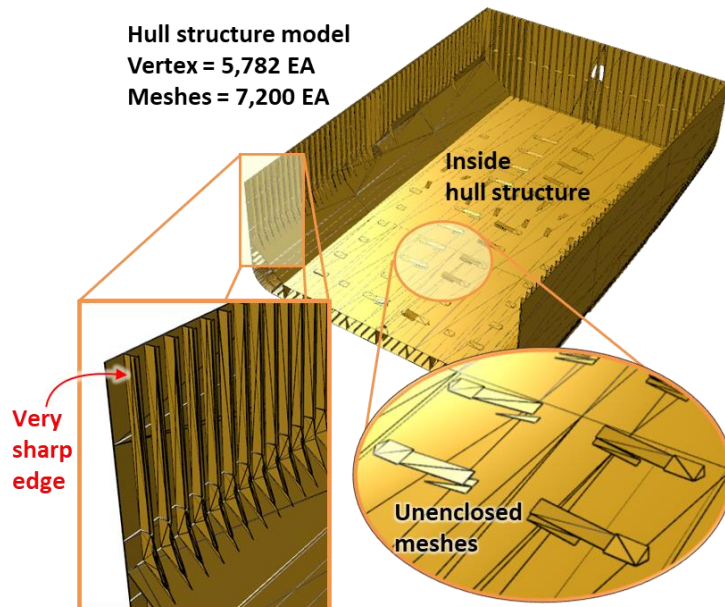


Figure 2-85. Example of complex shape: Hull structure.

We simply drop the LPG tank inside the hull structure. Two simulations are conducted in the case that the tank was not tilted and the case that it was tilted for 20 degrees, as shown in Figure 2-86. In spite of the unenclosed meshes and very sharp edges, the collision detection and response between two models are successfully performed.

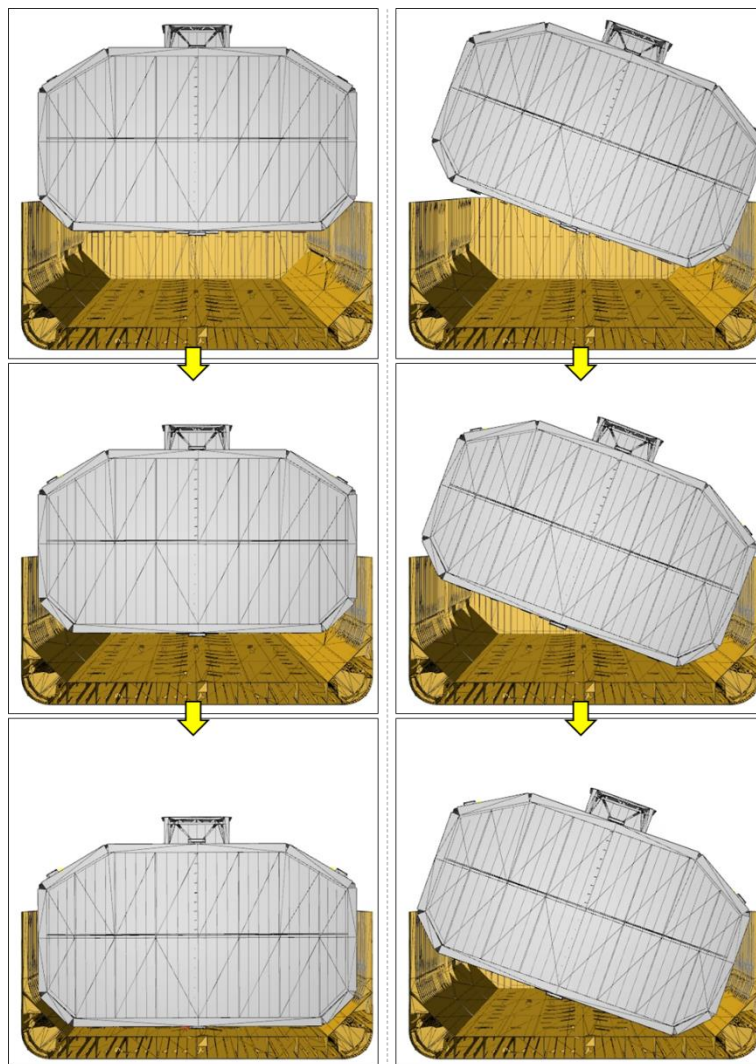


Figure 2-86. Collision test between complex shapes.

#### (4) Collision according to material properties

It was explained in section 2.6.2 that DELE, using non-interpenetration constraint, could consider material properties such as the restitution coefficient and softness. At first, the box drops on the plane according to different restitution coefficients, as shown in Figure 2-87. Collision test according to restitution coefficients. We choose the restitution coefficient as 0.0 (perfectly inelasticity), 0.5, and 1.0 (perfectly elasticity). The results are depicted as graphs in Figure 2-88. Position and velocity according to restitution coefficient. When the restitution coefficient is zero, the velocity is directly changed to zero right after the collision. When the restitution coefficient is 0.5, the velocity is reduced to half after the collision. When the restitution coefficient is one, the velocity before and after the collision is almost the same.

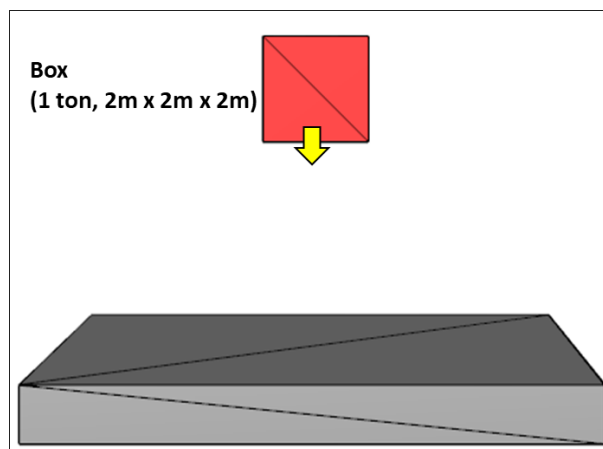


Figure 2-87. Collision test according to restitution coefficients.

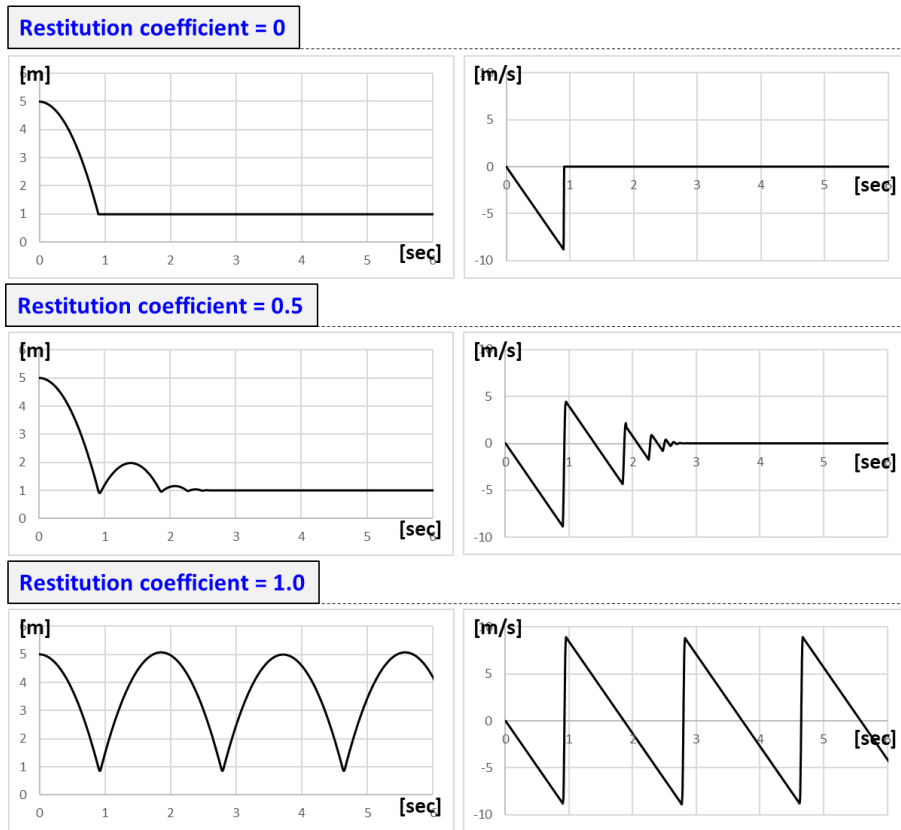


Figure 2-88. Position and velocity according to restitution coefficient.

To check the effect of the softness, the restitution coefficient is fixed to 0.8, and we change the softness by 1, 10, and 50. Due to the softness, the penetration depth is changed by 0.11, 0.35 and 0.84.

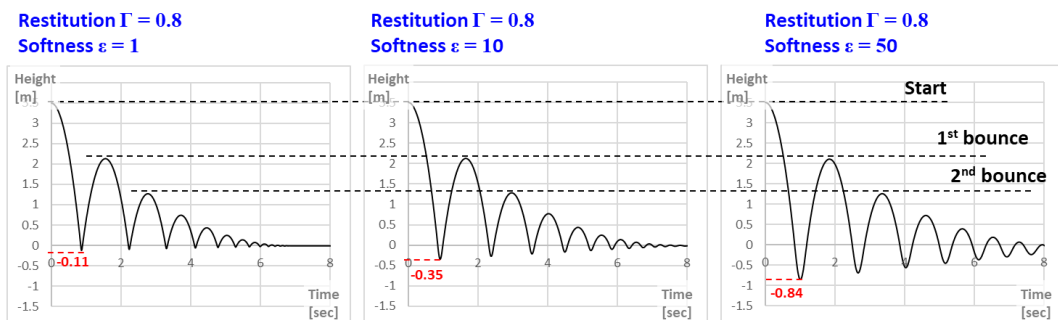


Figure 2-89. Position according to softness of the material.

### (5) Comparison with open source program

One of the famous open source library (Bullet [18]) is tested by colliding two objects. One of the object has unenclosed meshes as shown in Figure 2-90.

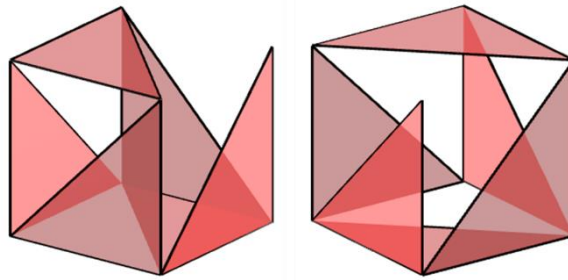


Figure 2-90. Unenclosed meshes for testing collision by Bullet.

A small box which color is blue is dropped on the box which has unenclosed meshes. Bullet shows unexpected motion such as stuck when the dropped box touches the edge on the other box. On the other hand, the proposed method shows good quality of the motion after collision.



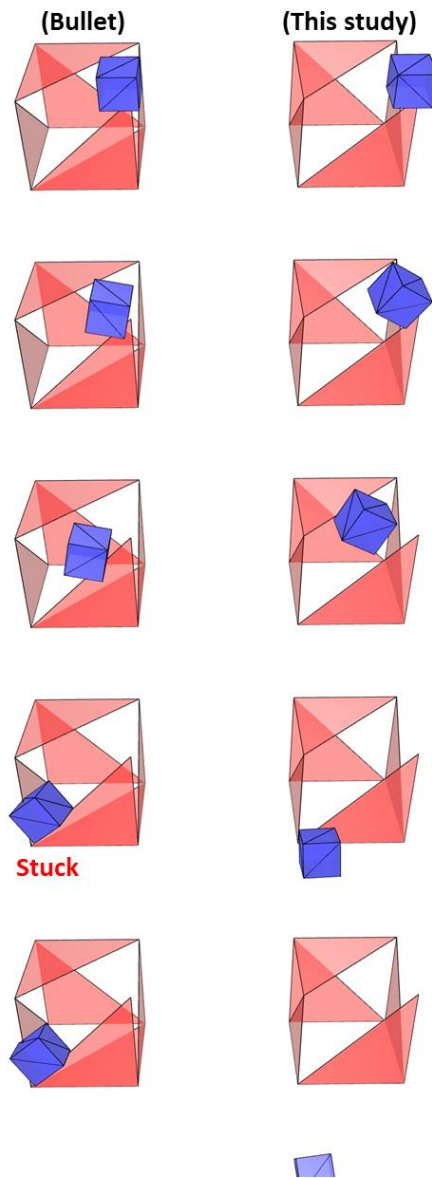


Figure 2-91. Comparison of collision with open source program (Bullet).

### 2.6.5. Consideration of impulse and impulsive force

An impulsive force is a large force exerted during a small interval of time when two objects collide. An impulse is integral of an impulsive force over the time interval which it

acts. The impulse is defined by the difference the momentum before and after the collision.

$$\text{Impulse} = \int_{t_1}^{t_2} F dt = mv'_1 - mv_1 \quad (216)$$

When the object hits the ground, the object experiences the compression and expansion within a very short time. During this duration, the velocity of the object is changed. The impulsive force and velocity graphs in the real collision are described in Figure 2-92.

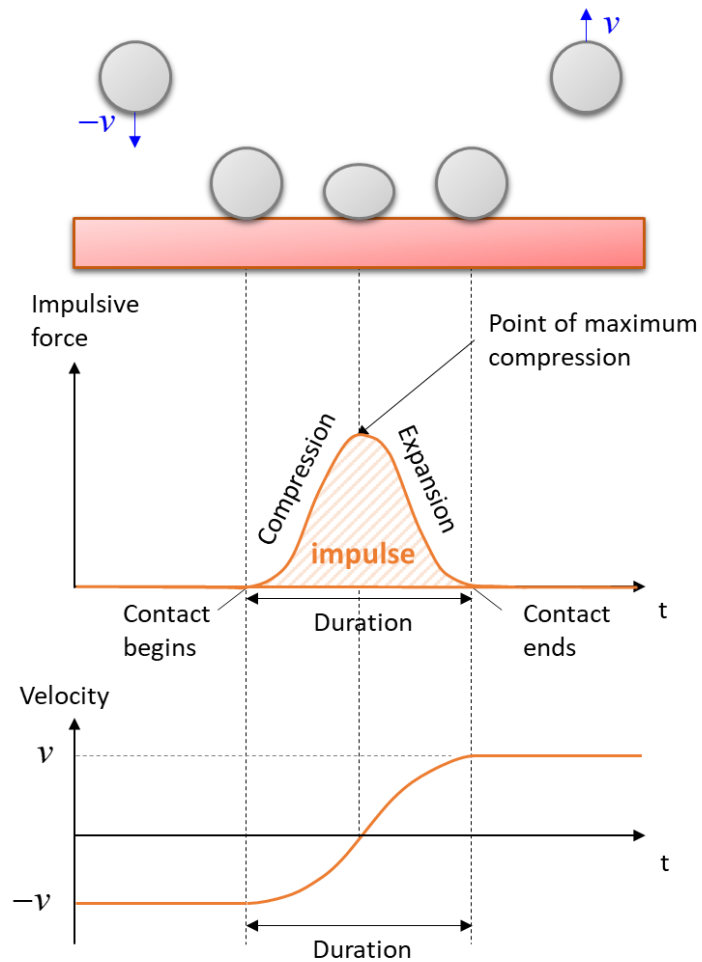


Figure 2-92. Compression and expansion in the real collision.

If the restitution is same, the difference of the momentum should be the same. This means that the impulse is also same. However, the impulsive force can be different from the other if the duration of the collision time is different. Therefore, we can divide the collision by three types such as hard, medium, and soft collisions as shown in Figure 2-93.

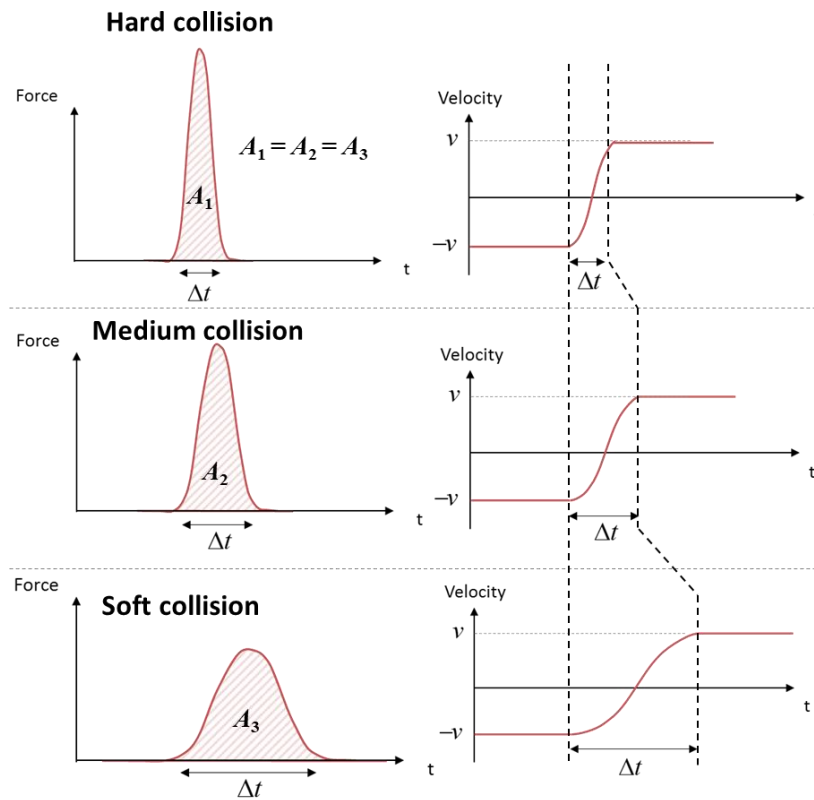


Figure 2-93. Hard, medium, and soft collisions.

The key factor which is closely related to the collision time is the softness which is adjusted by the parameter  $\epsilon$ . For example, the boxes which has same restitution, but different softness factors such as 1, 10, and 50 are dropped on the plane. The impulsive forces when the boxes hit the ground at the first time is depicted by graphs in Figure 2-94.

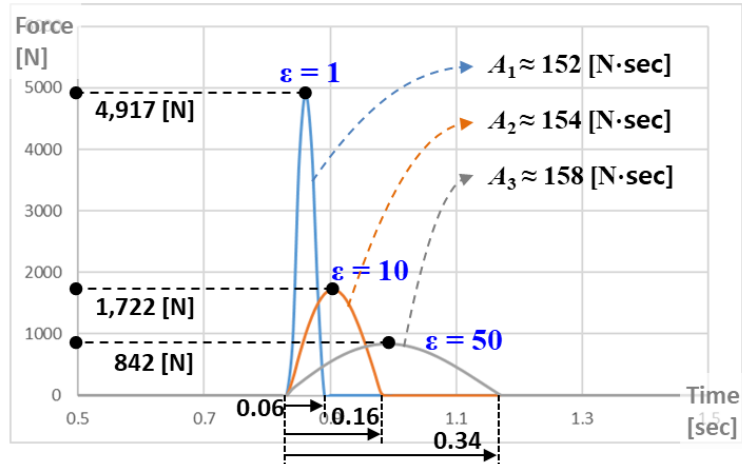


Figure 2-94. Graphs of impulsive forces when the three boxes with different softness drop on the plane.

The graphs shows that the maximum impulsive forces are different, but the area is almost same. The impulse is simply expressed by multiplying the impulsive force and the collision time.

$$mv' - mv = \int_{t_1}^{t_2} F dt \approx F \cdot \Delta t \quad (217)$$

Therefore, the impulsive force is obtained as follows.

$$F = \frac{mv' - mv}{\Delta t} \quad (218)$$

In this case, the force graph looks like a step function. However, the shape of the graph of the impulsive force is similar to triangle rather than a step. Therefore, we can be

estimated by the maximum impulsive force by multiplying 2.

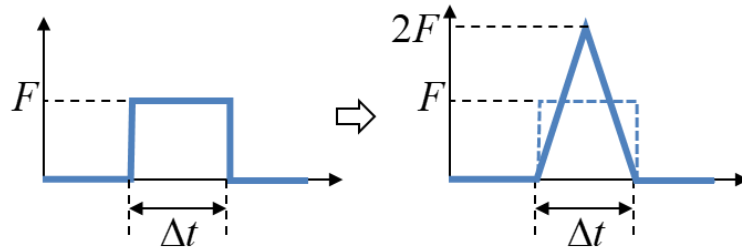


Figure 2-95. Estimation of impulsive force.

The estimation of the impulsive force are summarized in Table 2-6. The numerical solution shows almost same value to the estimated value.

Table 2-6. Estimation of impulsive forces

$\varepsilon$	$m$ [kg]	$\Delta t$ [sec]	$v$ [m/s]	$v'$ [m/s]	$F$ [N]	$2F$ [N]
1	10	0.06	8.2	6.5	2,450	4,900
	Numerical solution					4,917
	Error (%)					0.3%
10	10	0.17	8.2	6.5	865	1,730
	Numerical solution					1,722
	Error (%)					-0.4%
50	10	0.34	8.2	6.5	432	864
	Numerical solution					842
	Error (%)					-2.7%

## 2.7. Modeling of Equalizer

### 2.7.1. Real mechanism of the equalizer

Figure 2-96 shows how the fixed and moving pulleys are assembled. The equalizer is connected under the hook of the crane. Inside the equalizer, several fixed and moving pulleys are placed by turns. All of the pulleys are connected by a single wire rope, which should have the same tension anywhere in its length. Thus, if the tension is denoted by  $T$ , all of the moving pulleys are exerted by  $2T$  from the equalizing wire rope.

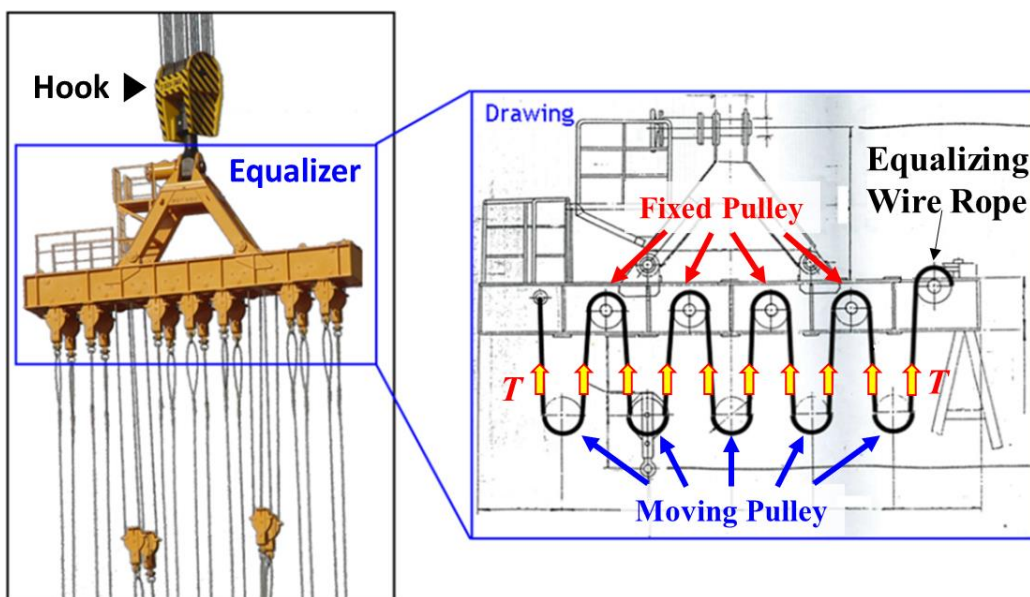


Figure 2-96. Internal structure of the equalizer.

Figure 2-97 shows how the wire rope tensions connected to the moving pulleys and the load are adjusted. It is assumed that only three moving pulleys,  $p_0$ ,  $p_1$ , and  $p_2$ , are connected, and their tensions are denoted by  $f_0$ ,  $f_1$ , and  $f_2$ , respectively. At the first time point,  $f_1$  is acting on the middle moving pulley  $p_1$ ; however, the others are still zero (Figure 2-97-(a)).

As  $p_1$  is the only moving pulley where a force is exerted,  $p_1$  starts to move down. Due to the equalizing wire rope, the other two pulleys –  $p_0$  and  $p_2$  – move up simultaneously. Sometime later,  $f_0$  which is larger than  $f_1$  is acting on  $p_0$ . To make the tension equal,  $p_0$  moves down, and the other two pulleys move up (Figure 2-97-(b)). As  $f_1$  is larger than  $f_2$ , the moving distance of  $p_2$  is larger than that of  $p_1$ . Until all of the wire rope tensions –  $f_1, f_2$ , and  $f_3$  – are exactly same, the pulleys are repeatedly moving up and down. Finally, they stop moving when all the wire ropes have the same tension (Figure 2-97-(c)).

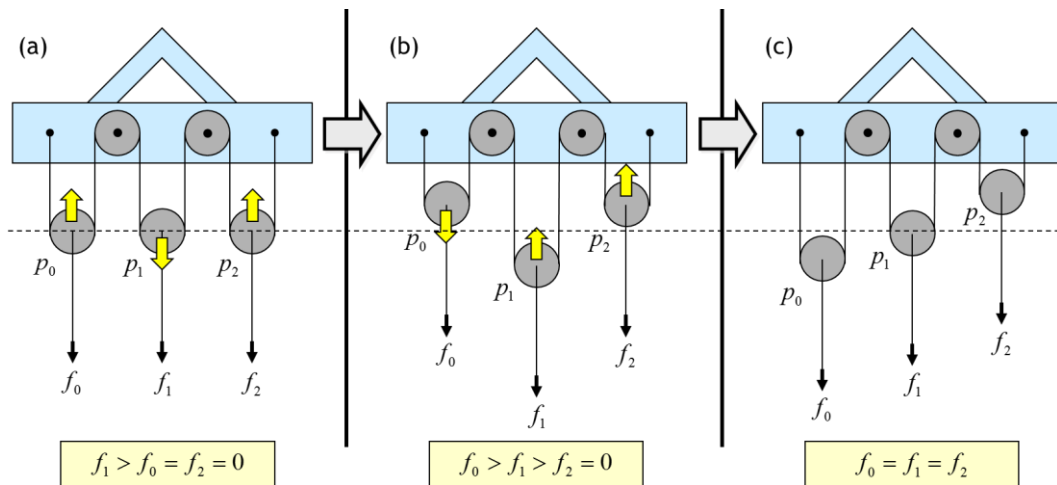


Figure 2-97. Procedure of the adjustment of tensions acting on wire ropes through the equalizer.

## 2.7.2. Modeling of pulleys and the equalizer

A constraint-based wire rope defined in Section 2.4.7 can be applied to make fixed and moving pulleys. Figure 2-98 shows an example of fixed and moving pulleys using the constraint-based wire rope. If the total length is denoted as  $l_{total}$ , the total length is equal to the sum of the segments between the fixed and moving pulleys, and the circumference of the pulleys.

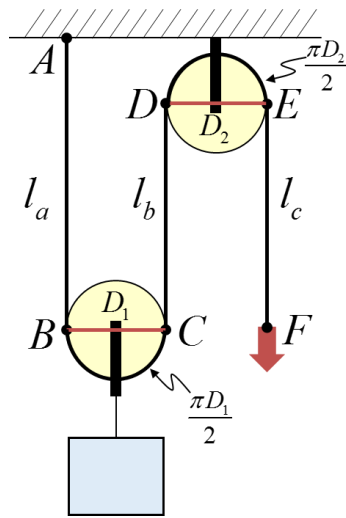


Figure 2-98. Fixed and moving pulleys using the constraint-based wire rope.

Thus, the constraint equation of the wire rope connecting the fixed and moving pulleys in the above example is given by:

$$\begin{aligned}
 g(\mathbf{q}) &= \left( l_a + l_b + l_c + \frac{\pi D_1}{2} + \frac{\pi D_2}{2} \right) - l_{total} \\
 &= \left( |\mathbf{r}_A - \mathbf{r}_B| + |\mathbf{r}_C - \mathbf{r}_D| + |\mathbf{r}_E - \mathbf{r}_F| + \frac{\pi D_1}{2} + \frac{\pi D_2}{2} \right) - l_{total} = 0
 \end{aligned} \tag{219}$$

The equalizer can be realized by a combination of several fixed and moving pulleys, as shown in Figure 2-99.



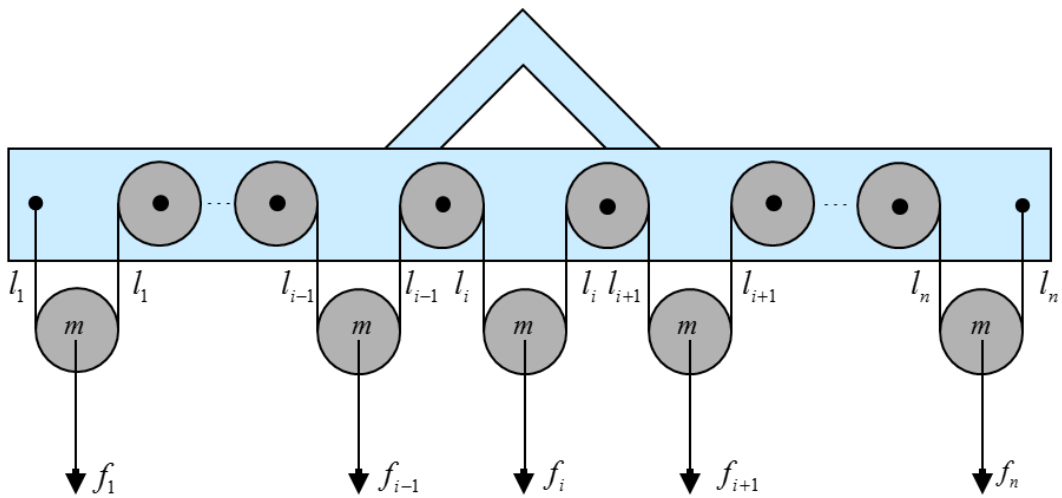


Figure 2-99. Arrangement of fixed and moving pulleys of the equalizer.

If there are a number of  $n$  moving pulleys with the same diameter  $D$ , the constraint equation of the equalizing rope can be written as a given equation:

$$g(\mathbf{q}) = \left( \sum_{i=1}^m 2l_i + m \frac{\pi D}{2} \right) - l_{total} = 0 \quad (220)$$

### 2.7.3. Case studies

This section presents two test cases to validate the mathematical model explained in the previous section. One involves several fixed and moving pulleys, and the other is an equalizer.

#### (1) Pulleys

This test case uses pulleys with a constraint-based wire rope. The purpose of this case is to show that the constraint-based wire rope can model fixed and moving pulleys, as

explained in Section 2.7.2. Figure 2-100 shows two fixed pulleys and two moving pulleys. One end of a wire rope is attached to the fixed body, and the other is attached to a box of 11 kg weight.

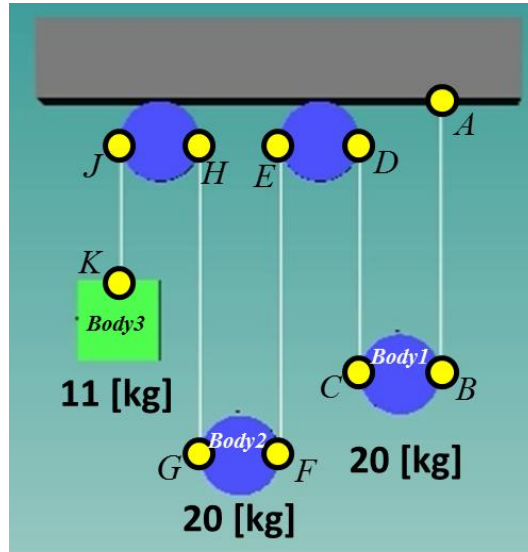


Figure 2-100. Modeling of moving and fixed pulleys with a wire rope constraint.

From Eq. (219), we obtain the constraint equation  $\mathbf{g}$  and its derivative  $\mathbf{G}$  of the wire rope constraint as follows:

$$\mathbf{g}_k = |\mathbf{r}_A - \mathbf{r}_B| + |\mathbf{r}_C - \mathbf{r}_D| + |\mathbf{r}_E - \mathbf{r}_F| + |\mathbf{r}_G - \mathbf{r}_H| + |\mathbf{r}_J - \mathbf{r}_K| - l_{total} = 0 \quad (221)$$

$$\mathbf{G}^T = \begin{bmatrix} -\mathbf{n}_{AB} + \mathbf{n}_{CD} \\ (\mathbf{n}_{AB} \times \mathbf{r}_{B/G1}) - (\mathbf{n}_{CD} \times \mathbf{r}_{C/G1}) \\ -\mathbf{n}_{EF} + \mathbf{n}_{GH} \\ (\mathbf{n}_{EF} \times \mathbf{r}_{F/G2}) - (\mathbf{n}_{GH} \times \mathbf{r}_{G/G2}) \\ -\mathbf{n}_{JK} \\ \mathbf{n}_{JK} \times \mathbf{r}_{K/G3} \end{bmatrix} \quad (222)$$

where,  $\mathbf{r}_{B/G1}$  is the vector from the center of gravity of *Body1* to point *B* in the inertial frame, and  $\mathbf{n}_{ij} = \frac{\mathbf{r}_i - \mathbf{r}_j}{|\mathbf{r}_i - \mathbf{r}_j|}$  is the normal vector from the point *i* to the point *j*.

Because the weight of each pulley is set to 20 kg, the box starts to move downward, whereas the moving pulleys move upward, as shown in Figure 2-101.

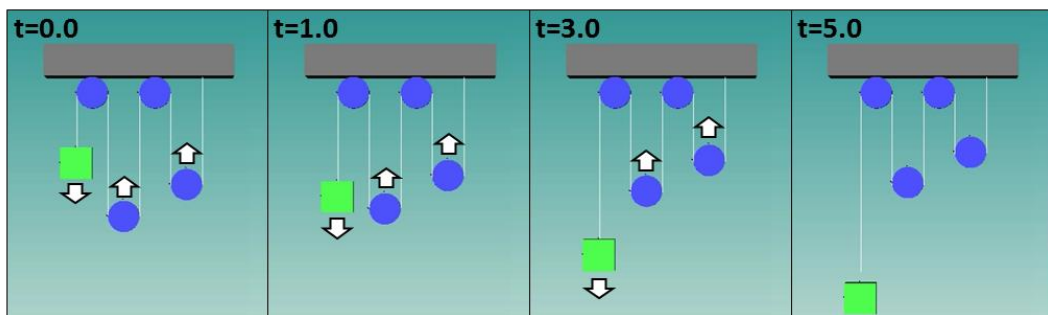


Figure 2-101. Simulation result of moving and fixed pulleys with the constraint-based wire rope.

## (2) Equalizer

This test case shows the modeling of the equalizer and the wire rope tension adjusted equally by the real mechanism, as explained in Section 2.7.1.

By adding more fixed and moving pulleys, we can construct an equalizer. For example, an equalizer with five moving pulleys is modeled, as shown in Figure 2-102. The hook and the equalizer are connected by hinge joints, where the rotating axis is aligned to the vertical vector. The sheave diameter of the moving pulleys is 0.8 m. The main dimensions of the equalizer are indicated in Figure 2-102.

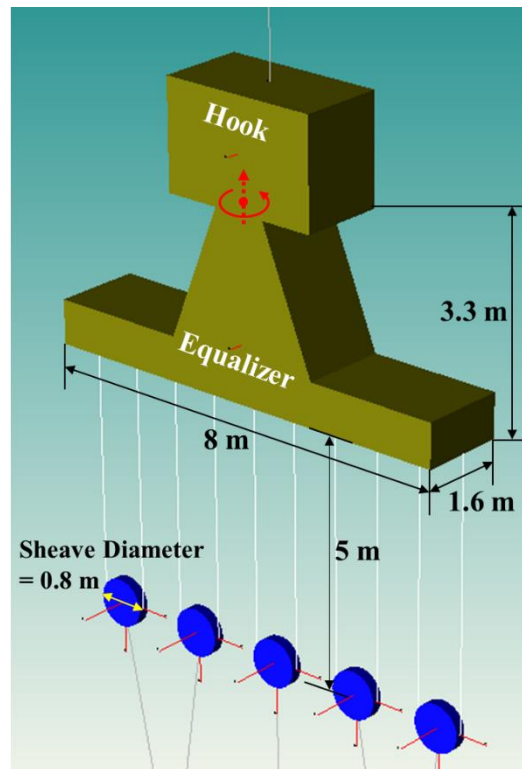


Figure 2-102. Modeling of the equalizer.

To test the mechanism of the equalizer, a simple load was lifted with one equalizer. Figure 2-103 shows the modeling of the equalizer test case and connections between the equalizer and the load. The load is assumed to be a  $10 \times 10 \times 5$  m box, with a weight of 300 ton. To check the equalizing process, the initial length of each wire rope is set at 23 m or 26 m.

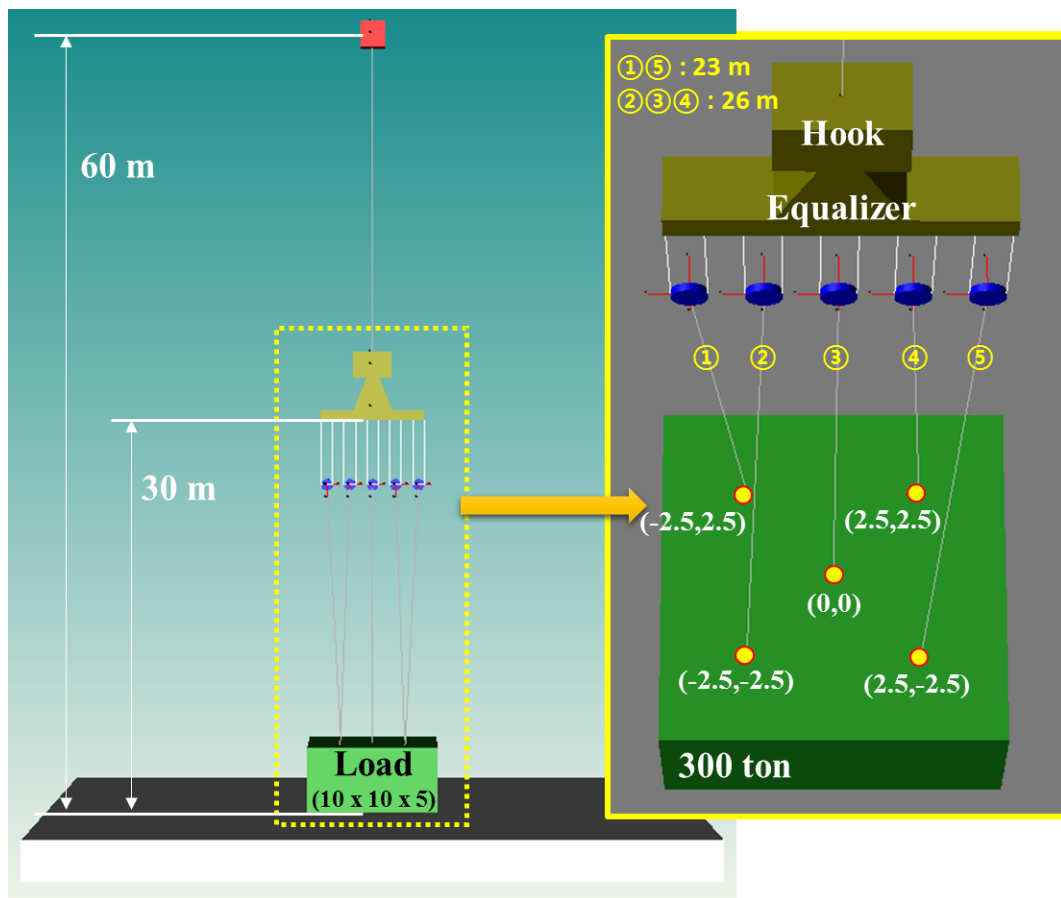


Figure 2-103. Modeling of connections between the equalizer and the load.

The motion of the equalizer and the load are shown in Figure 2-104. Because 'Line1' and 'Line5' are shorter than the others, wire rope tensions are acting on the sheaves connected by 'Line1' and 'Line5' at the first time point. Due to these tensions, the sheaves start to move up and down. The motions of the sheaves are enlarged in Figure 2-105. In addition, we can also see that the equalizer is rotated due to the hinge joint, which is used to connect the equalizer and the hook.

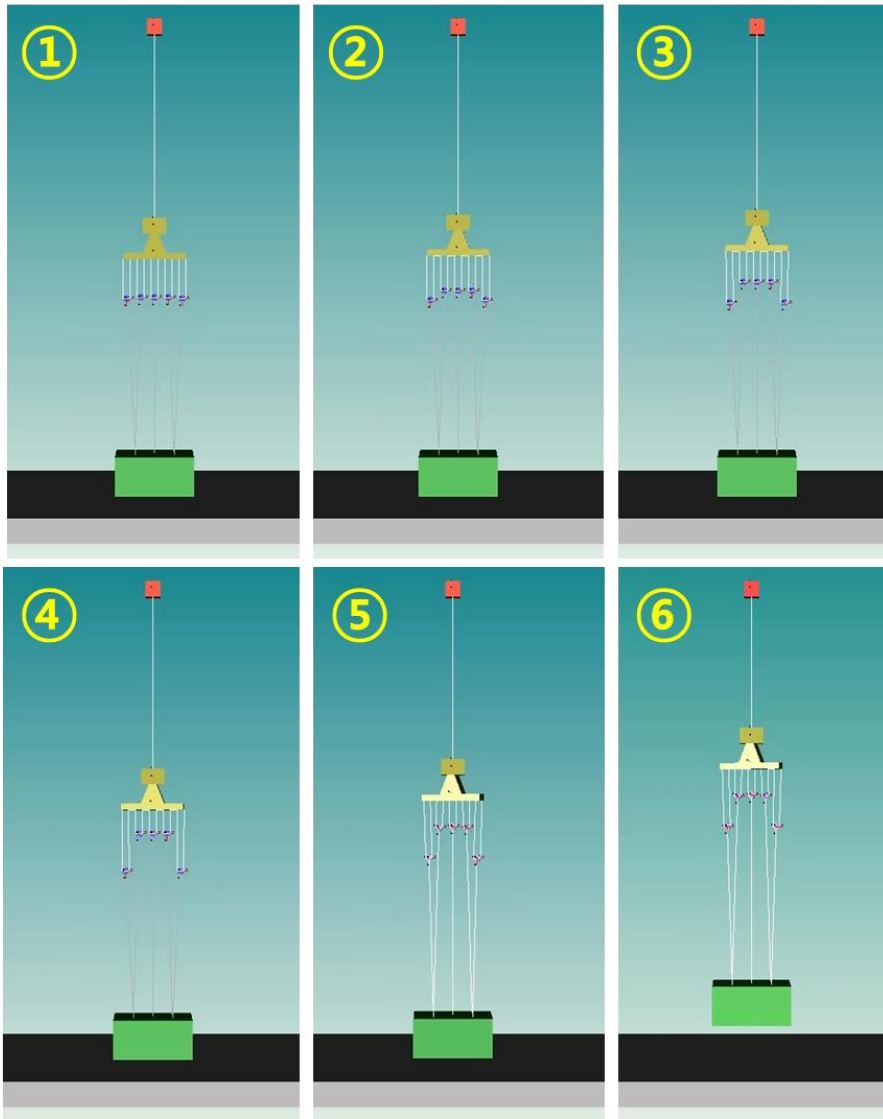


Figure 2-104. Simulation result: Motion of the equalizer and the load.

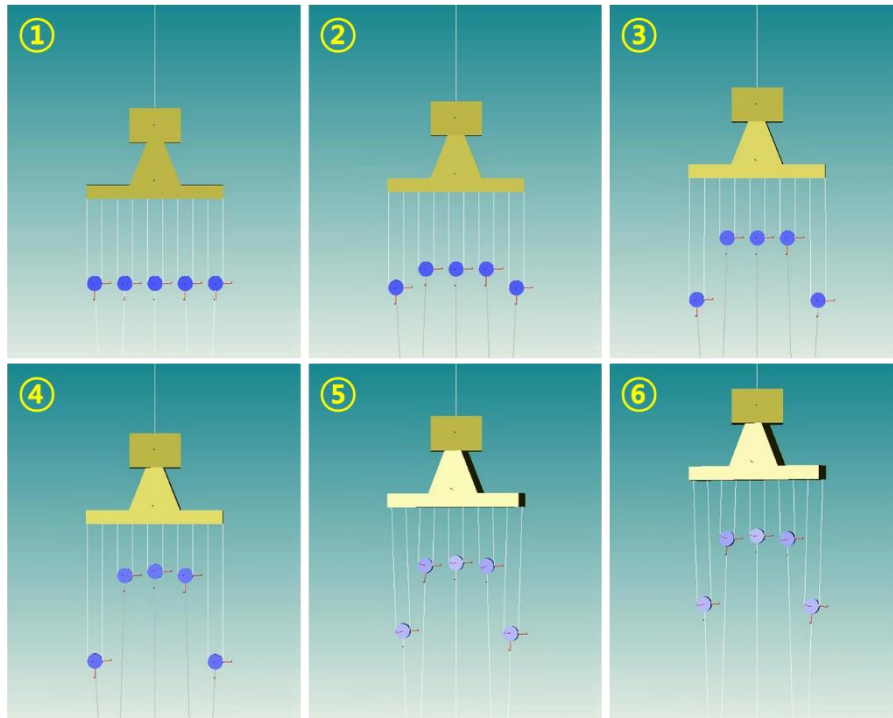


Figure 2-105. Simulation result: Motion of the sheaves in the equalizer.

Figure 2-106 shows the wire rope tensions of ‘Line1’, ‘Line2’, ‘Line3’, ‘Line4’, and ‘Line5’. If one of the tensions is larger or smaller than the others, the length is shortened or extended to adjust the tension equally. Finally, all of the wire rope tensions become equal.

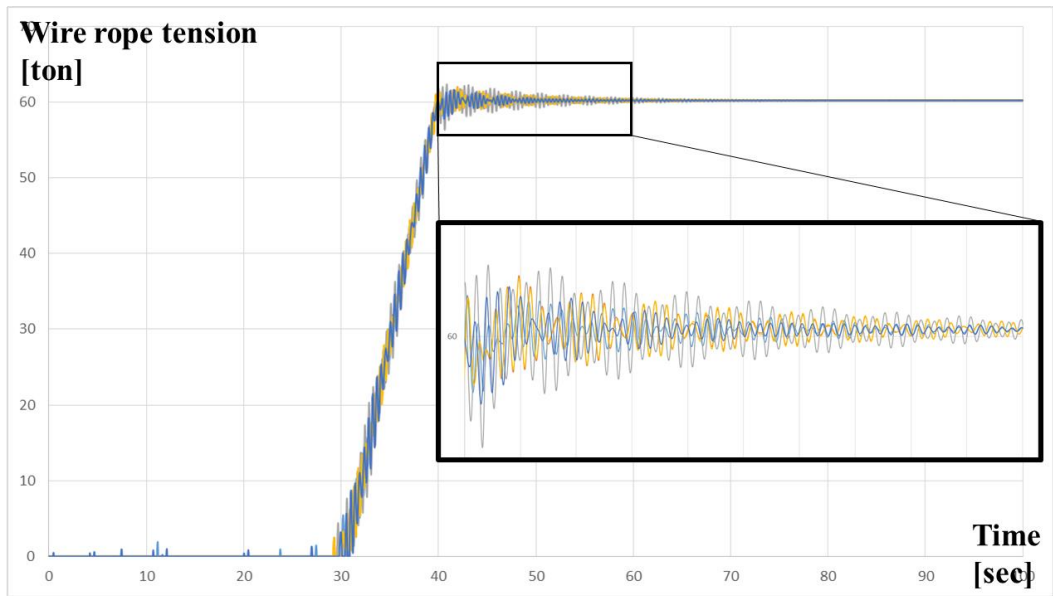


Figure 2-106. Graphs of wire rope tensions between the load and the equalizer.



## 2.8. Modeling of Self-propelled modular transporter (SPMT)

### 2.8.1. Modeling of SPMT and axle compensation mechanism

The SPMT is a platform vehicle with a large array of wheels that is used for transporting massive objects from one location to another. Several SPMTs can be connected with others as if they are just one body. The dimensions and loads of the SPMT are summarized in Table 2-7 [59].

Table 2-7 Dimensions and loads of the SPMT.

KAMAG modular transporter		Type 2406
Dimension	Length	8,400 mm
	Breadth	2,430 mm
	Height	1,490 ± 350 mm
Load	Max. weight	240 ton
	Dead weight	24.3 ton
	Max. capacity	215.7 ton
	No. of wheel	12 EA
	Max. wheel capacity	20 ton

As shown in Figure 2-107, the platform and wheels are connected by bogies, which are composed of hydraulic cylinders and other mechanical parts. The power pack supplies hydraulic powers to the hydraulic cylinders to lift the platform up. The hydraulic force can be modeled by the compressible springs, which are resisted only when they are compressed (Figure 2-107). Meanwhile, the hydraulic cylinder can be modeled by the slider joint. The wheel is connected by hinge joints at the bottom of the hydraulic cylinder. Slider and hinge joints restrict five among six degrees of freedom, respectively. If the slider and hinge joints

are modeled separately, the matrix to solve in the equations of motion is increased by ten per one hydraulic cylinder and wheel set. Therefore, a slider-hinge joint that has two degrees of freedom is used to connect the wheel and the platform. This increases the size of the equation matrix by four rather than ten per one wheel of the SPMT.

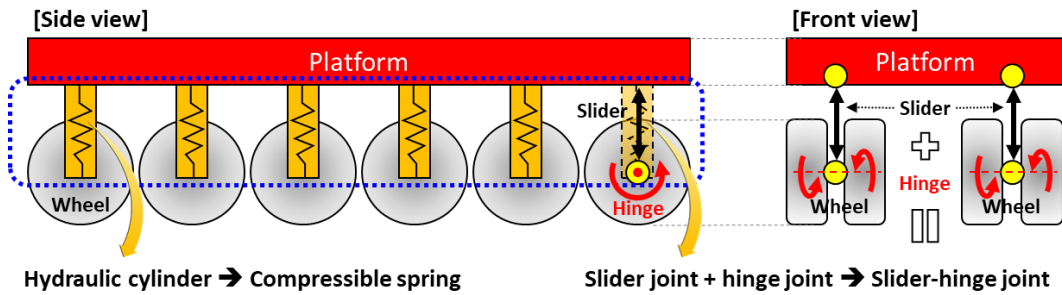


Figure 2-107. Modeling of the SPMT.

Hydraulic cylinders can be tied into three or four suspension groups (Figure 2-108). The hydraulic axle compensation shall guarantee equal loads on each group, independent of the road conditions. Each hydraulic cylinder acts as a cushion when the SPMT drives over an uneven roadway. If the SPMT drives over a bump in the road, the wheels lift up and down.

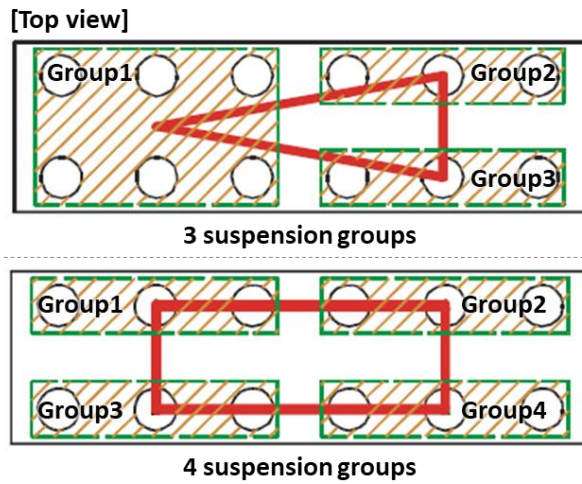


Figure 2-108. Hydraulic suspension groups.

Figure 2-109 shows the compensation mechanism in detail. For example, one SPMT lifts the block, whose weight is 90 tons, and the wheels are divided into two groups (Figure 2-109-(1)). Since the center of gravity of the block is located at the front side, the loads acting on the groups are different. The hydraulic force of groups 1 and 2 are 10 and 20 tons, respectively. Due to the curvature of the road, the uneven forces are acting on the wheels (Figure 2-109-(2)). In the meantime, the hydraulic cylinder is compressed or extended until the reaction and hydraulic forces are the same (Figure 2-109-(3)). Therefore, regardless of the curvature of the road, the SPMT keeps on maintaining the level of the platform.

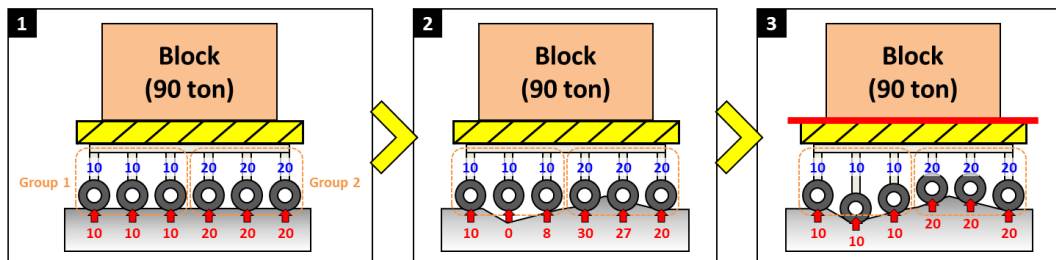


Figure 2-109. Compensation mechanism of the SPMT.

In this study, all of the bodies involved in block offloading simulation are treated as rigid bodies. Therefore, the deformation effect due to the uneven load acting on the platform of the SPMT as shown in Figure 2-110 was not considered. However, it is supposed to be a key factor to the simulation results. Therefore, further research will consider the deformation of SPMTs for more accurate results.

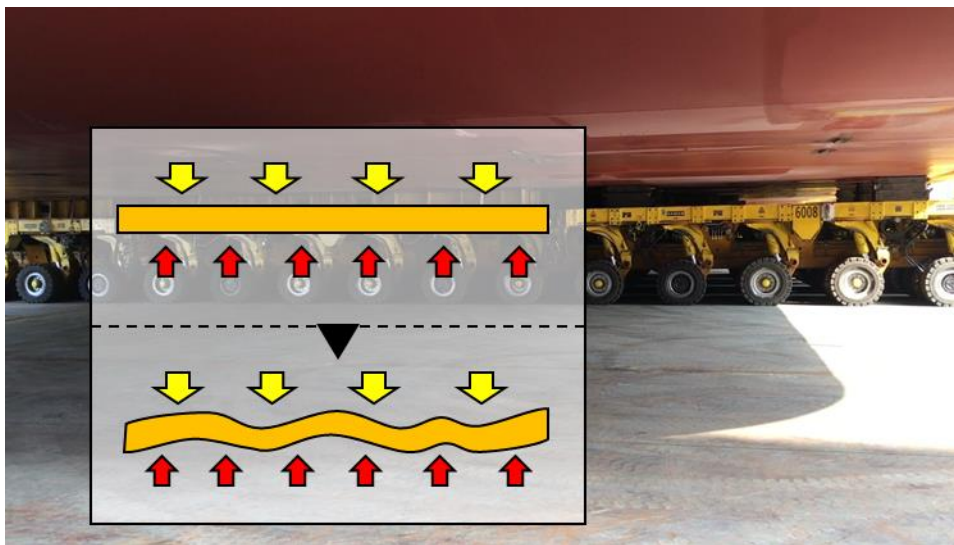


Figure 2-110. Deformation of the platform of a SPMT.

### 2.8.2. Replication of ballasting and de-ballasting for the floaters

As the SPMTs lift the block and move towards the FD, the trims of the TB and FD occur. The trim disturbs the movement of the SPMTs and applies the unexpected load on the wheel. Therefore, maintaining an even keel is important in the real operation. It is done by ballasting or de-ballasting, which means pumping in or out of water inside tanks. Figure 2-111 shows de-ballasting of the TB.

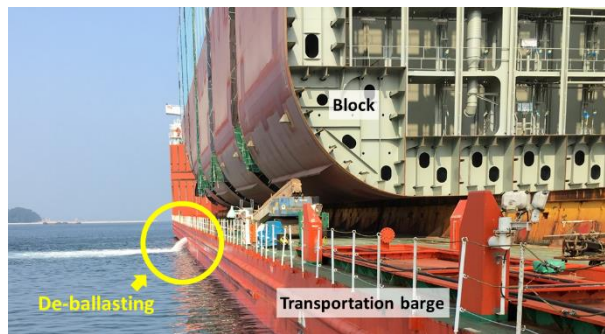


Figure 2-111. De-ballasting of the TB.

It is not easy to simulate the filling or emptying of several ballast tanks. Therefore, we replicate ballasting and de-ballasting by shifting the center of gravity (COG) of the TB and FD, with reference to the trim without ballasting and de-ballasting. According to the position of the block and SPMTs, the trims are changed without ballasting and de-ballasting as shown in Figure 2-112. At first, the TB leans to the FD. The weight of the block then crosses over to the FD, and the trim of the TB is recovered. However, the trim of the FD is increased.

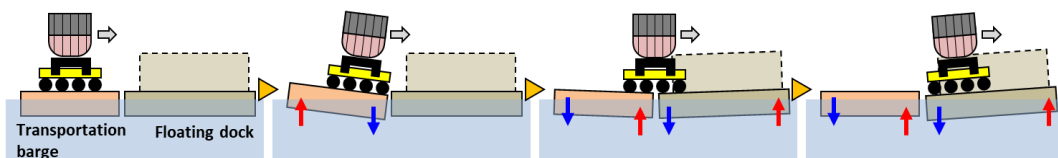


Figure 2-112. Trim change without ballasting and de-ballasting.

Figure 2-113 shows how to shift the COG according to the position of the block. To maintain an even keel, the COG of the TB moves to the opposite direction of the FD. When the SPMTs enter the FD, the COG of the TB moves towards the FD, and the COG of the FD moves to the opposite direction of the block. Finally, when all of the weight of the block and SPMTs transfer to the FD, the COG of the TB is moved back to the center, and the

COG of the FD is located far from the COG of the block.

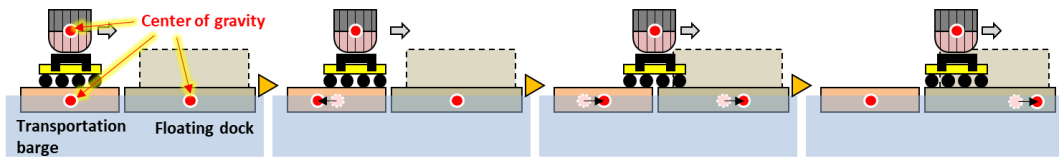


Figure 2-113. Shift of center of gravity.

The draft is also changed when the block moves from the TB to FD. Therefore, in accordance with the shift of the COG, the weight of the TB and FD should be increased or decreased to keep the constant draft.

### 2.8.3. Case studies of SPMT

#### (1) Pass through small bump

We modeled the SPMT with twelve wheels based on the dimensions listed in Table 2-7 (Figure 2-114). Each heel was connected to the platform by a slider-hinge joint. The wheels can collide to the ground using the non-interpenetration constraint method between the cylinder and plane.

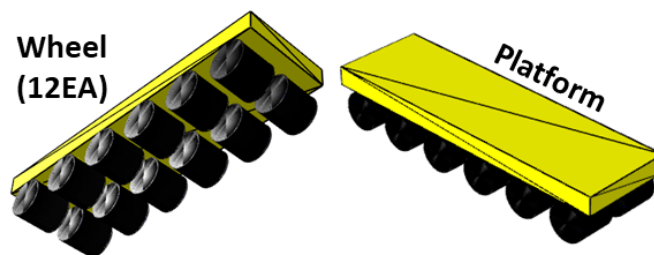


Figure 2-114. Modeling of the SPMT.

The third test was to transport the block passing through the small bump using two SPMTs (Figure 2-115). The weight of the block was 300 ton, and the length, width, and height was 20 m, 10 m, and 10 m, respectively. The small bump protrudes 100 mm above the floor. The wheels of the first SPMT make one compensation group (Group 1), and the wheels of the second SPMT belong to the second compensation group (Group 2).

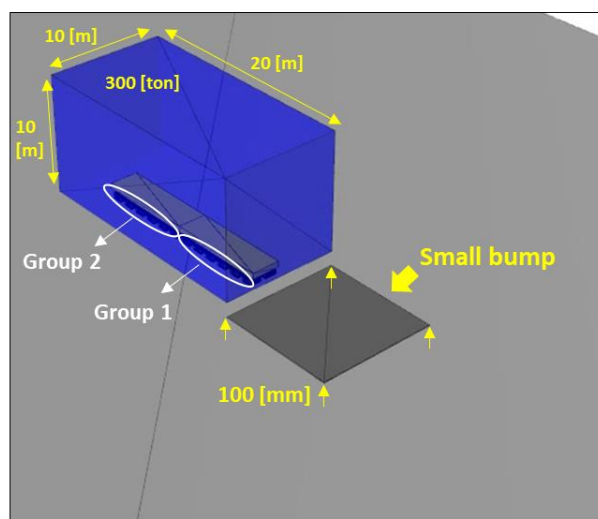


Figure 2-115. Modeling of the block, two SPMTs, and the small bump.

The simulation results are depicted in Figure 2-116. The wheels on the bump were lifted up to maintain the level of the platform. The height of the first wheel and the load acting on the wheel from the ground are shown as graphs in Figure 2-117. At the moment when wheels got out of the bump, the wheel load became zero. Afterward, the wheel was laid down on the ground. This resulted in a sudden change of the wheel loads. Moreover, to maintain the level of the platform, the load of the wheel is also affected by loads of the other wheels in the same group. Therefore, the load shows several peaks when the other wheels are entering or leaving the bump.

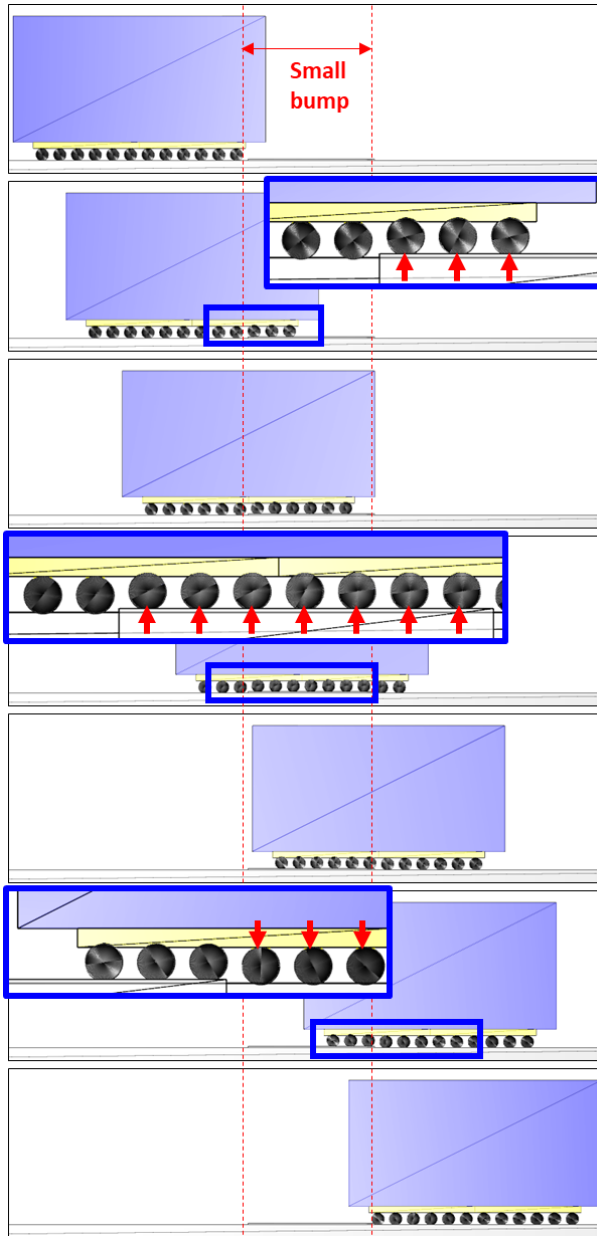


Figure 2-116. SPMT test: Transport the block passing through the small bump.



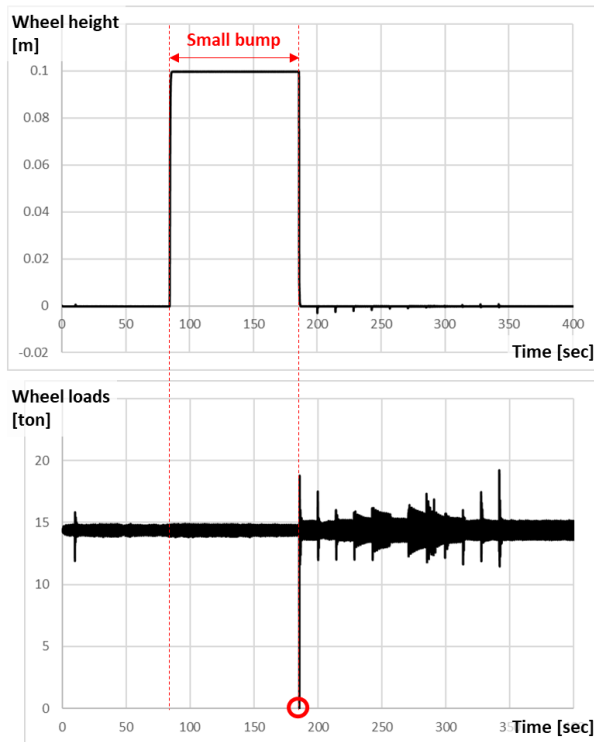


Figure 2-117. Wheel height and loads.

## (2) Pass through inclined bump

The fourth test was to transport the block passing through the inclined bump using two SPMTs. The only difference from the previous example was the bump. It was modeled by the three boxes, which were tilted by 10 degrees to make the inclined and declined bumps (Figure 2-118).

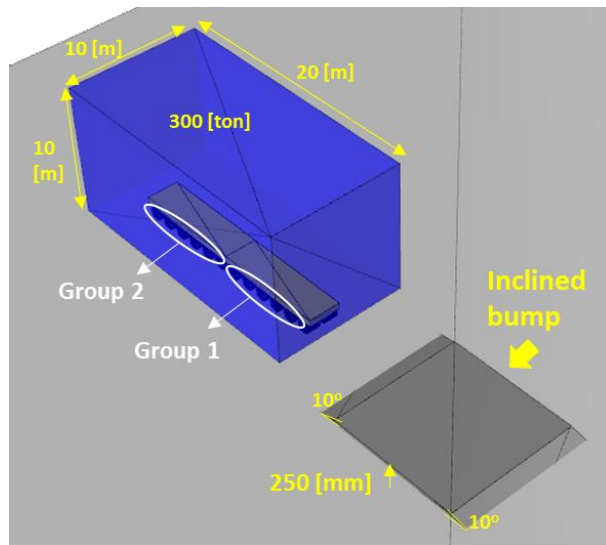


Figure 2-118. Modeling of the inclined bump.

The simulation results are depicted in Figure 2-119. The wheels on the bump were lifted up to maintain the level of the platform. The height of the first wheel and the load acting on the wheel from the ground are shown as graphs in Figure 2-120. The height of the wheel was smoothly changed compared to the previous test.

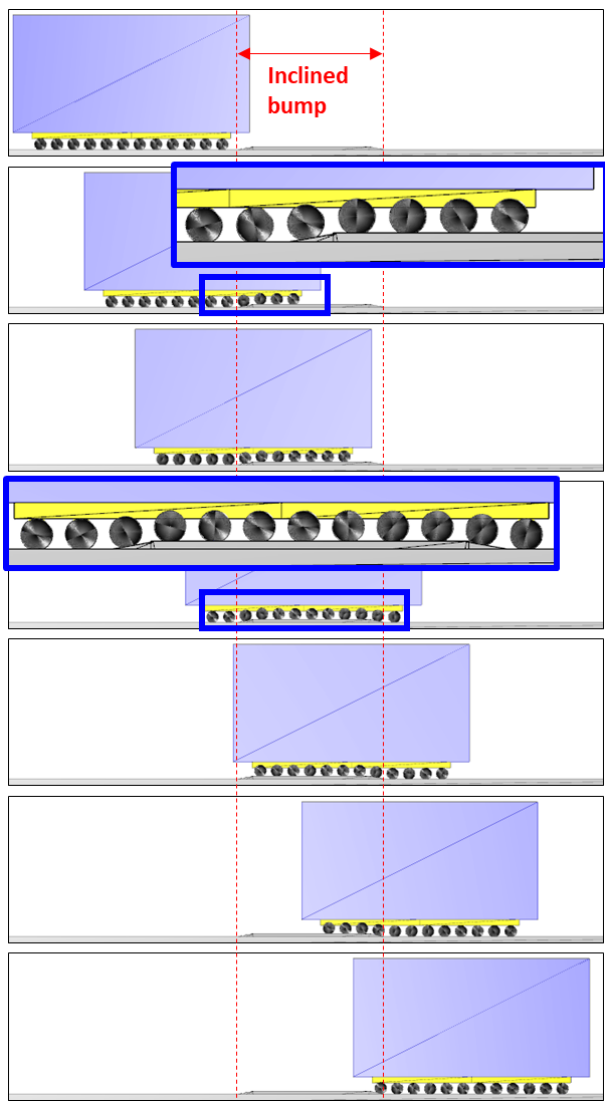


Figure 2-119. SPMT test: Transport the block passing through the inclined bump.

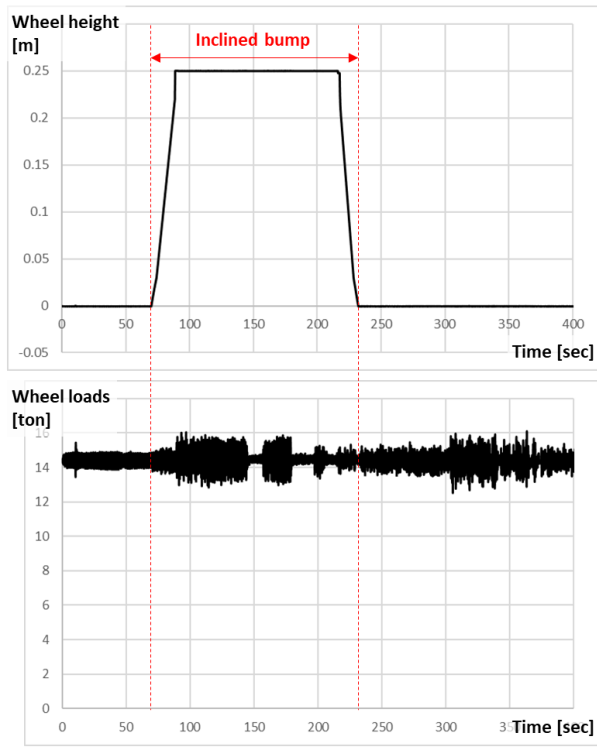


Figure 2-120. Wheel height and loads.

## 2.9. External forces

### 2.9.1. Hydrodynamic force

The lifting force is dynamically changed due to the motion of the floating cranes induced by the hydrodynamic force. The hydrodynamic force can be divided into two parts: the wave exciting force, which is exerted by the incident wave; and the radiation force from the wave due to the motion of the corresponding body in still water. The radiation force is composed of two terms, one is the force proportional to the acceleration of the motion, and the other one is the force proportional to the velocity of the motion.

$$\mathbf{F}_{hydrodynamic} = \mathbf{F}_{exciting} + \mathbf{F}_{radiation} \quad (223)$$

$\mathbf{F}_{exciting}$  is calculated by multiplying the force RAO (Response Amplitude Operator) with the sinusoidal function at a given frequency. The force RAO can be obtained from a commercial solver, such as WADAM by DNV. The Cummins equation [60] can be used to calculate  $\mathbf{F}_{radiation}$ , which considers the impulse response of the floater in the time domain. The frequency-dependent added mass coefficient  $a_{ij}(\omega)$  and the frequency-dependent damping coefficient  $b_{ij}(\omega)$  at a given frequency  $\omega$  can also be obtained from the commercial solver. Using the frequency-dependent coefficients  $a_{ij}(\omega)$ , and  $b_{ij}(\omega)$ , the added mass  $\mathbf{A}$  and retardation function  $\mathbf{B}(\tau)$  can be determined. The added mass at infinite motion frequency ( $\mathbf{A}_\infty$ ), which is a constant matrix, is often used rather than calculating the integral because the equation is valid for any value of  $\omega$ , and thus also for  $\omega = \infty$ . Figure 2-121 summarizes the calculation procedure.

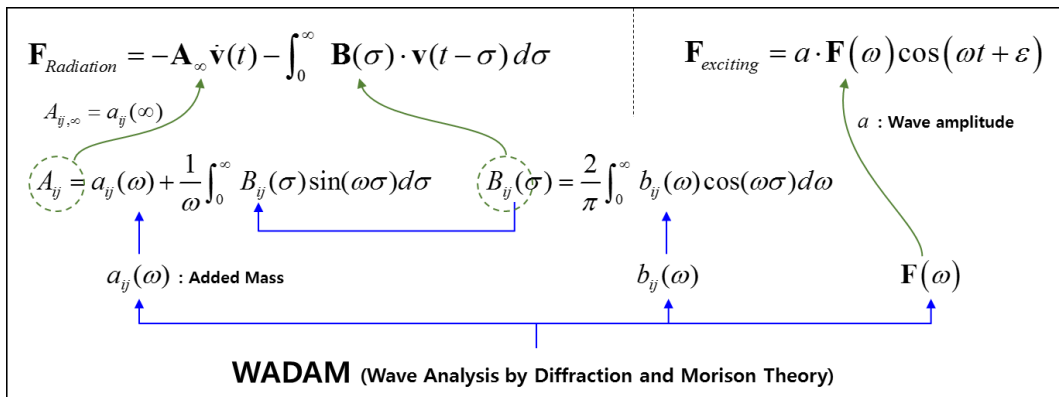


Figure 2-121. Calculation of the hydrodynamic force.

In the case of a regular wave, one wave frequency ( $\omega$ ) and one wave amplitude ( $a$ ) are chosen. According to the wave frequency, only one force RAO ( $\mathbf{F}(\omega)$ ) and a phase angle ( $\varepsilon$ ) are also selected. However, in the case of an irregular wave, there are a number of  $N$  wave frequencies and amplitudes according to the given wave spectrum. Therefore,  $\mathbf{F}_{exciting}$  of the irregular wave is calculated as follows.

$$\mathbf{F}_{exciting} = \sum_{m=1}^N a_m \cdot \mathbf{F}(\omega_m) \cos(\omega_m t + \varepsilon_m) \quad (224)$$

where,  $a_m$  is the wave amplitude at a given frequency, and  $\varepsilon_m$  is the phase angle.

Meanwhile, if the wave height, period, and direction is given stochastically, the analysis results such as motions and tensions can be regarded stochastically. As a result, the expectation maximum value of the simulation results can be used to indicate the operation limit stochastically.

### **2.9.2. Buoyant force**

The buoyant force is the upward force exerted by a fluid that opposes the weight of an immersed object. A 3 by 3 restoring matrix can be used, if we assume that the motion is very small. However, most cases are not satisfied with this assumption. Therefore, we need to find the exact volume and the center of the volume. This is done by the direct volume calculation method under the water plane. If the body shape is composed of triangular meshes, we can obtain new triangles after the plane intersection shown in Figure 2-122. Once we obtain the triangular meshes under the water plane, the volume and the center of volume can be calculated by the sum of the volumes and the 1<sup>st</sup> order moments of the tetrahedral under the water plane [16].

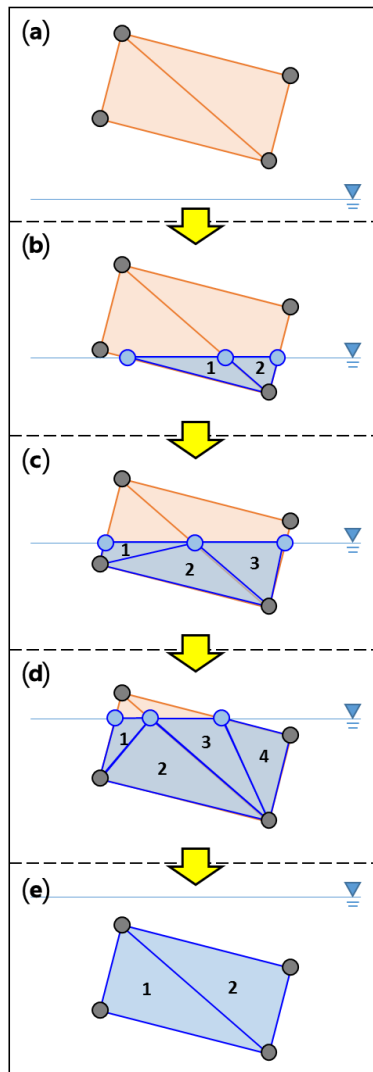


Figure 2-122. Plane intersection under the water plane.

### 2.9.3. Wind force

The wind force is calculated by the same equations as the current force.



$$\begin{aligned}
F_x &= C_x \frac{1}{2} \rho_{air} V(t)_{wind}^2 A_f \\
F_y &= C_y \frac{1}{2} \rho_{air} V(t)_{wind}^2 A_s \\
M_z &= C_N \frac{1}{2} \rho_{air} V(t)_{wind}^2 A_s L_{oa}
\end{aligned} \tag{225}$$

The wind speed ( $V_{wind}$ ) is not constant, but a value that varies with time. Therefore, we have to find the mean wind speed at  $H$  m above the water plane. This can be obtained by the following equation:

$$U(H) = U(10) \cdot \left( \frac{H}{10} \right)^\alpha \tag{226}$$

where,  $H$  is the height above the water plane,  $U(10)$  is the average speed at 10 m above the water plane, and  $\alpha$  is the height coefficient, which according to ISO 19901-1 [61] is usually 0.11 . Meanwhile, the wind fluctuation is calculated from the wind spectrum. In this study, the NPD spectrum given by ISO 19901-1 is adopted to calculate the wind fluctuation.

$$\begin{aligned}
S(f) &= \frac{320 \cdot \left( \frac{U(10)}{10} \right)^2 \cdot \left( \frac{H}{10} \right)^{0.45}}{\left( 1 + f_m^n \right)^{\frac{5}{3n}}} \\
f_m &= 172 \cdot f \cdot \left( \frac{H}{10} \right)^{\frac{2}{3}} \cdot \left( \frac{U(10)}{10} \right)^{-0.75}
\end{aligned} \tag{227}$$

As a result, the wind speed in the time domain is the summation of the mean wind speed at  $H$  and the wind fluctuation. Figure 2-123 summarizes the overall procedure.

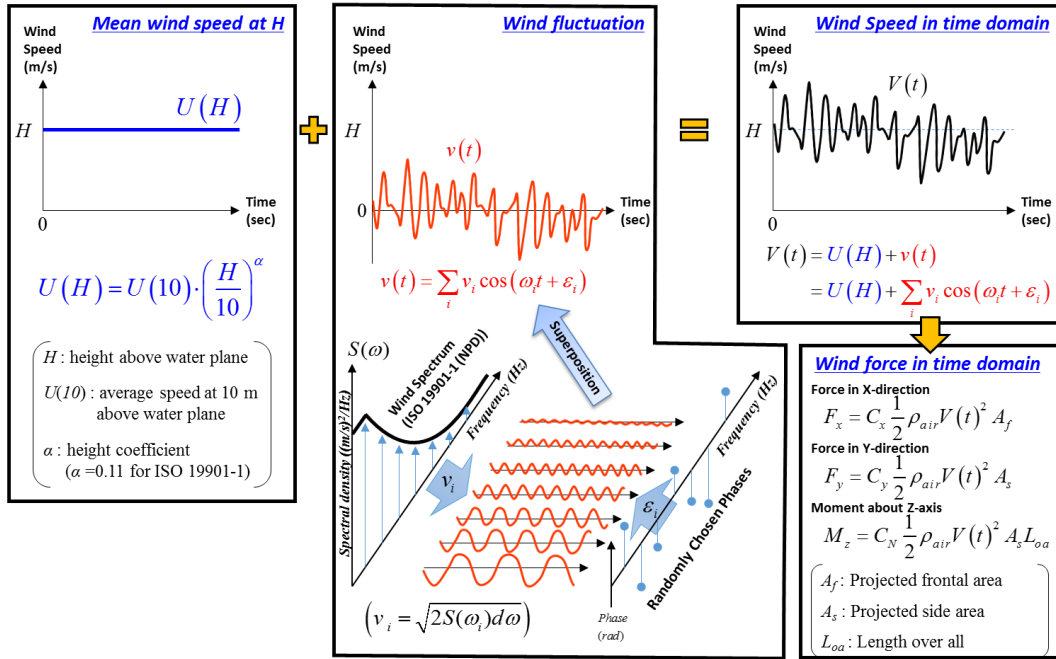


Figure 2-123. Wind speed, including mean wind speed and wind fluctuation.

## 2.9.4. Current force

The current force in the  $x, y$  directions ( $F_x, F_y$ ) and the moment about the  $z$  axis ( $M_z$ ) can be simply calculated as follows:

$$\begin{aligned}
 F_x &= C_x \frac{1}{2} \rho_{water} V_{current}^2 A_f \\
 F_y &= C_y \frac{1}{2} \rho_{water} V_{current}^2 A_s \\
 M_z &= C_N \frac{1}{2} \rho_{water} V_{current}^2 A_s L_{oa}
 \end{aligned} \tag{228}$$

where,  $\rho_{water}$  is the sea water density,  $C_x$ ,  $C_y$ , and  $C_N$  are the coefficients that are obtained by experiment,  $A_f$  is the projected frontal area,  $A_s$  is the projected side area, and  $V_{current}$  is the current velocity, which is constant.

### 2.9.5. Catenary mooring

The mooring force is induced by a mooring line. A mooring line is modeled by the self-weight of a catenary cable. If the two endpoints are fixed, Figure 2-124 shows the shape of the cable considering the deflection due to its own weight.

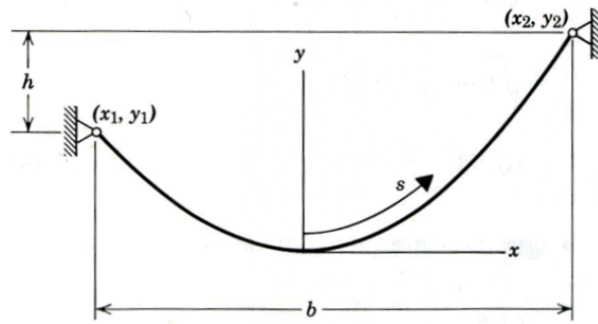


Figure 2-124. Catenary cable with its own weight.

From the shape information and the force equilibrium equations, we can obtain one equation that contains the horizontal tension ( $T_H$ ) [62]:

$$\frac{\frac{bq}{2T_H}}{\sinh\left(\frac{bq}{2T_H}\right)} - \frac{b}{\sqrt{S^2 - h^2}} = 0, \begin{cases} b = x_2 - x_1 \\ h = y_2 - y_1 \end{cases} \quad (229)$$

where,  $b$  is the horizontal length,  $h$  is the vertical length,  $S$  is the total cable length, and  $q$  is the weight per unit length. We can find  $T_H$  by solving Eq. (229) by the Newton-Raphson method.

### 2.9.6. Wire rope tension

The floating cranes use the wire rope to lift the wreck from the seabed to the sea surface. In this study, the wire rope is modeled by the incompressible spring, which adds force only when it is extended. The principle of the incompressible spring is shown in Figure 2-125.

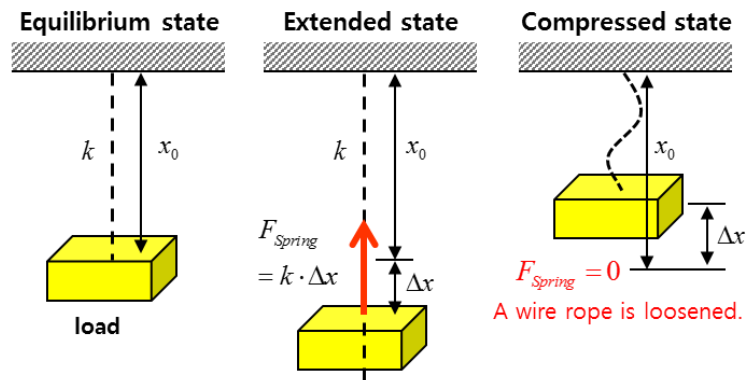


Figure 2-125. Principle of the incompressible spring.

This wire rope model is applied to each sling or cable used in the wreck removal analysis. It is calculated as follows.

$$\mathbf{F}_{Spring} = k \cdot (x - x_0), \text{ (only if } x > x_0 \text{)} \quad (230)$$

## 3. Verification and validation

This section will provide several verification examples compared with the analytic solutions or commercial software to increase the reliability. For validation, two simulation cases will be compared to the real operations.

### 3.1. Verification of multibody dynamics for rigid bodies

#### 3.1.1. Multibody benchmarking tests

MBS Benchmark (Multibody Systems Benchmark) is a collaborative project dedicated to develop and maintain a standardized set of problems and procedures which enable easy and objective performance evaluation of multibody systems simulation software [63], [64].

##### (1) A01. Simple pendulum

The simple planar pendulum is composed by a lumped mass of 1 kg and a massless link of 1 m length. The system is under gravity effects (9.81 N/kg acting in the negative  $y$  direction). The position of the global reference frame is shown in Figure 3-1.

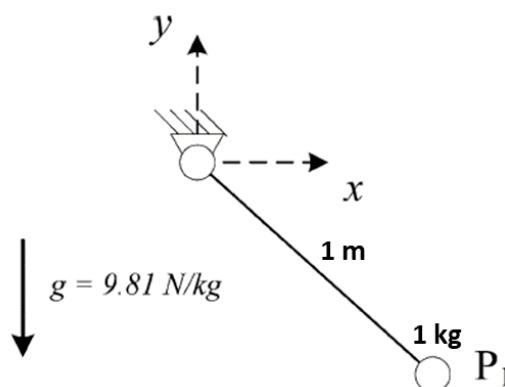


Figure 3-1. MBS benchmarking test A01. Simple pendulum.

The values of  $x$  (red line) and  $y$  (blue dot line) are depicted as the graphs in Figure 3-2. By comparing two graphs, we can conclude that those values are almost identical with each other.

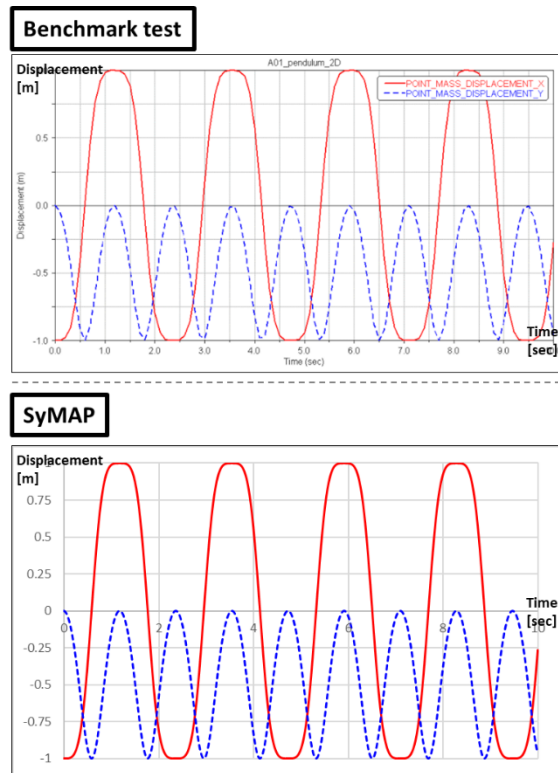


Figure 3-2. Graphs of the displacement of simple pendulum.

## (2) A02. N-four-bar mechanism

The one degree-of-freedom assembly of  $N$  four-bar linkages is composed of  $2N+1$  links of 1 m length with a uniformly distributed mass of 1 kg. The system is under gravity effects (9.81 N/kg acting in the negative  $y$  direction). The mechanism is a one-degree-of-freedom assembly of four-bar linkages with  $N$  loops. When the mechanism reaches a horizontal position, the number of degrees of freedom instantaneously increases from 1 to  $N+1$ . Figure 3-3 shows  $N$  four-bar models.

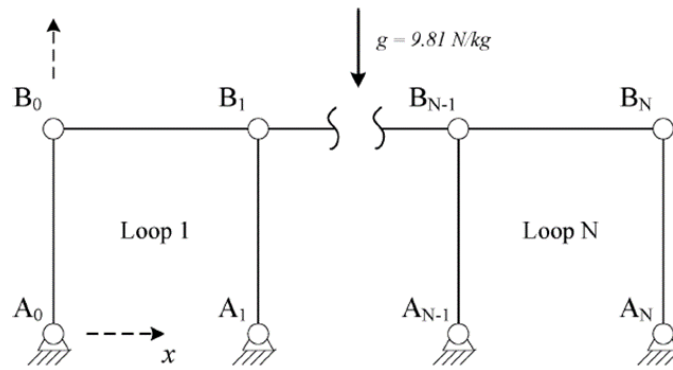


Figure 3-3. MBS benchmarking test A02. N-four-bar mechanism.

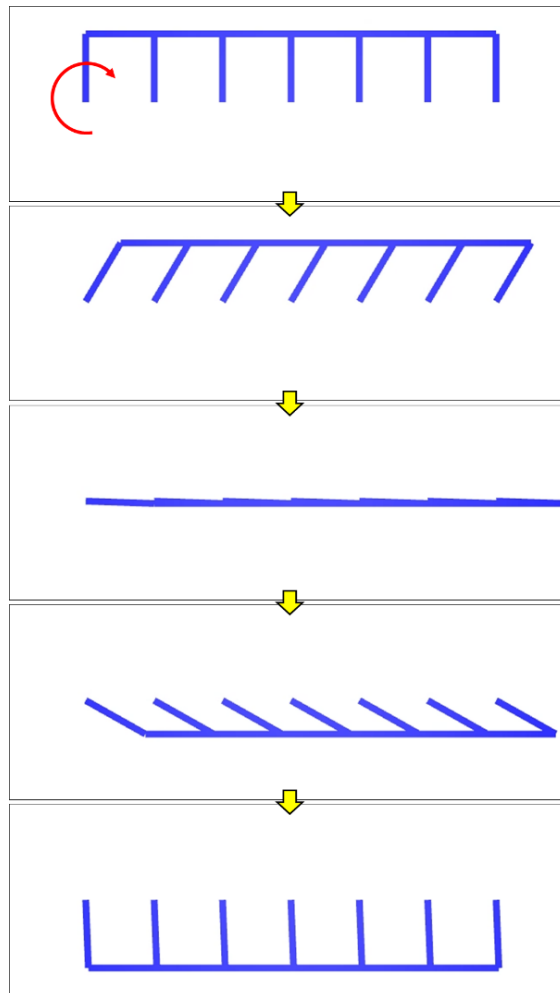


Figure 3-4. Simulation results of A02 (N four-bar mechanism)

The values of  $x$  (red line) and  $y$  (blue dot line) of the first link are depicted as the graphs in Figure 3-5. By comparing two graphs, we can conclude that those values are almost identical with each other.

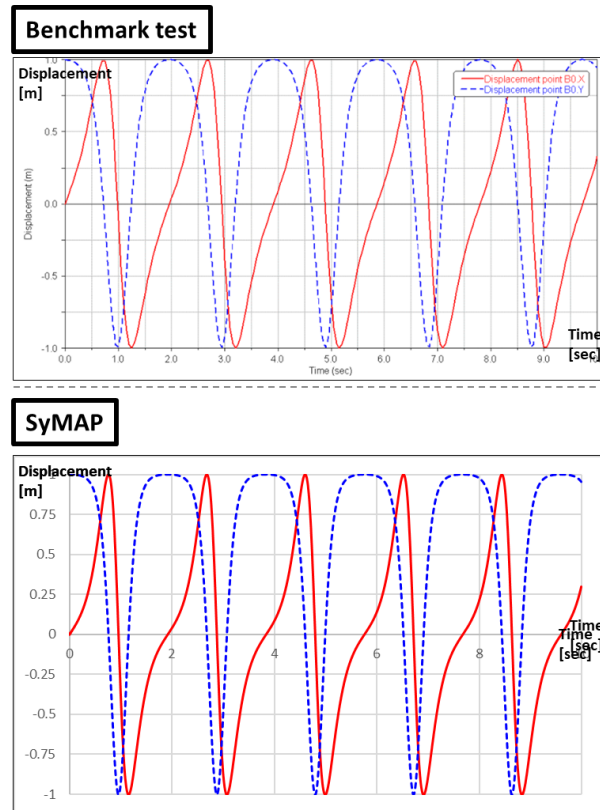


Figure 3-5. Graphs of the displacement of N four-bar mechanism.

### (3) A03. Andrew's mechanism

This plane mechanism is composed of seven bodies interconnected by revolute joints. The assembly is driven by a motor located at point O, with a constant drive torque of 0.033 Nm. This system has a very small time scale, thus making it difficult to simulate for solvers that can't reach small time steps. Figure 3-6 shows the seven bodies and the connection



points. Initially, the system is at rest, and the  $\beta$  angle has a value of  $-0.0620$  rad.

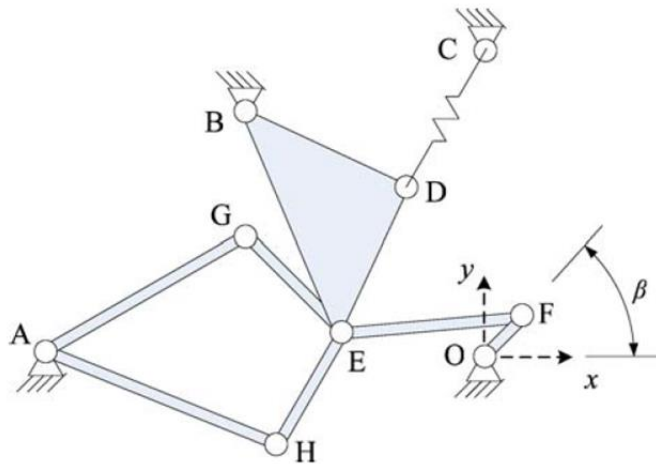


Figure 3-6. MBS benchmarking test A03. Andrew's mechanism.

When the simulation starts, the link OF rotate counterclockwise. Due to the interconnected joints, the other links are also moved as shown in Figure 3-7.

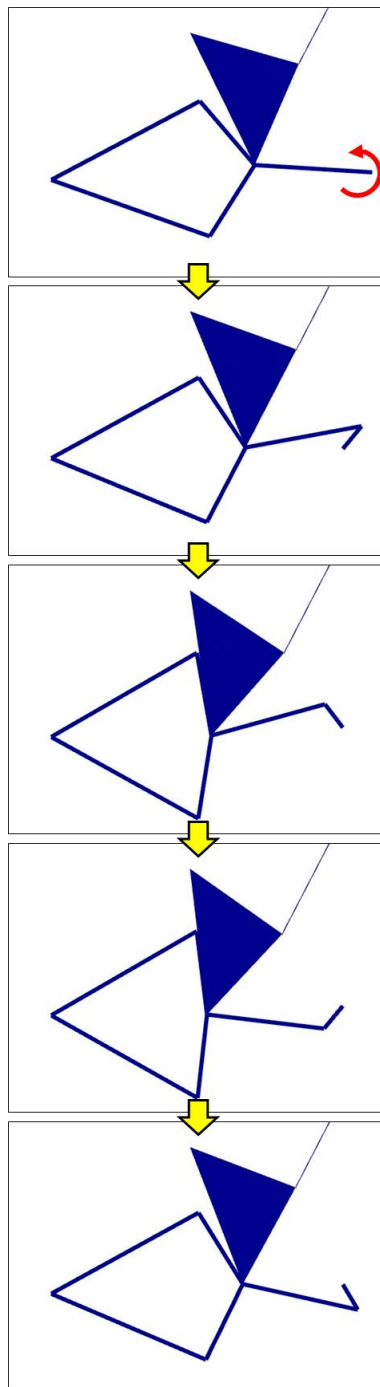


Figure 3-7. Simulation results of A03 (Andrew's mechanism).

The values of  $x$  (red line) and  $y$  (blue dot line) of the position of  $F$  are depicted as the graphs in Figure 3-8. By comparing two graphs, we can conclude that those values are almost identical with each other.

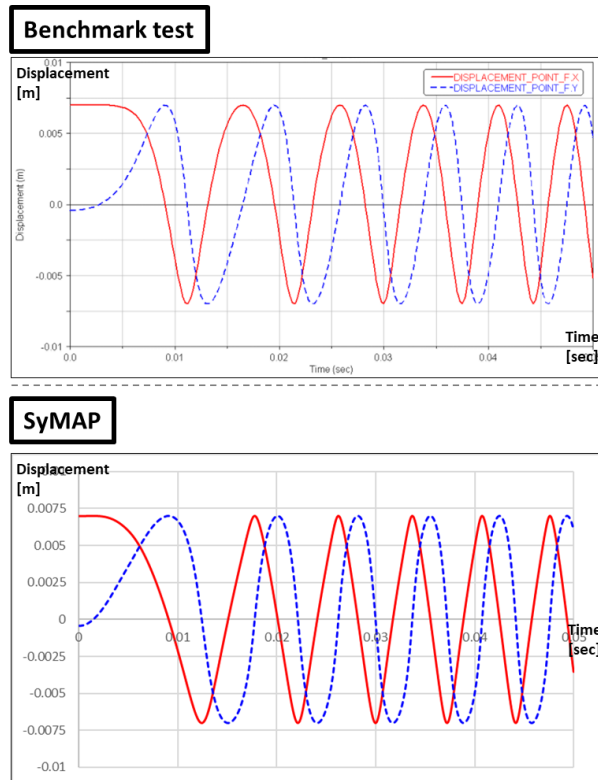


Figure 3-8. Graphs of the position  $F$ .

#### (4) A04. Bricard's mechanism

The Bricard mechanism is a classic example of the overconstrained system. It is composed of five rods of 1 m length with a uniformly distributed mass of 1 kg, and 6 revolute joints. The system is under gravity effects (9.81 N/kg acting in the negative  $y$  direction). Grübler formula gives 0 degrees-of-freedom for this mechanism, but the particular orientation of the revolute pairs yields a system with 1 degree-of-freedom. Figure

3-9 shows the bodies and connections of Bricard's mechanism.

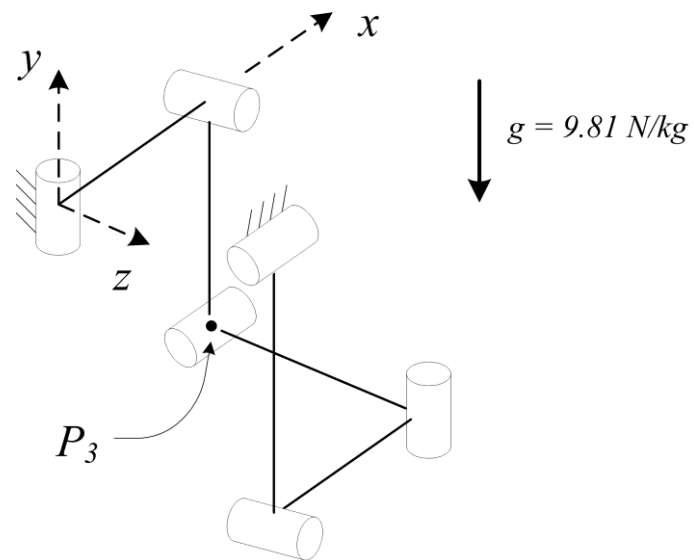


Figure 3-9. MBS benchmarking test A04. Bricard's mechanism.

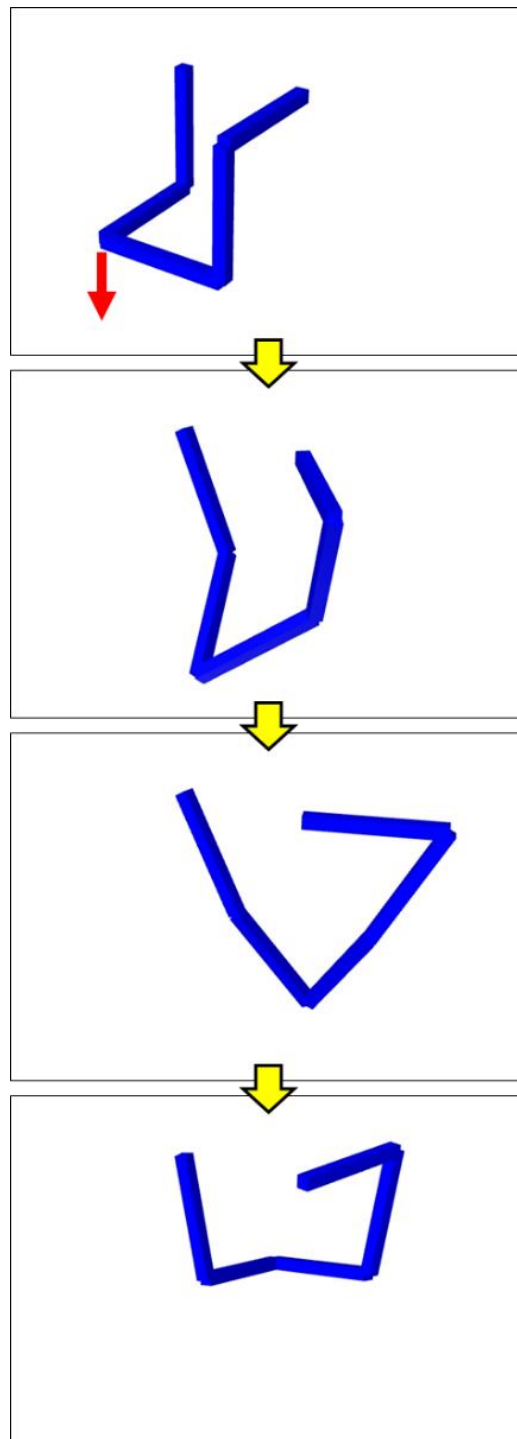


Figure 3-10. Simulation results of A04 (Bricard's mechanism).

The values of  $x$  (red line),  $y$  (blue dot line), and  $z$  (pink dot line) of the position of F are depicted as the graphs in Figure 3-11. By comparing two graphs, we can conclude that those values are almost identical with each other.

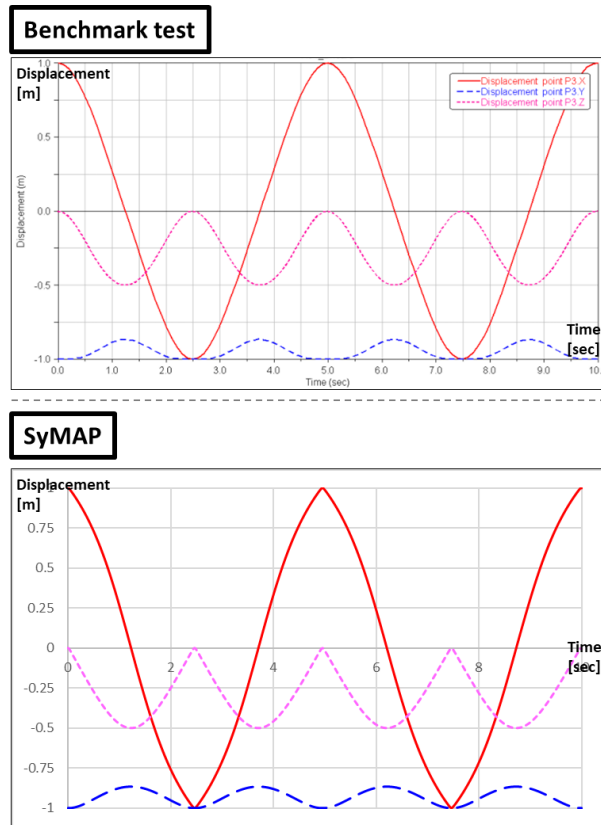


Figure 3-11. Graphs of the position of point P3.

### 3.1.2. Verification by commercial software

DAFUL [65] is one of the most famous multibody dynamics software developed in South Korea. We decided to simulate the following two examples to be compared with DAFUL for verification.

### (1) Three links connected by hinge joints (Open loop system)

The first example is the three links connected by hinge joints as shown in Figure 3-12. The link is 10 m length, and its weight is 1 ton. This example is open loop, which does not contain any kinematic loops to reach from one body to another.

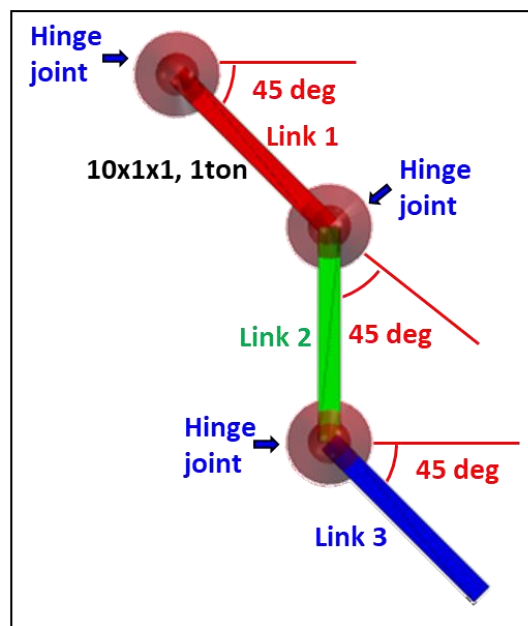


Figure 3-12. Three links connected by hinge joints (open loop).

When the simulation starts, the links are dropped down due to the gravitational force. However, the constraint forces due to the hinge joints make the links rotate based on the hinge point.

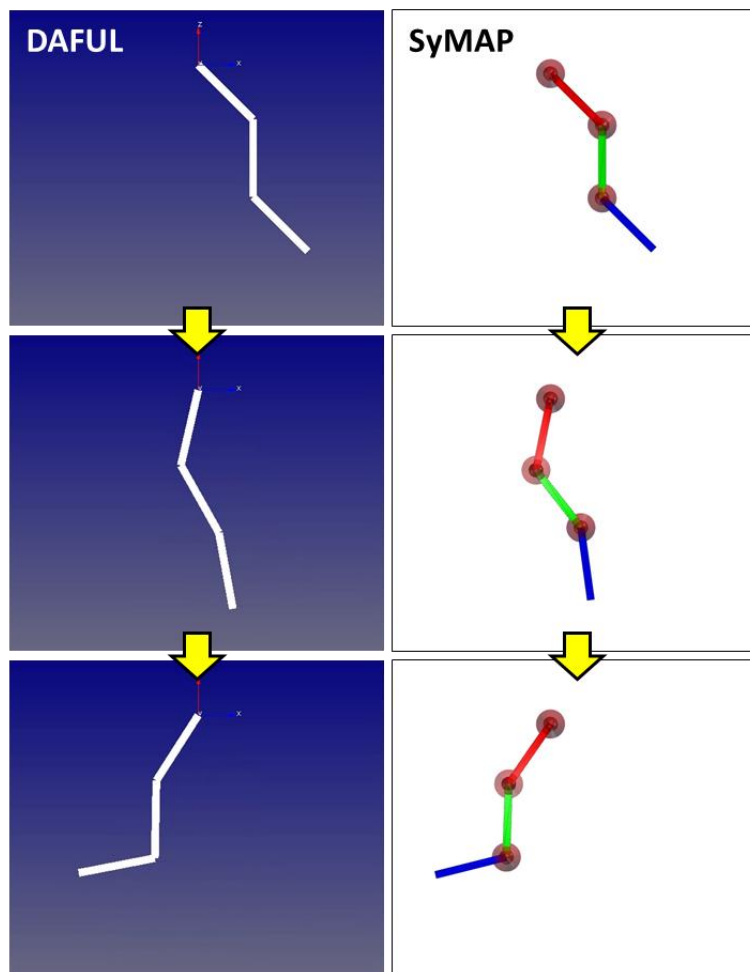


Figure 3-13. Simulation results of three links connected by hinge joints (open loop).

The values of  $z$  displacement of link1 (red line), link2 (green line), and link3  $z$  (blue line) are depicted as the graphs in Figure 3-14. By comparing two graphs, we can conclude that those values are almost identical with each other.



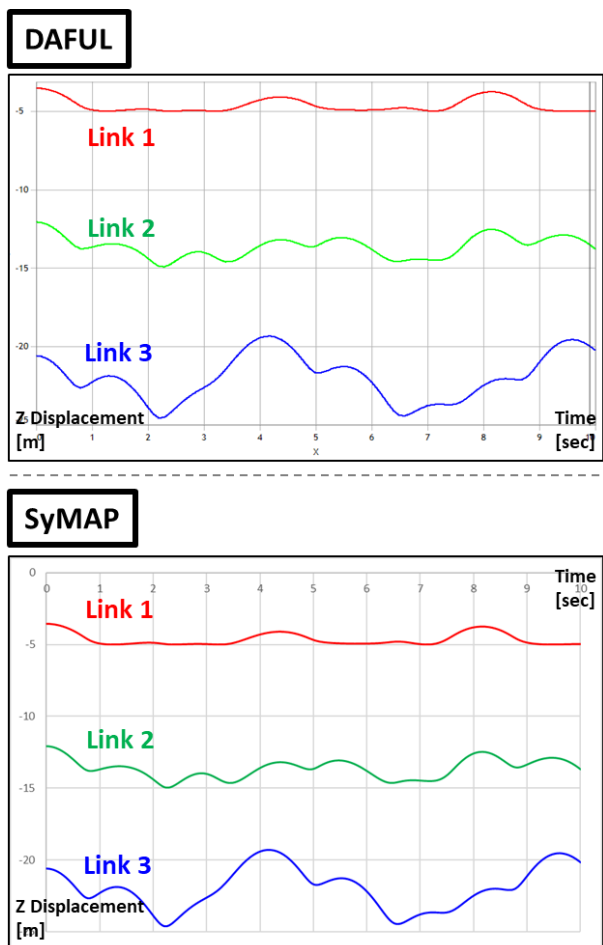


Figure 3-14. Graphs of z displacement of three links.

**(2) Three links connected by hinge joints (Closed loop)**

The second example is three links connected by four hinge joints. The last hinge joint makes the degree of freedom of the system from three to one. This example is to test the closed loop, which contains kinematic loops.

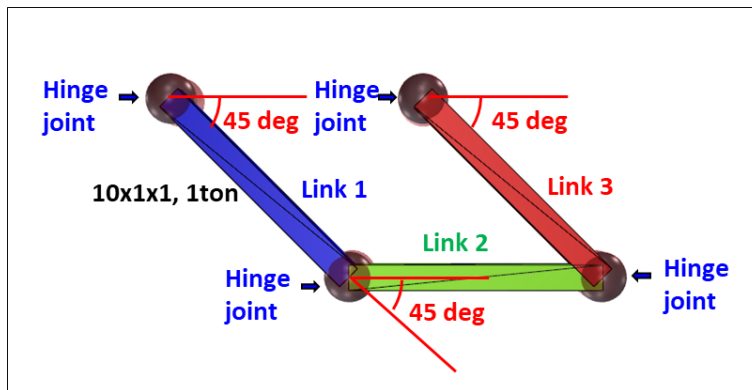


Figure 3-15. Three links connected by hinge joints (closed loop).

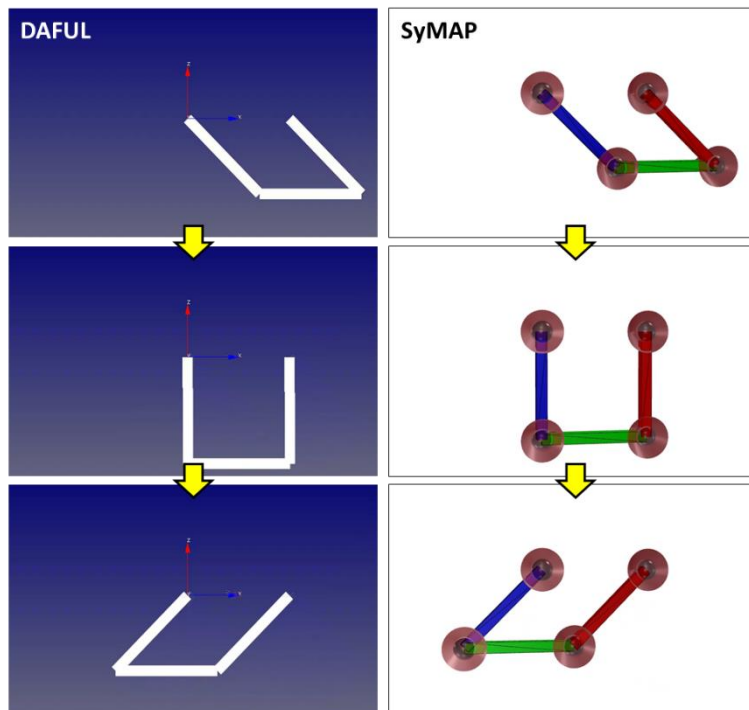
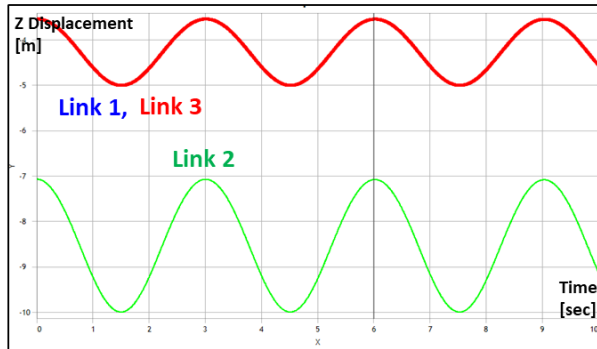


Figure 3-16. Simulation results of three links connected by hinge joints (closed loop).

The values of  $z$  displacement of link1 (blue line), link2 (green line), and link3  $z$  (red line) are depicted as the graphs in Figure 3-17. By comparing two graphs, we can conclude that those values are almost identical with each other.

**DAFUL**



**SyMAP**

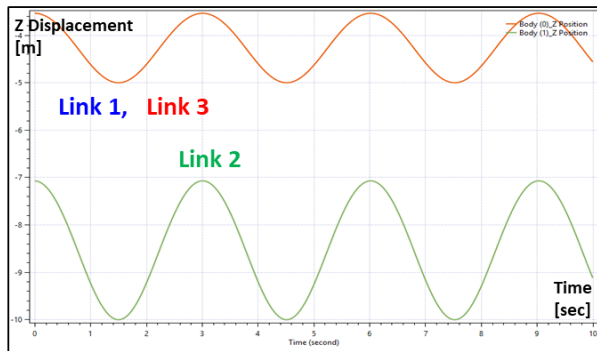


Figure 3-17. Graphs of z displacement of three links.

## 3.2. Verification of multibody dynamics for deformable bodies

### 3.2.1. Verification of 1D frame element

The first example is the simple support with uniform distributed load ( $w$ ) as shown in Figure 3-18.

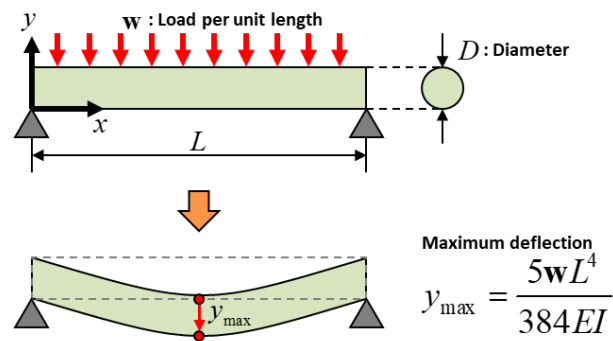


Figure 3-18. Simple support of 1D frame element.

The maximum deflection derived by beam theory of the simple support is as follows.

$$y_{\max} = \frac{5wL^4}{384EI} \quad (231)$$

where  $L$  is the length of the beam,  $E$  is Young's modulus, and  $I$  is area moment of inertia. Uniform load per length is determined by multiplying the density ( $\rho$ ) and the cross-section area. According to different  $E$  and  $\rho$ , the analytic solution is listed in Table 3-1.

Table 3-1. Analytic solution of simple support beam according to different beam properties.

Case	Material property						Simple support (Analytic solution)
	$E$	$Density$	$L$	$D$	$I$	$w$	$y_{max}$ (Center)
	[GPa]	[ton/m <sup>3</sup> ]	[m]	[m]	[m <sup>4</sup> ]	[ton/m]	[mm]
1	1	1	10	1	0.0491	0.7854	20.438
2	10	1	10	1	0.0491	0.7854	2.044
3	100	1	10	1	0.0491	0.7854	0.204
4	210	7.85	10	1	0.0491	6.1654	0.764

The simulation results according to the number of elements are summarized in Table 3-2. If the number of elements is more than 5, the results are very close to the analytic solutions.

Table 3-2 Simulation results of simple support beam according to the number of elements.

Case	Simple support (Simulation)				
	$y_{max}$ (Center)				
	1 EA	2 EA	3 EA	5 EA	10 EA
1	16.334	20.404	20.353	20.396	20.403
2	1.635	2.044	2.039	2.043	2.044
3	0.163	0.204	0.204	0.204	0.204
4	0.624	0.764	0.762	0.764	0.764

The second example is the cantilever as shown in Figure 3-19.

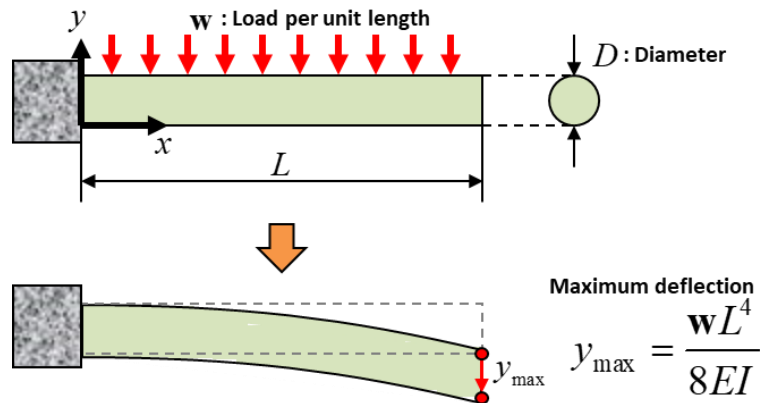


Figure 3-19. Cantilever of 1D frame element.

The maximum deflection derived by beam theory of the cantilever is as follows.

$$y_{\max} = \frac{wL^4}{8EI} \quad (232)$$

We use the same property used in simple support. The analytic solution of the cantilever beam is listed in Table 3-3.

Table 3-3. Analytic solution of cantilever beam according to different beam properties.

Case	Material property						Cantilever (Analytic solution)
	$E$	Density	$L$	$D$	$I$	$w$	$y_{\max}$ (Center)
	[GPa]	[ton/m <sup>3</sup> ]	[m]	[m]	[m <sup>4</sup> ]	[ton/m]	[mm]
1	1	1	10	1	0.0491	0.7854	196.200
2	10	1	10	1	0.0491	0.7854	19.620
3	100	1	10	1	0.0491	0.7854	1.962
4	210	7.85	10	1	0.0491	6.1654	7.334

Simulation results according to the number of elements are summarized in Table 3-4. If the number of elements is more than 5, the results are very close to the analytic solutions.

Table 3-4 Simulation results of cantilever beam according to the number of elements.

Case	Cantilever (Simulation)				
	$y_{\max}$ (Center)				
	1 EA	2 EA	3 EA	5 EA	10 EA
1	195.920	195.622	196.108	196.140	196.140
2	19.620	19.620	19.620	19.620	19.620
3	1.962	1.962	1.962	1.962	1.962
4	7.334	7.334	7.334	7.334	7.334

The third example is free falling pendulum suggested by Berzeri and Shabana [44]. The main dimension and material properties are shown in Figure 3-20 and Table 3-5.

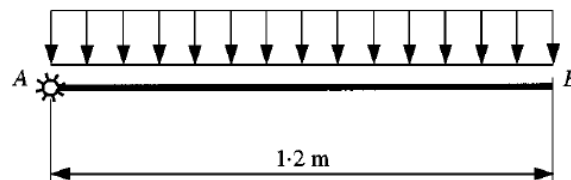


Figure 3-20. Free falling pendulum of 1D frame element.

Table 3-5. Main dimension and properties of free falling pendulum.

Item	Value
Length	1.2 [m]
Density	5,540 [kg/m <sup>3</sup> ]
Cross section area	0.0018 [m <sup>2</sup> ]
2 <sup>nd</sup> moment of area	1.215 x 10 <sup>-8</sup> [m <sup>4</sup> ]
Modulus of elasticity	0.7 x 10 <sup>6</sup> [Pa]

Configurations of the free falling pendulum at different times for the case that gravitational acceleration is 50 m/s are compared in Figure 3-21. The top graph is the results depicted in the Berzeri and Shabana [44], and the bottom graph is the results calculated by SyMAP. Two graphs are almost identical to each other.

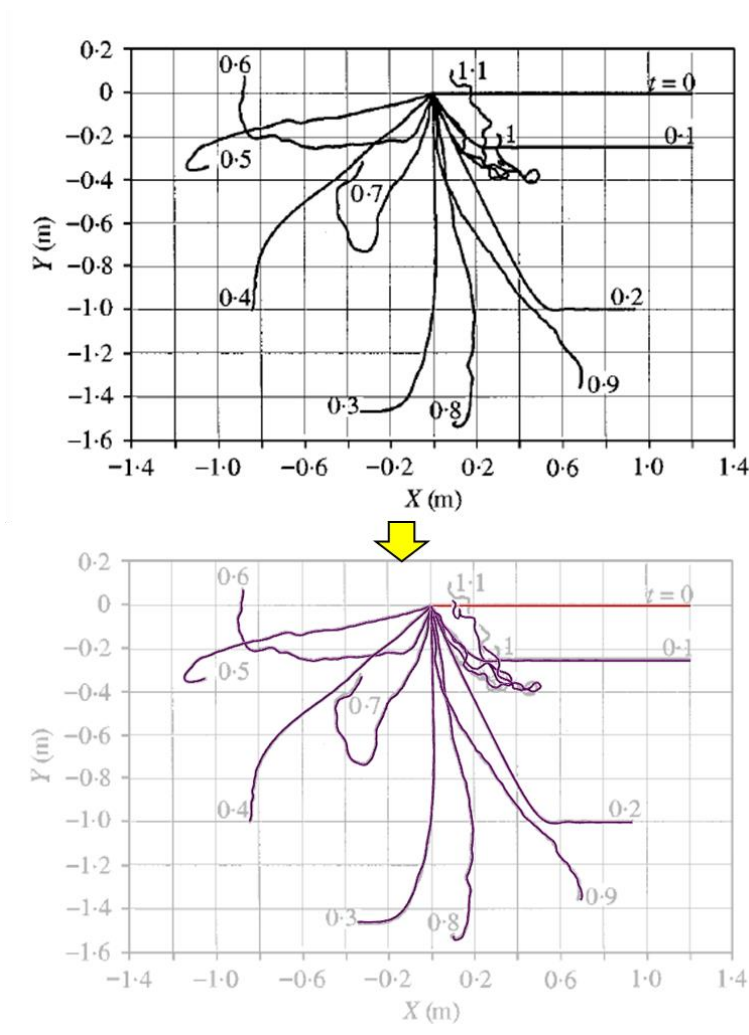


Figure 3-21. Comparison of the configuration of the free falling pendulum.



### 3.2.2. Verification of 2D shell element

The first example is the simple support plate as shown in Figure 3-22. The ball joints are modeled all around the edges.

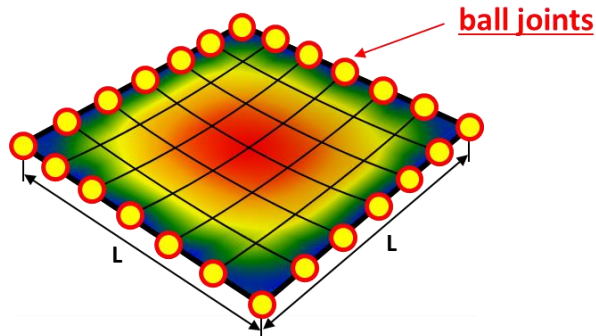


Figure 3-22. Simple support plate.

The maximum deflection at the center derived by plate theory of the simple support is as follows.

$$w_{\max} = \frac{qL^4}{D} \times 0.0040624 \quad (233)$$

where,  $D$  is flexural rigidity, and  $q$  is load per area. According to different Poisson's ratio, the analytic solution is listed in Table 3-6.

Table 3-6. Analytic solution of simple support plate according to Poisson's ratio.

Case	Material property							Simple support (Analytic solution)
	L	h	Density	E	v	D	q	$w_{\max}$ (Center)
	[m]	[m]	[ton/m <sup>3</sup> ]	[GPa]	-	-	[kN/m <sup>2</sup> ]	[mm]
1	10	0.1	1	1	0	8.333E-05	0.981	478.226
2	10	0.1	1	1	0.3	9.158E-05	0.981	435.185

The simulation results according to the number of elements are summarized in Table 3-7. Due to the approximation when the maximum deflection of the simple support plate is derived, the results show some errors. However, it is converged to the value within the acceptable range of accuracy.

Table 3-7 Simulation results of simple support plate according to the number of elements.

Case	Simple support (Simulation)				
	$w_{\max}$ (Center)				
	2 x 2	4 x 4	6 x 6	8 x 8	10 x 10
1	534.681	479.981	478.447	478.257	478.215
2	478.060	430.689	427.761	427.016	426.712

The second example is the plate with clamped edges. It is simply done by changing the ball joints of the simple support plate to the fixed joints. The maximum deflection at the center derived by plate theory of the plate with clamped edges is as follows.

$$w_{\max} = \frac{qL^4}{8D\pi^4} \quad (234)$$

According to different Poisson's ratio, the analytic solution is listed in Table 3-8.

Table 3-8. Analytic solution of simple support plate according to Poisson's ratio.

Case	Material property							Simple support (Analytic solution)
	L	h	Density	E	$\nu$	D	q	$w_{\max}$ (Center)
	[m]	[m]	[ton/m <sup>3</sup> ]	[GPa]	-	-	[kN/m <sup>2</sup> ]	[mm]
1	10	0.1	1	1	0	8.333E-05	0.981	151.064
2	10	0.1	1	1	0.3	9.158E-05	0.981	137.468

The simulation results according to the number of elements are summarized in Table 3-9. It also shows some errors due to the approximation. However, it is converged to the value within the acceptable range of accuracy.

Table 3-9 Simulation results of the plate with clamped edges according to the number of elements.

Case	Clamped edges (Simulation)				
	$w_{\max}$ (Center)				
	2 x 2	4 x 4	6 x 6	8 x 8	10 x 10
1	187.112	155.602	150.913	149.765	149.367
2	170.232	141.300	136.593	135.333	134.856

The third example is the heavy membrane hanged on four corners. The ball joint is connected only at the four corners. The main dimension and material properties are shown in Figure 3-23 and Table 3-10. The maximum deflection (Point E) is 0.58 m.

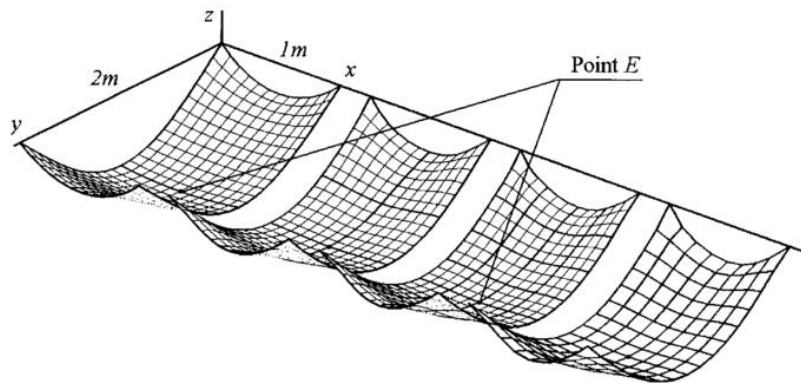


Figure 3-23. Heavy membrane hanged on four corners: 2x1, 4x2, 8x4, 16x8 elements.

Table 3-10. Main dimension and properties of free falling pendulum.

Item	Value
Length	2.0 [m]
Width	1.0 [m]
Density	1,000 [kg/m <sup>3</sup> ]
Thickness	0.01 [m]
Modulus of elasticity	10,000 [Pa]
Poisson ratio	0.3

The simulation results shows the good convergence to the maximum deflection as the number of element is increased. The maximum deflection is summarized in Table 3-13.

Table 3-11 Simulation results of the heavy membrane hanged on four corners according to the number of elements.

Heavy membrane hanged on four corners (Simulation)			
Point <i>E</i> (Center)			
2 x 1	4 x 2	8 x 4	16 x 8
0.571	0.582	0.583	0.583

### 3.3. Verification of hydrodynamic force

#### 3.3.1. Barge motion by a regular wave (I)

To validate the characteristics of the motion due to the hydrodynamic forces, the equations of motion of the floating barge in the case of the following sea (heading= 0 deg), quartering sea (heading = 45 deg) and beam sea (heading = 90 deg) are solved with different sizes of barges. The results (the box point in figures) are compared with the motion RAO obtained from the commercial solver (the blue line in figures). Figure 3-24, Figure 3-25 and Figure 3-26 show that the results almost follow the tendency of the line.

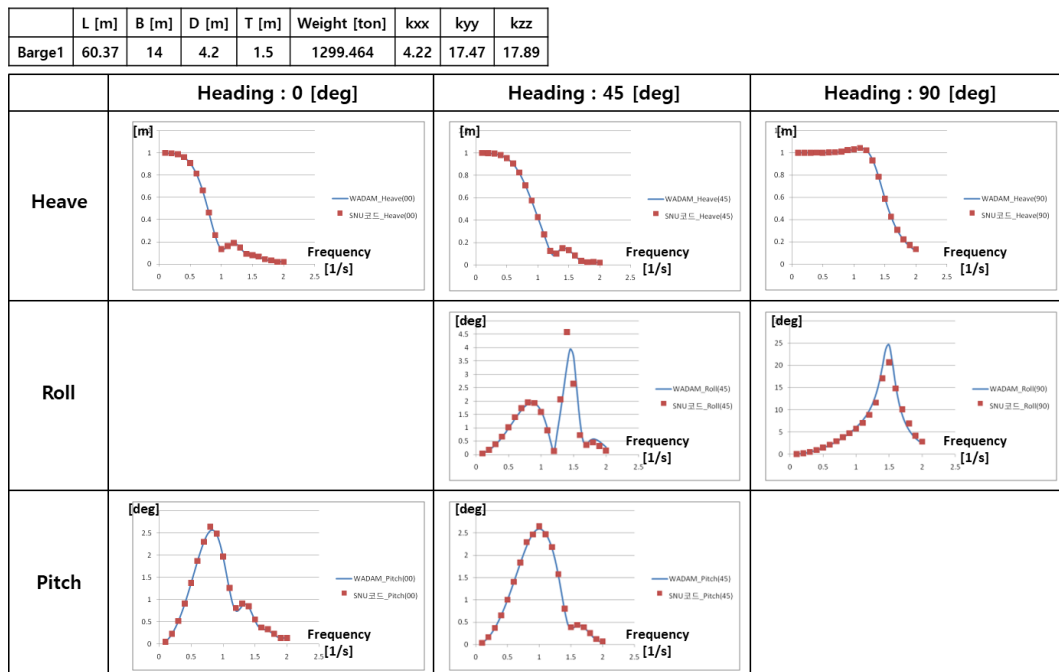


Figure 3-24. Motion RAO of the floating barge 1.

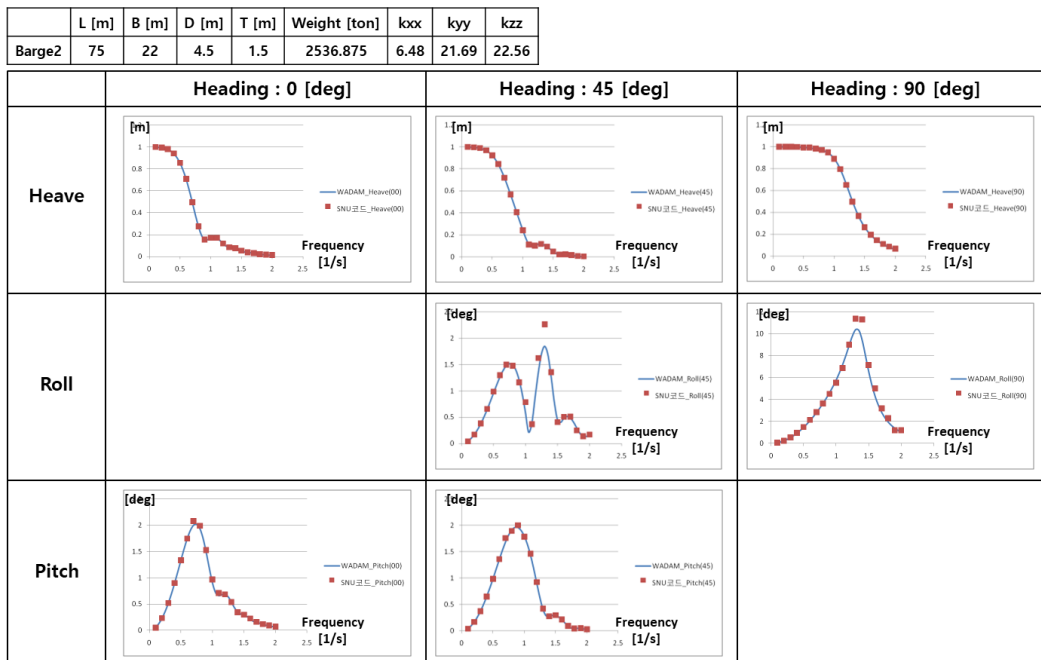


Figure 3-25. Motion RAO of the floating barge 2.

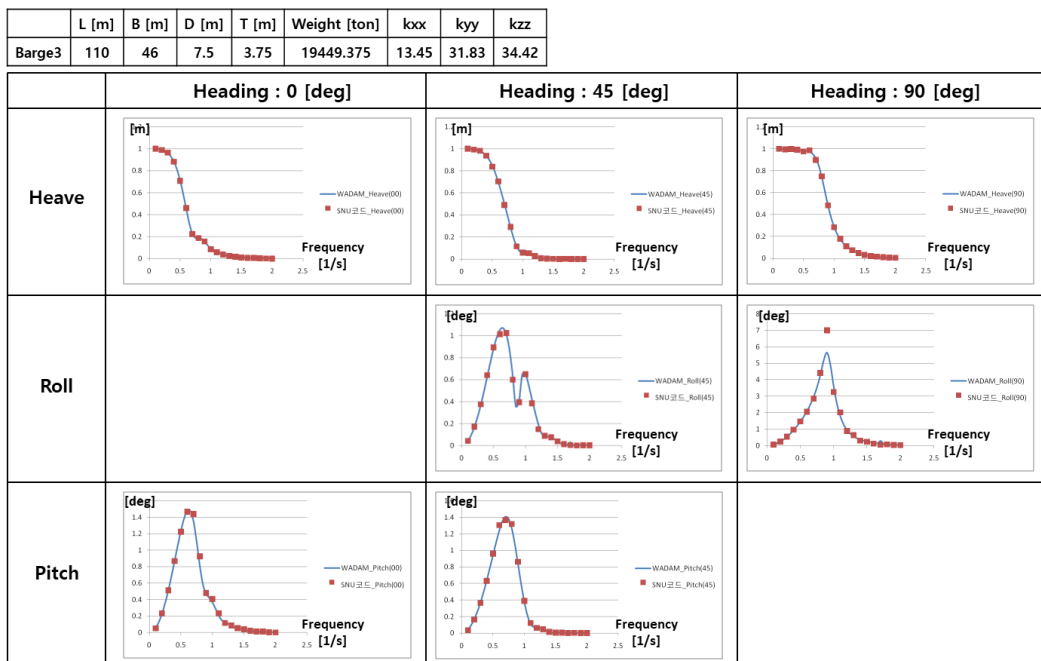


Figure 3-26. Motion RAO of the floating barge 3.

### 3.3.2. Barge motion by a regular wave (II)

We applied three regular waves to the floating barge, whose size is the same as that of the floating crane. The results are compared with SIMA [2]. We changed the heading angle as 0, 45, and 90 degrees with 1 m wave height and 10 sec wave period. Figure 3-27, Figure 3-28 and Figure 3-29 show the results. The graphs below show that the results from the mega floating crane simulator and the results from SIMA are almost identical.

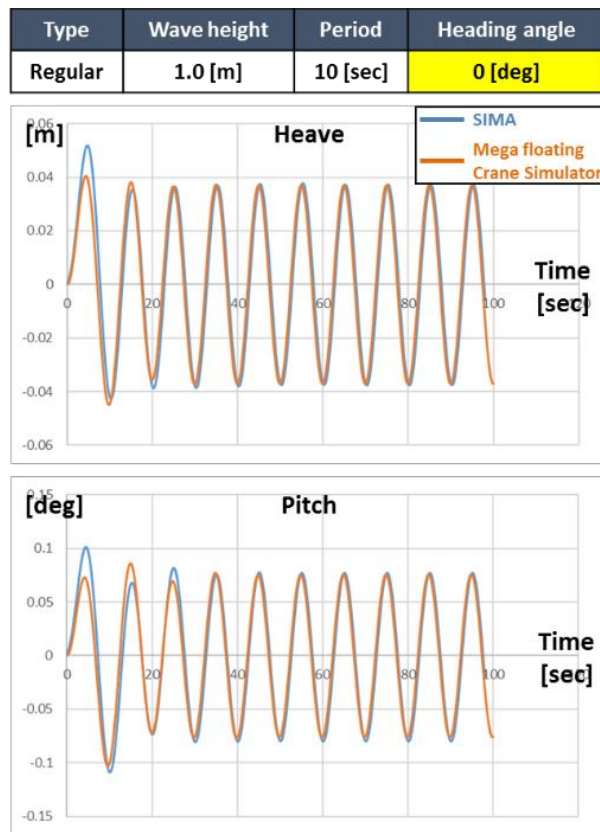


Figure 3-27. Verification of the barge motion with SIMA (heading angle 0 deg).

Type	Wave height	Period	Heading angle
Regular	1.0 [m]	10 [sec]	45 [deg]

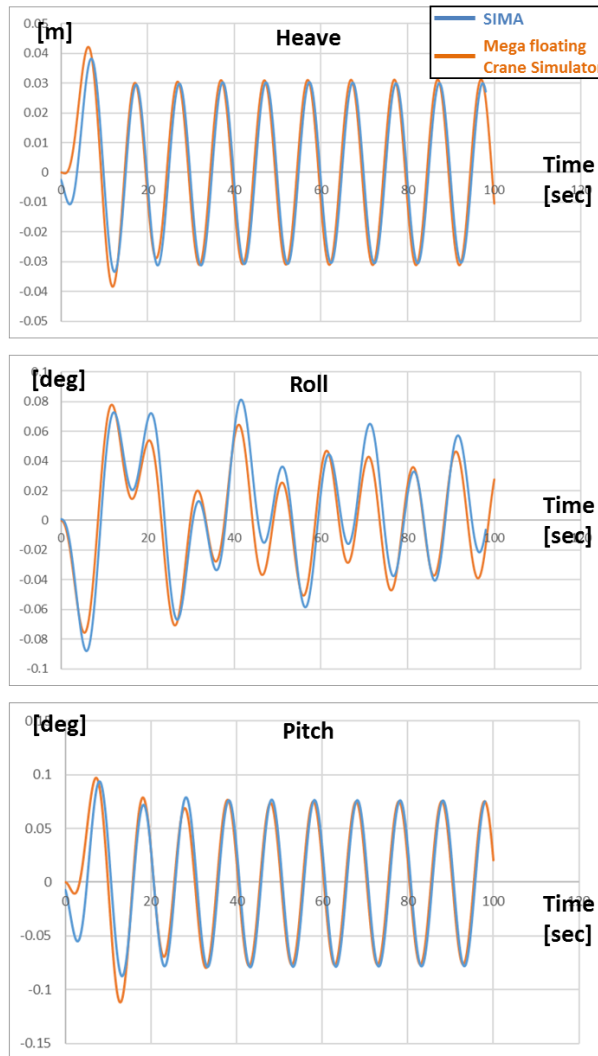


Figure 3-28. Verification of the barge motion with SIMA (heading angle 45 deg).



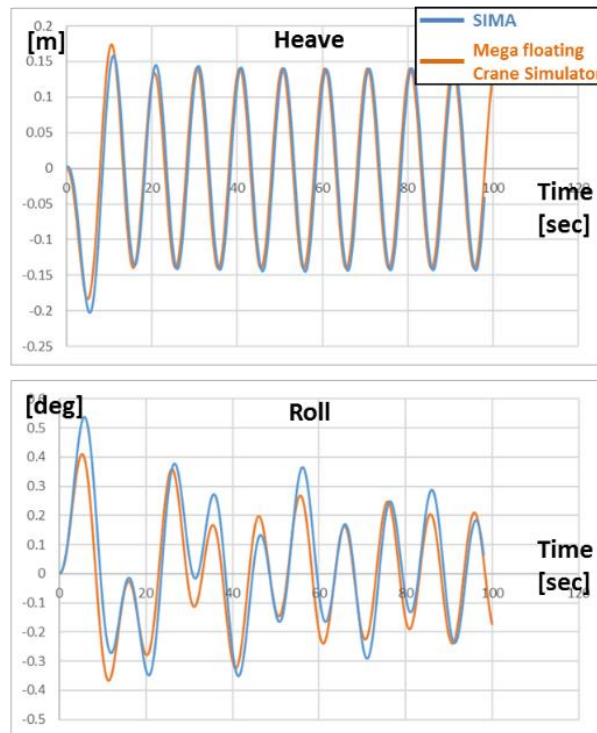


Figure 3-29. Verification of the barge motion with SIMA (heading angle 90 deg).

### 3.3.3. Barge motion connected by 4 springs

We applied several regular waves to the floating barge to verify the wave, wind, and current modules. These results were compared with OrcaFlex [3] this time. We connected four springs, to prevent the barge from being swept away. The pre-tension of each spring is set to 10 tons. Figure 3-30 shows how the barge is modeled in each program.

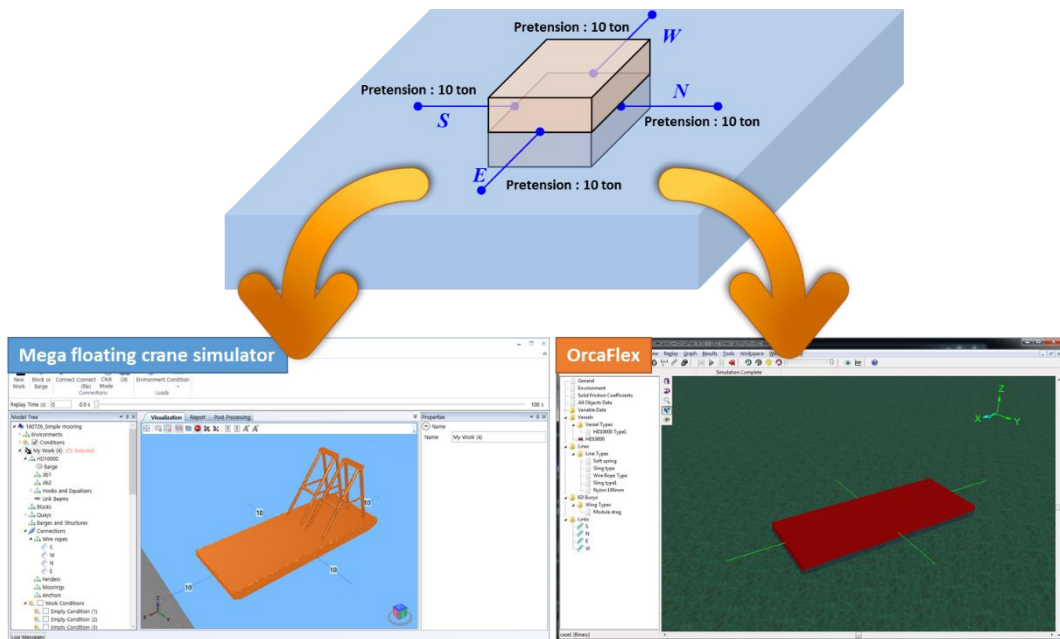


Figure 3-30. Modeling results in the mega floating crane simulator and OrcaFlex.

First, to verify the hydrodynamic force module, 9 cases were selected, as shown in Table 3-12.

Table 3-12. Simulation cases according to the wave conditions.

Case	Type	Height [m]	Period [sec]	Heading angle [deg]
1	Regular	1	8	0
2				30
3				90
4			10	0
5				30
6				90

Table 3-13 and Table 3-14 compare the motions and tensions, respectively. The gray cells are ignored according to the wave direction. The error (%) is less than 10 % in most of the cases.

Table 3-13. Comparison of motions according to the wave conditions.

Case		Surge [m]	Sway [m]	Heave [m]	Roll [deg]	Pitch [deg]	Yaw [deg]
Case 1	OrcaFlex	0.088	0.000	0.048	0.000	0.092	0.000
	Mega floating crane simulator	0.089	0.000	0.050	0.000	0.091	0.000
	Error (%)	-1.1	0.0	-4.2	0.0	1.1	0.0
Case 2	OrcaFlex	0.045	0.002	0.034	0.052	0.093	0.079
	Mega floating crane simulator	0.044	0.002	0.036	0.054	0.092	0.081
	Error (%)	2.2	0.0	-5.9	-3.8	1.1	-2.5
Case 3	OrcaFlex	0.000	0.331	0.139	0.474	0.000	0.000
	Mega floating crane simulator	0.001	0.331	0.145	0.483	0.000	0.000
	Error (%)	0.0	0.0	-4.3	-1.9	0.0	0.0
Case 4	OrcaFlex	0.102	0.000	0.072	0.000	0.180	0.000
	Mega floating crane simulator	0.107	0.000	0.076	0.000	0.187	0.000
	Error (%)	-4.9	0.0	-5.6	0.0	-3.9	0.0
Case 5	OrcaFlex	0.117	0.084	0.082	0.111	0.129	0.023
	Mega floating crane simulator	0.122	0.087	0.087	0.110	0.134	0.024
	Error (%)	-4.3	-3.6	-6.1	0.9	-3.9	-4.3
Case 6	OrcaFlex	0.000	0.481	0.268	0.952	0.000	0.000
	Mega floating crane simulator	0.000	0.482	0.280	0.971	0.000	0.000
	Error (%)	0.0	-0.2	-4.5	-2.0	0.0	0.0

Table 3-14. Comparison of tensions according to the wave conditions.

Case		S [kN]	N [kN]	E [kN]	W [kN]
Case 1	OrcaFlex	98.112	98.112	118.689	118.612
	Mega floating crane simulator	98.113	98.113	119.085	119.050
	Error (%)	0.0	0.0	-0.3	-0.4
Case 2	OrcaFlex	99.026	99.242	109.453	109.522
	Mega floating crane simulator	98.657	98.723	109.486	109.568
	Error (%)	0.4	0.5	0.0	0.0
Case 3	OrcaFlex	177.569	178.847	98.325	98.406
	Mega floating crane simulator	173.819	173.794	98.423	98.462
	Error (%)	2.1	2.8	-0.1	-0.1
Case 4	OrcaFlex	98.120	98.120	123.300	123.183
	Mega floating crane simulator	98.123	98.123	125.128	125.090
	Error (%)	0.0	0.0	-1.5	-1.5
Case 5	OrcaFlex	117.222	117.407	125.686	125.495
	Mega floating crane simulator	118.595	118.705	127.340	127.254
	Error (%)	-1.2	-1.1	-1.3	-1.4
Case 6	OrcaFlex	217.567	221.176	99.178	99.234
	Mega floating crane simulator	220.585	219.670	99.134	99.175
	Error (%)	-1.4	0.7	0.0	0.1

Second, to verify the wind force module, two cases were selected, as shown in Table 3-15.

Table 3-15. Simulation cases according to the wind conditions.

Case	Wind speed [m/s]	Wind direction [deg]
7	10	0
8		90

Table 3-16 and Table 3-17 compare the motions and tensions. In spite of the wave generation methods and random effects of phases, the results show that the errors (%) are within acceptable levels.

Table 3-16. Comparison of motions according to the wind conditions.

Case		Surge [m]	Sway [m]	Yaw [deg]
Case 7	OrcaFlex	0.567	0.000	0.000
	Mega floating crane simulator	0.565	0.000	0.000
	Error (%)	0.4	0.0	0.0
Case 8	OrcaFlex	0.038	0.475	0.858
	Mega floating crane simulator	0.040	0.484	0.853
	Error (%)	-5.2	-1.9	0.6

Table 3-17. Comparison of tensions according to the wind conditions.

Case		S [kN]	N [kN]	E [kN]	W [kN]
Case 7	OrcaFlex	99.697	112.719	0.000	682.960
	Mega floating crane simulator	100.703	111.642	0.000	682.601
	Error (%)	-1.0	1.0	0.0	0.1
Case 8	OrcaFlex	694.291	0.000	629.700	521.089
	Mega floating crane simulator	700.769	0.000	594.641	554.119
	Error (%)	-0.9	0.0	5.6	-6.3

Finally, to verify the current force module, three cases were selected as listed in Table 3-18.

Table 3-18. Simulation cases according to the current conditions.

Case	Current speed [m/s]	Current direction [deg]
9	1	0
10		30
11		90

Table 3-19 and Table 3-20 compare the motions and tensions. Comparison of the results also shows that they are very similar.

Table 3-19. Comparison of motions according to the current conditions.

Case		Surge [m]	Sway [m]	Yaw [deg]
Case 9	OrcaFlex	0.144	0.0000	0.0000
	Mega floating crane Simulator	0.144	0.0000	0.0000
	Error (%)	0.0	-	-
Case 10	OrcaFlex	0.141	0.196	-2.119
	Mega floating crane Simulator	0.134	0.202	-2.119
	Error (%)	5.0	-2.9	0.0
Case 11	OrcaFlex	-0.007	0.701	0.025
	Mega floating crane Simulator	-0.007	0.701	0.026
	Error (%)	0.0	0.0	-4.0

Table 3-20. Comparison of tensions according to the current conditions.

Case		S [kN]	N [kN]	E [kN]	W [kN]
Case 9	OrcaFlex	98.1884	98.1884	36.4886	159.7114
	Mega floating crane Simulator	98.1885	98.1885	36.4793	159.7207
	Error (%)	0.0	0.0	0.0	0.0
Case 10	OrcaFlex	198.1347	33.1688	107.2660	239.6341
	Mega floating crane Simulator	200.6350	30.6517	110.4845	236.4443
	Error (%)	-1.3	7.6	-3.0	1.3
Case 11	OrcaFlex	399.0217	0.0000	103.4241	96.9959
	Mega floating crane Simulator	399.0813	0.0000	103.5041	96.9422
	Error (%)	0.0	0.0	-0.1	0.1

### 3.4. Verification of catenary mooring

The catenary mooring is verified by comparing the initial profile of this study with that of OrcaFlex [3]. When the depth, tension at the end and axial stiffness are given, we can obtain total length and length on the seabed. The meaning of each term is depicted in Figure 3-31.

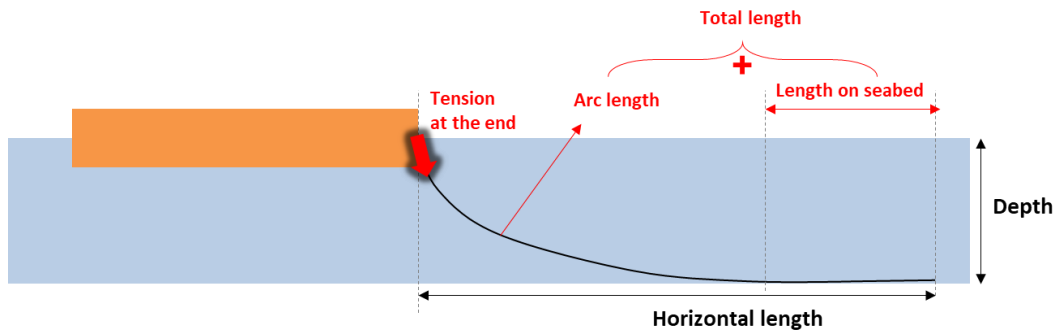


Figure 3-31. Profile of catenary mooring.

The results are summarized in Table 3-21. Errors between the output values from SyMAP and OrcaFlex is less than 1.0 %.

Table 3-21. Summary of verification for catenary mooring.

Input data					Output value		
Tension at the end [m]	Weight per length [m]	Axial stiffness [kN/m]	Depth [m]	Horizontal length [m]		Total length [m]	Length on seabed [m]
5.0	19.1	215,893	12	400	SyMAP	401.23	322.79
					OrcaFlex	401.09	322.14
					Error (%)	0.03	0.20
	18	213,622	15	300	SyMAP	301.67	211.53
					OrcaFlex	301.53	210.06
					Error (%)	0.05	0.69
	22.8	270,375	11	350	SyMAP	351.18	282.55
					OrcaFlex	351.08	283.11
					Error (%)	0.03	-0.20

### 3.5. Validation by real operation (1) – Module erection

In this section, we present modeling, scenario, and simulation results of the module erection. The views and tensions among the simulation results are compared with the data collected in the real operation.

#### 3.5.1. Modeling

For the erection simulation, several models should be prepared. Figure 3-32 shows the overall models included in the erection simulation.

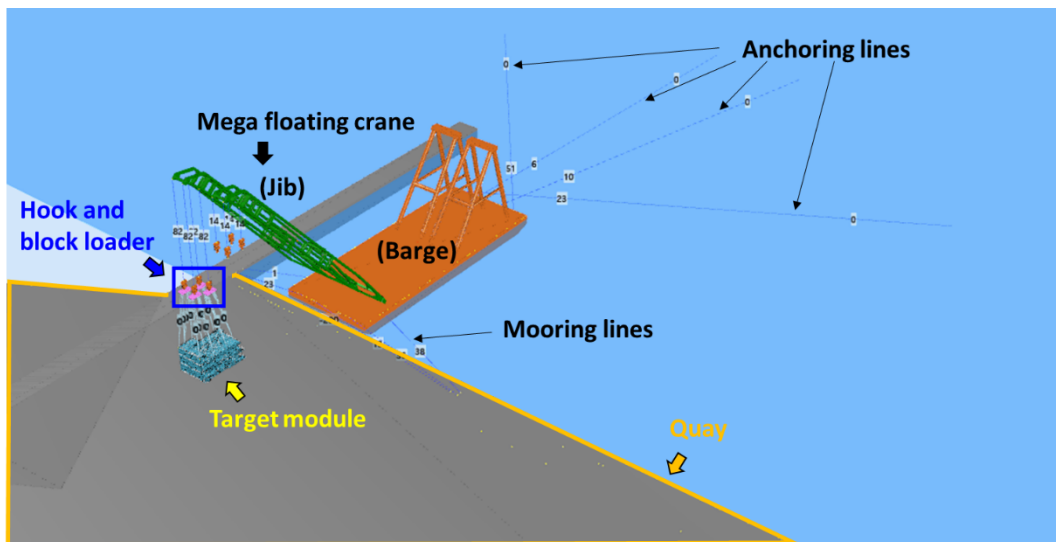


Figure 3-32. Overall models included in the erection simulation.

Figure 3-33 shows the main dimensions and weight of the target modules. The length, breadth, and height of the target module are about 38 m, 28 m, and 20 m, respectively. The weight is about 1,411 ton. This model is exported from the CAD database in the shipyard.



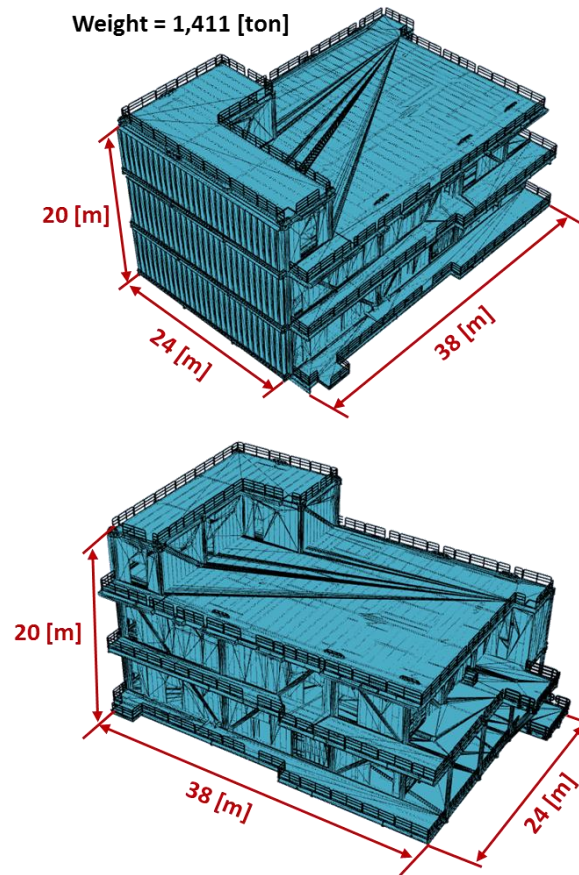


Figure 3-33. Main dimensions and weight of the target module.

The mega floating crane is composed of the barge, two jibs, eight hooks, and the lifting load, which are connected by hinge joints and wire ropes. Every time the simulation is performed, it takes much effort and time to model the components of the mega floating crane. Therefore, the mega floating crane is modeled by default as shown in Figure 3-34.

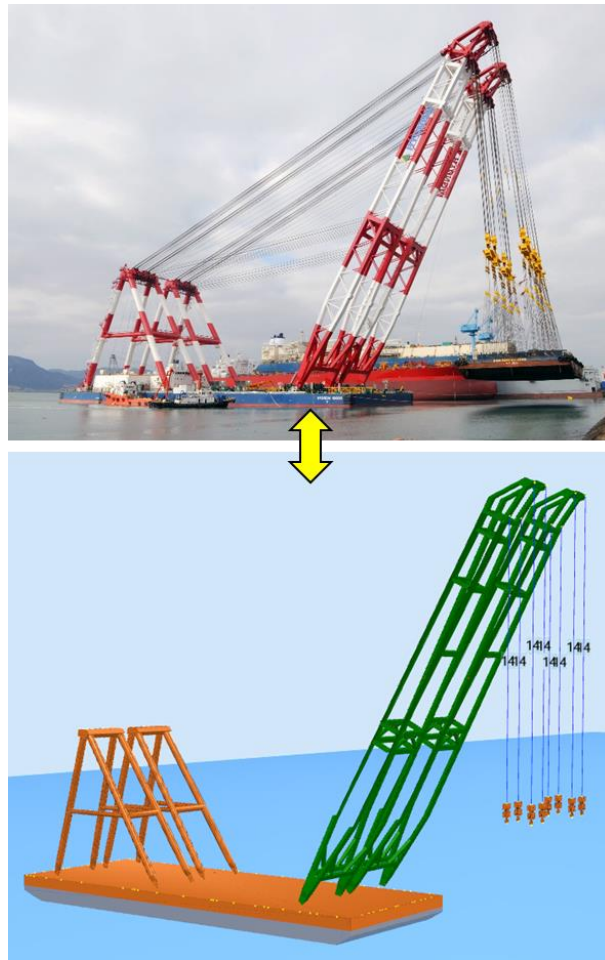


Figure 3-34. Model of the mega floating crane.

Because one hook capacity is 1,250 [ton], two hooks are enough to lift the target module. However, the production engineer decided to use four hooks hanging on one jib, considering the size of the target module. Figure 3-35 shows the names of the four hooks used in operation.

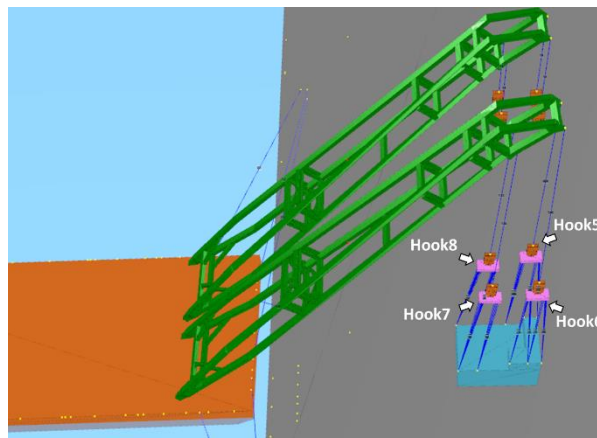


Figure 3-35. The names of the four hooks used in operation.

There are a total of 32 connection points per one block loader. Two or more lines are normally connected to one lug. In this operation, four lines from the block loader are connected to one lug on the target module, and 2 or 3 lugs are connected to one block loader. Figure 3-36 shows that the wire ropes are connected correctly according to the connection plan.

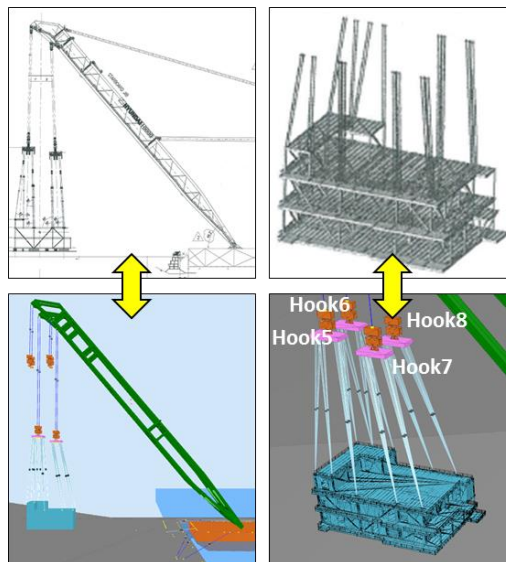


Figure 3-36. Connection plan and simulation views between hooks and the module.

The mooring and anchoring lines are modeled with reference to the drawing. 6 mooring lines connect from the bow of the floating crane to the bitt on the quay. 4 anchoring lines connect from the stern of the floating crane to the seabed. Figure 3-37 shows the mooring/anchoring plan and the simulation view.

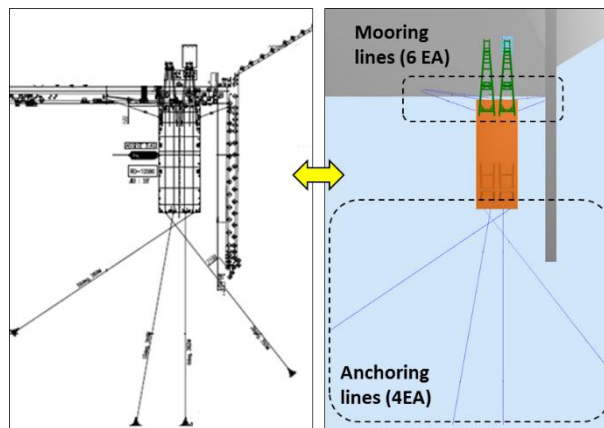


Figure 3-37. Mooring/anchoring plan and simulation views.

### 3.5.2. Scenario

During the real operation, the weather data is gathered for 600 seconds (= 10 minutes).

Figure 3-38 shows the wind speed and direction.

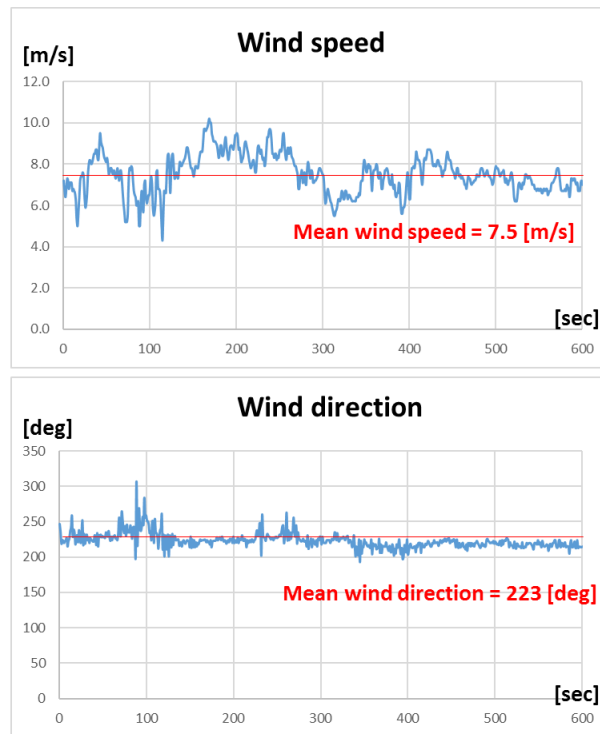


Figure 3-38. Graphs of the wind speed and the wind direction.

The mean wind speed for 10 minutes is about 7.5 m/s, and the mean wind direction is 223 deg. Therefore, we use these mean values as inputs to calculate the wind force in the erection simulation. Meanwhile, we use the significant wave height 0.1 m and the mean period 2 sec, which were announced by the weather forecast on the operation day.

For the operation scenario, the hoisting speed of the hooks is about 3 ~ 5 m/min, which is the operation standard in the shipyard. Therefore, we set the hoisting speed as 3 m/min (= 0.05 m/s). Figure 3-39 shows the simulation results from the different viewpoints.

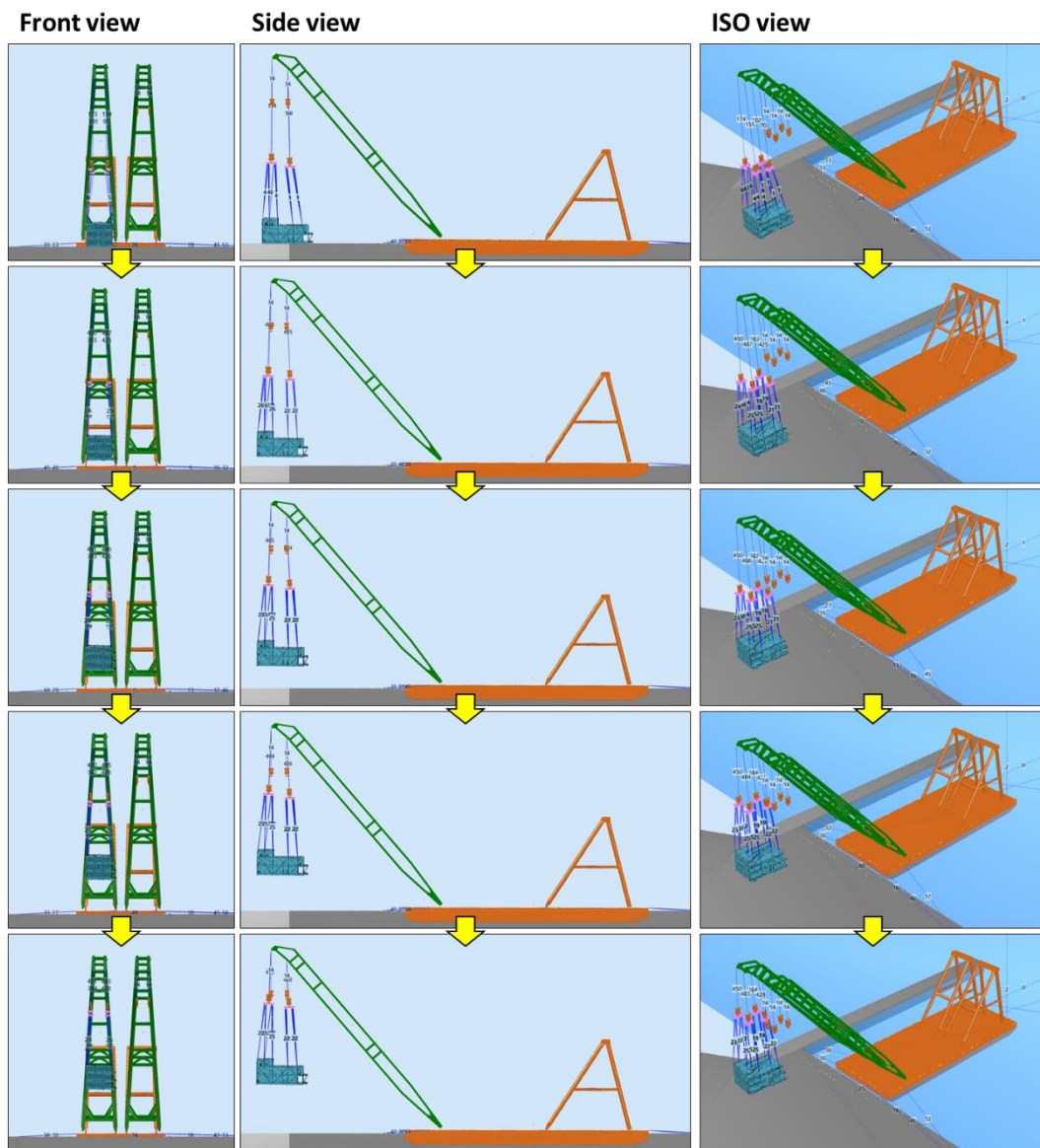


Figure 3-39. Simulation results from the different viewpoints.

### 3.5.3. Comparison of the posture by images

In this section, we present images of the real operation and the simulation to compare the posture during operation. First, the target module is laid on the quay (Figure 3-40).

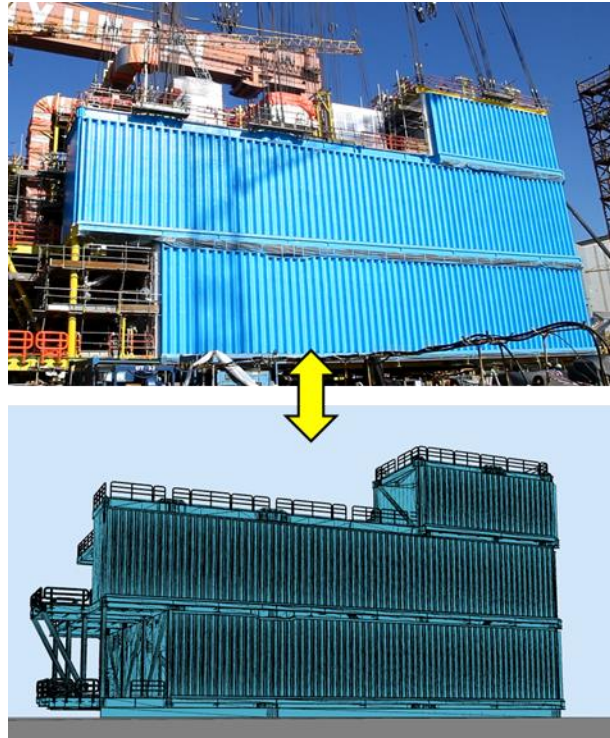


Figure 3-40. Comparison of the target module laid on the quay.

As the operation starts, the target module takes off from the ground and keeps on moving upward. Figure 3-41 shows the comparison result of the posture in the air.



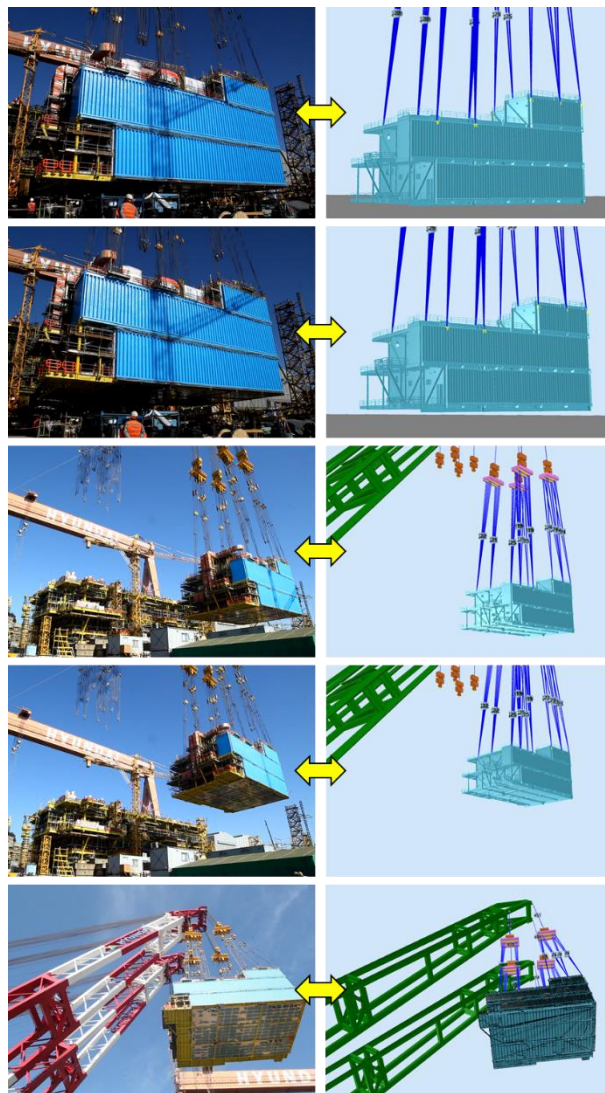


Figure 3-41. Comparison of the target module lifted by the mega floating crane.

### 3.5.4. Comparison of tensions

In this section, the wire rope tensions of each hook are compared with the tension obtained by the simulation. The first graph shown in Figure 3-42 is the total tension, which is the sum of all the results.



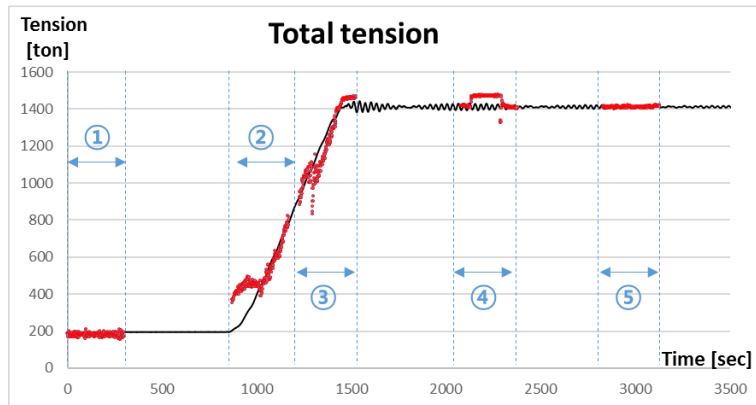


Figure 3-42. Graph of the total tension during module erection.

The mega floating crane does not have any recording system. Therefore, the hook tensions are recorded 5 times for 5 minutes by the video camera inside the operation room. The markers ①~⑤ in Figure 3-42 indicate the recorded data that are marked by red dots. The graph shows that the comparison is not exactly identical to the simulation results. However, it gives sufficient implications for validation. From this result, we can judge that the simulation results show a very similar tendency when compared with the real operation.

Figure 3-43 shows the tension graphs of each hook. Because the center of gravity of the target module at the operation time could be slightly different from the initial estimation, and the way to control the hook height could affect the hook tension, the simulation results differ slightly from the recorded data. However, the comparison can be interpreted to show that the simulation results are consistent with the real operation in terms of the tendency.

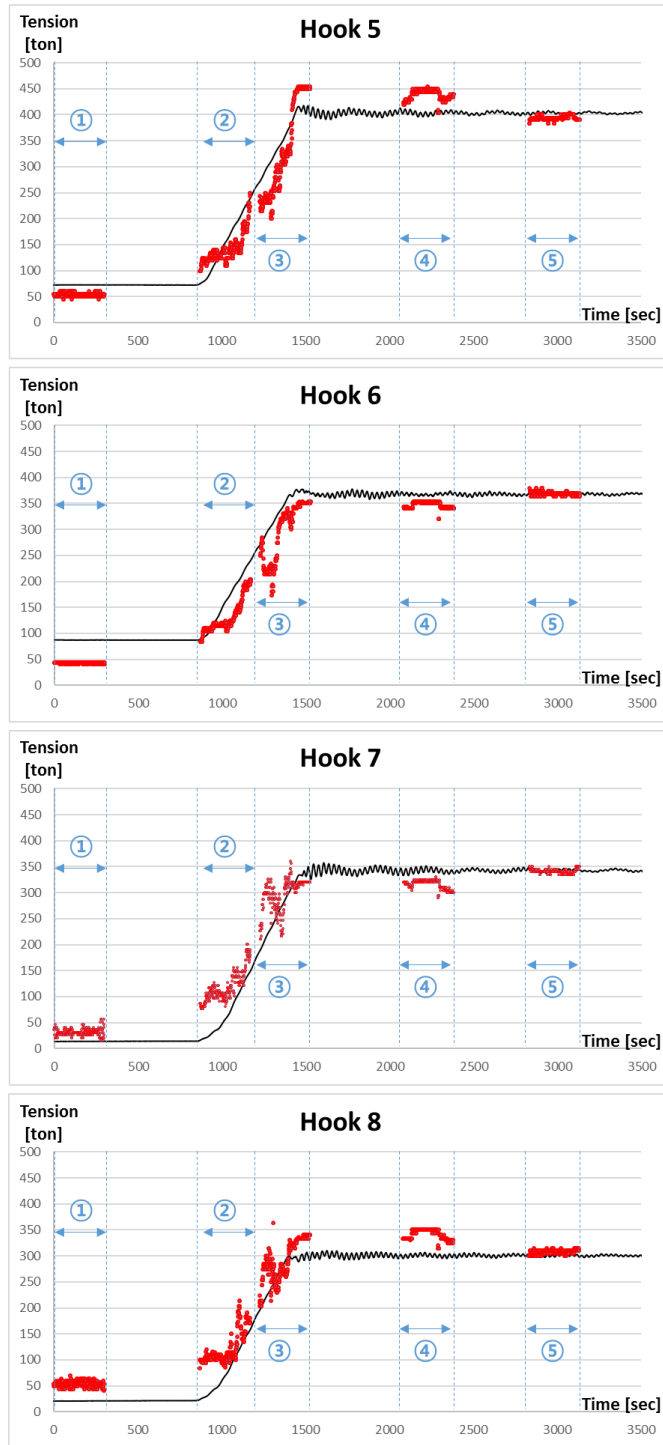


Figure 3-43. Graph of the wire rope tension of hooks 5, 6, 7 and 8.

### 3.6. Validation by real operation (2) – LQ erection

In this section, we present modeling, scenario, and simulation results of the LQ (Living Quarter) erection.

#### 3.6.1. Modeling

The LQ upper part is a huge structure as shown in Figure 3-44, which weight is 2,356.6 ton, and length, breadth, and height are about 52.8 m, 32.4 m and 11.65 m, respectively.

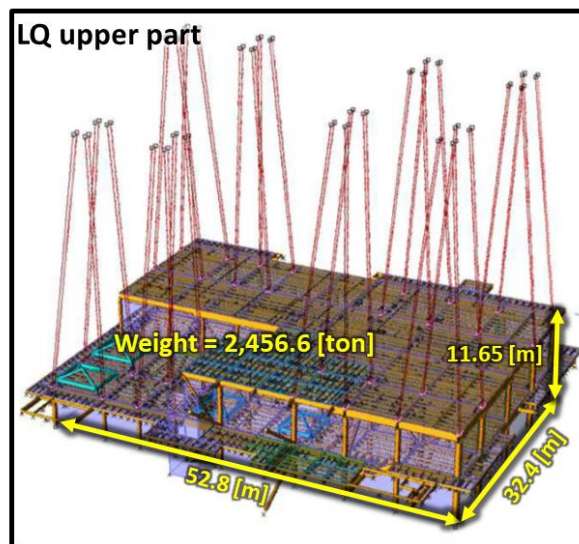


Figure 3-44. Model of LQ upper part.

This model is exported from the CAD database in the shipyard and is imported in SyMAP as shown in Figure 3-45. The same floating crane used in the previous validation is also selected for the erection. Figure 3-45 shows that overall models and connections are appropriately arranged.

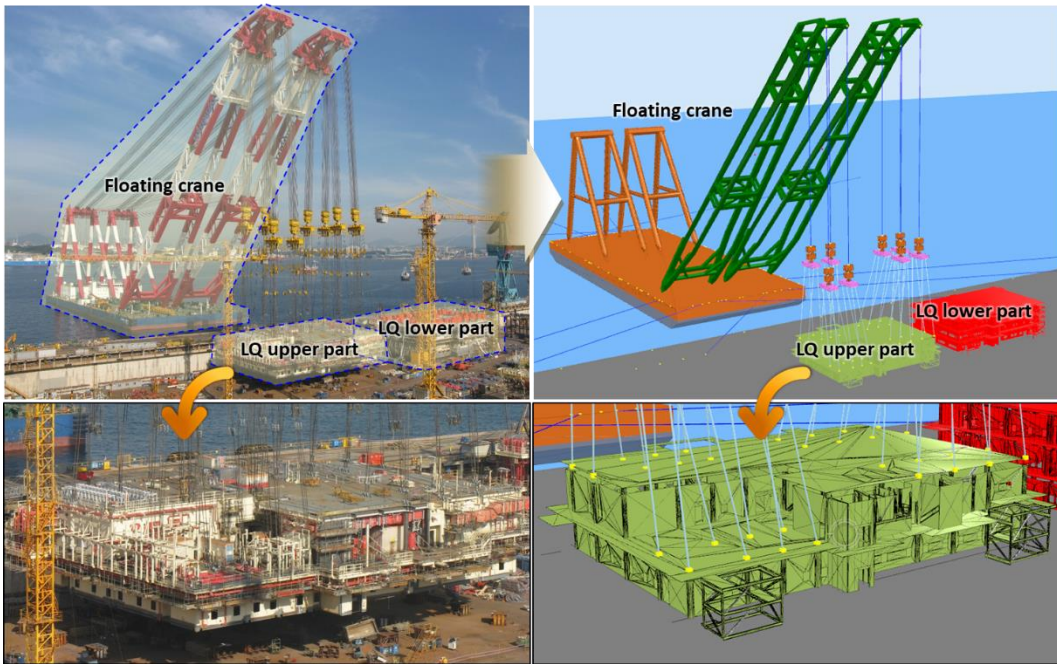


Figure 3-45. Overall models and connections.

The mooring and anchoring lines are modeled with reference to the drawing (Figure 3-46). 6 mooring lines connect from the bow of the floating crane to the bitt on the quay. 4 anchoring lines connect from the stern of the floating crane to the seabed.

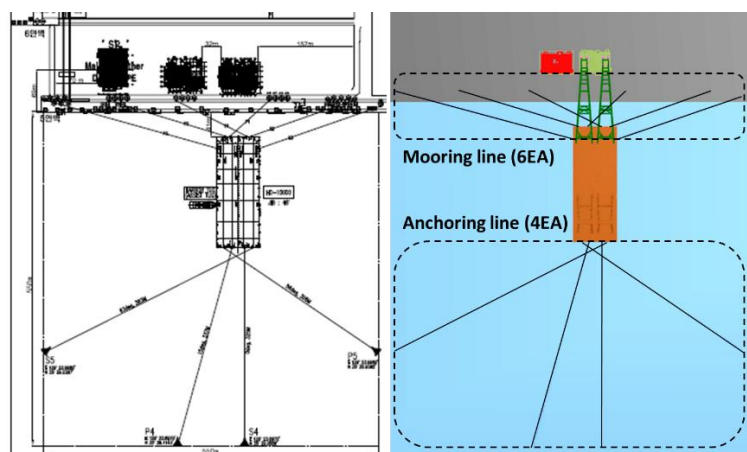


Figure 3-46. Mooring/anchoring plan and simulation views.

### 3.6.2. Operation sequence

Figure 3-47 shows the operation sequence in the real world.

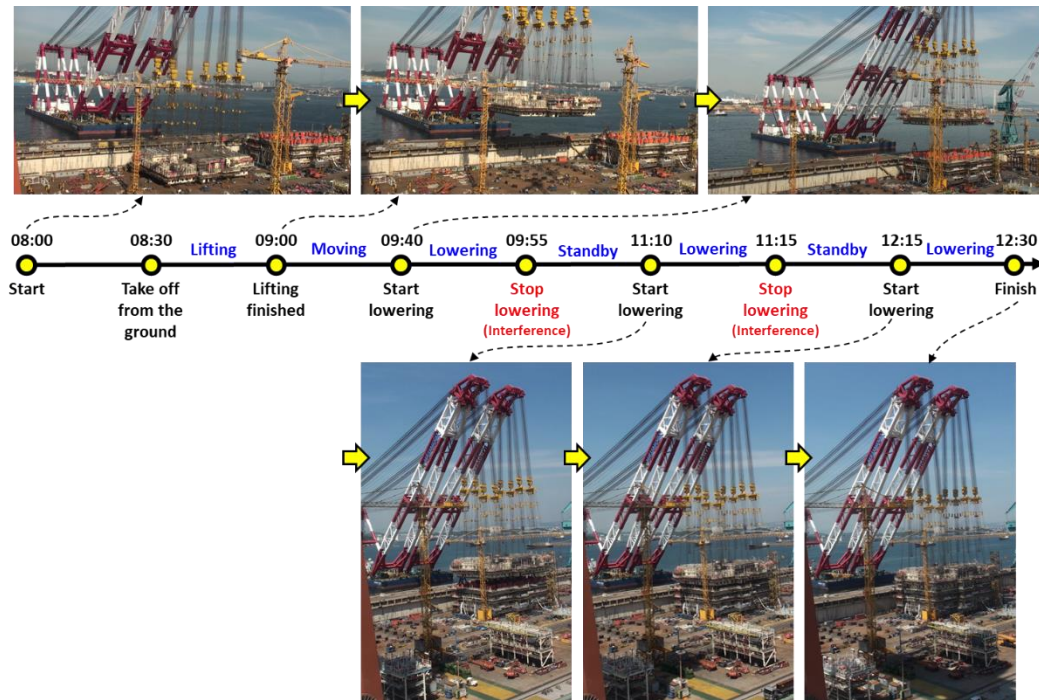


Figure 3-47 Operation sequence in real world.

The operation started at a.m. 8:00. Hoisting up the hook for 30 minutes, the bottom of the LQ upper part took off from the ground. For next half an hour, the LQ upper part is lifted up. And then, the floating crane moved toward the LQ lower part. For the few hours, the lowering operation was conducted. The lowering took much time due to interference between the lower and upper part of the LQ.

During the operation, we acquired the tensions of the hooks. Because there is no recording system in the floating crane, we recorded the screen by the camcorder. Total tension includes the weights of hooks, and equalizer as well as the LQ upper part.



Figure 3-48. Tensions of the hooks displayed on the screen.

### 3.6.3. Comparison of tensions

In this section, the wire rope tensions of each hook are compared with the tension obtained by the simulation. The graph shown in Figure 3-49 is the total tension, which is the sum of all the results. The graphs shown in Figure 3-50 show the sum of two pairs of hooks.

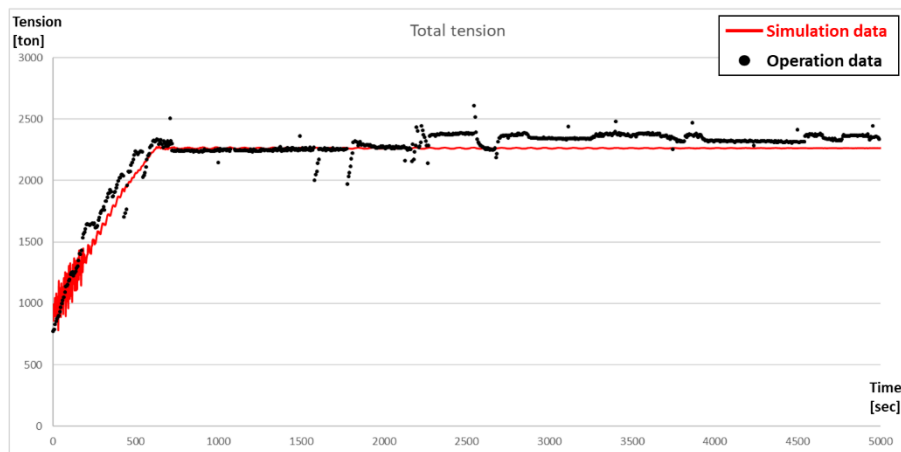


Figure 3-49. Graphs of the total tension during LQ upper part erection.



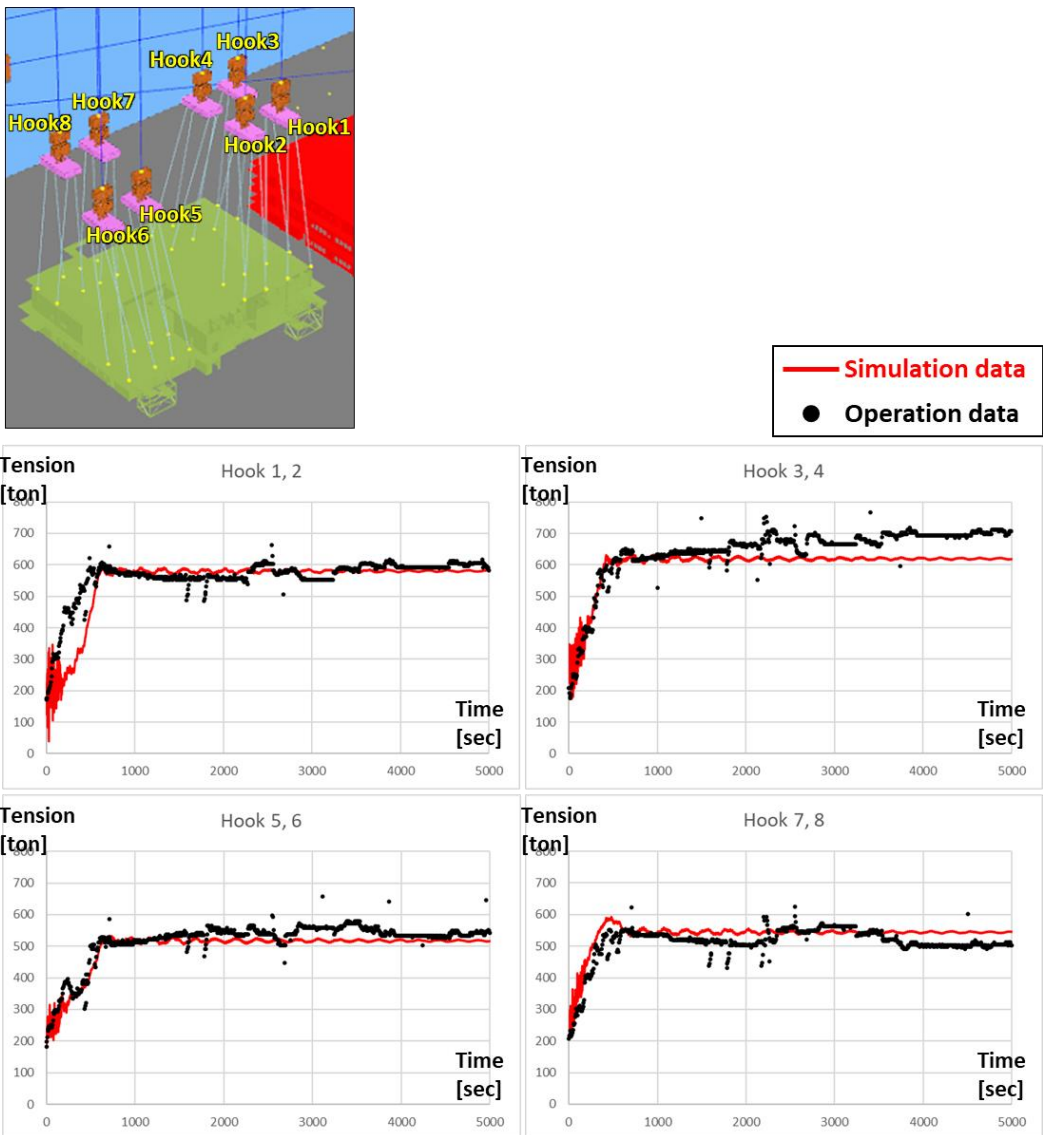


Figure 3-50. Graph of the wire rope tension of two pairs of hooks.

During the real operation, the uncertainty of the recording sensors and environmental conditions induce the unexpected dot on the graph. However, we conclude that the tensions are within the acceptable range of accuracy.

## **4. Applications**

This section will provide four representative applications such as block lifting using equalizers, LPG tank erection considering a collision, thin plate block lifting considering deformation, and block offloading using SPMT which have not been solved before.

### **4.1. Block lifting using equalizers**

This section presents the two load lifting simulations using a Goliath crane and a floating crane, which are commonly used in shipbuilding.

#### **4.1.1. Load lifting simulation using a gantry crane**

The first application is load lifting simulation using a gantry crane to erect loads from a pre-erection area to the dock. It is widely used in shipyards.

Figure 4-1 shows the modeling of the load, the dock, and the gantry crane. At the top of the crane, there are lower and upper trolleys. Three equalizers are suspended by the trolleys. The load model was exported from ship CAD data, including hull plates and outfitting. Its size is  $43 \times 23 \times 11$  m (length  $\times$  breadth  $\times$  height), and its weight is 350 ton.





Figure 4-3 shows the pulley height change of the equalizer during the simulation. At the first time point, the heights of the equalizer moving pulleys are at the same level. However, to control the wire rope tension equally, the pulleys are moved up and down.

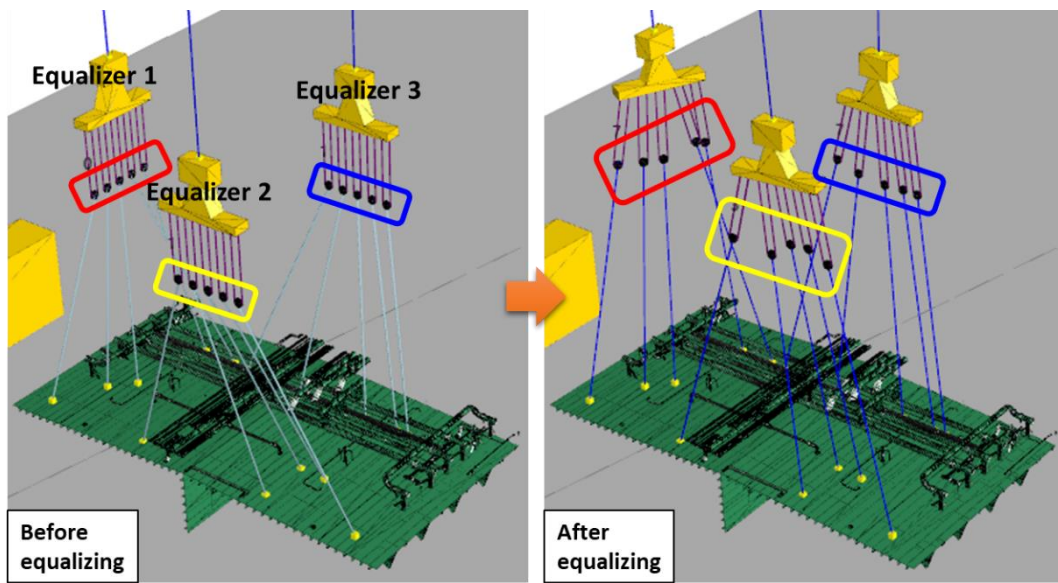


Figure 4-3. Height change of pulleys of the equalizer during the simulation.

Simulation procedure of load lifting using the equalizer is summarized in Figure 4-4. From Figure 4-4 (1) to (3), the three equalizers move to their equilibrium positions and orientations. From Figure 4-4 (4) to (6), the load lifts off the ground.

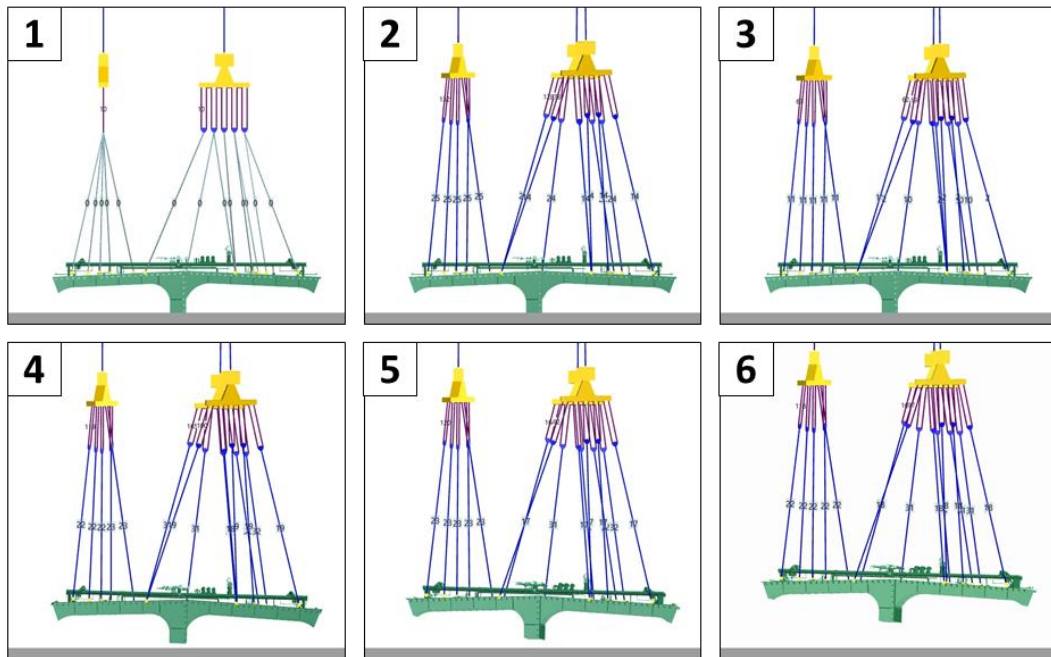


Figure 4-4. Simulation procedure of load lifting using the Goliath crane.

The wire rope tensions between the load and each equalizer are shown in Figure 4-5. The five lines of the wire ropes in the graphs almost overlap. If one of the tensions goes high, the others are also increased in a moment. Thus, the wire rope tensions become similar even though they show oscillating results during lifting the load.

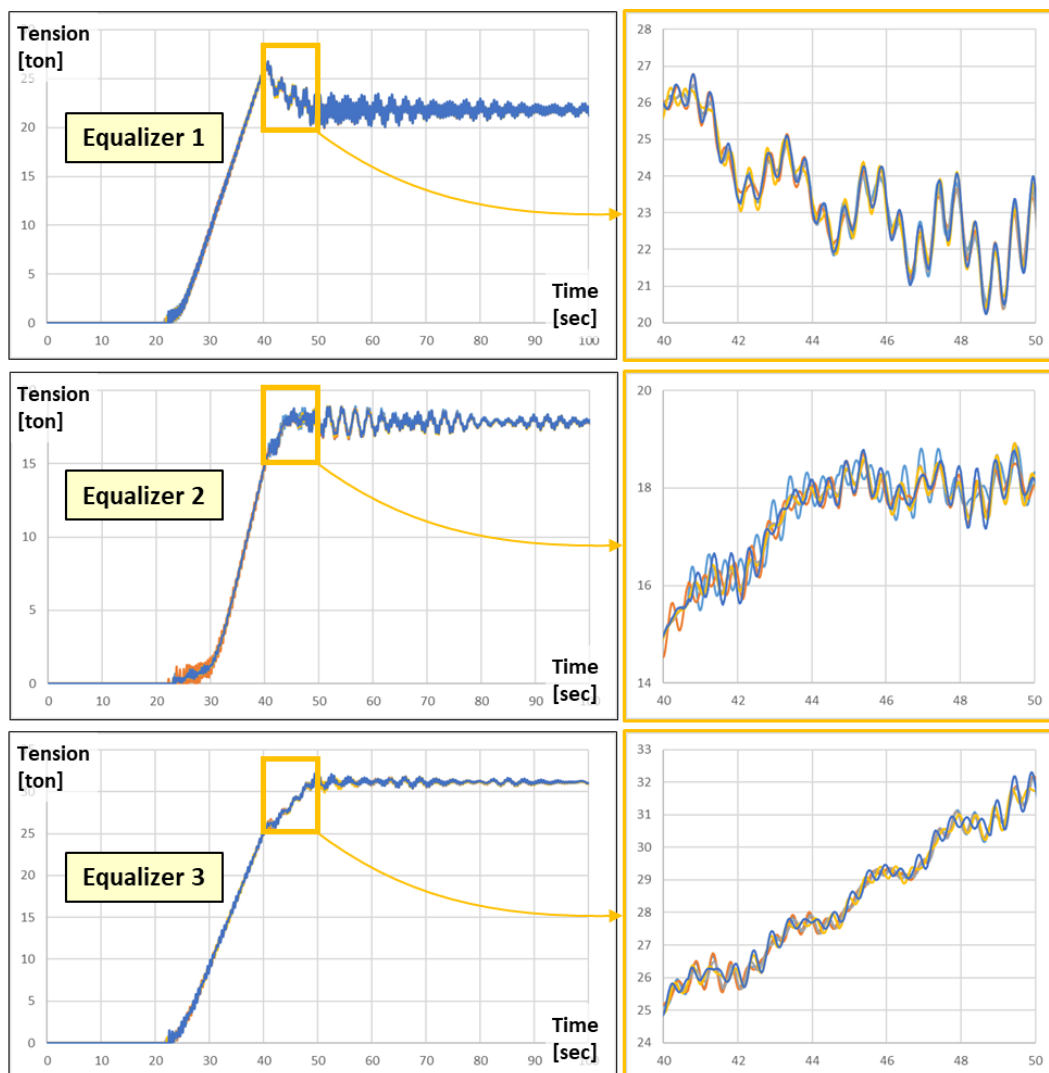


Figure 4-5. Graphs of wire rope tensions between the load and each equalizer.

#### 4.1.2. Load lifting simulation using a floating crane

The second application is a load lifting simulation using a floating crane. As the weight and size of erected loads and modules of the offshore project have increased, floating cranes have recently been used to lift heavy loads, exceeding 1,000 tons.

Figure 4-6 shows the modeling of the load and the floating crane. In this simulation, a 3,600-ton capacity floating crane with four hooks and equalizers, possessed by many shipbuilding companies, was used. The load model was also exported from ship CAD data including hull plates and outfitting. Its size is  $34 \times 27 \times 11$  m (length  $\times$  breadth  $\times$  height), and its weight is 1,000 ton. The wave condition is assumed that the direction is 0 deg (following sea) and wave type is irregular wave based on JONSWAP spectrum which significant wave height is 1.65 m and peak period is 6.12 sec.

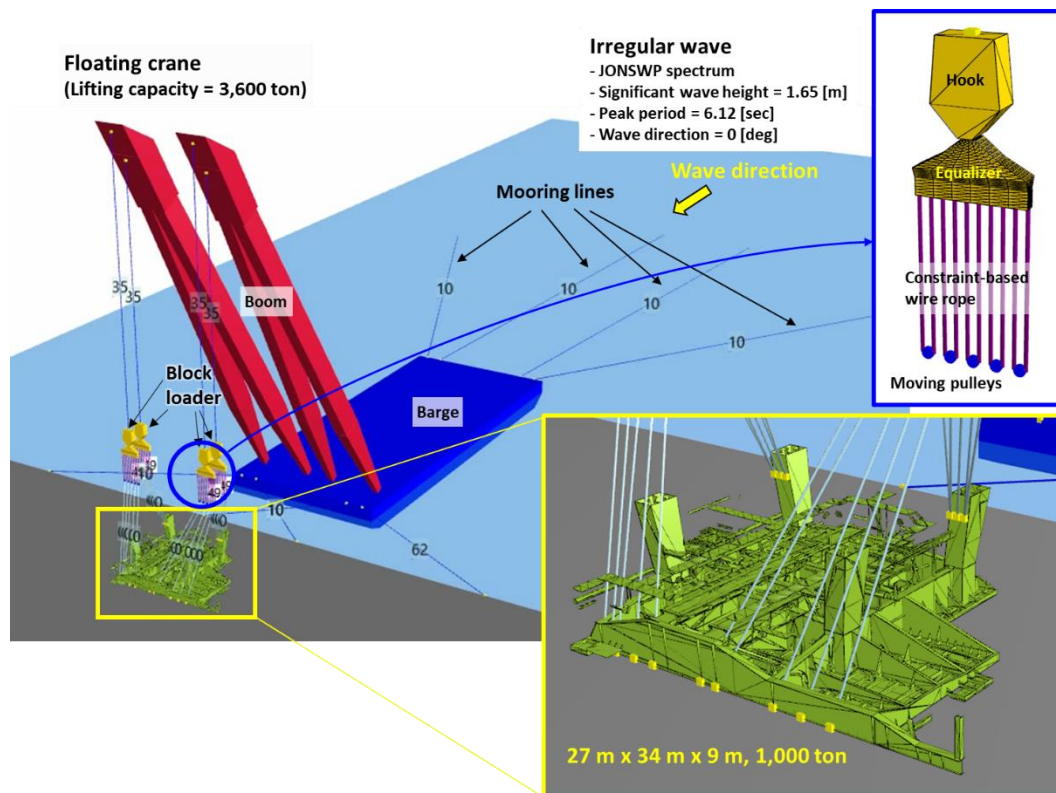


Figure 4-6. Modeling of load lifting using a floating crane.

We used the same equalizers as in the previous example. In total, 20 connection points of the load are connected to four equalizers, as shown in Figure 4-7.

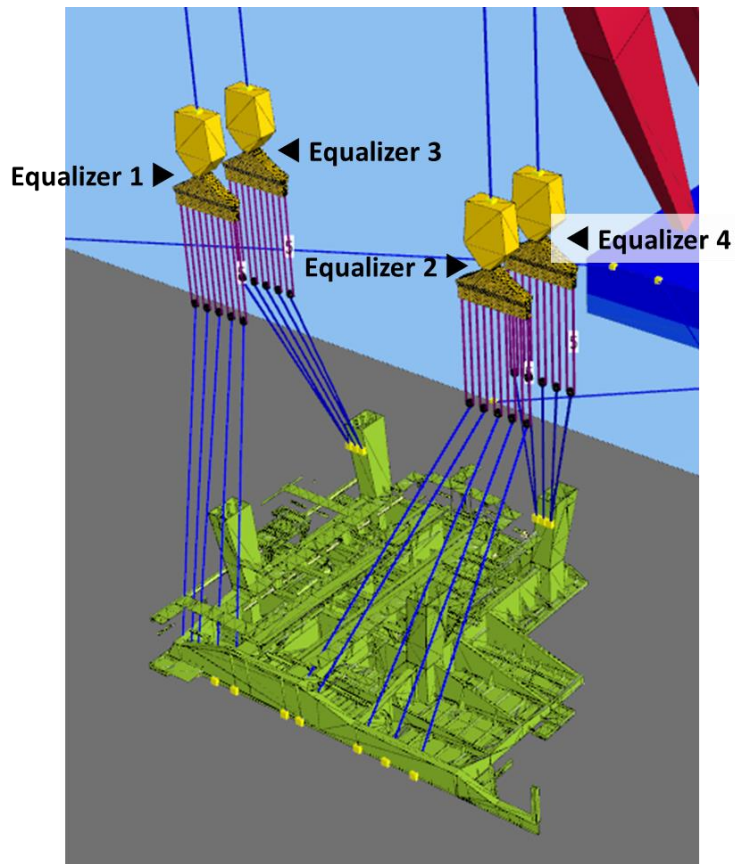


Figure 4-7. Wire ropes connected between the load and four equalizers.

Figure 4-8 shows the equalizers before and after equalizing. Before equalizing, the heights of the moving pulleys of the equalizers are at the same level. However, after equalizing, the pulleys move up and down to find equilibrium positions.



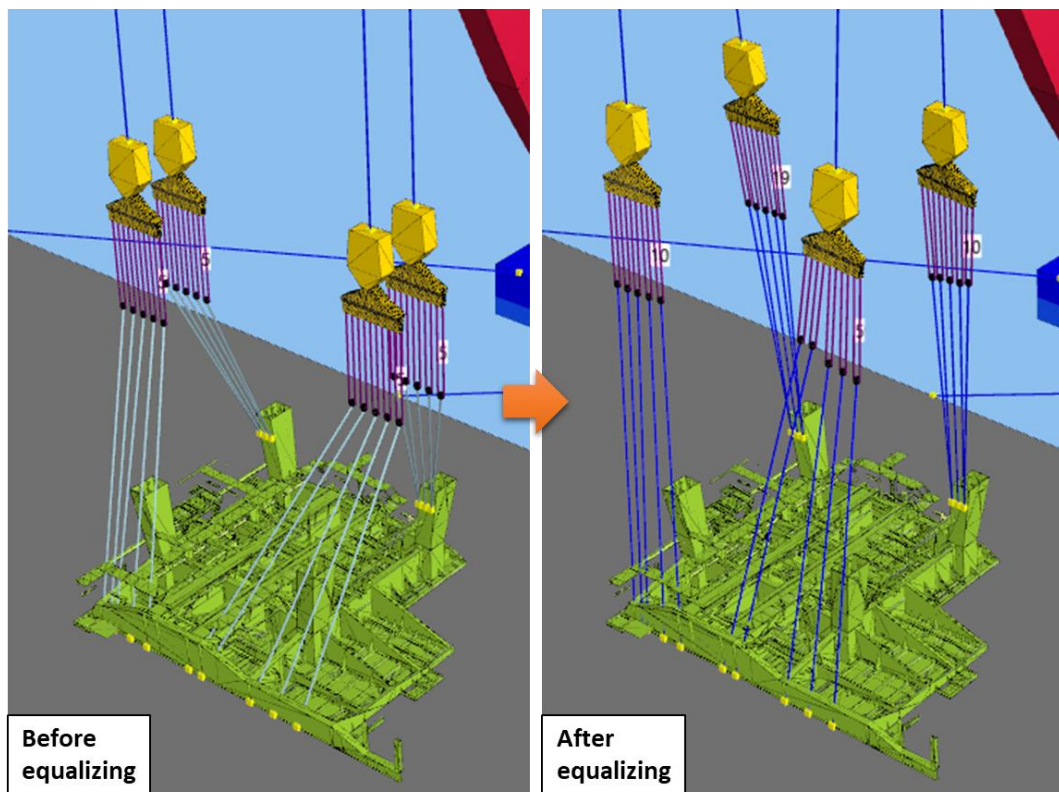


Figure 4-8. Position change of the equalizers before and after equalizing.

The wire rope tensions between the load and each equalizer are shown in Figure 4-9. Even though the wave induces the motion of the floating crane and the block, the five lines of the wire ropes in the graphs almost overlap as expected.

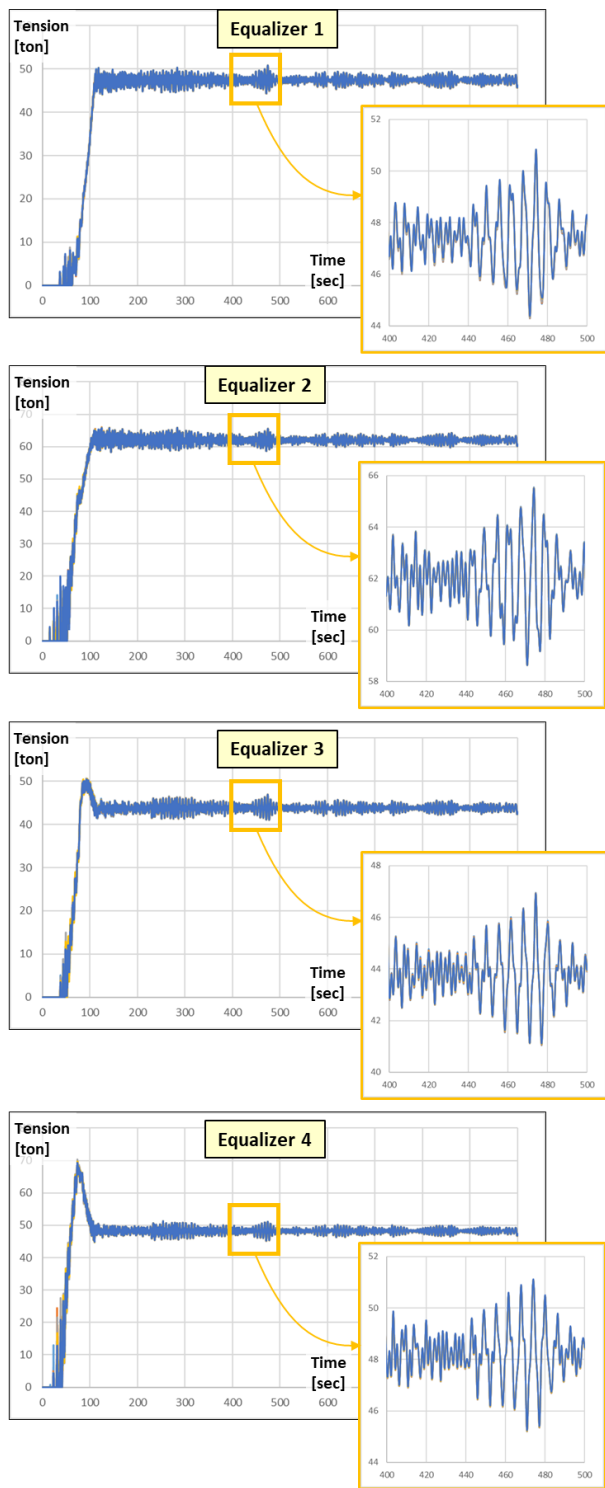


Figure 4-9. Graphs of wire rope tensions between the load and each equalizer.



## 4.2. LPG tank erection considering collision

This section presents the dynamic analysis of the LPG tank erection inside the hull structure by the floating crane. Figure 4-10 shows the modeling result. The floating crane has four block loaders. Each block loader is connected to the LPG tank with five wire ropes. When the simulation starts, the LPG tank is lowered into the hull structure.

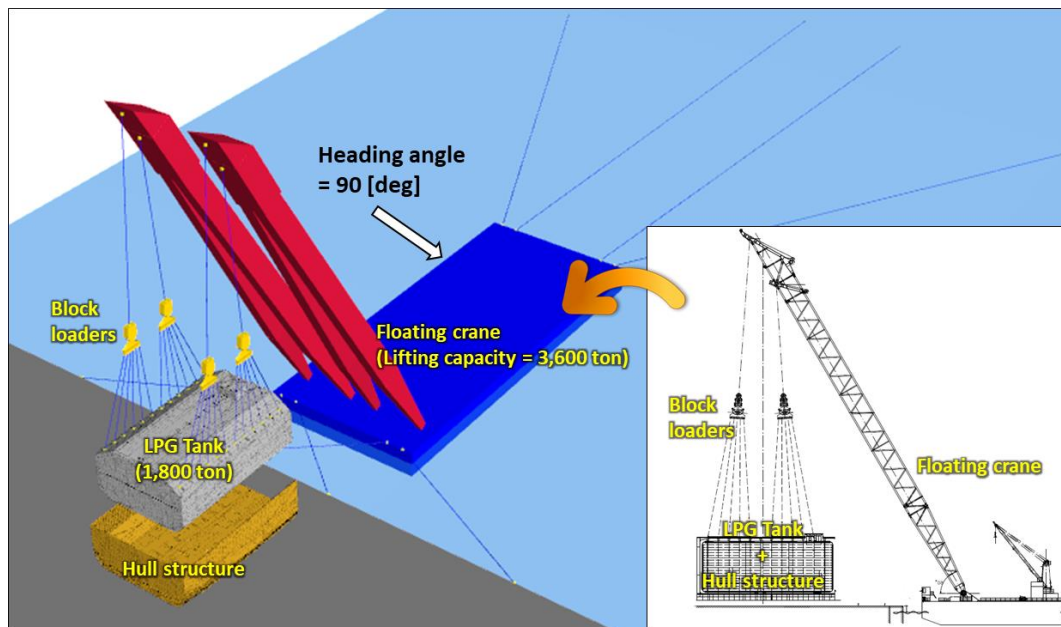


Figure 4-10. Modeling of LPG tank, hull structure, and the floating crane.

The left, right sides, and the bottom of LPG tank, and the hull structure participate in the collision. Therefore, unnecessary meshes are ignored by using the exclusion boxes, as shown in Figure 4-11. The number of meshes of LPG tank and the hull structure is reduced to 1,352 and 2,916, respectively.

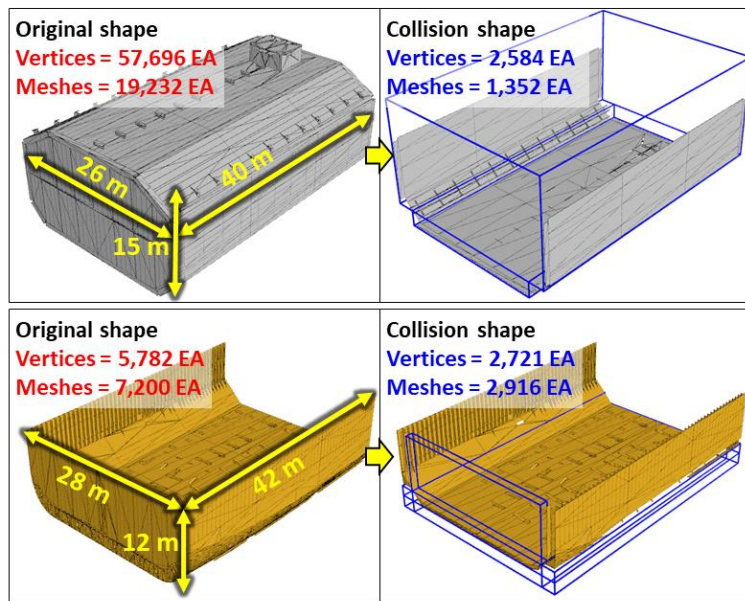


Figure 4-11. Original and collision shape using exclusion boxes.

The collision detection and response between the LPG tank and the hull structure are applied according to various wave conditions. The wave conditions are summarized in Table 4-1. The heading angle is fixed to 90°, which is marked in Figure 4-10. From Case 1 to 4, we will check the occurrence of the collision according to wave periods. From Case 3, 5, and 6, we will check the occurrence of the collision according to wave heights.

Table 4-1. Wave conditions for LPG tank erection.

Case	Wave condition		
	Heading angle [deg]	Wave period [sec]	Wave height [m]
1	90	6	1.0
2		8	
3		10	
4		12	
5		10	1.5
6			2.0

As the wave period is increased from 6 to 12 sec., the motions of the floating crane and LPG tank are also increased. There is no collision between the LPG tank and the hull structure when the wave period is less than 10 sec., as shown in Figure 4-12. However, when the wave period is more than 12 sec. (Case 4), the collision occurs, as shown in Figure 4-13. Meanwhile, when the wave height is changed from 1.0 m to more than 1.5 m (Case 5, 6), the collision also occurs. From these results, we can find safe environmental conditions, which are that the wave period is less than 10 sec., and the wave height is less than 1.0 m.

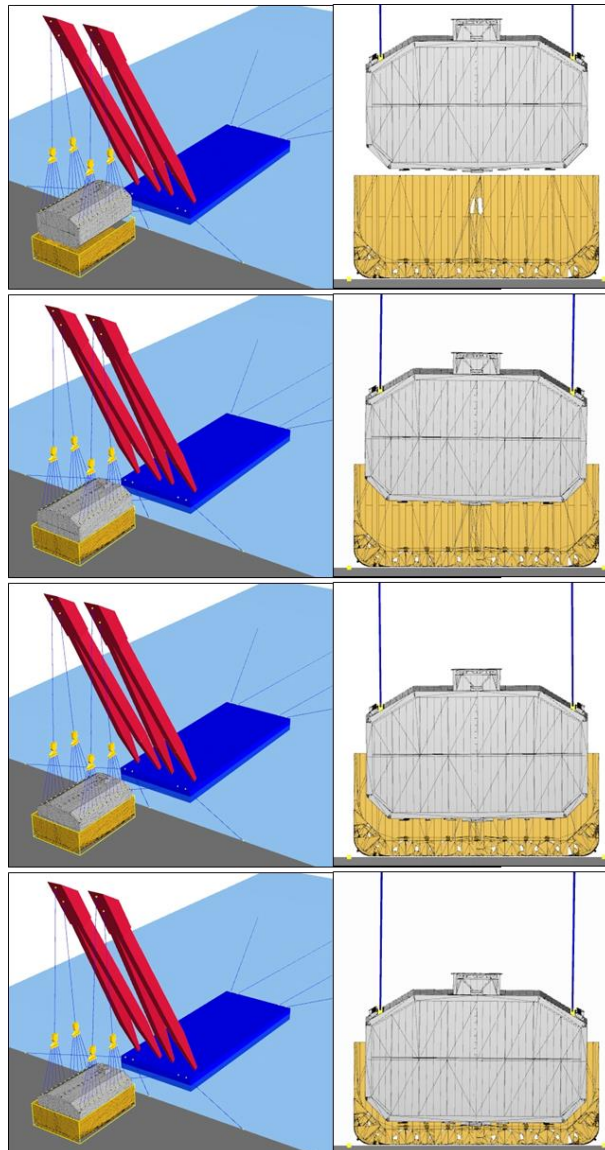


Figure 4-12. Simulation results of Case 3: No collision.

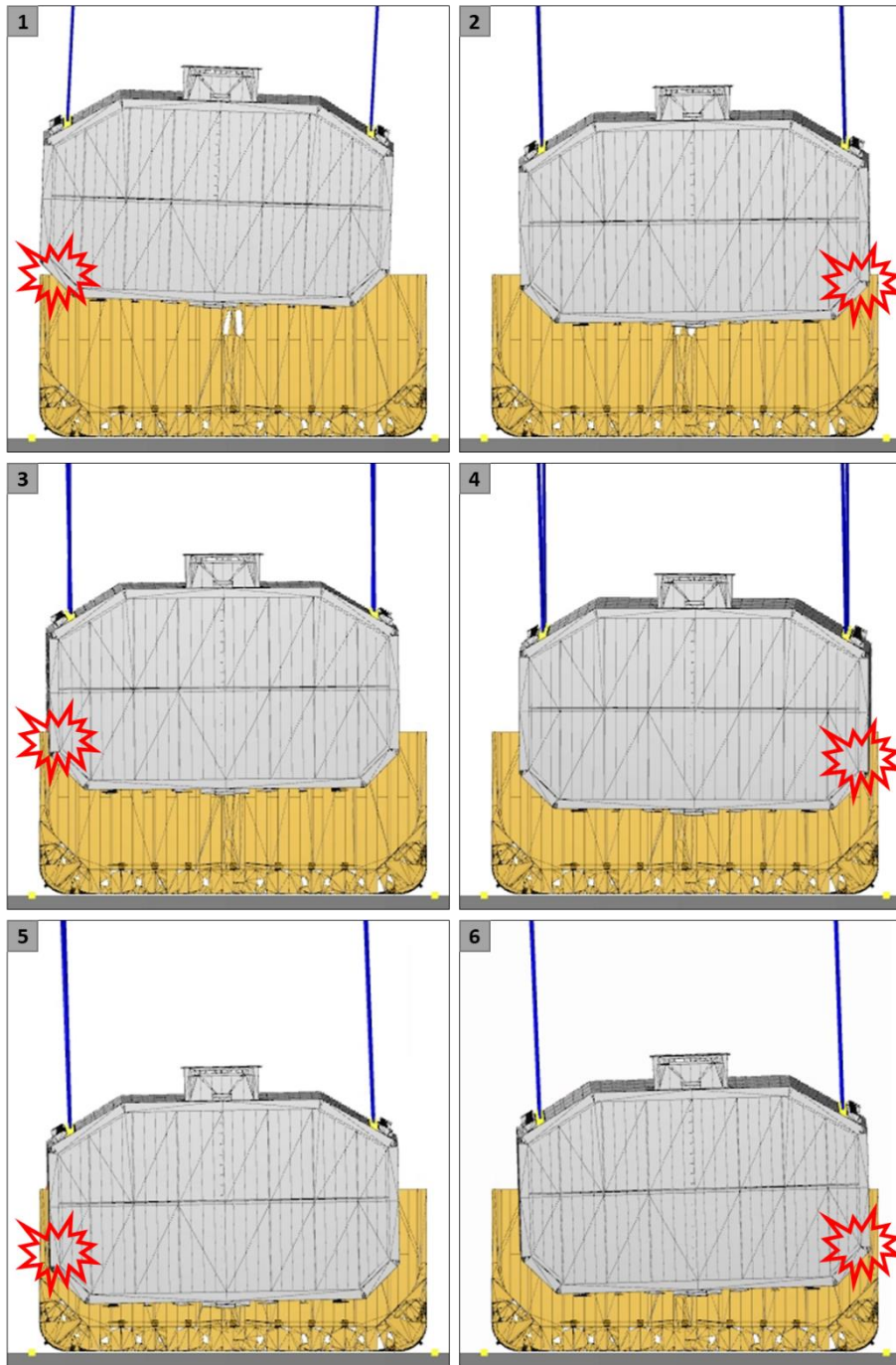


Figure 4-13. Simulation results of Case 4: Occurrence of the collision.

Figure 4-14 shows the graphs of the maximum collision force, which is the maximum value among collision forces acting at several collision positions. There is no collision force in Case 1, 2, and 3. The collision forces in Case 4, 5, and 6 are measured as 3,939 ton, 4,196 ton, and 6,822 ton, respectively. These results can be used as one of the parameters to design guide bumpers between the LPG tank and the hull structure.

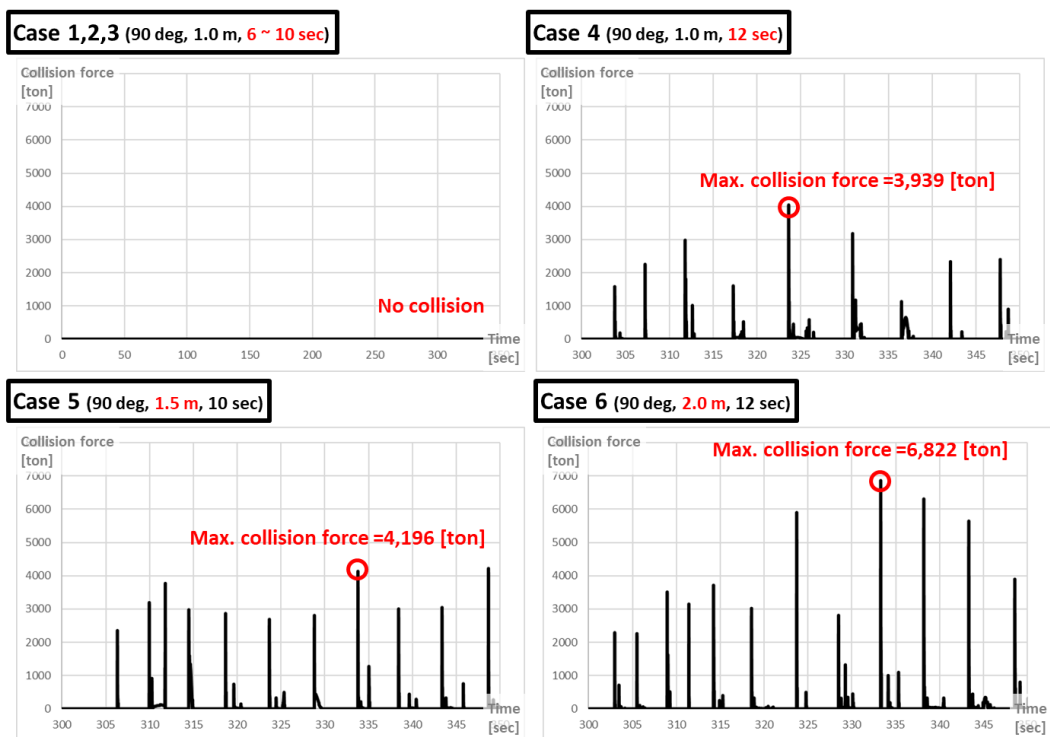


Figure 4-14. Graphs of maximum collision forces according to time.

### 4.3. Thin plate block lifting considering deformation

This section presents the dynamic analysis of the thin plate block lifting by a gantry crane and a floating crane. Von-Mises stress is analyzed to check the safety due to the dynamic effect.

#### 4.3.1. Thin plate block turn-over by a gantry crane

The first example is the thin plate block turn-over operation by a gantry crane. The gantry crane and the block are modeled as shown in Figure 4-15.

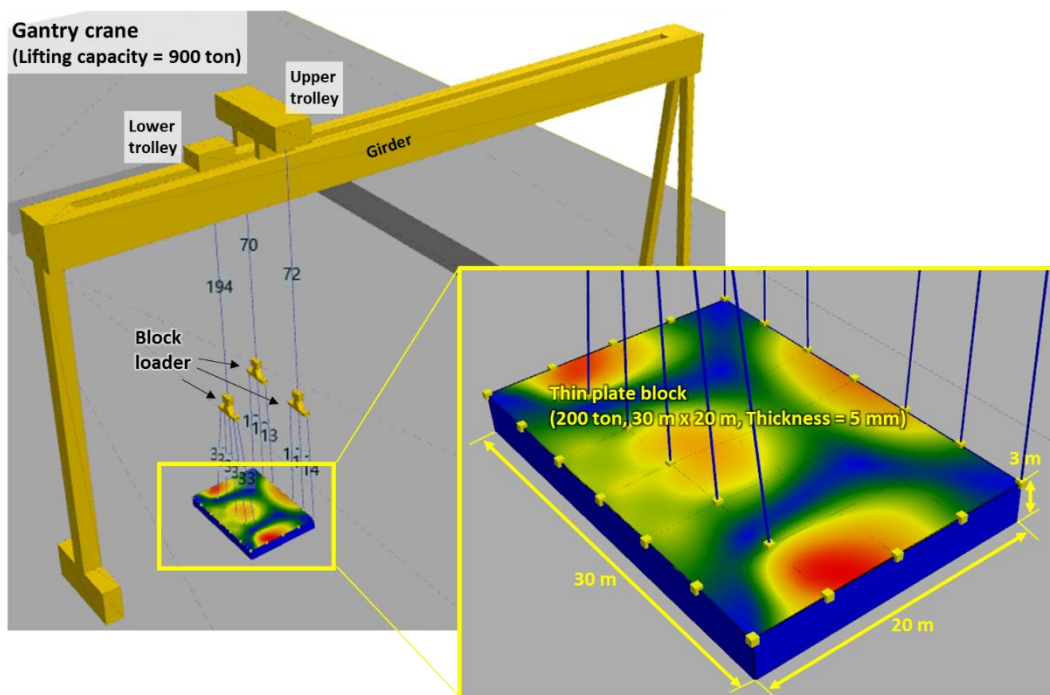


Figure 4-15. Modeling of the gantry crane and the thin plate block.

The thin plate block is 200 ton, 30 m length, 20 m width, and 5mm thickness. It is composed of 6 by 4 shell elements. Each edge is connected with four rigid plates by the



fixed joints. For turn-over, the wire ropes of the block loaders from the upper trolley are connected at one of the edges. The other wire ropes from the lower trolley are connected to inside nodes on the thin plate. Figure 4-16 shows the scenario of thin plate block turn-over.

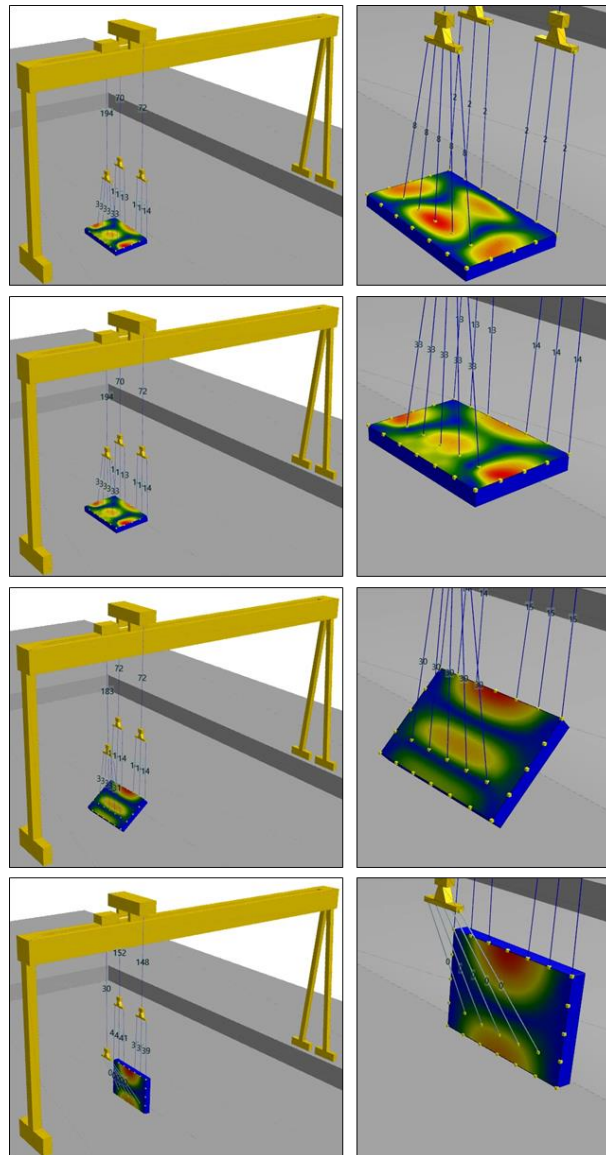


Figure 4-16. Scenario of thin plate block turn-over.



At first, those three block loaders are hoisted up at the same time. After the thin plate block reaches a certain height, the two block loaders keep on being hoisted up, and the other is started to be hoisted down. Finally, the block is erected by 90 deg.

Von-Mises stress is depicted as a color on the thin plate. The red and blue colors are the maximum and minimum stresses, respectively. During the turn-over operation, the maximum point marked as red color is changed from the inside of the plate toward the edge which is connected by wire ropes. The graph of the stress according to simulation time is shown in Figure 4-17. When the thin plate block is tilted, the stress exceeds its yield stress in case of a mild steel (250 MPa). After the turn-over is finished, the maximum stress increases up to 606 MPa. In an aspect of the safety, this operation needs to be re-evaluated after structural reinforcement or changing the operation itself.



Figure 4-17. Graph of the maximum von-Mises stress.

### 4.3.2. Thin plate block lifting by a floating crane

The second example is the same block lifted by a floating crane, which capacity is 3,600 ton. In this case, the wave condition affects to the stress inside the thin plate block. Figure 4-18 shows the modeling of the floating crane and the thin plate block. There are four hooks, and each hook has five wire ropes connected with the block.

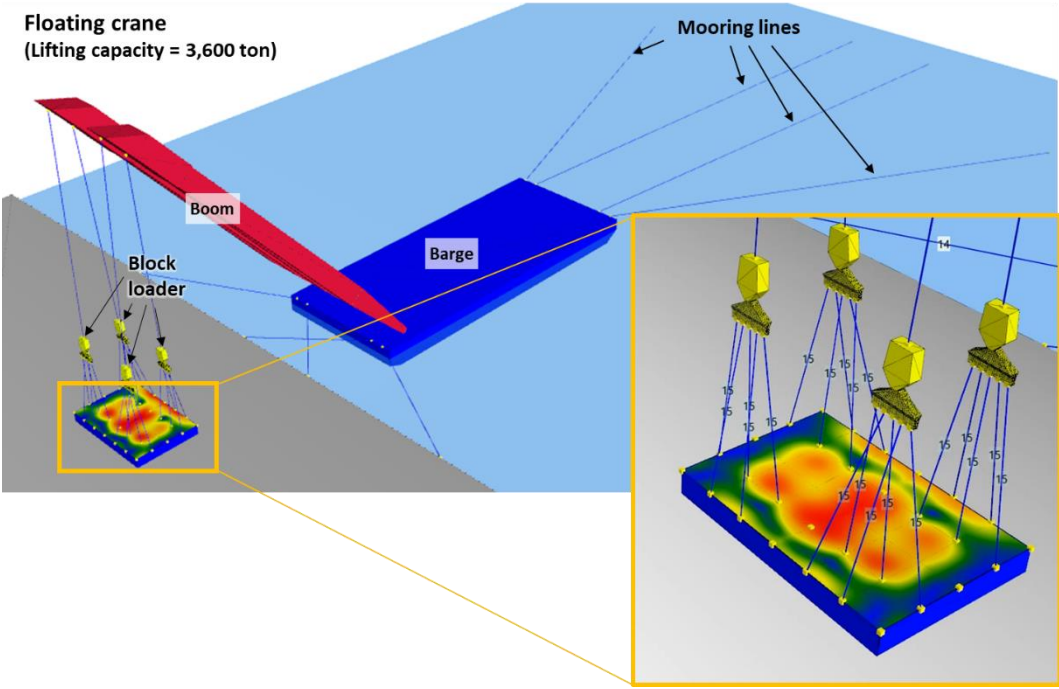


Figure 4-18. Modeling of the floating crane and the thin plate block.

We assume that the regular wave which height is 1.0 m and period is 10 sec applies to the floating crane from the different directions such as 0 deg (following sea), 45 deg (quartering sea), and 90 deg (beam sea). According to the wave heading angle, the stress inside the thin plate block shows different tendency as shown in Figure 4-19.

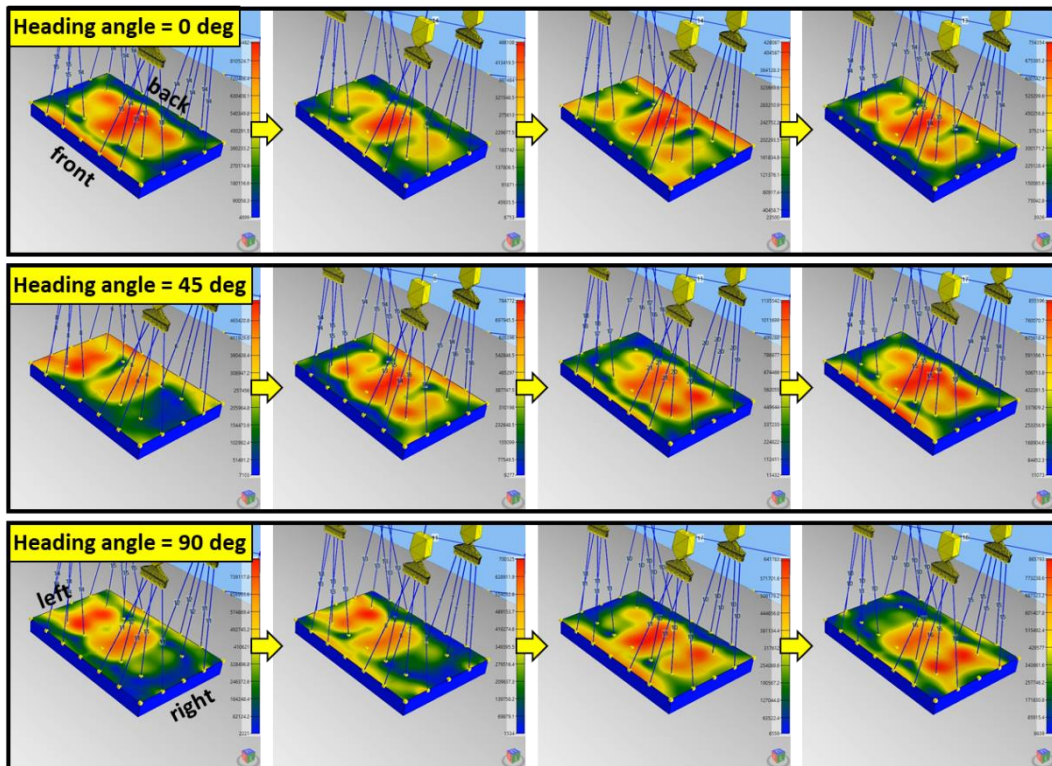


Figure 4-19. Stress inside the thin plate block according to the wave heading angle.

When the heading angle is 0 deg, the maximum stress changes between the front edge and the back edge. When the heading angle is 45 deg, the maximum stress changes along the edges. Finally, when the heading angle is 90 deg, the maximum stress changes between the left edge to the right edge.

We also plot the maximum stresses according to the wave heading angles as shown in Figure 4-20. Due to the regular wave, the stress shows regular oscillation.

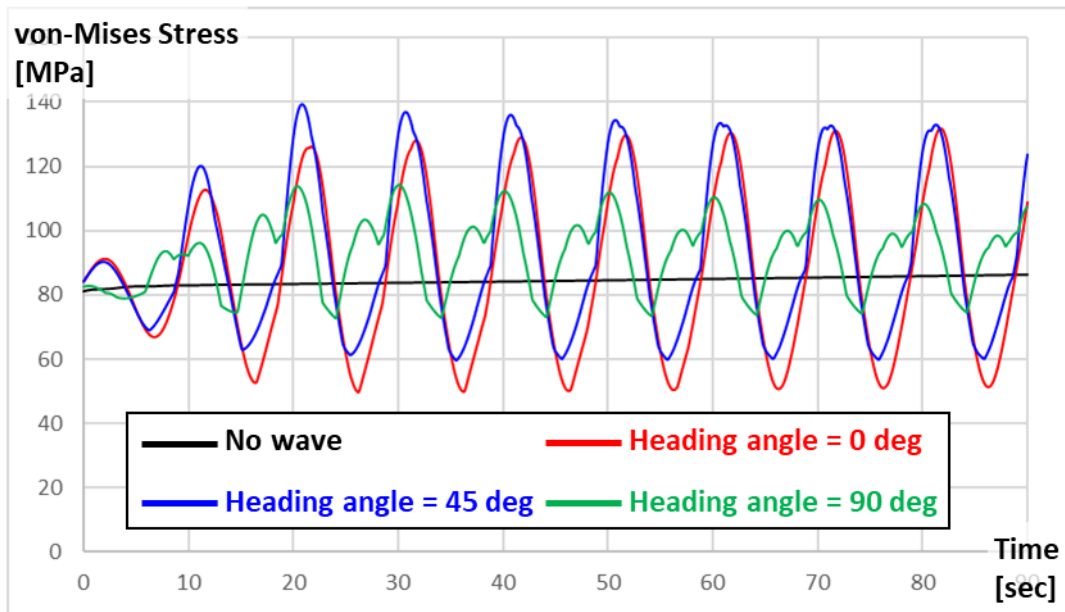


Figure 4-20. Graphs of the maximum stress according to wave heading angle.

Maximum stress is summarized in Table 4-2. DAF (dynamic amplification factor) is calculated based on the no wave condition. When the wave heading angle is 45 deg, the stress becomes maximum.

Table 4-2. Maximum stress and dynamic amplification factor

Wave condition			Maximum stress [MPa]	DAF
Wave height [m]	Wave period [sec]	Heading angle [deg]		
No wave			87	1.00
1.0	10	0	132	1.52
		45	140	1.61
		90	114	1.31

#### **4.4. Block offloading using SPMTs**

This section presents the dynamic analysis of the block offloading using SPMTs, based on the combination of multibody dynamics, a collision between the wheel and the plane, modeling of the SPMT, and ballasting and de-ballasting methods given in the theoretical backgrounds.

Figure 4-21 and Figure 4-22 show the modeling results for the block offloading from the TB to FD. The weight of the block is 1,600 ton, and its length, breadth, and height is 20 m, 52 m, and 20 m, respectively. The FD is moored on the seabed and quay to prevent the motion due to the environmental loads. The TB is connected by two link beams with hinge joints. The total lifting capacity of twelve SPMTs is 2,588.4 ton which is obtained by multiplying 215.7 ton with 12 EA. Therefore, it is enough to lift the block with twelve SPMTs. The initial lifting height of the SPMTs is set to 350 mm, and the load is set to 13.028 ton, which is obtained by dividing the total weight of the block and platform by the number of wheels. The main dimensions and other properties are summarized in Table 4-3.

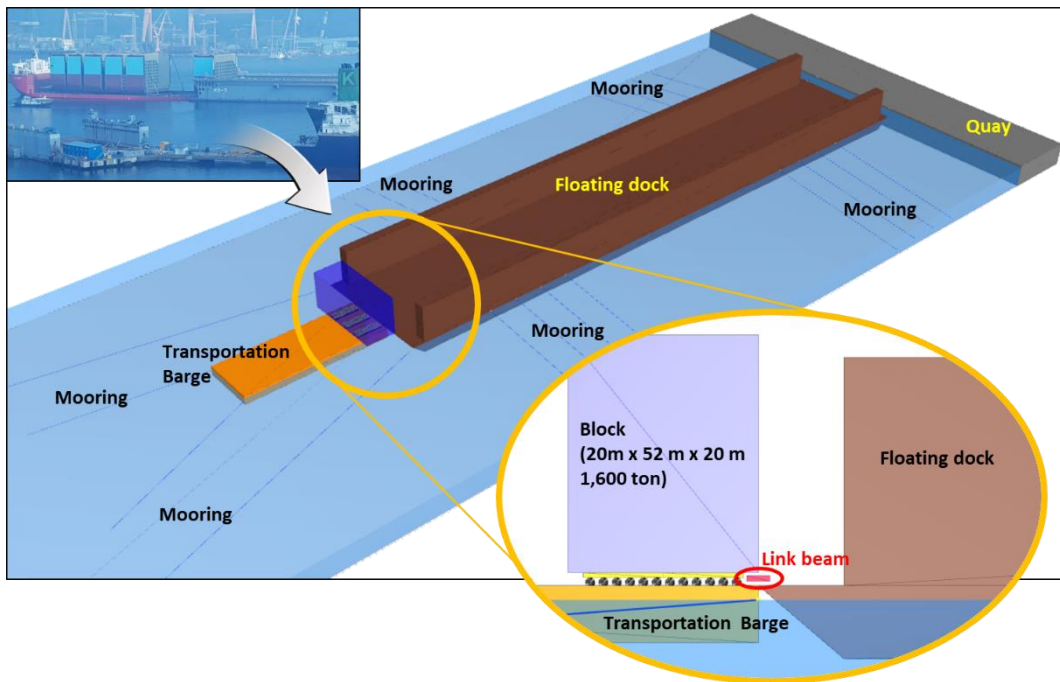


Figure 4-21. Modeling of the TB, FD, SPMTs, and the block.

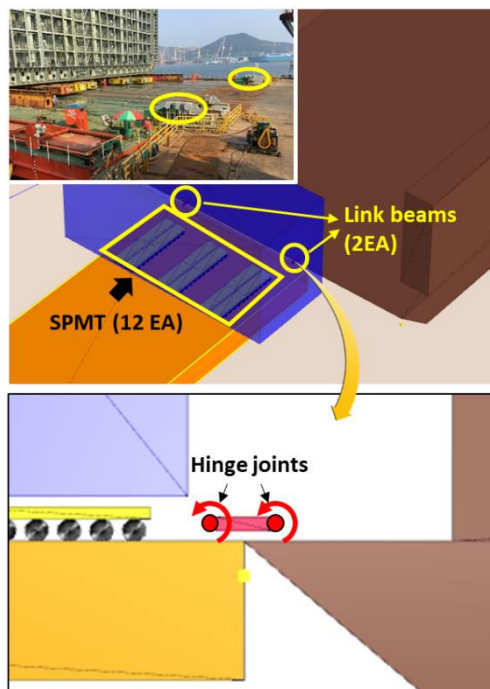


Figure 4-22. Link beams connected between the TB and FD.

Table 4-3. Main dimensions and other properties of the models.

Model	Item	Value
Block	Length	25 m
	Breadth	52 m
	Height	20 m
Transportation barge	Length	97.5
	Breadth	36 m
	Height	6 m
	Draft	4.5 m
	Displacement	16,190 ton
Floating dock	Length	438 m
	Breadth	84 m
	Height	31.7 m
	Draft	6.2 m
	Displacement	228,073 ton
SPMT	Initial loads per a wheel	13.028 ton
	Initial height	350 mm

The dynamic simulation of the block offloading by SPMTs was performed according to the various wave conditions listed in Table 4-4. The heading angle was fixed to 0 degrees, which means the wave is coming from the TB to FD. From Cases 1 to 4, we checked the effect of wave heights and periods to the dynamic loads on the wheels. Cases 5 and 6, which use JONSWAP spectrum, check the dynamic loads in the moderate and storm conditions, respectively. The wave period means peak period, and the wave height means the significant wave height for the irregular wave in Table 4-4.

Table 4-4. Wave conditions.

Case	Type	Heading angle [deg]	Wave period [sec]	Wave height [m]
1	Regular	0	10	0.5
2				1.0
3				1.5
4			12	1.0
5	Irregular (JONSWAP)		6.12	1.65
6			10.47	6.1

The dynamic analysis is conducted in the same scenario. Concerning the operation manual [59], the moving speed should be less than 0.5 km/h when the maximum payload is posted. For safety, we selected half of the given speed for the operation speed, which is 0.25 km/h (=0.07 m/s). According to the position of the block and SPMTs, the COG of both the TB and FD are shifted by the method explained in section 2.8.2.

The simulation results are depicted in Figure 4-23. Our target block was located at the center of the TB (Figure 4-23-(1)). The SPMTs start to move from the initial locations to the FD (Figure 4-23-(2), (3)). The first row of the wheels of the SPMTs arrived at the end of the TB (Figure 4-23-(4)). The end row of the wheels is left of the TB (Figure 4-23-(5)). Finally, the block successfully arrived inside the FD (Figure 4-23-(6)).



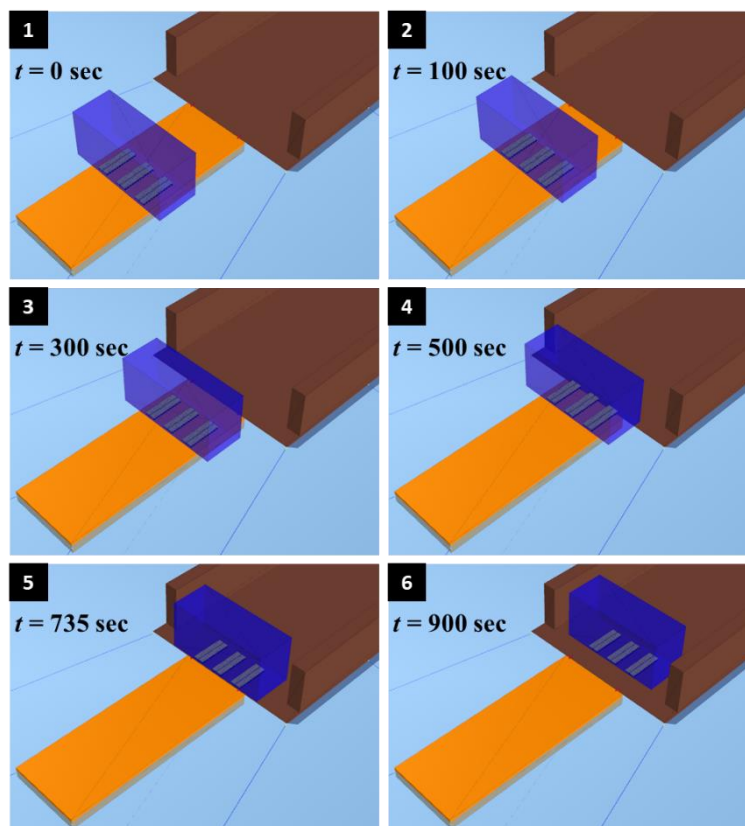


Figure 4-23. Simulation results of the block offloading.

From the dynamic analysis under the given wave conditions, we can check the following results for the safety. The difference of the block height ( $z_{block}$ ) and attitude ( $\theta_{block}$  = pitch angle) from the initial value should be maintained at zero. The movement of the wheel ( $z_{wheel}$ ) should be less than 350 mm and more than -350 mm. The load of the wheel should be less than 20 ton. These criteria are listed in Table 4-5.

Table 4-5. Safety criteria for dynamic analysis of block offloading.

Item	Criteria
Block height and attitude	$  z_{block} - z_{block, initial}   \leq 10^{-2}$ $  \theta_{block} - \theta_{block, initial}   \leq 10^{-2}$
Wheel movement	$-0.35 \text{ m} \leq z_{wheel} \leq 0.35 \text{ m}$
Wheel loads	$F_{wheel} \leq 20 \text{ ton}$

To check the safety criteria listed in Table 4-5, the simulation results are shown in the graphs (Figure 4-24 to Figure 4-29). The graph of the block height and pitch angle shows the difference from the initial value. Since there is a total of 144 wheels, the wheel located in the middle was selected as a representative. We checked that the height and load of the selected wheel are sufficiently representative because the other wheels show a similar tendency. Finally, the results are compared with the criteria in Table 4-6.

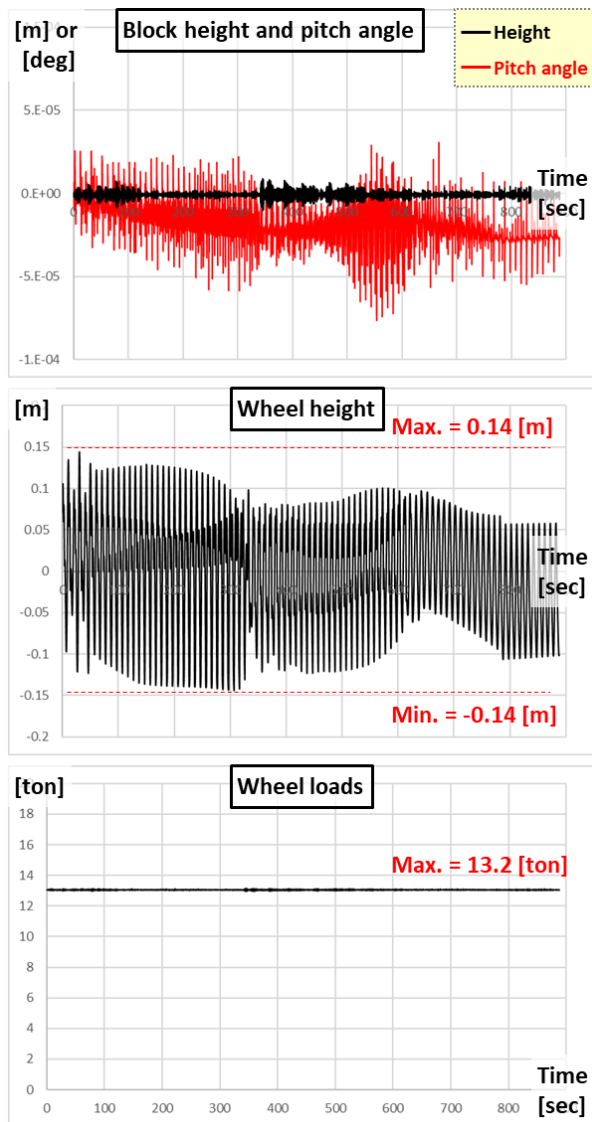


Figure 4-24. Graphs of block height, pitch angle, wheel height and loads for Case 1.

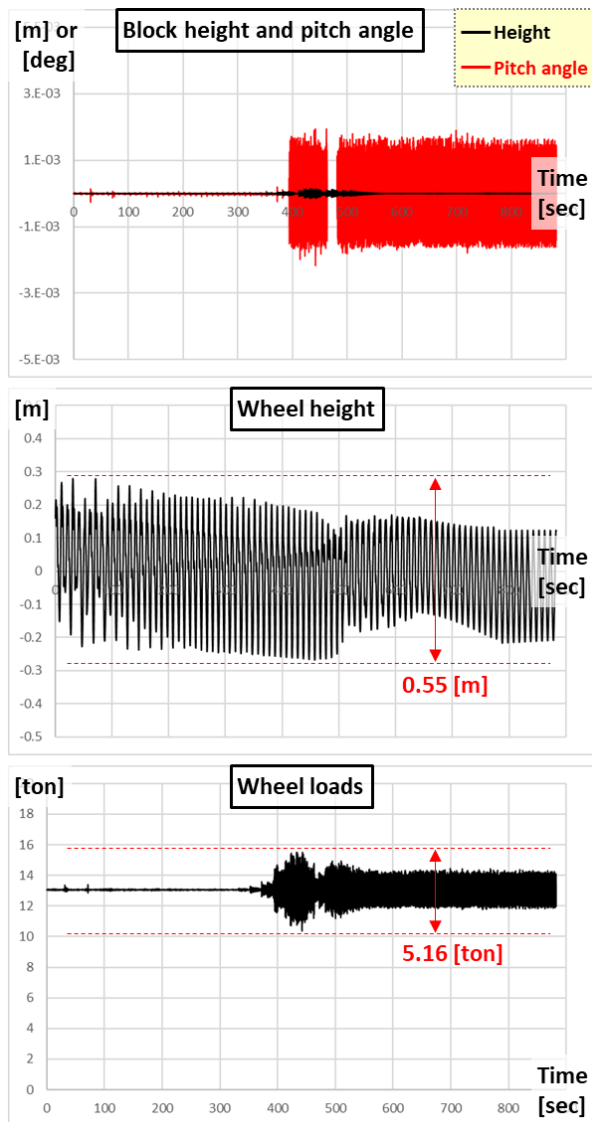


Figure 4-25. Graphs of block height, pitch angle, wheel height and loads for Case 2.

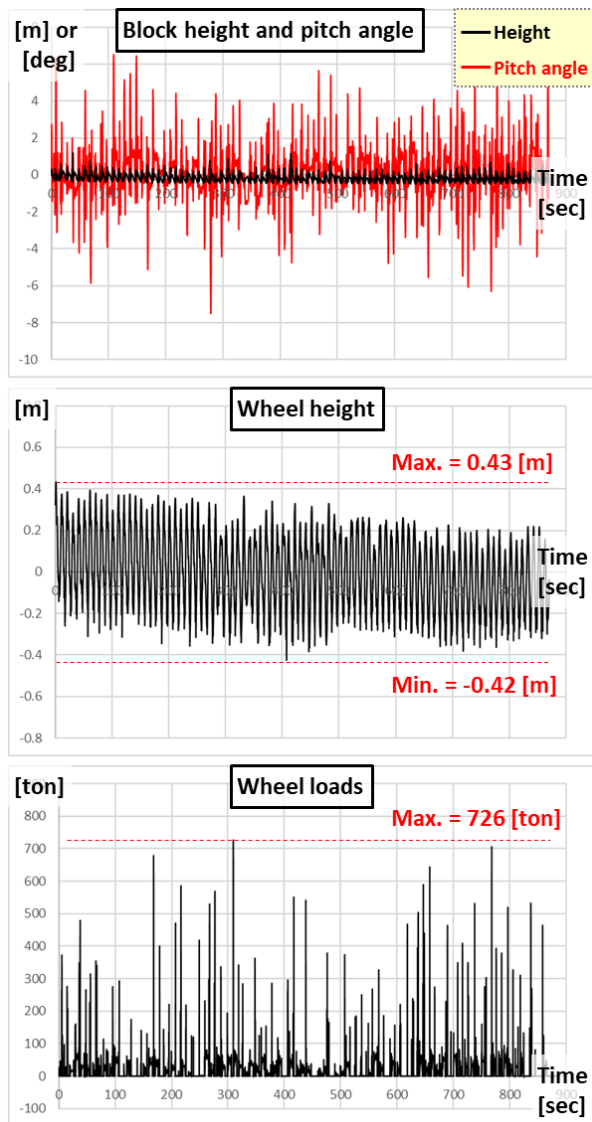


Figure 4-26. Graphs of block height, pitch angle, wheel height and loads for Case 3.

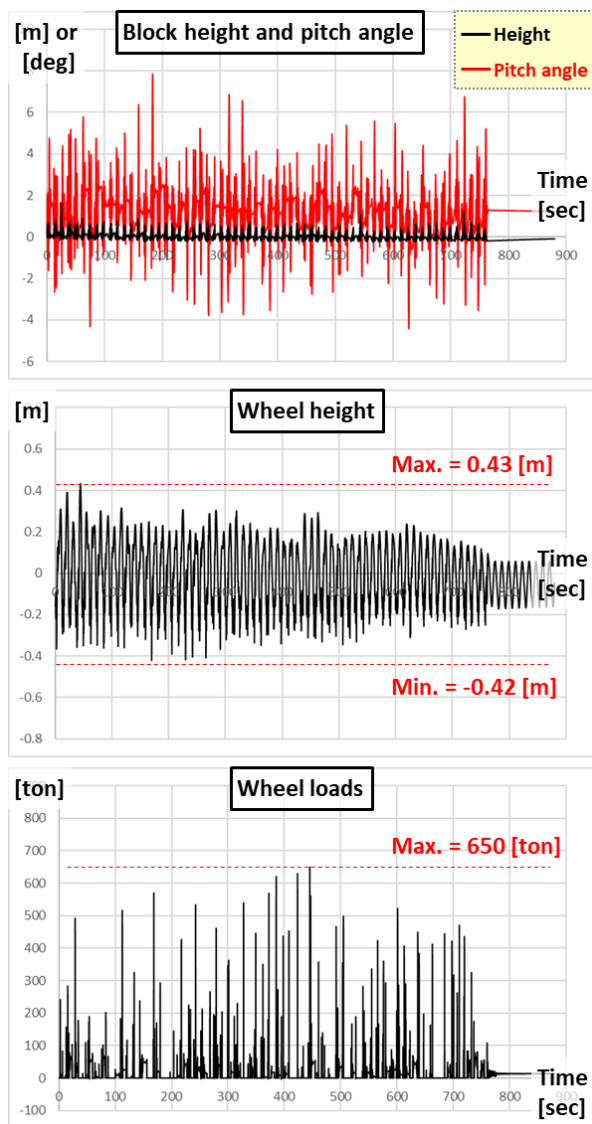


Figure 4-27. Graphs of block height, pitch angle, wheel height and loads for Case 4.

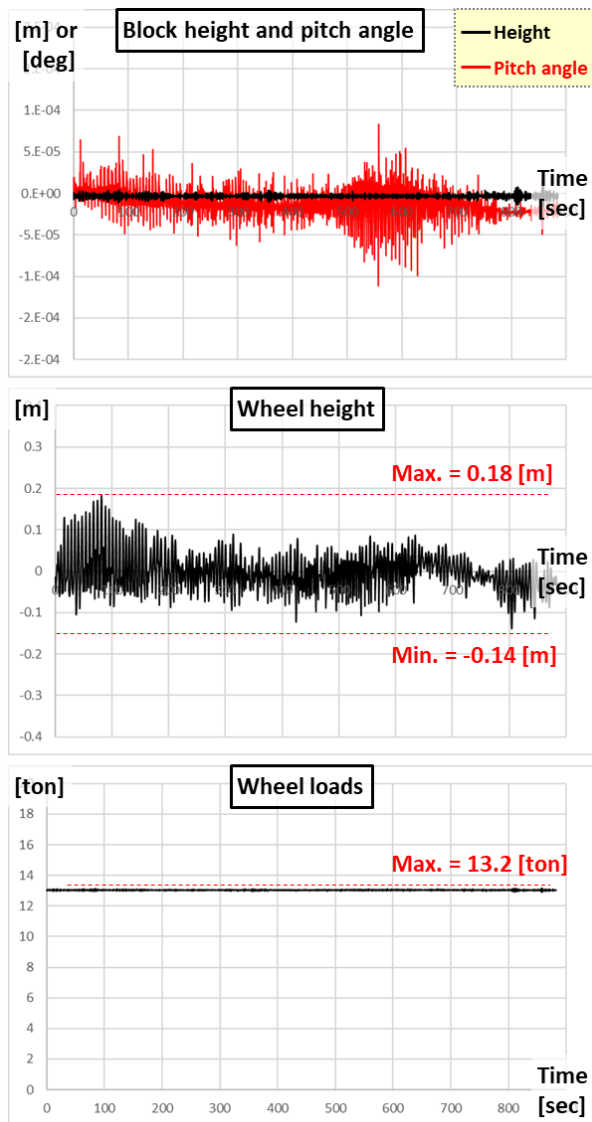


Figure 4-28. Graphs of block height, pitch angle, wheel height and loads for Case 5.

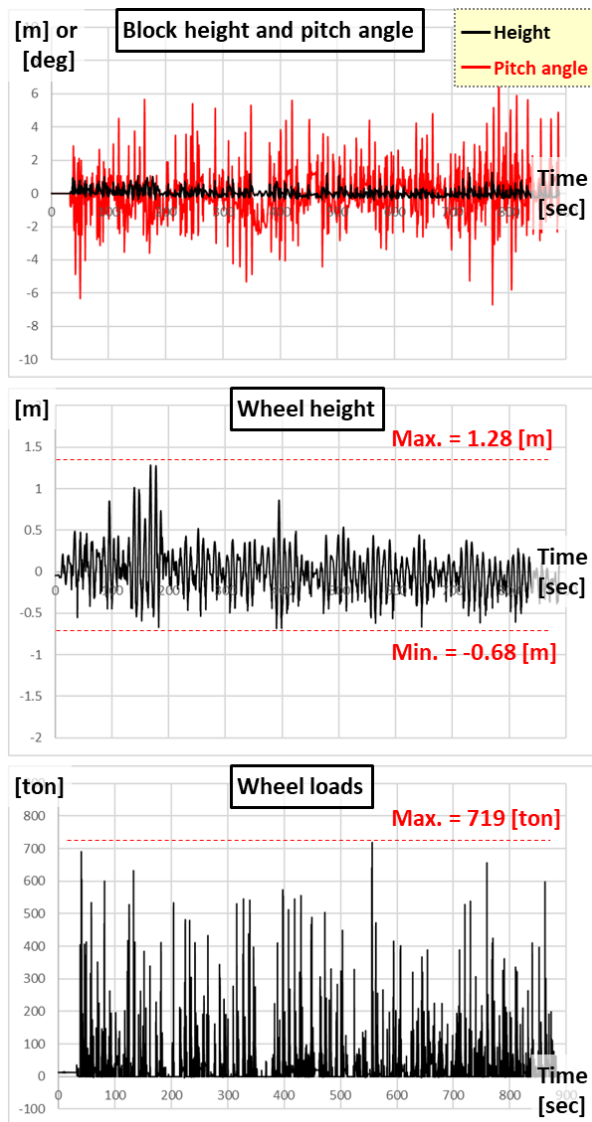


Figure 4-29. Graphs of block height, pitch angle, wheel height and loads for Case 6.



Table 4-6. Comparison of safety criteria with the simulation results according to wave conditions

Criteria	Case 1	Case 2	Case 3	Case 4	Case 5	Case 6
Block height and attitude (below $10^{-2}$ )	O (below $10^{-2}$ )	O (below $10^{-2}$ )	X (above $10^{-2}$ )	X (above $10^{-2}$ )	O (below $10^{-2}$ )	X (above $10^{-2}$ )
Wheel movement (-0.35, 0.35)	O (-0.14,0.14)	O (-0.27,0.28)	X (-0.42,0.43)	X (-0.42,0.43)	O (-0.14,0.18)	X (-0.68,1.28)
Wheel loads (20)	O (13.2)	O (15.5)	X (726)	X (650)	O (13.2)	X (719)

For Cases 1, 2, and 5, the block offloading was successfully performed without violating the criteria. However, if the wave height is increased from 1.0 m to 1.5 m (Case 3), from 10 seconds to 12 seconds (Case 4), the motions of the TB and FD exceed the limit of the axle compensation of SPMTs. It is also the same for Case 6 in the storm case. Therefore, we can find safe environmental conditions, which are that the wave period is less than 10 seconds and the wave height is less than 1.0 m for the regular waves, and the significant wave height is less than 1.65 m and the peak period is less than 6.12 seconds for the irregular waves. Furthermore, we also found out that the operation is not allowable in storm conditions.

## 5. Conclusion and future work

### 5.1. Summary

This study was focused on the integrated simulation framework to develop new design verification software. The requirements for the new design software were derived from the real operation in shipbuilding and offshore installation. Based on the requirements, we presented integrated simulation framework based on multibody dynamics which was composed of five layers such as simulation core, interface, simulation components, equipment, and service.

In section 2, theoretical backgrounds of the equations of motion and simulation components were derived in detail. The equations of motion were based on multibody dynamics. Among the several formulations, we adopted the DELE to achieve the stability during numerical integration. Furthermore, we formulated the equations of motion of the 1D frame element and 2D shell element based on ANCF. Kinematic constraints including joints and constraint-based wire rope between the rigid bodies, and between the rigid and flexible bodies were also derived. As external forces, hydrodynamic force, wind force, current force, and mooring force were also explained.

We also dealt with special issues in collision detection and response. Because the shape exported from the ship CAD system contains unenclosed meshes, we proposed the position difference method which checks an intersection using the line segment made by the two vertices or the trigonal prism consisting of the two triangular meshes at time  $t_0$  and  $t_1$ . Furthermore, BVH and exclusion boxes were adopted to increase the performance. For collision response, non-interpenetration constraint method between a vertex and a plane

was derived. This method is applicable when two bodies collide at the multiple points, and it did not compulsively violate the kinematic constraint because the collision force was also solved together when the equations of motion were solved numerically. Moreover, the collision force could be determined automatically, reflecting material properties such as restitution and softness. However, it was not easy to represent the body surfaces as continuously differentiable functions. Therefore, we derived a simple non-interpenetration constraint equation between a vertex and a plane. This equation could also be extended to the collision response between two bodies by using the collision pair which was obtained from the collision detection.

Special equipment such as equalizer and SPMT was also modeled. We presented the real mechanism of an equalizer, which is operated by fixed and moving pulleys sequentially connected by a single equalizing wire rope. The modeling of the mechanical parts of the SPMT taking into consideration the axle compensation mechanism to maintain the level of the platform when the SPMT drives over an uneven roadway by lifting up the wheel was also proposed.

We provided several verification examples compared with the analytic solutions or commercial software to increase the reliability. For validation, two simulation cases were compared to the data acquired from the real operations.

Finally, we provided four representative applications such as block lifting using equalizers, LPG tank erection considering a collision, thin plate block lifting considering deformation, and block offloading using SPMT, which have not been solved before. We concluded that the problems issued in section 1 were solved by the proposed or adopted methods. We convinced that the developed program based on the proposed integrated simulation framework could cover all operation in ships and offshore structures.

## **5.2. Contributions (Originality)**

This study has several contributions distinguished from the other work.

### **5.2.1. Theoretical contributions**

Formulation of ANCF (Absolute Nodal Coordinate Formulation) in DELE (Discrete Euler-Lagrange Equation) is formulated. Moreover, derivation of joints attached at any position between flexible and rigid bodies is also fully explained. Furthermore, we develop collision detection and force calculation module by using non-interpenetration constraint. Non-interpenetration constraint between the plane and vertex (or sphere, cylinder) is derived and then is extended to a collision between two meshes.

From this study, the accuracy and reliability of the simulation results are dramatically increased as multibody dynamics for rigid and flexible bodies are adopted. It is because the more realistic models based on the real mechanical relation can be generated. Moreover, this study allows to calculate the collision force and collision analysis between the ship blocks or modules. It was impossible to use the model exported directly from the ship CAD systems because the meshes are not enclosed or have reverse normal.

### **5.2.2. Contributions for applications**

We propose modeling special equipment in ships and offshore structures. Firstly, the equalizer including fixed and moving pulleys modeled by constraint-based wire rope is introduced. Secondly, SPMT which contains hydraulic cylinder connected by slider-hinge joint and axle compensation mechanism is also derived. Therefore, it is possible to simulate operations using special equipment such as equalizer and SPMTs in ships and offshore structures.

### **5.2.3. Other contributions**

We propose integrated simulation framework to integrate various physical theories and to develop software conveniently. Based on the framework, we develop production design verification software which is dedicated to ships and offshore structures. Some features that are not supported by existing software can be supported by this program.

The developed program is verified and validated by comparing with analytic solutions, benchmarking tests, commercial software, and real operation data. Finally, this study provides several applications which have not been tried before in ships and offshore structures.

### **5.3. Future works**

Further research will focus on new operations which have not been solved before due to the absence of the simulation program. For this, we will find new requirements and make up for the framework. Additionally, the simulation results will be compared with real operations or the model tests to validate the program in further research.

## Reference

- [1] Bentley, “MOSES.” [Online]. Available: <https://www.bentley.com/en/products/product-line/offshore-structural-analysis-software/moses>. [Accessed: 15-Mar-2018].
- [2] DNVGL, “Simulation of marine operations - Sima.” [Online]. Available: <https://www.dnvgl.com/services/simulation-of-marine-operations-sima-2324>. [Accessed: 15-Mar-2018].
- [3] Orcina, “OrcaFlex.” [Online]. Available: <https://www.orcina.com/SoftwareProducts/OrcaFlex/>. [Accessed: 15-Mar-2018].
- [4] J. H. Cha, M. I. Roh, and K. Y. Lee, “Integrated simulation framework for the process planning of ships and offshore structures,” *Robot. Comput. Integr. Manuf.*, vol. 26, no. 5, pp. 430–453, Oct. 2010.
- [5] B. P. Zeigler, H. Praehofer, and T. G. Kim, *Theory of modeling and simulation : integrating discrete event and continuous complex dynamic systems*. Academic Press, 2000.
- [6] R. Smith, “Open Dynamics Engine,” 2012. [Online]. Available: <http://www.ode.org/>. [Accessed: 15-Jan-2018].
- [7] J.-H. Cha, K.-P. Park, and K.-Y. Lee, “Development of a simulation framework and applications to new production processes in shipyards,” *Comput. Des.*, vol. 44, no. 3, pp. 241–252, Mar. 2012.
- [8] N. Ku and M. Il Roh, “Dynamic response simulation of an offshore wind turbine suspended by a floating crane,” *Ships Offshore Struct.*, vol. 10, no. 6, pp. 621–634, 2015.
- [9] J. H. Cha, S. H. Ham, K. Y. Lee, and M. I. Roh, “Application of a topological modelling approach of multi-body system dynamics to simulation of multi-floating cranes in shipyards,” *Proc. Inst. Mech. Eng. Part K J. Multi-body Dyn.*, vol. 224, no. 4, pp. 365–373, Dec. 2010.
- [10] S. H. Ham, M. I. Roh, H. W. Lee, and S. Ha, “Multibody dynamic analysis of a heavy load suspended by a floating crane with constraint-based wire rope,” *Ocean Eng.*, vol. 109, pp. 145–160, 2015.
- [11] N. Ku, S. Ha, and M.-I. Roh, “Crane Modeling and Simulation in Offshore Structure Building Industry,” *Int. J. Comput. Theory Eng.*, vol. 6, no. 3, pp. 278–284, 2014.
- [12] “TSV-BLS – TechnoStar Co. Ltd.” [Online]. Available: <http://www.e-technostar.com/products/shipbuildingsolution/tsv-bls/?lang=en>. [Accessed: 04-Apr-2018].

- [13] K.-P. Park, J.-H. Cha, and N. Ku, "The flexible multibody dynamics of a floating offshore wind turbine in marine operations," *Ships Offshore Struct.*, vol. 12, no. 4, pp. 563–574, May 2017.
- [14] Z. Ming, Z. Peng, and Z. Changming, "Dynamic response analysis of offshore wind turbine installation suspended by a floating crane," *Proc. Inst. Mech. Eng. Part C J. Mech. Eng. Sci.*, vol. 231, no. 14, pp. 2650–2663, Jul. 2017.
- [15] H. W. Lee, M. I. Roh, and S. H. Ham, "Block turnover simulation considering the interferences between the block and wire ropes in shipbuilding," *Autom. Constr.*, vol. 67, pp. 60–75, 2016.
- [16] D. H. Jeong, M. I. Roh, and S. H. Ham, "Lifting simulation of an offshore supply vessel considering various operating conditions," *Adv. Mech. Eng.*, vol. 8, no. 6, pp. 1–13, 2016.
- [17] NVIDIA, "Nvidia physx," 2012. [Online]. Available: <https://www.geforce.com/hardware/technology/physx>. [Accessed: 15-Jan-2018].
- [18] E. Coumans, "Real-Time Physics Simulation," 2012. [Online]. Available: <http://bulletphysics.org/wordpress/>. [Accessed: 15-Jan-2018].
- [19] E. Imanishi, T. Nanjo, and T. Kobayashi, "Dynamic simulation of wire rope with contact," *J. Mech. Sci. Technol.*, vol. 23, no. 4, pp. 1083–1088, Apr. 2009.
- [20] U. Lugrís, J. L. Escalona, D. Dopico, and J. Cuadrado, "Efficient and accurate simulation of the rope–sheave interaction in weight-lifting machines," *Proc. Inst. Mech. Eng. Part K J. Multi-body Dyn.*, vol. 225, no. 4, pp. 331–343, Dec. 2011.
- [21] I. García, I. García, M. Pla-Castells, M. Pla-Castells, R. J. Martínez-Durá, and R. J. Martínez-Durá, "Elevation cable modeling for interactive simulation of cranes," *Proc. ACM SIGGRAPH/Eurographics Symp. Comput. Animat.*, 2008.
- [22] D. Naqvi, E. Wey, J. Morgan, M. Miller, and T. Nguyen, "Transportation considerations in module design," in *Structures Congress 2014*, 2014, pp. 1771–1781.
- [23] I. A. Ali, "Structural modelling of offshore module for loadout, transportation and installation," University of Stavanger, Norway, 2014.
- [24] J. Zhao, R. Gou, and Z. Wang, "Developing of independent suspension electro-hydraulic control system of heavy platform vehicle," *J. Northeast. Univ.*, vol. 29, no. S2, pp. 237–240, 2008.
- [25] L. Lu, X. Wang, and H. Wang, "Leveling system controlled by electro-hydraulic proportional valves in self-propelled modular transporter (SPMT)," *Int. J. Sci. Eng. Res.*, vol. 5, no. 6, pp. 1250–1254, 2014.
- [26] T. D. Vu, D. W. Dong, B. Yan, C. R. Hua, and Q. Y. Tu, "Durability analysis on hydraulic suspension system of modular assembled trailer," *Appl. Mech. Mater.*, vol. 105–107, pp. 227–232, Sep. 2011.

- [27] A. A. Shabana, *Computational dynamics*. John Wiley & Sons, 2010.
- [28] S. H. Ham, M. Il Roh, and H. Lee, "Simulation of load lifting with equalizers used in shipyards," *Autom. Constr.*, vol. 61, pp. 98–111, 2016.
- [29] C. Lacoursiere, "Ghosts and machines: regularized variational methods for interactive simulations of multibodies with dry frictional contacts," Umeå university, 2007.
- [30] S. Ha, N. K. Ku, M. I. Roh, and H. J. Hwang, "Multibody system dynamics simulator for process simulation of ships and offshore plants in shipyards," *Adv. Eng. Softw.*, vol. 85, pp. 12–25, Jul. 2015.
- [31] R. Featherstone, *Rigid Body Dynamics Algorithms*. 2008.
- [32] J. H. Cha, M. I. Roh, and K. Y. Lee, "Dynamic response simulation of a heavy cargo suspended by a floating crane based on multibody system dynamics," *Ocean Eng.*, vol. 37, no. 14–15, pp. 1273–1291, Oct. 2010.
- [33] O. A. Bauchau, *Flexible Multibody Dynamics*, vol. 176. 2010.
- [34] J. M. Wendlandt and J. E. Marsden, "Mechanical integrators derived from a discrete variational principle," *Phys. D Nonlinear Phenom.*, vol. 106, no. 3–4, pp. 223–246, Aug. 1997.
- [35] J. E. Marsden and M. West, "Discrete mechanics and variational integrators," *Acta Numer.* 2001, vol. 10, pp. 357–514, 2001.
- [36] A. Lew, "Variational time integrators in computational solid mechanics," vol. 2003, 2003.
- [37] G. R. Fowles and G. L. Cassiday, *Analytical mechanics*. Thomson Brooks/Cole, 2005.
- [38] E. Hairer, C. Lubich, and G. Wanner, "Geometric numerical integration illustrated by the StörmerVerlet method," *Acta Numer.*, vol. 12, p. S0962492902000144, 2003.
- [39] J. Baumgarte, "Stabilization of constraints and integrals of motion in dynamical systems," *Comput. Methods Appl. Mech. Eng.*, vol. 1, no. 1, pp. 1–16, Jun. 1972.
- [40] H. E. M. Eich, "Regularization Methods for Constrained Mechanical Multibody Systems," *ZAMM - J. Appl. Math. Mech. / Zeitschrift für Angew. Math. und Mech.*, vol. 75, no. 10, pp. 761–773, 1995.
- [41] C. Lanczos, *Variational Principles of Mechanics Lanczos.Pdf*. Dover Publications, 1986, p. 418.
- [42] H. Yoshimura, A. Yoshida, T. E. Simos, G. Psihoyios, and C. Tsitouras, "Discrete Constrained Lagrangian Systems and Geometric Constraint Stabilization," in *AIP Conference Proceedings*, 2010, vol. 1281, no. 1, pp. 1292–1295.
- [43] A. A. Shabana, *Dynamics of Multibody Systems*. Cambridge: Cambridge



University Press, 2005.

- [44] M. Berzeri and A. A. Shabana, “Development of Simple Models for the Elastic Forces in the Absolute Nodal Co-Ordinate Formulation,” *J. Sound Vib.*, vol. 235, no. 4, pp. 539–565, 2000.
- [45] O. N. Dmitrochenko and D. Y. Pogorelov, “Generalization of plate finite elements for absolute nodal coordinate formulation,” *Multibody Syst. Dyn.*, vol. 10, no. 1, pp. 17–43, 2003.
- [46] L. K. Abbas, X. Rui, and Z. S. Hammoudi, “Plate/shell element of variable thickness based on the absolute nodal coordinate formulation,” *Proc. Inst. Mech. Eng. Part K J. Multi-body Dyn.*, vol. 224, no. 2, pp. 127–141, 2010.
- [47] D. García-Vallejo, J. Mayo, J. L. Escalona, and J. Domínguez, “Efficient evaluation of the elastic forces and the jacobian in the absolute nodal coordinate formulation,” *Nonlinear Dyn.*, vol. 35, no. 4, pp. 313–329, 2004.
- [48] P. E. Nikravesh and P. E., *Computer-aided analysis of mechanical systems*. Prentice-Hall, 1988.
- [49] B. V. Mirtich, “V-Clip: Fast and Robust Polyhedral Collision Detection,” *ACM Trans. Graph.*, vol. 17, no. 3, pp. 1–30, 1997.
- [50] E. G. Gilbert, D. W. Johnson, and S. S. Keerthi, “A fast procedure for computing the distance between complex objects in three-dimensional space,” *IEEE J. Robot. Autom.*, vol. 4, no. 2, pp. 193–203, Apr. 1988.
- [51] S. A. Ehmman and M. C. Lin, “Accurate and Fast Proximity Queries Between Polyhedra Using Convex Surface Decomposition,” *Comput. Graph. Forum*, vol. 20, no. 3, pp. 500–511, 2001.
- [52] S. Redon, A. Kheddar, and S. Coquillart, “Fast Continuous Collision Detection between Rigid Bodies,” *Comput. Graph. Forum*, vol. 21, no. 3, pp. 279–288, 2002.
- [53] G. Van Den Bergen, “A Fast and Robust GJK Implementation for Collision Detection of Convex Objects,” *J. Graph. Tools*, vol. 4, no. 2, pp. 7–25, Jan. 1999.
- [54] R. Weller, *New Geometric Data Structures for Collision Detection and Haptics*. Springer, Heidelberg, 2013.
- [55] P. Bauszat, M. Eisemann, and M. Magnor, “The Minimal Bounding Volume Hierarchy,” *Vision, Model. Vis.*, pp. 227–234, 2010.
- [56] U. Schmucker, V. Rusin, M. Konyev, and U. U. Schmucker, “Contact preprocessing in the simulation of the multibody systems,” in *6th EUROSIM Congress on Modelling and Simulation*, 2007.
- [57] D. E. Stewart, “Rigid-Body Dynamics with Friction and Impact,” *SIAM Rev.*, vol. 42, no. 1, pp. 3–39, 2000.
- [58] M. Anitescu and F. A. Potra, “A time-stepping method for stiff multibody

- dynamics with contact and friction,” *Int. J. Numer. Methods Eng.*, vol. 55, no. 7, pp. 753–784, 2002.
- [59] KAMAG Transporttechnik Gmbh & Co., “OPERATION MANUAL MODULAR TRANSPORTER TYPE 2400-S HS 4E,” 2005.
- [60] W. E. Cummins, “The impulse response function and ship motions,” *Schiffstechnik*, vol. 57, no. 9, pp. 101–109, 1962.
- [61] ISO19901-1, “Petroleum and natural gas industries -- Specific requirements for offshore structures -- Part 1: Metocean design and operating considerations.” 2005.
- [62] O. M. (Odd M. Faltinsen, *Sea loads on ships and offshore structures*. Cambridge University Press, 1990.
- [63] M. González, D. Dopico, U. Ligrís, and J. Cuadrado, “A benchmarking system for MBS simulation software: Problem standardization and performance measurement,” *Multibody Syst. Dyn.*, vol. 16, no. 2, pp. 179–190, 2006.
- [64] M. González, F. González, A. Luaces, and J. Cuadrado, “A collaborative benchmarking framework for multibody system dynamics,” *Eng. Comput.*, vol. 26, no. 1, pp. 1–9, 2010.
- [65] Solution Haneol, “DAFUL.” [Online]. Available: <http://www.ihaneol.kr/product1.html>. [Accessed: 09-Apr-2018].

## 국문 초록

### 선박 및 해양구조물의 공법 설계 검증을 위한 다물체 동역학 기반의 통합 시뮬레이션 방법

선박 및 해양구조물의 공법 설계 검증을 위해서 경험에 의존하거나 규정을 따르는 것은 과설계를 유발하기 때문에 소프트웨어를 통해 보다 정확한 해석을 수행하고자 한다. 하지만 기존에 개발된 상용 소프트웨어의 경우 조선 해양 공법을 사전에 검증하는 데에는 여러 가지 한계점이 존재한다. 따라서 본 연구에서는 기존 상용 소프트웨어가 수행하지 못하는 조선 해양 분야의 여러 공법을 대상으로 요구 조건을 분석하고 이를 기반으로 하는 역학 기반의 통합 시뮬레이션 프레임워크를 제안하였다. 본 연구에서 제안한 프레임워크는 운동 방정식을 담당하는 시뮬레이션 코어층, 시뮬레이션 구성 요소 간 정보 전달을 위한 인터페이스층, 관절, 외력 등으로 구성된 시뮬레이션 구성 요소층, 조선 해양에 특화된 장비층, 마지막으로 서비스 층의 총 5 개의 층(layer)로 구성되어 있다. 제안된 시뮬레이션 프레임워크를 기반으로 본 연구에서는 조선 해양 전용의 역학 기반 공법 검증 프로그램 SyMAP 을 개발하였다.

본 연구에서 제안한 통합 시뮬레이션 프레임워크는 다양한 이론적 배경을 기반으로 하고 있다. 우선 다물체 운동 방정식으로 강성 (stiffness)이 큰 경우에도 수치적으로 안정한 DELE 를 선정하였다. 더불어 1 차원 빔 요소와 2 차원 판 요소의 실시간 구조 해석이 가능한 유연 다물체 동역학 이론을 정리하였고, 이를 DELE 로 나타내었다. 본 연구에서는 다양한 관절 (joints)과 구속 기반의 와이어 로프 (constraint-based wire rope)를 유도하였다. 특히 구속 기반 와이어 로프를 사용하여 도르래를 모사함으로써 이퀄라이저 (조선 해양 분야에서 장력을 동일하게 분배시키기 위해 사용되는 특수 장치)의 작동 원리를 그대로 구현하였다.

한편, 충돌 검사 (collision detection) 및 반응 (collision response)은 본래 역학 해석에서 가장 어려운 문제 중 하나이다. 우선 충돌 물체 검사의 경우 다면체가 아니고, 둘러싸여 있지 않은 메쉬로 구성되어 있기 때문에 잘 알려진 다면체 알고리즘을 사용할 수 없다. 따라서 본 연구에서는 시간 차를 두고 위치를 비교하는 방법으로 둘러싸여 있지 않은 메쉬 간 충돌 검사를 수행하는 방법을 제안하였다. 충돌 반응의 경우 충돌점과 평면의 거리가 0 보다 작을 경우 구속 조건을 위배하는 것으로 판단하는 비관통 상호 제약 조건 (non-interpenetration constraint)를 사용하였다. 본 연구에서는 이를 확장하여 일반적인 두 물체 간에

적용하는 방법을 제안하였다. 이 방법은 충돌 시 반발 계수 (restitution)나 물체 표면의 부드러움 (softness)를 고려하여 보다 현실적인 충돌 해석을 가능하게 한다.

본 연구에서는 SPMT (self-propelled modular transporter)에 대한 모델링과 굴곡 있는 땅을 통과함에도 상판의 수평을 유지할 수 있는 축 보상 메커니즘 (axle compensation mechanism)을 구현하였다. 그 밖에, 유체력, 부력, 바람, 조류 등 다양한 외력도 구현하였다.

검증을 위해서 다물체 동역학의 벤치 마킹 테스트, 상용 다물체 동역학 프로그램 DAFUL 과의 비교를 수행하였다. 유연체의 경우는 해석해와 시뮬레이션 결과를 비교하였다. 유체력의 경우 WADAM RAO, OrcaFlex, SIMA 등 상용 소프트웨어와도 비교를 수행하였다. 마지막으로 해양 모듈 및 LQ 탑재의 현장 데이터를 수집하여 시뮬레이션과 검증을 수행하였다.

개발된 프로그램을 사용하여 본 연구에서는 이퀄라이저를 사용 블록 리프팅, 충돌을 고려한 LPG 탱크 탑재, 변형을 고려한 박판 블록 리프팅, 그리고 SPMT 를 사용한 블록 이동의 4 가지 해석을 수행하였다. 각각의 해석을 통해 본 연구에서 개발한 모듈들이 성공적으로 적용될 수 있음을 확인하였다.

향후에는 신규 공법에 대한 수요를 추가로 파악하고, 신규 공법에 맞는 새로운 검증 방법을 개발하고자 한다. 또한 각 조선소와의 협업을 통해 실제 현장 데이터를 확보하고, 모형 시험을 통해 프로그램에 대한 검증 작업을 수행할 계획이다.

**Keywords:** 통합 시뮬레이션 프레임워크; 공법 설계 검증; 다물체 동역학; 유연 다물체 동역학; Absolute nodal coordinate formulation; Discrete Euler-Lagrange equation; 구속 기반 와이어 로프; 비관통 상호제약 조건; 충돌; 이퀄라이저; Self-propelled modular transporter (SPMT);

Student number: 2014-30335